ACOUSTIC AND ELASTIC MULTIPLE SCATTERING AND RADIATION FROM CYLINDRICAL STRUCTURES

BY FERUZA ABDUKADIROVNA AMIRKULOVA

A dissertation submitted to the

Graduate School—New Brunswick

Rutgers, The State University of New Jersey

in partial fulfillment of the requirements

for the degree of

Doctor of Philosophy

Graduate Program in Mechanical and Aerospace Engineering

Written under the direction of

Andrew Norris

and approved by

_____

_____

_____

_____

New Brunswick, New Jersey

October, 2014

ABSTRACT OF THE DISSERTATION

Acoustic and elastic multiple scattering and radiation from cylindrical structures

by Feruza Abdukadirovna Amirkulova

Dissertation Director: Andrew Norris

Multiple scattering (MS) and radiation of waves by a system of scatterers is of great theoretical and practical importance and is required in a wide variety of physical contexts such as the implementation of "invisibility" cloaks, the effective parameter characterization, and the fabrication of dynamically tunable structures, etc. The dissertation develops fast, rapidly convergent iterative techniques to expedite the solution of MS problems. The formulation of MS problems reduces to a system of linear algebraic equations using Graf's theorem and separation of variables. The iterative techniques are developed using Neumann expansion and Block Toeplitz structure of the linear system; they are very general, and suitable for parallel computations and a large number of MS problems, i.e. acoustic, elastic, electromagnetic, etc., and used for the first time to solve MS problems. The theory is implemented in Matlab and FORTRAN, and the theoretical predictions are compared to computations obtained by COMSOL.

To formulate the MS problem, the transition matrix is obtained by analyzing an acoustic and an elastic single scattering of incident waves by elastic isotropic and anisotropic solids. The mathematical model of wave scattering from multilayered cylindrical and spherical structures is developed by means of an exact solution of dynamic

3D elasticity theory. The recursive impedance matrix algorithm is derived for radially heterogeneous anisotropic solids. An explicit method for finding the impedance in piecewise uniform, transverse-isotropic material is proposed; the solution is compared to elasticity theory solutions involving Buchwald potentials.

Furthermore, active exterior cloaking devices are modeled for acoustic and elastic media using multipole sources. A cloaking device can render an object invisible to some incident waves as seen by some external observer. The active cloak is generated by a discrete set of multipole sources that destructively interfere with an incident wave to produce zero total field over a finite spatial region. The approach precisely determines the necessary source amplitudes and enables a cloaked region to be determined using Graf's theorem. To apply the approach, the infinite series of multipole expansions are truncated, and the accuracy of cloaking is studied by modifying the truncation parameter.

Acknowledgements

First of all, I would like to thank my adviser, Dr. Andrew Norris, for patiently educating and guiding me throughout my research, and giving me valuable advice. He is ingenious, patient, and easygoing. I am also grateful for the financial support and learning opportunities that he has provided. I came to Rutgers with a theoretical background in math and solid mechanics, and when I started working with Dr. Norris, he taught me everything related to engineering, starting with basic ideas of wave propagation and going further into detailed explanation of complex problems such as modeling multiple scattering and cloaking phenomena. I will always keep in my mind what I learned from him.

I would also like to thank Dr. Haim Baruh, Dr. Haym Benaroya, and Dr. Yook-Kong Yong for serving on my dissertation committee. Dr. Baruh is the one who had accepted me to the graduate program. I took courses on Analytical Dynamics with Dr. Baruh and Random Vibration with Dr. Benaroya. I learned a lot from them, and they both always have been helpful. They also served in my M.Sc. Thesis committee; I am very grateful to them for their useful structural comments. Dr. Yook-Kong Yong of the Rutgers Civil Engineering Department is my out-of department committee member. I am very thankful for his willingness to serve on my dissertation committee, his interest in my work, and constructive commentary.

I would like to thank all my instructors: Dr. Ellis Dill, Dr. William Bottega, Dr. Mitsunori Denta, Dr. George Weng, Dr. Prosenjit Bagchi, Dr. Alberto Cuitino, Dr. Eugene Speer, Dr. Richard Falk, and Dr. Roe Goodman. I learned a lot about engineering at Rutgers that I could learn nowhere else. I am grateful to the Rutgers Mechanical and Aerospace Engineering Department for the teaching assistantship opportunities.

I would like to give special appreciation to Dr. Yuriy Gulak for his advice and things

he has done for me during my time at Rutgers. He had an answer to almost every question that I asked regarding programming, computers and science. His knowledge is broad. After just looking at the phenomenon, he gives ideas on which method to use to solve the problem. His programming advice always helped me when I needed it.

I would like to thank Dr. Alexey Kotelnikov for programming advice and helping me with access to SOE HPC clusters.

I would like to mention Dr. Linda Kurth to whom I very thankful for valued advice. I assisted her with her Senior Design and Manufacturing course; she treated me as a colleague and not as a subordinate.

I am very grateful to Dan Herbert, my English tutor from Plangere Writing Center at Rutgers, for reviewing my dissertation.

Last but not least, I would like to thank my family, my parents and my children. Six years at Rutgers took some of my time that I was supposed to spend with my children. Being a student and mother of three children was not so easy. My parents were the ones who gave me the opportunity to achieve what I have accomplished, my M.Sc. and Ph.D. degrees from Rutgers University and my B.Sc., M.Sc. and Ph.D. degrees from Samarkand State University.

Dedication

To my parents, Abdukadir Rabimov and Qambar Mirkamilova, and to my children, Dilnoza, Parvina, and Jahongir Amirkulov.

Table of Contents

Abstract ii

Acknowledgements iv

Dedication vi

1. Introduction 2

1.1. Background and Motivation 2

1.2. Current objective 4

1.3. Review of elastic and acoustic scattering from cylindrical structures and cloaking models 6

1.3.1. Review of single scattering from cylindrical structures 7

1.3.2. Scattering from multi-layered cylindrical shells and solids 9

1.3.3. Scattering from spherical shells and solids 12

1.3.4. Review of acoustic and elastic MS from solids and shells 15

1.3.5. Review of cloaking models 21

1.4. Research Outline 23

2. Preliminaries 25

2.1. The governing equations of elasticity theory 25

2.1.1. Cylindrically anisotropic media 26

2.1.2. Spherically anisotropic media 29

2.1.3. Impedance and matricant matrices 34

2.2. Displacement potentials 36

2.2.1. The Helmholtz potentials 36

2.2.2. Displacement potentials using Buchwald decomposition 36

2.2.3. Alternative decomposition 37

2.3. Scattering from homogeneous isotropic cylinders 37
2.3.1. Acoustical preliminaries 39
2.3.2. P/SV in-plane wave propagation 42

3. Scattering from multilayered cylindrical and spherical structures . . 50
3.1. Impedance matrix method 50
3.1.1. Calculating the global impedance matrix 52
3.1.2. Impedance for uniform transversely isotropic cylinders 53
3.1.3. Example: Acoustic scattering from an elastic cylinder in water . 57
3.1.4. Impedance for multilayered radially inhomogeneous sphere . . . 60
3.2. Elastic and acoustic scattering from TI cylinders 63
3.2.1. Elastic incident and scattered waves 64
3.2.2. Boundary Conditions 66
3.2.3. Impedance matrix 67
3.2.4. Acoustic SH wave 69
3.3. Global matrix method for an isotropic multilayered elastic cylinder . . . 73
3.3.1. Acoustic scattering from an isotropic multilayered cylinder . . . 74
3.3.2. Elastic scattering of P/SV waves from a multilayered cylinder embedded in elastic medium 94

4. Acoustic and elastic multiple scattering and radiation from planar configuration of parallel cylindrical shells 102
4.1. Acoustic multiple scattering and radiation from planar configuration of parallel cylindrical shells 102
4.1.1. Multiple scattering theory 102
4.1.2. Numerical results: small M and k 110
4.2. Elastic Multiple Scattering and Radiation from Planar Configuration of Parallel Cylindrical Shells 120
4.2.1. Elastic multiple scattering theory 120
4.2.2. Numerical results 124

5. Iterative methods for solution of multiple scattering problems . . . 127

5.1. Matrix types . . . 128

5.1.1. Toeplitz matrices . . . 128

5.1.2. Multilevel matrices . . . 132

5.2. Biorthogonal polynomials . . . 136

5.2.1. Orthogonal polynomials . . . 137

5.2.2. Biorthogonal polynomials . . . 144

5.3. Iterative methods for solution of a linear system of equations . . . 148

5.3.1. A Neumann series expansion at a fixed value of frequency . . . 148

5.3.2. An iterative approach for a band of frequencies . . . 150

5.3.3. Fast preconditioned iterative methods . . . 151

5.3.4. Iterative methods for a Block Toeplitz systems . . . 153

5.4. Numerical results . . . 158

5.4.1. Neumann expansion study . . . 158

5.4.2. Numerical results using an iterative method for Block Toeplitz matrix of level 1 . . . 165

6. Acoustic active exterior cloaking . . . 170

6.1. Introduction . . . 170

6.2. Source amplitudes for active exterior cloaking . . . 171

6.2.1. Problem overview . . . 171

6.2.2. Proofs of Theorems 1 and 2 . . . 175

6.3. Velocity field in an acoustic cloaked region . . . 180

6.4. Acoustic Scattering from a Cylinder in a Cloaked Region . . . 181

6.4.1. Scattering from cylinder . . . 181

6.4.2. Cylinder in a cloaked region . . . 182

6.5. Numerical examples . . . 183

6.5.1. Active source configuration . . . 183

6.5.2. Near and farfield amplitudes . . . 184

6.5.3. Total field . . . 189
6.5.4. Scattering examples . . . 191
6.6. Discussions and Conclusions . . . 193

7. Elastic active exterior cloaking . . . 197
7.1. Problem formulation and main results . . . 198
7.1.1. Problem overview . . . 198
7.1.2. Summary of the main results . . . 200
7.2. Solution for the source amplitudes . . . 202
7.2.1. Integral equation . . . 202
7.2.2. General expressions for the source amplitudes . . . 203
7.2.3. Integral expressions for arbitrary incidence . . . 204
7.2.4. Plane wave incidence . . . 206
7.2.5. Arbitrary incident field as superposition of plane incident waves 210
7.2.6. Necessary and sufficient conditions on the source amplitudes . . 211
7.2.7. Divergence of the active field summation . . . 212
7.3. Numerical examples . . . 213
7.3.1. The scattering amplitudes . . . 214
7.3.2. Farfield response . . . 217
7.3.3. Total displacement field . . . 220

8. Concluding remarks and future work . . . 227
8.1. Conclusions . . . 227
8.2. Future work . . . 228
References . . . 229

Chapter 1

Introduction

Chapter 1 starts with the discussion of the background and motivation for the topics considered in this work. Next, this chapter establishes the questions we aim to answer in this dissertation, specifically it considers current objectives of multiple scattering problems, and provides an overview and literature review of research on scattering and cloaking phenomena. At the end of the chapter, the outline of research is presented.

1.1 Background and Motivation

Multiple scattering (MS) by a system of obstacles is an important topic, of great practical and theoretical interest in a wide variety of physical contexts. A computation of the wave field scattered by multiple objects that takes into account the interaction between the obstacles is required in numerous wave propagation problems. These problems include modeling acoustic devices that precisely control and guide propagating waves in a defined manner for specific applications, i.e.: the implementation of "invisibility" cloaks; the fabrication of dynamically tunable structures such as the gradient index lenses and waveguides; and the characterization of effective parameters of heterogeneous media. A broad literature review on single and MS and the concepts of MS are given in [98].

The development of numerically efficient techniques and algorithms that are appropriate for a wide range of problems is one of the main interests of wave propagation analysis. The expensive costs of direct matrix inversion of a linear system motivates the development of numerically efficient iterative methods. The use of the method of separation of variables and Graf's addition theorem leads a formulation of an MS problem to the linear system of an infinite number of equations which can be reduced to

the finite dimensional system of equations of the form:

$$\mathbb{X}\,\mathbf{b} = \mathbf{d}, \tag{1.1}$$

where $\mathbb{X}$ is the known interaction matrix that defines the coupling between each scatterer of the configuration, $\mathbf{b}$ is the column vector of the unknown scattering coefficients, and $\mathbf{d}$ is the column vector of the known coefficients of the excitation field. The matrix $\mathbb{X}$ is a complex valued dense $\mathtt{N} \times \mathtt{N}$ matrix, and $\mathtt{N}$ is proportional to the number of scatterers M multiplied by $2n+1$ where n is the mode number. For high frequencies and a large number of scatterers, the system (1.1) becomes an extremely large scaled linear system. The computational complexity of inversion of matrix $\mathbb{X}$ by direct methods is $O(\mathtt{N}^3)$, i.e. Gauss-Jordan method requires n^3 multiplication operations and n^3 addition-subtraction operations, Gauss method using LU decomposition requires $n^3/3$ multiplication and $n^3/3$ addition-subtraction operations. The memory requirements to solve (1.1) by direct methods grow as $O(\mathtt{N}^2)$. This is prohibitive for many realistic multiple scattering problems at high frequencies and a large number of scatterers. For a large $\mathtt{N}$ and required number of iterations, the most widely used Krylov Space methods such as GMRES, BICGSTAB, and etc. can cause excessive run times [127, 3]. If the $\mathbb{X}$ matrix has some specific characteristics than the computational complexity can differ. When the $\mathbb{X}$ matrix has a Toeplitz structure, its inversion requires $O(\mathtt{N}^2)$ arithmetic operations using Levinson and Trench algorithms [167, 9]. The inverse of Toeplitz matrix can be decomposed into the sum of two multiplications of triangular Toeplitz matrices using fast recursive algorithms [15, 185, 65, 74]. These algorithms have a simple description and use a simple storage; they require $O(\mathtt{N}log_2\mathtt{N})$ arithmetic operations and the memory of order $O(\mathtt{N})$. There is a correspondence between the scalar algorithms [15, 65, 74] for Toeplitz matrix and their block analogs [185, 9] according to which block multiplications and additions in block algorithms correspond to multiplications and additions in scalar case. Specifically, for some planar configuration of cylindrical structures, $\mathbb{X}$ matrix has a Block Toeplitz structure which allows us to use such algorithms and greatly reduce a simulation run time. This question will be investigated in this work in detail.

Another subject considered in this work is the cloaking phenomenon which is currently a very popular research topic in Acoustics. This phenomenon is studied using different approaches such as transformation acoustics, impedance acoustics, the homogenization of layered media, and the multipole expansion method. A cloak can make objects invisible to some wave as seen by some external observer. There are two quite distinct types of cloaking models: passive and active. A passive cloak guides the incident waves around an object that is to be cloaked and suppresses scattering from it. Passive cloaking requires designing a metamaterial that can bend acoustic waves and guide the wave energy around the object regardless of the incident wave. In recent times a rather different approach to cloaking has been noted as an alternative. We call it *active exterior cloaking* in keeping with prior terminology [179]. An active cloak generated by a set of discrete of active sources cancels out the incoming waves in cloaked region and produces a negligible far-radiated field. The method proposed in this work allows us to explicitly calculate the necessary source amplitudes and enables us to identify a cloaked region using Graf's addition theorem. Cloaking devices have broad applications, including national defense, healthcare, microelectronics, civil engineering, and aerospace engineering. These devices can be exploited for biomedical imaging, earthquake mitigation, and heat protection; to build better insulated backgrounds for laboratories, concert halls, and soundproofing homes; to conceal objects from sonar such as stealth warships and submarines; and for other uses that would benefit society.

1.2 Current objective

We want to develop a methodology that will allow us to study acoustic and elastic multiple scattering and radiation from cylindrical structures for its future application to wave propagation problems, i.e. modeling waveguides, lenses [162], resonators, and cloaking devices.

Despite much fundamental research, as detailed in Section 1.3, there are still many issues that need to be studied more thoroughly. Specifically, the formation of effective methods of studying the influence of interaction between the scatterers on MS; the

creation of efficient iterative techniques that are general and applicable for a large number of complex scattering problems; the development of advanced techniques for a solution of MS problems at a high frequency range and large number of obstacles; the formation of feasible methodology that will improve cloaking and diminish a trade-off between a cloaking performance and construction difficulty; and the development of innovative techniques for material characterization.

In this work, the scatterers are cylindrical and spherical structures of circular shape, such as elastic shells, solids, and multilaminates, as well as rigid bodies and holes. Therefore, an MS problem is solved by using the MS theory that best fits such configurations. The approach is to reduce the MS problem to a family of single scattering problems. The single scattering solution for an elastic scatterer is utilized to develop a T-matrix for each scatterer. Then, a global matrix is developed by means of MS theory that includes the effect of MS between the scatterers, and enables us to find the scattering coefficients and far-field behavior. This method leads to a linear algebraic system; its complexity grows as the number of scatterers and frequency increases, requiring the development of iterative algorithms for parallel computing. Taking advantage of the Block-Toeplitz structure of the system, the iterative Krylov subspace methods are applied, and some iterative approaches are proposed with the use of the Neumann expansion and bi-orthogonal polynomials to increase the efficiency and reduce the computational cost.

Although cloaking phenomena have been well researched, there is no precise model which has a realistic physical implementation. Therefore, we are interested in modeling wave propagation in general anisotropic solids in order to develop scattering solutions related to metamaterial devices such as “invisibility” cloaks. Passive acoustic cloaking devices [117, 111, 143] can be modeled as radially inhomogeneous anisotropic solids. One of our goals is to produce a stable solution method for such materials which was proposed in our work [114] for a cylindrically anisotropic medium. We are also interested in designing active exterior cloaking generated by multipole sources. The aim of active exterior cloaking is to render the total field zero inside some prescribed domain and to produce a non-radiating active field in the farfield. The technique introduced in

our early work [112] on acoustic active exterior cloaking enables us to find a cloaked region using Graf's addition theorem and to reduce the integral representations of Vasquez et al. [181] for the source amplitudes to closed-form explicit formulas. Using this technique, one can avoid the reduction of the integral equation of Vasquez et al. [179, 180] to a system of linear equations which require a numerical solution or evaluation of line integrals, as proposed in [181]. An active exterior cloaking has been applied to the elastodynamic context for the first time in our succeeding work [108]. The approach enables us to precisely determine the necessary source amplitudes of nearfield and farfield. The infinite series of multipole expansion of the source is divergent inside the circle that is centered on the source itself. Therefore the determined source amplitudes are not valid in the domain in which the active sources are located. This issue was not considered in active cloak modeling but was noted in [84] in designing an anti-sound device. To overcome this issue in practice, the infinite series are required to be truncated, which reduces the accuracy of solution. Thus, by varying the truncation number, we investigate the accuracy of cloaking which requires only a small number of multipoles as will be shown in Chapter 6 and Chapter 7.

1.3 Review of elastic and acoustic scattering from cylindrical structures and cloaking models

A computation of a field that is scattered by multiple objects that takes into account the interaction between the obstacles is required in numerous problems of acoustic, electromagnetic, and elastodynamic wave propagation. These problems include the MS of acoustic waves by obstacles, the scattering of sound in the environment, and elastic and electromagnetic waves in composites and human bodies. Our interest here is with examining an acoustic and elastic MS from obstacles.

Two analytic methods extensively employed in the literature on scattering are the separation of variables [98], and the integral equations formulation [186]. For single obstacles whose geometries conform to separable coordinates, i.e. cylindrical or spherical, the scattering problem can be solved by the eigenfunction expansion method, which is

also called the multipole expansion method. For scatterers with geometries that do not conform to separable coordinates, an integral equation method can be used, such as the direct numerical solution of integral equations, or the null field method also known as T-matrix approach [186, 177, 98]. These analytical approaches allow us to reduce an MS problem for an arbitrary configuration of a finite number of scatterers to a family of single scattering problems. Hence, the analytical tools used to find the response of configurations of multiple objects follow from the analysis of scattering by single scatterers [169, 176, 141, 28]. Below we will give a literature study of single scattering problems, followed by a literature review of investigations conducted on MS problems for obstacles of different geometries.

1.3.1 Review of single scattering from cylindrical structures

A good review on acoustics of cylindrical and spherical shells on scattering from cylindrical and spherical solids is given by Überall [171]. Both theoretical and experimental aspects are considered. Gaunaurd [63] gives an extensive and comprehensive bibliography and a review of topic on scattering from cylindrical and spherical shells and solids. More recent studies address cylinder scattering with relation to fiber scattering in composites, piezoelectrics, anisotropic solids, and inhomogeneous solids and take into account multiple scattering in a scatterer.

Elastic and acoustic wave scattering from a solid cylinder

An investigation of acoustic scattering of normal incident plane acoustic waves by isotropic elastic cylinders and spheres was initiated by Faran in 1951 [55]. Faran extended the theory of the scattering of plane sound waves to include SH waves. The scattering field was given as a function of specular reflection and circumferentially traveling geometric waves and elastic circumferential waves. Computed scattering patterns were in a good agreement with experimental measurements. The normal scattering of incident plane waves by cylinders and plates immersed in water was studied by Maze et al.[99]. Backscattered spectrum was calculated using the Resonance Isolation and Identification Method; supplementary resonances were obtained for aluminum. It was

shown that resonances correspond to natural modes of vibration. Experimentally detected resonances were considered as normal modes of the target. The solution of the problem of scattering of an obliquely incident plane wave from an isotropic elastic cylinder was obtained and compared with experimental measurements by Li et al. [92]. The solution was given in terms of phase angles. The excitation of supplementary resonances was noticed for small incidence angles. A theoretical model of the scattering of an obliquely incident plane wave from an infinite aluminum cylinder was developed by Flax et al. [57] to study the influence of axial coupling on the geometric diffraction from a cylinder of infinite length and resonance behavior. In the limiting case of taking the angle of incidence as zero, the solutions given in [92] and [57] correspond to the previously given scattering description of Faran [55].

Honanvar et al. [78] provides the first complete theory applicable to a uniform transversely isotropic cylinder in 1996. The displacement field was decomposed into scalar and vector potentials using the displacement decomposition proposed by Morse and Feshbach [105] that will be discussed in Section 2.2. Potentials were expanded in series of normal modes. In this model the influence of each element of the stiffness matrix on the various vibration resonant modes was shown. In the case of weak anisotropy the solution reduces to a simple model for an isotropic cylinder. Numerical calculations were performed first for an isotropic aluminum cylinder. Then the effect of perturbation of the elastic constants of an aluminum cylinder on the form function was evaluated. Ahmad et al. [5] also studied the scattering of acoustic waves from a transversely isotropic cylinder immersed in a fluid. The solution was obtained by employing Buchwald's potentials [26] and a normal mode expansion. The existence of two distinct types of transversely isotropic materials, namely type I and type II, was shown. The expected behavior of the form functions of such materials was described. Critical angles of the incidence were shown, away from these angles an angular pattern of scattering field alters significantly. Honarvar et al. [77] showed the physical differences between two types of transversely isotropic materials classified by Ahmad et al. [5]. Rahman et al. [132] and Ahmad et al. [5] showed that the displacement decomposition [105] used by Honanvar et al. [78] results in 5th order PDEs, lengthy coupled equations for

potential functions, whereas Buchwald's representation yields much simpler equations, in the form of compact second order PDEs. They also noted that these representations lead to identical characteristic equations and the same final result. Buchwald's potential yields simpler expressions; it is less laborious and much more efficient in application for an isotropy, transverse isotropy [107], [4], [32] and general anisotropy [116].

Scattering from cylindrical shells consisting of one layer

Scattering from an infinite isotropic elastic hollow cylindrical shell by an obliquely incident plane acoustic wave was investigated by Maze et al. [89]. The far-field form function was calculated for an aluminum hollow cylindrical shell in water by the direct summation of the Rayleigh series. The theoretical results are compared with the experimental results showing a good agreement between them. Veksler et al. [183] presents an analytical solution to the scattering problem of a plane compressional wave by a circular cylindrical shell embedded in an elastic matrix. The resonances were computed from the dispersion relations. The behavior of different scattered waves were studied, and the resonance contribution of these waves were shown for a thick walled shell. When the inner radius of the shell b tended to the outer radius, the scattering by an empty cavity was considered. When the inner radius b tended to 0 another limiting situation was obtained: the scattering by an elastic cylinder in an elastic matrix. In [109] an asymptotic solution of the problem of acoustic wave scattering from heavily fluid loaded thin isotropic cylindrical and spherical shells is derived by Norris et al. from combined outer and inner fields using matched asymptotic expansions. The proposed method is developed on the basis of thin shell theory and is effective in the midfrequency range, and it describes the total acoustic response as the sum of background response and resonant contribution.

1.3.2 Scattering from multi-layered cylindrical shells and solids

Scattering by single multilayered scatterers has been conducted extensively. Most scatterers have simple geometry, such as a cylindrical or spherical shape. Below we will consider these works in detail. At the end of this section we will consider some works on

multiple scattering (MS) in a single scatterer. The effect of MS between the scatterers will be considered in Section 1.3.4.

Acoustic scattering from multi-layered cylindrical shells and solids

The scattering field of an oblique plane wave of incidence from a circular clad rod of infinite length was calculated by Honarvar et al. [79]. Using Resonance Scattering Theory (RST) the effect of various resonance frequencies on the variation of cladding thickness was evaluated, where high frequency resonances were shown to be more sensitive than low frequency resonances. Form functions of a copper-clad aluminum rod were evaluated for different incident angles of a plane wave. The comparison of numerical calculations with experimental measurements show good agreement. Orthotropic cylindrical shells submerged in and filled with compressible ideal fluids were considered by Hasheminejad et al. [72] using a state space formulation for the sequentially laminated piecewise homogeneous configuration. The method of wavefunction expansion is used to study the effects of inner fluid loading along with the shell thickness on the frequency response of the shell. The correlation between the perturbation in elastic constants of loaded shell material and the sensitivity of resonances associated with various modes appearing in the backscattered field is obtained.

The methods developed in [72] are generalized in [73] for an axially polarized piezoelectric material. Hasheminejad et al. [73] examined 3D acoustic scattering of a plane incident sound wave from thick bilaminated circular cylindrical shells consisting of an axially polarized piezoelectric cylindrically orthotropic inner layer and orthotropic outer layer. Shells are submerged in and filled with compressible ideal fluids. Numerical calculations for the total form function amplitude including the associated global scattering, the far-field inherent background and the resonance scattering coefficients of the n th normal mode are performed based on acoustical RST for different electrical boundary conditions. Jamali et al. [82] studied a scattering by functionally graded cylindrical shells and calculated an acoustic radiation force in shell caused by a plane harmonic wave incidence using the eigenfunction expansion method. They employed a laminate approximate model and T-matrix approach to present an analytical solution based on

2D elasticity. Numerical results are presented for a form function and radiation force.

Elastic scattering from multi-layered cylindrical shells and solids

Beattie et al. [17] both theoretically and experimentally studied backscattering of incident compressional and shear SH waves from an isotropic elastic cylinder embedded in an elastic matrix. Scattering from a fiber-matrix interphase in a four-phase composed system, consisting of a matrix and a three-phase fiber, was studied by Huang et al. [81] for incident longitudinal and transverse waves using a standard normal-mode expansion method. Different simplified approximate models were considered to show the effect of the fiber-matrix interphase on scattering. Sinclair et al. [152] proposed a mathematical model for the scattering of elastic waves from a reinforcing fiber, consisting of a graphite core and surrounded by a vapor-deposited SiC layer embedded in a titanium alloy matrix. A normal mode technique was used to derive the scattering spectrum. Numerical calculations were compared with experimental data for a form function.

The original formulation of scattering from a transversely isotropic cylinder submerged in an acoustic medium given in [78] was generalized by Fan et al. in [54] to the case of a cylinder embedded in an elastic matrix. The formulation of scattering problem was provided for incident plane longitudinal, axially polarized shear and transversely polarized modes. The solution was obtained using normal mode expansions. Obtained results point to the sensitivity of several resonances to the perturbation of elastic constants of the cylinder for each type of scattered waves. Niklasson et al. [107] provided an alternative but similar formulation of the scattering problem for the solid-solid case. The problem is solved by employing the method of separation of variables and Buchwald's potentials [26] for the displacement field. It was noted that in the case when there is a cavity in a transversely isotropic medium, the reflected shear waves are much stronger than in the case with a solid cylinder. Fan et al. [53] discuss physical characteristics displayed by the original general solution of Honarvar et al. [78]. The circumferential resonance modes of a submerged cylinder were studied over a large range of incidence angles using RST. The shift of resonance frequencies to higher frequencies was noticed with the growth of incidence angle.

Piezoelectric hollow cylinders have been considered in [130]. Qian et al. [130] studied the scattering of incident elastic P-waves from a transversely isotropic piezoelectric cylinder embedded in an infinite polymer matrix. The solution was obtained using the method of wavefunction expansion. The stress distribution, mechanical displacements and electrical potential around the piezoelectric cylinder were calculated. The effects of incident angles over a range of normalized frequency along with the change in radius of the cylinder on the mechanical stress field and electric field concentrations were studied in detail, and the physical explanations were given for such effects. The results of this paper can be used in modeling piezoelectric composites, particularly, when piezoelectric cylinders are aligned sparsely in a matrix medium.

Cai [30] presented an analytical solution for the scattering of antiplane elastic waves by a layered circular elastic cylinder embedded in an elastic medium of infinite extent. Numerical calculations are performed for a ceramic-fiber reinforced metal-matrix composite system. The effects of the geometrical and physical properties of the interphase were investigated. When the outer cylindrical layer is more compliant and the inner core undergoes a rigid body motion, a resonance mode was noticed. This approach was generalized by Cai, in [27], to study scattering by a multilayered scatterer using MS process, which is based on the observation that elastic MS occurs in a single scatterer which has an inner structure. The proposed approach can be extended for studying multi-core structures, i.e. multiconductor cable, and can be used for analyzing scatterers of more complicated geometrical and physical compositions.

1.3.3 Scattering from spherical shells and solids

Acoustic scattering from spherical shells and solids

Acoustic scattering by elastic spherical shells and solids submerged in water has been investigated widely [135], [75], [55], [109], [171], [76]. Early work was conducted almost one and a half centuries ago by Rayleigh [135] on the scattering of sound-waves by small elastic discontinuities, e.i. perfectly rigid and fluid spheres of small size, considering scatterers in which $ka << 1$ (where k is wave number and a is radius). This case of

scattering is referred to as *Rayleigh scattering*. Herzfeld [75] modified and extended Rayleigh's approach to a solid sphere with finite elastic constants. Herzfeld studied the scattering of longitudinal waves by an elastic sphere submerged in a viscous fluid, but he did not include the scattered shear wave. The scattering field was obtained in the form of a progressing series of zonal harmonics where each harmonic depends on the radius vector and is multiplied by an unknown coefficient. Therefore, the unknowns were determined from the surface conditions at the interface by taking the factors of each zonal harmonic separately.

Epstein et al. [51] conducted research on sound absorption in fogs and considered the longitudinal wave scattering problem for fluid spheres in a fluid medium incorporating both thermal conductivity and viscosity. Explicit expressions for the attenuation to water particles in air were derived from general results, considering the particular case of liquid droplets suspended in gases. The comparison of calculated and experimental data was shown for an attenuation. Hickling [76] both theoretically and experimentally studied the scattering of shear and compressional waves from a homogeneous solid sphere submerged in an acoustic medium; numerical calculations of backscattering spectrum and pulse forms of echoes were presented.

An approach that describes the acoustical background of a submerged elastic isotropic spherical shell for a suitable thickness over an entire frequency range was developed by Werby [187]. It was shown that a background at a higher frequencies and thicker shells is equivalent to a rigid background, whereas low frequencies with a thin shell approximation it tended toward a soft background. Dacol et al. [42] presented the numerical solution of the secular equation obtained by Fikioris and Waterman for the effective wave number of an acoustic field propagating in a medium with a random distribution of identical spherical scatterers. This method was further generalized to the case of an arbitrary two-point correlation function in the positions of any two scatterers. Martin [97] studied the problem of acoustic scattering from a sphere, specifically scattering by an inhomogeneous sphere submerged in a homogeneous fluid, and scattering by a homogeneous sphere with a concentric inhomogeneous coating. It was assumed that the

material parameters are spherically symmetric functions of the position vector. The radial parts of the solutions were given in terms of Coulomb wave functions or Whittaker functions.

Elastic scattering from spherical shells and solids

The idea of acoustic scattering from a sphere was generalized to model elastic scattering problems from a sphere embedded in an elastic matrix [190], [86], [50], [56], [147]. Ying et al. [190] generalized Herzfeld's [75] formulation of scattering by a solid sphere of an incident acoustic compressional wave to include elastic properties of incident and scattered waves. The scattered field was obtained using continuity conditions for displacements and stresses at the interface. Calculations were performed for the problem of scattering of a longitudinal wave by an isotropic elastic sphere and a rigid sphere embedded in an elastic medium, and a spherical cavity surrounded by an elastic medium. Mechanical properties of scatterers differed from those of the surrounding matrix material. Rayleigh scattering and some other limiting cases were discussed in detail. Expressions for the scattering cross section were derived for an elastic sphere, a fluid sphere and a spherical cavity.

Knopoff [86] studied the scattering of incident plane shear waves by a perfectly rigid, infinitely dense sphere situated in an elastic medium. The scattered field includes both longitudinal P and transverse S modes. One S modes corresponded to the SH mode and the other to the SV mode. Numerical calculations were shown for a group of obstacles with radii very small compared with wave length and radii equivalent to the wave length. Einspruch et al. [50] and [49] employed the method of Ying et al. [190] to study the scattering of delitational [49] and distortional [50] elastic waves by spherical obstacles. For incident longitudinal waves, the scatterer was considered as a fluid-filled cavity embedded in an isotropic elastic matrix and the scattering coefficients were obtained from the 3 by 3 system of linear equations. For incident transverse waves the scattering problem was considered as 3D and the obstacle was taken as a fluid-filled cavity, an empty cavity, a rigid sphere, and an elastic sphere embedded in an elastic medium with different physical parameters. In the last case, an elastic sphere

embedded in a matrix, the boundary conditions yielded the 6 by 6 system of linear equations from which the scattering coefficients were obtained. The scattering cross section for a transverse wave was calculated and the Rayleigh limit was considered.

Flax et al. [56] studied the resonance effects in the elastic scattering of shear waves from solid spherical inclusions. Numerical results are presented for resonances and a backscattered form function of the solid inclusions surrounded by a Lucite or iron sphere embedded in an elastic matrix. Sessarego [147] studied the scattering by an elastic sphere embedded in sediment. A physical interpretation of scattered circumferential waves was given in terms of monostatic and bistatic scattering cross sections. The resonance behavior of the target was determined numerically in the individual normal mode amplitudes. Numerical computations were in agreement with experimental measurements for an aluminum sphere embedded in Plexiglas.

1.3.4 Review of acoustic and elastic MS from solids and shells

Here, we will review an acoustic and elastic MS from scatterers of different geometries. The extended bibliographical overview and concept of MS from obstacles are given by Martin [98]. There are several analytical methods to solve MS problems. An MS solution can follow from the analysis of wave scattering by single obstacles. For obstacles with variable-separable geometries, the solution of an MS problem can be obtained by the multipole expansion method [141, 169, 98, 177]. The multipole expansion method for variable-separable geometries can be applied in two ways. The first one allows us to find the total multiple scattered field of the configuration in terms of the scattered waves from each obstacle using a Fourier series expansion and combining separable solutions for each obstacle with Graf's addition theorem. The method is exact, and leads to an infinite system of algebraic equations; in the system, the infinite sums are truncated to use in practice. The approach was first used by Záviška [191] to solve 2D electromagnetic scattering problem for circular cylinders, and was broadly applied to tackle MS problems due its conceptual simplicity and numerical effectivity [98, 177, 175, 176, 7]. This approach will be used in the analysis to follow.

The "Ordered scattering" is another technique in the multipole method used by

Twersky [169] for acoustic and electromagnetic MS problems. This iterative procedure can be described as follows. The first-order scattering results from the excitation of scatterers by primary incident wave. The field scattered by each scatterer is found by translating the primary incident wave to the origin of local coordinate system and using single scattering analysis. The second order scattering from one of the scatterers results from the excitation by the first order of scattering from the remaining scatterers, and so on to higher order of scattering. The calculation of higher orders of scattering is continued until the convergence of results is reached.

For scatterers with geometries that do not conform to separable coordinates, MS solutions can be calculated using the integral equation methods [58], [186], [177]. The T-matrix formulation introduced by Waterman [186] for acoustic scattering from a single scatterer was applied by Peterson and Ström [123] to study acoustic MS from elastic scatterers including the full interaction between the scatterer. The method was generalized in [124] to investigate an acoustic MS from elastic multilayered scatterers, and further by Peterson et al. [126] to study an elastic MS of in-plane(P/SV) waves from fluid inclusions in elastic medium. Varadan and Varadan employed T-matrix formulation using the multipole expansions to examine an elastic MS of both SH waves [175] and P/SV waves [173, 176] from elastic scatterers embedded in elastic medium.

Review of acoustic MS from solids and shells

Radlinski and Meyers [131] have investigated the scattering of waves radiated by an oscillating cylinder surrounded by a circular cage of rigid cylinders. They have shown a good agreement between a 2D analysis and experimental measurements of a farfield radiation for cages consisting of 6 and 12 cylinders. Klyukin [85] has investigated both theoretically and experimentally the problem of an acoustic MS of plane waves by a 2D grating of rigid cylinders; a comparison of results for reflection characteristics shows a good agreement with the experimental data.

Three different solutions for an MS problem for 2 cylinders are presented and compared with experimental data by Gustafson and Stepanishen [69]. Their theoretical

solutions are based on the eigenfunction expansion method or thin cylinder approximation, including either the effects of all orders of MS or the effects of only zeroth order scattering, or excluding all effects of scattering and interactions between the cylinders. An acoustic MS of plane waves by an array of rigid cylinders moving in an ideal inviscid fluid has been examined by Lin and Raptis [93]. Their technique involves formulating analytical expressions of scattering functions, and determining the effects of MS and vibration of cylinders on the scattering pattern; calculations are performed for a cluster of carbon and brass cylinders submerged in water, having different geometrical configurations of one, two, three, and seven circular cylinders. The scattering matrix S and its relationship with the scattering resonances and the cross sections have been explicitly obtained by Gaspard and Rice [62] for the scattering of a point particle from three hard discs fixed on a plane using Green's theorem. They have also reported a comparison of results for the semiclassical and quantum dynamics of the point particle-three hard disc system giving hints for more complex dynamical systems. Kubenko, V.D [88] has presented an analytical solution to the problem of MS of acoustic waves by two nonparallel circular cylinders based on successive application of Graf's addition theorem; the soft cylinders are considered specifically. Scharstein [144] researched the effects of coupling between two parallel soft cylinders of different radii via a comparison of far scattered fields computed by his proposed method and a superposition of non-interacting far fields of the isolated cylinders.

The effect of incident waves on circular arrays of identical circular cylinders has been considered by Evans and Porter [52]; resultant forces versus wavenumber are calculated for symmetric and asymmetric arrangement of four, five and six cylinders; real parts and magnitudes of velocity potentials have been shown for a ring of four, five and six cylinders. Wirzba [188] has studied 2D convergence problems of periodic orbit expansions of the non-overlapping disconnected n-disk repellers, and derived the T-matrix of the n-disk scattering systems by the methods of stationary scattering theory. Decanini et al. [44] have proposed an exact formalism to obtain an S matrix for an N-disk system under different boundary conditions; explicit formulas for an S matrix, form function and scattering resonances are derived for $C_{2\nu}$, $C_{3\nu}$ and $C_{4\nu}$ symmetry

configurations. In the second part of paper [44], Decanini et al. [45] have determined the resonances of the two- and three-disk systems with $C_{2\nu}$ and $C_{3\nu}$ systems; numerical results are presented for various boundary conditions. Grote and Kirsch [67] have derived a Dirichlet-to-Neumann (DtN) boundary condition for the numerical solution of MS problems for the obstacle consisting of several disjointed components; being a natural boundary condition, the DtN condition fits into a variational formulation of BVP allowing easy use of FEM, and yields an exact formula for the far-field form function. Decanini et al. [43] have investigated MS by two identical cylinders with respect to the symmetry of configuration; positions of scatterer resonances and their physical interpretation are given for soft, hard, and elastic cylinders.

Hasheminejad and Alibakhshi [70] have studied MS effects of 2-D acoustic scattering in fiber suspensions considering the interactions of a plane compressional sound wave with a cluster of two flexible fibers submerged in a boundless viscous fluid medium; comparisons of angular distribution of the form function are presented for polymeric, elastic, and rigid cylinders at selected distances and frequencies. Sherer [149] studied acoustic MS generated by two types of axisymmetric sources by a grating of arbitrary parallel multiple rigid circular cylinders of varying radii; the incident field is determined from a cylindrical line source and a spatially distributed acoustic source.

Lethuillier et al. [91] studied both theoretically and experimentally MS by a finite linear grating of elastic cylindrical shells. Analytical solutions for MS problem were obtained using the multipole method in conjunction with the concept of T-matrix. Numerical and experimental results are given for grating of 2 to 5 shells to study the resonant interaction between close shells. This approach also was employed by Bas et al. [13] to study MS of acoustic plane harmonic incident waves from an arbitrary configuration of cylinders (aligned or not). The S (scattering) matrix of an N-shell cluster was defined and a resonance spectrum was investigated. Numerical results for aligned cylinders were in agreement with previously published results [91]. The multipole method via T-matrix formulation was further employed by Cai et al. [31] to study MS of acoustic waves by arrays of penetrable circular steel cylinders in waveguides. They showed that the evanescent modes are important and could become dominant at

some frequency range. An isovelocity examples were given for waveguide with uniform physical properties and constant waveguide depth. MS in the waveguide is compared with the corresponding 2D case for the cluster of 20 by 40 identical cylinders. Along this line Antoine et al. [7] investigated acoustic high-frequency MS from realistic complex configurations consisting of numerous circular cylinders; calculations were performed for a single-row configuration, a centered uniform square lattice, a triangular lattice, and an unstructured geometrical configuration. Iterative Krylov space methods were applied taking the advantage of the structure of algebraic linear system.

Sodagar et al. [153] studied MS of an oblique incident plane wave from a grating of cylindrical shells submerged in an acoustic medium. For shells, the general solutions of governing equations of 3D elasticity are found using the Helmholtz decomposition. MS solutions are obtained iteratively using Twersky's [169] "Ordered scattering" technique. A detailed study of resonances of the shells and the effect of the center-to-center distance of the shells on these resonances is conducted. Numerical results are compared with experimental data for a grating of 2-3 aligned cylinders.

Schwartz et al. [146] proposed a multiple-scattering theory of longitudinal coherent wave propagation in composite structures consisting of spherical solid grains submerged in an ideal fluid. It was shown that for primitive ordered cubic suspensions, governing equations reduced to a system of coupled equations which had a solution of the form predicted by Biot; for disordered suspensions the Biot formula did not hold. Illustrative numerical calculations for the case of densely packed composites were presented.

Review of elastic MS from solids and shells

An extensive bibliography and a wide variety of problems that have been solved using the T-matrix approach was given in [177, 174]. Waterman's [186] T-matrix formulation was employed by Varadan and Varadan [175] to study MS of SH waves from elastic cylinders of arbitrary cross section using the multipole expansion method. The T-matrix approach was further elaborated by Varadan and Varadan [177, 176] to study MS of P and SV waves from an elastic scatterer in an elastic medium. The formulation includes a full interaction between the scatterers and involves only the T-matrix of a

single obstacle. This method conceptually differs from the integral equation formulation used by Peterson and Ström [123], Boström [21], and Peterson et al. [126, 125] that deals with a total transition matrix resulting from all scatterers together.

Twersky's [169] "Ordered scattering" technique was applied to investigate elastic MS from grating of scatterers in the following works [37, 141, 28]. Cheng [37] provided a formal solution of MS of incident elastic P waves from a grating of rigid cylinders embedded in an elastic medium. Distributions of normalized stress and maximum normalized stress were shown for 2 identical circular cylinders. Sancar and Pao [141] derived a power spectral function of pulses backscattered from two cylindrical cavities in a solid. The MS of waves from two cylindrical cavities in a solid was investigated. Luppe et al. [96] generalized Twersky's theory [169] of MS by a uniform random distribution of cylinders in an inhomogeneous medium. Biot's theory was employed for a high frequency regime. The dispersion relations of coherent fast longitudinal and slow longitudinal waves as well as shear waves were calculated. The shear wave decouples and propagates independently. The coupling effects of the longitudinal waves are noticed when forward scattering by a single cylinder of the slow wave into the fast is larger than forward scattering with no conversion.

Combining Twersky's [169] "Ordered scattering" method and Varadan's [175] T-matrix approach, Cai[29] provided a solution for a elastic MS of P/SV waves from an arbitrary configuration of scatterers having arbitrary cross section, similar or dissimilar, provided that the corresponding single-scatterer T-matrices are known. Following the same idea, Cai and Williams [28] studied MS of SH waves from an arbitrary grating of scatterers and proposed a "scatterer polymerization" technique to construct abstract scatterers and handle a large-scale deterministic analysis.

Yang and Mal [189] analyzed an elastic MS of both SH waves and P/SV waves in composites containing randomly distributed parallel fibers to predict the overall elastodynamic constants. They employed MS theory and statistical averaging procedure via the Generalized Self Consistent Model. This approach was employed by Lonne [95] to predict attenuation of a unidirectional layer of Carbon fibers in an epoxy matrix, including the coupling between MS by fibers and viscoelastic losses phenomena. The

results were experimentally verified and applied to arbitrary two-phase fiber reinforced composites for different values of fiber volume fraction.

Sato and Shindo [142] examined MS of elastic P and SV waves from randomly distributed parallel fibers with graded interfacial layers embedded in a metal matrix composite containing randomly distributed parallel fibers with graded interfacial layers. They obtained an analytical solution based on the multipole expansion method. The effect of an imperfect layer on phase velocity versus frequency was shown for both P and SV waves. Biwa et al. [18] studied MS of elastic SV waves in unidirectional composites by the multiple expansion method and T-matrix. The scattering coefficients are found numerically using a collocation method. This idea was generalized by Sumiya et al. [155] to study MS of P and SV waves from an arbitrary number of cylinders. Sheikhhassani and Dravinski [148] investigated MS of SH wave by an arbitrary number of multilayered inclusions in half space using a direct boundary integral equation method. They analyzed the effects of MS, geometry, and impedance contrast of the layers on the surface motion. Conoir and Norris [40] employed the multipole expansion method to study MS of P/SV waves in an elastic medium containing randomly distributed cylindrical inclusions in a half-space and to obtain the explicit formulas for the effective wavenumbers and reflection coefficients of the medium.

Norris [110] studied MS of of P/SV waves by spherical inclusions via the multipole method to apply to a low frequency wave propagation in composites. The effective wave speed and attenuation were given in explicit form when inclusions were voids. Liu and Cai [94] incorporated the multipole expansion method and T-matrix approach and extended the "scatterer polymerization" methodology to study 3D MS of elastic waves by spherical inclusions. The method allows them to reduce the number of actual scatterers to a lesser number of abstract scatterers.

1.3.5 Review of cloaking models

The main purpose of a cloaking device is to render an object invisible to some incident wave as seen by some external observer. Over the past decade, a great deal of effort has been focused on passive cloaking, using metamaterials to guide waves around

specific regions of space, see i.e. the highly cited works [90, 122, 41]. Within transformation acoustics, scholars such as Cummer et al. [41], Chen and Chan [33, 34], and Norris [111] have all focused on metamaterials that may have either spatially varying anisotropic density (inertial cloak IC) or stiffness (pentamode PM) or both (PM+IC). A perfect cloak has either an infinite mass (IC) or zero stiffness (PM) which is unrealistic. Norris and Nagy [113] adopted a discrete layered approach to achieve IC made from three acoustic fluids; meanwhile, Urzhumov et al. [172] included the effect of shear in IC. Torrent and Sanchez-Dehesa [165, 166] used a homogenization technique on an acoustic cloak based upon multilayered structures. They showed a trade-off between cloaking performance and construction difficulty. To overcome this drawback, Norris [111] showed that perfect cloaking can be achieved with finite mass through the use of PM. However, the manufacturing difficulty remains because the cell size of the PM material has to be the same order as the wave length. Within impedance acoustic cloaking, scholars such as Chen et al. [35] and Bobrovnitskii [20] developed a cloak for low frequencies. On the other hand, active cloaking has the advantage of being broadband [179, 181, 112].

Despite the main interest in modeling passive cloaking devices, active exterior cloaking has been investigated broadly, and interest has focused on the Helmholtz equation in two dimensions [101, 179, 180, 182, 181, 112]. Miller [101] created a cloak based on wave measurement and showed how the necessary surface sources should be calculated. He provided a formula for source amplitudes which depends on the measurements at all sensing points in the near-field, but could not derive a unique relationship between the source amplitudes and the incident field. Vasquez et al. [179, 180] proposed a solution to this problem. Using Green's formula and Graf's addition theorems for Bessel functions, Vasquez et al. formulated an integral equation, which was converted to a linear system of equations for the unknown source amplitudes. Importantly, this integral equation yields a linear relation between the source amplitudes and the incident wave field. A more explicit form of the linear relation for the source amplitudes as a function of the incident field was developed in [181] where it was shown, by construction, that

active cloaking can be realized using as few as three active sources in 2D. In the proceeding work [181], the linear relation was given in more explicit form using multipole sources and numerical results were compared with SVD solutions of the linearized system [179, 180]. The approach was further generalized and extended to a 3D case in [182] to handle the three-dimensional Helmholtz equation and seek non-resonant frequencies of the cloaked object.

Active exterior cloaking is linked to the concept of "anti-sound", also known as active noise control, e.g., the cancellation of a sound field. Paul Lueg first formulated the basic ideas of anti-sound in his U.S. patent in 1936, see e.g. [68]. In an elastodynamic context, the concept is known as "anti-vibration". The idea is to produce negligible radiated field or to generate "quiet zones" in some domains, i.e. aircraft cabins using a discrete set of sources. Nelson and Elliott [106] described the idea of completely suppressing the sound field in a finite volume inside an unbounded domain using the Kirchhoff-Helmholtz integral formula and continuous distribution of monopoles and dipoles. The principles and practical application of anti-vibration techniques have been developed in [100, 61]. The main function of anti-sound is to reduce the sound radiated from a sound source or to create a silence zone using sources but this active field is not required to be non-radiating.

1.4 Research Outline

The dissertation is presented in eight chapters. Chapter 2 formulates the mathematical model of the problem of scattering of incident waves from solids, and gives definitions of the impedance and matricant matrices and preliminaries on acoustics and elasticity theory. Impedance matrices are defined for both spherically and cylindrically anisotropic media. Chapter 3 analyzes the mathematical models described in Chapter 2 in detail, and presents a global impedance matrix method for a multilaminate general anisotropic medium and an explicit method for finding the impedance in piecewise uniform, transversely isotropic materials. It also describes the Global Matrix Methods for scattering from a multilaminate isotropic solid. Acoustic and elastic scattering from a single scatterer is considered and a T-matrix is developed for the scatterer. An emphasis is

placed on the special case of acoustic and elastic waves. Numerical results represent the form function, total scattering cross section, and total fields. Chapter 4 generalizes ideas given in Chapter 3 to study an MS and radiation from cylindrical structures, and includes a full interaction between the scatterers in both acoustic and elastic media. Numerical results for MS represent total fields and form functions in near and far-radiated fields for different configurations such as waveguides, Helmholtz resonators, slabs, and rings of cylinders. Chapter 5 details the iterative methods suitable with parallel computing for solving the MS problems considered in Chapter 4. Iterative approaches by means of Neumann series expansions are given for a fixed value of frequency and generalized for a band of frequencies. Taking advantage of the Block Toeplitz structure of the linear system, another iterative technique is presented. Chapters 6 and 7 describe the modeling of active cloaking devices generated by active multipole sources that render an object invisible to incident waves in the acoustic and elastic media. Finally, Chapter 8 gives conclusions and discusses future work.

Chapter 2

Preliminaries

In this chapter, we formulate the mathematical model of the problem of scattering of incident waves from solids. In Section 2.1, the governing equations of 3D elasticity theory are given for a general anisotropic, cylindrically anisotropic, and spherically anisotropic medium. The impedance and matricant matrices are defined in Section 2.1.3. In Section 2.2, three different types of displacement decompositions are considered. Scattering from homogeneous isotropic cylinders is considered in Section 2.3. In Section 2.3.1, acoustical preliminaries are reviewed and the expressions for incident wave coefficients are given. P/SV in-plane wave propagation is studied in Section 2.3.2; here the general solutions are given for solid, hollow, and rigid cylinders.

2.1 The governing equations of elasticity theory

In the absence of body forces the governing equations for an anisotropic elastic solid are:

I_a) the equations of motion of three-dimensional elasticity

$$\boldsymbol{\nabla} \cdot \boldsymbol{\sigma} \;=\; \rho \ddot{\mathbf{u}} + \mathbf{f}, \tag{2.1}$$

I_b) the general Hooke's law (the stress-strain relations)

$$\sigma_{ij} = C_{ijkl}\varepsilon_{kl} \quad \big(= (\mathbf{t}_i)_j \big), \tag{2.2}$$

I_c) the Cauchy relations (the linear strain-displacement relations)

$$\varepsilon_{ij} = \frac{1}{2}(u_{i,j} + u_{j,i}). \tag{2.3}$$

Here u_i are the components of displacement vector $\mathbf{u}$, $\mathbf{f}$ is the forcing, $\boldsymbol{\sigma} = [\sigma_{ij}]$ is the stress tensor, $\mathbf{t}_i = \mathbf{e}_i^T \boldsymbol{\sigma}$ are the traction vectors, $\mathbf{e}_i$ are the unit vectors, ε_{ij} are the

deformation tensor components, ρ is the density, the elastic stiffness tensor elements C_{ijkl} have the usual symmetries: $C_{ijkl} = C_{jikl} = C_{klij}$, Einstein notation with the summation over repeated indices is used, and a comma suffix denotes partial differentiation. We may use Voigt's notation to simplify the indices of elastic stiffness tensor elements C_{ijkl}:

$$C_{IJ} = C_{ijkl}, \tag{2.4}$$

where we equate

$$\begin{array}{lllllllll} ij & = & 11 & 22 & 33 & 23,32 & 13,31 & 12,21 & \\ \Downarrow & & \Downarrow & \Downarrow & \Downarrow & \Downarrow & \Downarrow & \Downarrow & . \\ \alpha & = & 1 & 2 & 3 & 4 & 5 & 6 & \end{array} \tag{2.5}$$

2.1.1 Cylindrically anisotropic media

In cylindrical coordinates (r, θ, z) with the basis $\mathbf{e}_r, \mathbf{e}_\theta, \mathbf{e}_z$, in the absence of body forces, the equilibrium equations of linear elastodynamics can be written in the form [150, 116, 161]

$$(r\mathbf{t}_r)_{,\,r} + \mathbf{t}_{\theta,\,\theta} + \mathbf{K}\,\mathbf{t}_\theta + \mathbf{t}_{z,\,z} = r\,\rho\ddot{\mathbf{u}}, \tag{2.6}$$

where $\mathbf{u} = \begin{pmatrix} u_r & u_\theta & u_z \end{pmatrix}^T$ is the displacement vector, $'T'$ denotes transpose, and the traction vectors and $\mathbf{K}$ matrix have the form

$$\mathbf{t}_r = \begin{pmatrix} \sigma_{rr} \\ \sigma_{r\theta} \\ \sigma_{rz} \end{pmatrix}, \quad \mathbf{t}_\theta = \begin{pmatrix} \sigma_{\theta r} \\ \sigma_{\theta\theta} \\ \sigma_{\theta z} \end{pmatrix}, \quad \mathbf{t}_z = \begin{pmatrix} \sigma_{zr} \\ \sigma_{z\theta} \\ \sigma_{zz} \end{pmatrix}, \quad \mathbf{K} = \begin{pmatrix} 0 & -1 & 0 \\ 1 & 0 & 0 \\ 0 & 0 & 0 \end{pmatrix}. \tag{2.7}$$

See [160] for a static derivation.

The Cauchy relations in cylindrical coordinates can be written as

$$\begin{aligned} &\varepsilon_{rr} = u_{r,r}, \qquad \varepsilon_{\theta\theta} = r^{-1}(u_{\theta,\theta} + u_r), \qquad \varepsilon_{zz} = u_{z,z}, \\ &\varepsilon_{\theta z} = \frac{1}{2} r^{-1}(u_{z,\theta} + r u_{\theta,z}), \qquad \varepsilon_{rz} = \frac{1}{2}(u_{z,r} + u_{r,z}), \\ &\varepsilon_{r\theta} = \frac{1}{2} r^{-1}(u_{r,\theta} + r u_{\theta,r} - u_\theta). \end{aligned} \tag{2.8}$$

Using the Cauchy relations (2.8), a relationship between the traction vectors and displacement vector can be made where $(\mathbf{t}_i)_j = \sigma_{ij}$. For instance the j^{th} component of $\mathbf{t}_z$

is [160]

$$(\mathbf{t}_z)_j = C_{3j11}\varepsilon_{rr} + C_{3j22}\varepsilon_{\theta\theta} + C_{3j33}\varepsilon_{zz} + 2C_{3j12}\varepsilon_{r\theta} + 2C_{3j13}\varepsilon_{rz} + 2C_{3j23}\varepsilon_{\theta z}. \tag{2.9}$$

Employing Voigt's notation (2.5) to simplify the analysis and combining eqs. (2.2), (2.7), (2.8), the traction vectors are [116]

$$\begin{pmatrix} \mathbf{t}_r \\ \mathbf{t}_\theta \\ \mathbf{t}_z \end{pmatrix} = \begin{pmatrix} \hat{\mathbf{Q}} & \hat{\mathbf{R}} & \hat{\mathbf{P}} \\ \hat{\mathbf{R}}^T & \hat{\mathbf{T}} & \hat{\mathbf{S}} \\ \hat{\mathbf{P}}^T & \hat{\mathbf{S}}^T & \hat{\mathbf{M}} \end{pmatrix} \begin{pmatrix} \mathbf{u}_{,r} \\ r^{-1}(\mathbf{u}_{,\theta} + \mathbf{K}\mathbf{u}) \\ \mathbf{u}_{,z} \end{pmatrix}, \tag{2.10}$$

where

$$\begin{aligned} &\hat{Q}_{ik} = C_{irkr} = \hat{Q}_{ki}, \quad \hat{T}_{ik} = C_{i\theta k\theta} = \hat{T}_{ki}, \quad \hat{M}_{ik} = C_{izkz} = \hat{M}_{ki}, \\ &\hat{R}_{ik} = C_{irk\theta}, \quad \hat{P}_{ik} = C_{irkz}, \quad \hat{S}_{ik} = C_{i\theta kz}, \ \ i,k = r,\theta,z. \end{aligned} \tag{2.11}$$

Because of the symmetry, the relations between matrices (2.11) are of the form

$$\hat{Q}_{i\theta} = \hat{R}_{ir}, \quad \hat{Q}_{iz} = \hat{P}_{ir}, \quad \hat{T}_{ir} = \hat{R}_{\theta i}, \quad \hat{T}_{iz} = \hat{S}_{i\theta}, \quad \hat{M}_{iz} = \hat{P}_{zi}, \quad \hat{M}_{i\theta} = \hat{S}_{zi}. \tag{2.12}$$

From [150] we have the following forms for the matrices

$$\hat{\mathbf{Q}} = \begin{pmatrix} C_{11} & C_{16} & C_{15} \\ C_{16} & C_{66} & C_{56} \\ C_{15} & C_{56} & C_{55} \end{pmatrix}, \quad \hat{\mathbf{R}} = \begin{pmatrix} C_{16} & C_{12} & C_{14} \\ C_{66} & C_{26} & C_{46} \\ C_{56} & C_{25} & C_{45} \end{pmatrix}, \quad \hat{\mathbf{P}} = \begin{pmatrix} C_{15} & C_{14} & C_{13} \\ C_{56} & C_{46} & C_{36} \\ C_{55} & C_{45} & C_{35} \end{pmatrix}, \tag{2.13}$$

$$\hat{\mathbf{M}} = \begin{pmatrix} C_{55} & C_{45} & C_{35} \\ C_{45} & C_{44} & C_{34} \\ C_{35} & C_{34} & C_{33} \end{pmatrix}, \quad \hat{\mathbf{T}} = \begin{pmatrix} C_{66} & C_{26} & C_{46} \\ C_{26} & C_{22} & C_{24} \\ C_{46} & C_{24} & C_{44} \end{pmatrix}, \quad \hat{\mathbf{S}} = \begin{pmatrix} C_{56} & C_{46} & C_{36} \\ C_{25} & C_{24} & C_{23} \\ C_{45} & C_{44} & C_{34} \end{pmatrix}. \tag{2.14}$$

General solution

Consider time harmonic wave motion in a radially inhomogeneous cylindrically anisotropic medium illustrated in Figure 2.1, for which the density, ρ, and elasticity tensor, $\mathbf{C}$, only depend on the radial coordinate r, i.e. $\rho = \rho(r)$ and $C_{ijkl} = C_{ijkl}(r)$ for $\forall\, i,j,k,l \in r,\theta,z$. Here the time dependence $e^{-i\omega t}$ is omitted but understood. We seek solutions

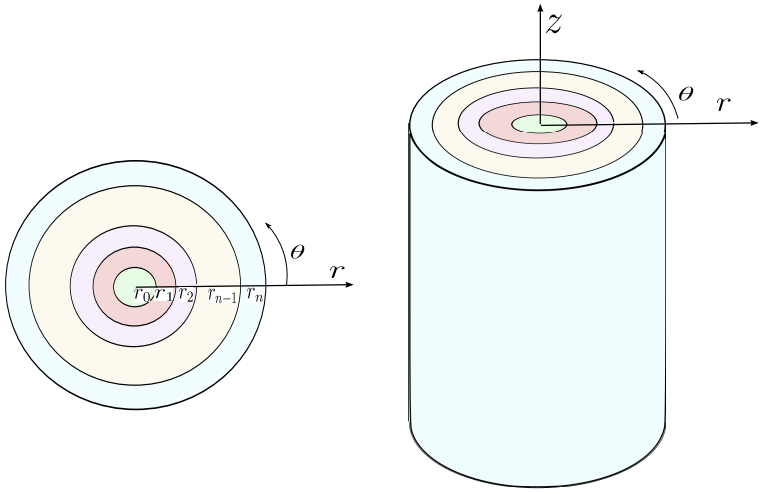

Figure 2.1: A cylindrically anisotropic multilayered medium is considered in the system of cylindrical coordinates. The medium consists of n anisotropic layers with different densities and elasticity tensors in general.

of eqs. (2.6) and (2.10) in the form of time-harmonic cylindrical waves where the displacement and radial traction vectors are of the form [150]

$$\mathbf{u} = C\mathbf{U}_n(r)e^{i(n\theta+k_z z)} \quad \mathbf{t}_r = C\boldsymbol{\Upsilon}_n(r)e^{i(n\theta+k_z z)}, \tag{2.15}$$

where C is a disposable normalization constant, $n = 0, 1, 2, ...$ is the circumferential number,

$$\mathbf{U}_n(r) = \begin{pmatrix} u_{rn}(r) \\ u_{\theta n}(r) \\ u_{zn}(r) \end{pmatrix}, \quad \boldsymbol{\Upsilon}_n(r) = \begin{pmatrix} \sigma_{rrn}(r) \\ \sigma_{r\theta n}(r) \\ \sigma_{rzn}(r) \end{pmatrix}. \tag{2.16}$$

We define $\boldsymbol{\eta}_n(r)$ as:

$$\boldsymbol{\eta}_n(r) = \begin{pmatrix} \mathbf{U}_n(r) \\ \mathbf{V}_n(r) \end{pmatrix} = \begin{pmatrix} \mathbf{U}_n(r) \\ ir\boldsymbol{\Upsilon}_n(r) \end{pmatrix}. \tag{2.17}$$

Premultiplying $\mathbf{t}_r$ in (2.15) by r and substituting it into (2.6) and (2.10) the following relation is derived in [150]

$$\begin{pmatrix} -\hat{\mathbf{Q}} & \hat{\mathbf{0}} \\ -\hat{\boldsymbol{\kappa}}\hat{\mathbf{R}}^T - ik_z r\hat{\mathbf{P}}^T & -\mathbf{I} \end{pmatrix} r\frac{d}{dr}\begin{pmatrix} \mathbf{u} \\ r\mathbf{t}_r \end{pmatrix} = \begin{pmatrix} \hat{\mathbf{R}}\boldsymbol{\kappa} + ik_z r\hat{\mathbf{P}} & -\mathbf{I} \\ \hat{\boldsymbol{\kappa}}\hat{\mathbf{T}}\hat{\boldsymbol{\kappa}} + ik_z r(\hat{\boldsymbol{\kappa}}\hat{\mathbf{S}} + \hat{\mathbf{S}}^T\hat{\boldsymbol{\kappa}}) + (ik_z r)^2(\hat{\mathbf{M}} - \rho\frac{\omega^2}{k_z^2}\mathbf{I}) & \hat{\mathbf{0}} \end{pmatrix}\begin{pmatrix} \mathbf{u} \\ r\mathbf{t}_r \end{pmatrix}, \tag{2.18}$$

where $\hat{\boldsymbol{\kappa}} = \mathbf{K} + in\mathbf{I} = -\hat{\boldsymbol{\kappa}}^+$, the superscript '+' means the adjoint of matrix, and $\mathbf{0}$ and $\mathbf{I}$ are the 3×3 zero and unity matrices. It is indicated in [150] that eq. (2.18) may

be further expressed in the form

$$\left(\frac{i}{r}\,\hat{\mathbf{G}}(r) - \frac{d}{dr}\right)\boldsymbol{\eta}_n(r) = \mathbf{0}, \tag{2.19}$$

where $\boldsymbol{\eta}_n(r)$ defined by eq. (2.17), the system matrix, $\hat{\mathbf{G}}$, provided in [150] contains the symmetry

$$\hat{\mathbf{G}} = \mathbb{T}\hat{\mathbf{G}}^{+}\mathbb{T}, \;\; \text{with} \;\; \mathbb{T} = \begin{pmatrix} \mathbf{0} & \mathbf{I} \\ \mathbf{I} & \mathbf{0} \end{pmatrix}. \tag{2.20}$$

Orthotropic cylinder

There are nine independent elastic constants C_{ij} for cylindrically orthotropic material and the stress-strain law is

$$\begin{pmatrix} \sigma_{rr} \\ \sigma_{\theta\theta} \\ \sigma_{zz} \\ \sigma_{\theta z} \\ \sigma_{rz} \\ \sigma_{r\theta} \end{pmatrix} = \begin{pmatrix} C_{11} & C_{12} & C_{13} & 0 & 0 & 0 \\ C_{12} & C_{22} & C_{23} & 0 & 0 & 0 \\ C_{13} & C_{23} & C_{33} & 0 & 0 & 0 \\ 0 & 0 & 0 & C_{44} & 0 & 0 \\ 0 & 0 & 0 & 0 & C_{55} & 0 \\ 0 & 0 & 0 & 0 & 0 & C_{66} \end{pmatrix} \begin{pmatrix} \varepsilon_{rr} \\ \varepsilon_{\theta\theta} \\ \varepsilon_{zz} \\ 2\varepsilon_{\theta z} \\ 2\varepsilon_{rz} \\ 2\varepsilon_{r\theta} \end{pmatrix}. \tag{2.21}$$

Therefore the matrices $\hat{\mathbf{Q}}$, $\hat{\mathbf{R}}$, $\hat{\mathbf{P}}$, $\hat{\mathbf{T}}$, $\hat{\mathbf{S}}$, $\hat{\mathbf{M}}$ in equations for the system matrix, $\hat{\mathbf{G}}$ [150], have a much more simplified form with three nonzero elements at most.

A transversely isotropic material is characterized by five non-trivial stiffnesses C_{ij}. The stress-strain law for the transversely isotropic material is a particular case of eq. (2.21) with stiffnesses $C_{11} = C_{22}$, $C_{13} = C_{23}$, $C_{44} = C_{55}$, and $C_{66} = (C_{11} - C_{22})/2$.

2.1.2 Spherically anisotropic media

In a spherical coordinate system (r, θ, φ), a dynamic equilibrium vector equation for a linearly elastic anisotropic medium has the form [118]:

$$r^{-2}(r^2\mathbf{t}_r)_{,\,r} + (r\,\sin\theta)^{-1}\left[(\sin\theta\mathbf{t}_\theta)_{,\,\theta} + \mathbf{t}_{\varphi,\,\varphi} + \sin\theta\mathbf{K}\,\mathbf{t}_\theta + \mathbf{H}\mathbf{t}_\varphi\right] = \rho\ddot{\mathbf{u}}, \tag{2.22}$$

where $\mathbf{u} = \begin{pmatrix} u_r & u_\theta & u_\varphi \end{pmatrix}^T$ is the displacement vector, $\mathbf{t}_i = \mathbf{e}_i^T \boldsymbol{\sigma}$ are the traction vectors, and

$$\mathbf{H} = \begin{pmatrix} 0 & 0 & -\sin\theta \\ 0 & 0 & -\cos\theta \\ \sin\theta & \cos\theta & 0 \end{pmatrix}. \tag{2.23}$$

The Cauchy relations in spherical coordinates are

$$\begin{aligned} &\varepsilon_{rr} = u_{r,r}, \qquad \varepsilon_{\theta\theta} = r^{-1}(u_{\theta,\theta} + u_r), \qquad \varepsilon_{r\theta} = \frac{1}{2} r^{-1}(u_{r,\theta} + r u_{\theta,r} - u_\theta), \\ &\varepsilon_{\theta\varphi} = \frac{1}{2} r^{-1}\big[(\sin\theta)^{-1} u_{\theta,\varphi} + u_{\varphi,\theta} - u_\varphi \cot\theta\big]; \qquad \varepsilon_{r\varphi} = \frac{1}{2} r^{-1}\big[(\sin\theta)^{-1} u_{r,\varphi} + r u_{\varphi,r} - u_\varphi\big], \\ &\varepsilon_{\varphi\,\varphi} = (r\,\sin\theta)^{-1}(u_{\varphi\,\varphi} + u_r \sin\theta + u_\theta \cos\theta). \end{aligned} \tag{2.24}$$

Using the Cauchy relations (2.24), a relationship between the traction vectors and displacement vector can be made

$$\begin{pmatrix} \mathbf{t}_r \\ \mathbf{t}_\theta \\ \mathbf{t}_z \end{pmatrix} = \begin{pmatrix} \hat{\mathbf{Q}} & \hat{\mathbf{R}} & \hat{\mathbf{P}} \\ \hat{\mathbf{R}}^T & \hat{\mathbf{T}} & \hat{\mathbf{S}} \\ \hat{\mathbf{P}}^T & \hat{\mathbf{S}}^T & \hat{\mathbf{M}} \end{pmatrix} \begin{pmatrix} \mathbf{u}_{,r} \\ r^{-1}(\mathbf{u}_{,\theta} + \mathbf{K}\mathbf{u}) \\ (r\,\sin\theta)^{-1}\big(\mathbf{u}_{,\varphi} + \mathbf{H}\mathbf{u}\big) \end{pmatrix}, \tag{2.25}$$

where matrices $\hat{\mathbf{Q}}$, $\hat{\mathbf{R}}$, $\hat{\mathbf{P}}$, $\hat{\mathbf{T}}$, $\hat{\mathbf{S}}$, $\hat{\mathbf{M}}$ are defined by eqs. (2.13) - (2.14) with material constants C_{IJ} defined by (2.5) using Voigt's notation (2.4)

The spherical harmonics

The vector spherical harmonics $\mathbf{P}$, $\mathbf{B}$ and $\mathbf{C}$ are defined as [105]

$$\begin{aligned} &\mathbf{P}_{mn\sigma}(\hat{\mathbf{r}}) = \hat{\mathbf{r}} Y_n^{m\sigma}(\hat{\mathbf{r}}), \\ &\mathbf{B}_{mn\sigma}(\hat{\mathbf{r}}) = \zeta_n \mathbf{D} Y_n^{m\sigma}(\hat{\mathbf{r}}), \\ &\mathbf{C}_{mn\sigma}(\hat{\mathbf{r}}) = -\zeta_n \hat{\mathbf{r}} \times \mathbf{D} Y_n^{m\sigma}(\hat{\mathbf{r}}) = \zeta_n \big(\frac{\hat{\boldsymbol{\theta}}}{\sin\theta}\frac{\partial}{\partial\phi} - \hat{\boldsymbol{\phi}}\frac{\partial}{\partial\theta}\big) Y_n^{m\sigma}(\hat{\mathbf{r}}), \end{aligned} \tag{2.26}$$

where

$$\zeta_n = [n(n+1)]^{-1/2}, \tag{2.27}$$

$\mathbf{D} = \hat{\theta}\frac{\partial}{\partial\theta} + \frac{\hat{\phi}}{\sin\theta}\frac{\partial}{\partial\phi}$ is the angular differential operator; the indices m, n are for the spherical harmonics (n azimuthal, n polar) and $\sigma = e, o$ is the even-or-odd index [105];

the functions $Y_n^{m\sigma}(\hat{\mathbf{r}})$ are the normalized spherical harmonics [98, p. 64]

$$Y_n^m \equiv Y_n^{me} + iY_n^{mo} = Q_n^m P_n^m(\cos\theta)e^{im\phi}, \quad Q_n^m = (-1)^m\sqrt{\frac{(2n+1)}{4\pi}\frac{(n-m)!}{(n+m)!}}. \quad (2.28)$$

The vector spherical harmonics $\mathbf{P}_{mn\sigma}, \mathbf{B}_{mn\sigma}, \mathbf{C}_{mn\sigma}$ were applied in [118] to develop separation of variables vector solutions and provide a complete basis for representing vector functions of the spherical angles.

General solutions

We consider time harmonic wave motion in a radially inhomogeneous spherically anisotropic medium. The density and the elasticity tensor of a radially inhomogeneous anisotropic cylinder depend on the coordinate r only. The dynamic equilibrium equation (2.22) can be written in the form

$$(r^2\mathbf{t}_r)_{,\,r} + r\boldsymbol{\tau} = -r^2\rho\omega^2\mathbf{u}, \quad (2.29)$$

with

$$\boldsymbol{\tau} \equiv (\sin\theta)^{-1}\big[(\sin\theta\mathbf{t}_\theta)_{,\,\theta} + \mathbf{t}_{\varphi,\,\varphi} + \sin\theta\mathbf{K}\,\mathbf{t}_\theta + \mathbf{H}\mathbf{t}_\varphi\big]. \quad (2.30)$$

Let us drop the subindices in $\mathbf{P}_{mn\sigma}, \mathbf{B}_{mn\sigma}, \mathbf{C}_{mn\sigma}$ and denote $\mathbf{A}(\mathbf{e}_r) = \mathbf{A}(\theta,\,\varphi) \equiv \mathbf{P}$, $\mathbf{B}$, $\mathbf{C}$. We seek solutions of eq. (2.29) in the form

$$\mathbf{u} = \sum_{\mathbf{A}} U_{\mathbf{A}}(r)\mathbf{A}(\theta,\,\varphi), \quad \mathbf{t}_r = \sum_{\mathbf{A}} \Upsilon_{\mathbf{A}}(r)\mathbf{A}(\theta,\,\varphi), \quad \boldsymbol{\tau} = \sum_{\mathbf{A}} \Gamma_{\mathbf{A}}(r)\mathbf{A}(\theta,\,\varphi), \quad (2.31)$$

where

$$\mathbf{U}(r) = \big(U_{\mathbf{P}},\, U_{\mathbf{B}},\, U_{\mathbf{C}}\big)^T, \quad \boldsymbol{\Upsilon}(r) = \big(\Upsilon_{\mathbf{P}},\, \Upsilon_{\mathbf{B}},\, \Upsilon_{\mathbf{C}}\big)^T, \quad \boldsymbol{\Gamma}(r) = \big(\Gamma_{\mathbf{P}},\, \Gamma_{\mathbf{B}},\, \Gamma_{\mathbf{C}}\big)^T, \quad (2.32)$$

and the vector spherical harmonics $\mathbf{P}, \mathbf{B}, \mathbf{C}$ are defined by eq. (2.26). Define $\boldsymbol{\eta}(r)$ as

$$\boldsymbol{\eta}(r) = \begin{pmatrix} \mathbf{U}(r) \\ \mathbf{V}(r) \end{pmatrix} = \begin{pmatrix} \mathbf{U}(r) \\ ir^2\boldsymbol{\Upsilon}(r) \end{pmatrix}, \quad (2.33)$$

where $\mathbf{U}(r)$ and $\boldsymbol{\Upsilon}(r)$ are defined by (2.32). It was shown in [118] that the separable solution of the form (2.31) is valid for a radially inhomogeneous spherically anisotropic

medium if the material is transversely isotropic about $\mathbf{e}_r$. Introducing the assumed form of solution (2.31) in eq. (2.29) yields the Stroh-like ODS [118]

$$\frac{d}{dr}\boldsymbol{\eta}(r) = \frac{i}{r^2}\,\hat{\mathbf{G}}(r)\boldsymbol{\eta}(r) \tag{2.34}$$

where $\boldsymbol{\eta}(r)$ defined by eq. (2.33), the system matrix, $\hat{\mathbf{G}}$, given in [118] has the symmetry property: $\hat{\mathbf{G}} = \mathbb{T}\hat{\mathbf{G}}^{+}\mathbb{T}$ where '+' means Hermitian conjugation, and $\mathbb{T}$ is defined in eq. (2.20).

Elastic waves in a radially inhomogeneous multilayered sphere

Let us investigate a spherically anisotropic medium as a radially inhomogeneous multilayered sphere consisting of J isotropic spherical layers. We consider an infinite plane elastic wave of circular frequency ω incident at angle α on an isotropic spherical layer with inner (r_{j-1}) and outer (r_j) radii a in spherical coordinate system (r, θ, φ). We define the elastic longitudinal (P) and shear (SV) wavenumbers for an isotropic medium, respectively as

$$k = \omega/c_p \quad \text{and} \quad K = \omega/c_s \tag{2.35}$$

where ω is the frequency, c_p, c_s are the wave speeds:

$$c_p^2 = (\lambda + 2\mu)/\rho, \quad c_s^2 = \mu/\rho, \tag{2.36}$$

the indices p and s stand for P and SV waves correspondingly, λ and μ are Lamé coefficients. We also define, for later use,

$$\widetilde{\kappa} \equiv k/K, \quad \text{or equivalently} \quad \widetilde{\kappa}^2 = 2(1-\nu)/(1-2\nu), \tag{2.37}$$

where ν is Poisson's ratio.

Based on vector spherical harmonic functions (2.26), the displacement in the solid shell region(s) can be written in the form

$$\mathbf{u} = \sum_{mn\sigma}^{l=1,3} \{R^l_{mn\sigma}\mathbf{L}^l_{mn\sigma} + S^l_{mn\sigma}\mathbf{M}^l_{mn\sigma} + T^l_{mn\sigma}\mathbf{N}^l_{mn\sigma}\}, \tag{2.38}$$

where $\mathbf{L}$, $\mathbf{M}$ and $\mathbf{N}$ are vector spherical wavefunctions [98, p. 106] related to the vector spherical harmonics $\mathbf{P}$, $\mathbf{B}$ and $\mathbf{C}$ by

$$\left(\mathbf{L}^l_{mn\sigma}\,\mathbf{N}^l_{mn\sigma}\,\mathbf{M}^l_{mn\sigma}\right) = \left(\mathbf{P}_{mn\sigma}(\hat{\mathbf{r}})\;\mathbf{B}_{mn\sigma}(\hat{\mathbf{r}})\;\mathbf{C}_{mn\sigma}(\hat{\mathbf{r}})\right)\mathbf{U}^l_n(r), \tag{2.39}$$

where $\mathbf{U}_n^l(r)$ is the 3×3 matrix:

$$\mathbf{U}_n^l(r) = \begin{pmatrix} g_n^{l\,\prime}(kr) & (\eta_n^2 Kr)^{-1} g_n^l(Kr) & 0 \\ (\eta_n kr)^{-1} g_n^l(kr) & (\eta_n)^{-1}\left(g_n^{l\,\prime}(Kr) + (Kr)^{-1} g_n^l(Kr)\right) & 0 \\ 0 & 0 & \eta_n^{-1} g_n^l(Kr) \end{pmatrix}, \tag{2.40}$$

the index l distinguishes regular ($l = 1$) from outgoing ($l = 3$) solutions. The associated spherical wavefunctions are

$$g_n^l(x) = \begin{cases} j_n(x), & l = 1, \\ y_n(x), & l = 2, \\ h_n^{(1)}(x), & l = 3, \\ h_n^{(2)}(x), & l = 4, \end{cases} \tag{2.41}$$

where $h_n^{(1)}(x)$ and $h_n^{(2)}(x)$ are the spherical Hankel functions of order n of type-1 and type-2 respectively, and $j_n(x)$ and $y_n(x)$ are the spherical Bessel and Neumann functions of order n.

Thus, incorporating equations (2.38)-(2.28) the displacement, $\mathbf{u}$, and the traction vector, $\mathbf{t}$, [105, eq. 13.3.78], [110], have the general form

$$\mathbf{u}(r) = \begin{pmatrix} \mathbf{P}_{mn\sigma}(\hat{\mathbf{r}}) & \mathbf{B}_{mn\sigma}(\hat{\mathbf{r}}) & \mathbf{C}_{mn\sigma}(\hat{\mathbf{r}}) \end{pmatrix} \begin{pmatrix} \mathbf{U}_n^1(r) & \mathbf{U}_n^3(r) \end{pmatrix} \begin{pmatrix} \mathbf{w}_{mn\sigma}^1 \\ \mathbf{w}_{mn\sigma}^3 \end{pmatrix}, \tag{2.42}$$

$$r\,\mathbf{t}(r) = \begin{pmatrix} \mathbf{P}_{mn\sigma}(\hat{\mathbf{r}}) & \mathbf{B}_{mn\sigma}(\hat{\mathbf{r}}) & \mathbf{C}_{mn\sigma}(\hat{\mathbf{r}}) \end{pmatrix} \begin{pmatrix} \boldsymbol{\Upsilon}_n^1(r) & \boldsymbol{\Upsilon}_n^3(r) \end{pmatrix} \begin{pmatrix} \mathbf{w}_{mn\sigma}^1 \\ \mathbf{w}_{mn\sigma}^3 \end{pmatrix}, \tag{2.43}$$

where $\mathbf{U}_n^l(r), (l = 1, 3)$ are defined by equation (2.40),

$$\boldsymbol{\Upsilon}_n^l(r) = K\mu \times \begin{pmatrix} t_{11} & t_{12} & 0 \\ t_{21} & t_{22} & 0 \\ 0 & 0 & t_{33} \end{pmatrix}, \qquad \mathbf{w}_{mn\sigma}^l = \begin{pmatrix} R_{mn\sigma}^l \\ T_{mn\sigma}^l \\ S_{mn\sigma}^l \end{pmatrix}, \tag{2.44}$$

$$t_{11} = \widetilde{\kappa}\left[2g_n^{l\,\prime\prime}(kr) - \left(\frac{K^2}{k^2} - 2\right)g_n^l(kr)\right]; \quad t_{33} = \eta_n^{-1}\left(g_n^{l\,\prime}(Kr) - \frac{g_n^l(Kr)}{Kr}\right);$$
$$t_{12} = 2(\eta_n^2 Kr)^{-1}\left(g_n^{l\,\prime}(Kr) - \frac{g_n^l(Kr)}{Kr}\right); \qquad t_{21} = 2(\eta_n Kr)^{-1}\left(g_n^{l\,\prime}(kr) - \frac{g_n^l(kr)}{kr}\right);$$
$$t_{22} = \eta_n^{-1}\left(g_n^{l\,\prime\prime}(Kr) + (n^2+n-2)\frac{g_n^l(Kr)}{(Kr)^2}\right). \tag{2.45}$$

2.1.3 Impedance and matricant matrices

The Stroh like ODS (2.19) for a cylindrically anisotropic medium, and ODS (2.34) for spherically anisotropic medium are analogous and can be written in the form of a system of $2m$ linear ordinary differential equations [116]

$$\frac{\mathrm{d}\,\boldsymbol{\eta}}{\mathrm{d}\,r} = \mathbf{Q}\boldsymbol{\eta} \quad \text{with } \boldsymbol{\eta}(r) = \begin{pmatrix}\mathbf{U}\\ \mathbf{V}\end{pmatrix}, \quad \mathbf{Q}(r) = \begin{pmatrix}\mathbf{Q}_1 & \mathbf{Q}_2\\ \mathbf{Q}_3 & \mathbf{Q}_4\end{pmatrix}, \tag{2.46}$$

where $\mathbf{Q}(r) = \frac{i}{r}\hat{\mathbf{G}}(r)$ for cylindrical anisotropy and $\mathbf{Q}(r) = \frac{i}{r^2}\hat{\mathbf{G}}(r)$ in the spherical case, $\hat{\mathbf{G}}(r)$ is the system matrix defined in [116] and [118] for cylindrical and spherical cases correspondingly. The vector function $\boldsymbol{\eta}(r)$ is defined in terms of vectors $\mathbf{U}(r)$ and $\mathbf{V}(r)$ associated with displacement and traction, respectively, and given by eqs. (2.32) and (2.33) for spherical, and by eq. (2.16) and (2.17) for cylindrical anisotropy; we omit the subscript n for simplicity. The relations derived hereinafter are valid for both cylindrically and spherically anisotropic media.

In this section, we study the relation between vectors $\mathbf{U}(r)$ and $\mathbf{V}(r)$. The dimension of each vector is taken as m, where m is either 3, 2 or 1; $m = 3$ in general, $m = 2$ if z - dependence is not considered, and $m = 1$ for pure out-of-plane shear horizontal (SH) motion. For the moment we may consider m as general. Let us define the $m \times m$ conditional impedance matrix $\mathbf{z}$ for a solid such that

$$\mathbf{V}(r) = -\mathrm{i}\mathbf{z}(r)\mathbf{U}(r). \tag{2.47}$$

It follows from eqs. (2.46) and (2.47) that $\mathbf{z}(r)$ satisfies a differential Riccati equation [116]

$$\frac{\mathrm{d}\,\mathbf{z}}{\mathrm{d}\,r} + \mathbf{z}\mathbf{Q}_1 - \mathbf{Q}_4\mathbf{z} - i\mathbf{z}\mathbf{Q}_2\mathbf{z} - i\mathbf{Q}_3 = \mathbf{0}, \tag{2.48}$$

with assumed initial condition $\mathbf{z}(r_0)$ at some specified $r = r_0$, hence the name conditional impedance. One approach to solving for the conditional impedance matrix, $\mathbf{z}$, is to first solve for the $2m \times 2m$ matricant $\mathbf{M}(r, r_0)$ which is defined as the solution of the initial value problem

$$\frac{\mathrm{d}\,\mathbf{M}}{\mathrm{d}\,r}(r, r_0) = \mathbf{Q}(r)\mathbf{M}(r, r_0),\ \mathbf{M}(r_0, r_0) = \mathbf{I}_{(2m)},\ \mathbf{M} = \begin{pmatrix} \mathbf{M}_1 & \mathbf{M}_2 \\ \mathbf{M}_3 & \mathbf{M}_4 \end{pmatrix}. \tag{2.49}$$

Hence

$$\boldsymbol{\eta}(r) = \mathbf{M}(r, r_0)\boldsymbol{\eta}(r_0). \tag{2.50}$$

Using the relations

$$\mathbf{U}\,(r) = (\mathbf{M}_1 - \mathrm{i}\mathbf{M}_2\mathbf{z}(r_0))\,\mathbf{U}\,(r_0)\,, \quad \mathbf{V}\,(r) = (\mathbf{M}_3 - \mathrm{i}\mathbf{M}_4\mathbf{z}(r_0))\,\mathbf{U}\,(r_0)\,, \tag{2.51}$$

which follow from (2.47), the conditional impedance can be expressed in terms of the matricant as

$$\mathbf{z}(r) = i\big(\mathbf{M}_3 - i\mathbf{M}_4\mathbf{z}(r_0)\big)\big(\mathbf{M}_1 - i\mathbf{M}_2\mathbf{z}(r_0)\big)^{-1}. \tag{2.52}$$

The propagator nature of the matricant is apparent from eq. (2.50) and from the property $\mathbf{M}(r, r_1)\ \mathbf{M}(r_1, r_0) = \mathbf{M}(r, r_0)$, and in particular $\mathbf{M}(r, r_0) = \mathbf{M}(r_0, r)^{-1}$. Also, the symmetry of the system matrix $\hat{\mathbf{G}}$, eq. (2.20) implies $\mathbf{M}(r, r_0) = \mathbb{T}\mathbf{M}^{+}(r_0, r)\mathbb{T}$. Hence, $\mathbf{M}^{-1}(r, r_0) = \mathbb{T}\mathbf{M}^{+}(r, r_0)\mathbb{T}$, that is, $\mathbf{M}$ is $\mathbb{T}$-unitary [121].

An alternative approach to finding $\mathbf{z}$ uses the two point impedance matrix, which by definition relates the traction and displacement vectors at two values of r according to [116]

$$\begin{pmatrix} \mathbf{V}(r_0) \\ -\mathbf{V}(r) \end{pmatrix} = -\mathrm{i}\mathbf{Z}(r, r_0) \begin{pmatrix} \mathbf{U}(r_0) \\ \mathbf{U}(r) \end{pmatrix}, \quad \mathbf{Z} = \begin{pmatrix} \mathbf{Z}_1 & \mathbf{Z}_2 \\ \mathbf{Z}_3 & \mathbf{Z}_4 \end{pmatrix}. \tag{2.53}$$

The two point impedance matrix has the important property that it is Hermitian, $\mathbf{Z} = \mathbf{Z}^{+}$ [116]. The relations between the matricant of (2.49) and the impedance matrix of (2.53) evaluated at cylindrical surfaces r, r_0 are easily deduced [116]

$$\begin{aligned} \mathbf{M}(r, r_0) &= \begin{pmatrix} -\mathbf{Z}_2^{-1}\mathbf{Z}_1 & \mathrm{i}\mathbf{Z}_2^{-1} \\ \mathrm{i}\mathbf{Z}_3 - \mathrm{i}\mathbf{Z}_4\mathbf{Z}_2^{-1}\mathbf{Z}_1 & -\mathbf{Z}_4\mathbf{Z}_2^{-1} \end{pmatrix}, \\ \mathbf{Z}(r, r_0) &= \begin{pmatrix} -\mathrm{i}\mathbf{M}_2^{-1}\mathbf{M}_1 & \mathrm{i}\mathbf{M}_2^{-1} \\ \mathrm{i}\mathbf{M}_4\mathbf{M}_2^{-1}\mathbf{M}_1 - \mathbf{M}_3 & -\mathrm{i}\mathbf{M}_4\mathbf{M}_2^{-1} \end{pmatrix}. \end{aligned} \tag{2.54}$$

Introducing (2.54) into (2.52), we can relate the conditional impedance $\mathbf{z}(r)$ to the two point impedance matrix $\mathbf{Z}(r, r_0)$ according to

$$\mathbf{z}(r) = \mathbf{Z}_3\big(\mathbf{Z}_1 - \mathbf{z}(r_0)\big)^{-1}\mathbf{Z}_2 - \mathbf{Z}_4. \tag{2.55}$$

2.2 Displacement potentials

In this section, we consider 3 different types of displacement decompositions, namely using the Helmholtz potentials [26], Buchwald potentials [26] and one proposed by Morse and Feshbach [105, p. 1764 -1767].

2.2.1 The Helmholtz potentials

The displacement vector $\mathbf{u}$ in terms of the Helmholtz potentials has the form [2]

$$\mathbf{u} = \boldsymbol{\nabla}\varphi + \boldsymbol{\nabla} \times \boldsymbol{\psi}, \tag{2.56}$$

where ϕ is a scalar potential function and $\boldsymbol{\psi}$ is a vector potential function. In cylindrical coordinates the components of the displacement vector $\mathbf{u} = (u_r, u_\theta, u_z)$ can be expressed as:

$$u_r = \frac{\partial\varphi}{\partial r} + \frac{1}{r}\frac{\partial\psi_z}{\partial\theta} - \frac{\partial\psi_\theta}{\partial z}, \tag{2.57a}$$

$$u_\theta = \frac{1}{r}\frac{\partial\varphi}{\partial\theta} + \frac{\partial\psi_r}{\partial z} - \frac{\partial\psi_z}{\partial r}, \tag{2.57b}$$

$$u_z = \frac{\partial\varphi}{\partial z} + \frac{1}{r}\frac{\partial(\psi_\theta r)}{\partial r} - \frac{1}{r}\frac{\partial\psi_r}{\partial\theta}. \tag{2.57c}$$

2.2.2 Displacement potentials using Buchwald decomposition

The displacement vector $\mathbf{u}$ decomposed in terms of scalar wave functions φ, χ and ψ [26] has the form

$$\mathbf{u} = \boldsymbol{\nabla}\varphi + \boldsymbol{\nabla} \times (\chi\mathbf{e_z}) + \left(\frac{\partial\psi}{\partial z} - \frac{\partial\varphi}{\partial z}\right)\mathbf{e_z} \tag{2.58}$$

or in component form in cylindrical coordinates as

$$u_r = \frac{\partial\varphi}{\partial r} + \frac{1}{r}\frac{\partial\chi}{\partial\theta}, \quad u_\theta = \frac{1}{r}\frac{\partial\varphi}{\partial\theta} - \frac{\partial\chi}{\partial r}, \quad u_z = \frac{\partial\psi}{\partial z}. \tag{2.59}$$

The wave function representation (2.58) was introduced into the theory of wave propagation by Buchwald [26].

2.2.3 Alternative decomposition

Alternative representation of a displacement vector through scalar potentials is introduced by Morse and Feshbach [105, p. 1764 -1767]

$$\mathbf{u} = \boldsymbol{\nabla}\varphi + \boldsymbol{\nabla} \times (\chi \mathbf{e_z}) + a\boldsymbol{\nabla} \times \boldsymbol{\nabla} \times (\psi \mathbf{e_z}), \tag{2.60}$$

where a is the radius of the cylinder which is constant with dimensions of length. In component form in cylindrical coordinates it has form

$$u_r = \frac{\partial \varphi}{\partial r} + \frac{1}{r}\frac{\partial \chi}{\partial \theta} + a\frac{\partial^2 \psi}{\partial r \partial z}, \tag{2.61a}$$

$$u_\theta = \frac{1}{r}\frac{\partial \varphi}{\partial \theta} - \frac{\partial \chi}{\partial r} + a\frac{\partial^2 \psi}{\partial \theta \partial z}, \tag{2.61b}$$

$$u_z = \frac{\partial \varphi}{\partial z} - a\left(\frac{\partial^2}{\partial r^2} + \frac{1}{r}\frac{\partial}{\partial r} + \frac{1}{r^2}\frac{\partial^2}{\partial \theta^2}\right)\psi. \tag{2.61c}$$

This approach was applied by Honarvar and Sinclair [78] in the analysis of a wave scattering problem for transversely isotropic material. Comparing Eqs. (2.59) and (2.61) we can notice that Eqs. (2.61) have extraneous terms. Therefore, the displacement decomposition (2.61) results in cumbersome coupled equations for φ and ψ, which are 5th order PDEs, whereas Buchwald's representation (2.59) yields much simpler equations, compact second order PDEs [132]. Ahmad and Rahman [5],[4], [132] showed that the above mentioned two representations lead to identical characteristic equations and the same final result. However, in [80], the response to [132], authors noted that their solution has a stronger physical basis. The authors mentioned that the potentials φ, χ, ψ in eq. (2.60) have a physical meaning, representing P, SH, and SV waves respectively that allows them to study the effect of each wave type separately; they noted that Buchwald potentials lack this physical meaning. Nonetheless, in this dissertation, we use the Buchwald potentials approach for the purpose of mathematical simplicity. Buchwald's potentials yield simpler expressions, and are less laborious.

2.3 Scattering from homogeneous isotropic cylinders

In a cylindrical coordinate system (r, θ, z) a wave of circular frequency ω incident on an infinite cylinder of outer radius a is considered, see Fig. 2.2. We will refer to obstacles

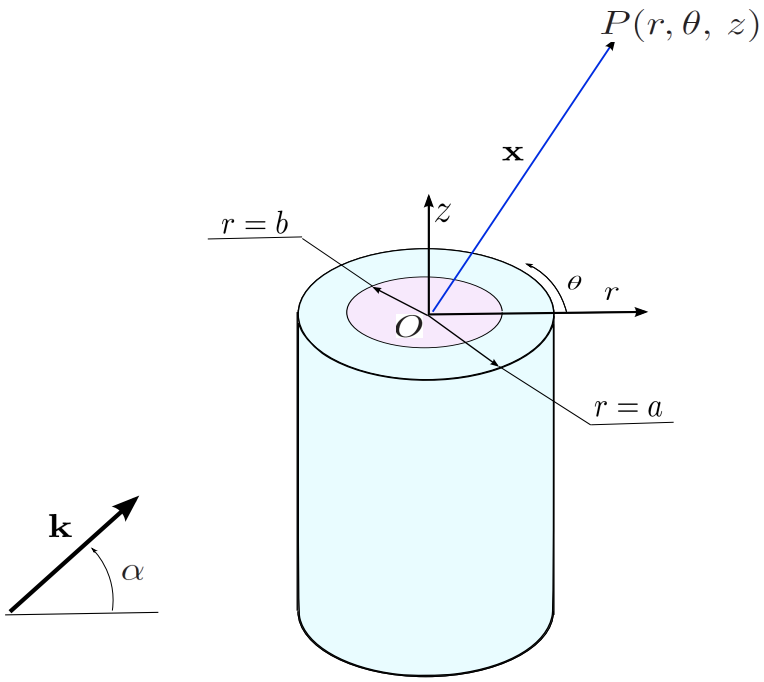

Figure 2.2: An oblique wave incidence at an angle α on cylindrical layer of inner b and outer a radii is considered in the cylindrical coordinate system. **k** vector denotes the wave front direction. A cylindrical layer is an elastic solid; the medium inside the cylinder is either fluid, gas, or elastic core; the outer region is either acoustic medium or elastic matrix.

as cylinders but may consider solid cylinders of outer radius a, as well as thin and thick cylindrical shells of outer a and inner b radii. A cylinder in $0 < b \leq r \leq a$ is an elastic solid; the medium inside the cylinder is either fluid, gas, or elastic core; the outer region is either acoustic medium or elastic matrix. The material of the cylinder in $0 < b \leq r \leq a$ is assumed to be homogeneous and isotropic. Note that the equations given in Section 2.3.1 for acoustic medium are independent of physical properties of cylinder.

In this section, we formulate the wave scattering problem, find the general solutions of governing equations and derive the formulas for pressure, displacements and stresses in acoustic and elastic media. The scattering coefficients will be calculated using the Impedance method and Global matrix method and verified with COMSOL results in the next chapter.

2.3.1 Acoustical preliminaries

The governing equation for the (time harmonic) pressure $p(\mathbf{x})$ is the acoustic Helmholtz wave equation

$$\nabla^2 p + k^2 p = p_s, \tag{2.62}$$

where ∇^2 is the Laplace operator, the term p_s represents sources, $k = \omega/c$ is the wavenumber, $c = \sqrt{\kappa/\rho_f}$ is the acoustic compressional wave speed in the liquid medium outside the cylinder, and κ is the bulk modulus. The particle velocity in the fluid $\mathbf{v}$ is related to the pressure by the momentum equation

$$-i\omega\rho_f \mathbf{v} = -\nabla p, \tag{2.63}$$

where ρ_f is the mass density of fluid. Both c and ρ_f are constants.

In a cylindrical coordinate system (r, θ, z), consider an acoustic wave of circular frequency ω obliquely incident at an angle α on infinitely long cylinder immersed in acoustic medium (see Fig. 2.2). Let $\mathbf{x} = (x, y, z)$ be a position vector of a typical point in Cartesian coordinates with origin at O, and let us define plane polar coordinates (r_1, θ_1, z_1) at the center O_1. Since we consider only one cylinder S_1, we may assume that $|\boldsymbol{l}_1| = 0$ for simplicity (see Fig. 2.3), i.e. O_1 and O coincide, and write the position of point P at the multipole O_1 as $P = P(\mathbf{x}_1) = P(\mathbf{x}) = P(r, \theta, z)$.

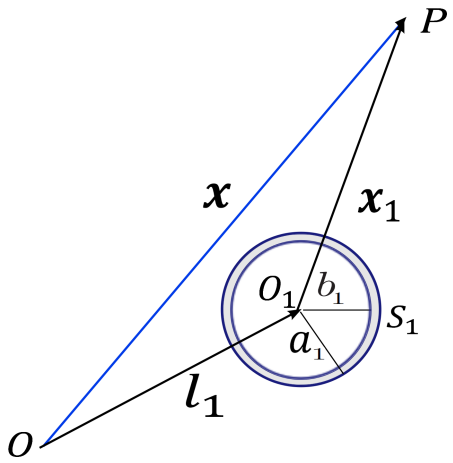

Figure 2.3: The planar position of cylinder $\mathtt{S}_1$ with the center located at the pole O_1 with the local coordinates (r_1, θ_1).

Total pressure field

The total pressure $p(\mathbf{x}) = p^{in}(\mathbf{x})$ in inner acoustic medium satisfies the acoustic Helmholtz wave equation (2.62) and momentum balance equation (2.63) and is given by

$$p^{in}(\mathbf{x}) = \sum_{n=-\infty}^{\infty} A_n^{in} U_n^+(k_\perp \mathbf{x}) e^{ik_z z} \tag{2.64}$$

where $\mathbf{x}$ is a position vector of point $P(r, \theta, z)$ inside the cylinder ($r < b$), and

$$k_\perp = k\cos\alpha, \qquad k_z = k\sin\alpha. \tag{2.65}$$

The function $U_n^{\pm}(\mathbf{x})$ is defined by

$$U_n^{\pm}(\mathbf{x}) = J_n(|\mathbf{x}|) e^{\pm in \arg \mathbf{x}}, \tag{2.66}$$

where $\arg \mathbf{x} \in [0, 2\pi)$ and $\arg(-\mathbf{x}) = \big(\arg \mathbf{x} \pm \pi\big) \mod 2\pi$, and $J_n(x)$ is the Bessel function of the first kind of order n.

The total pressure $p(\mathbf{x})$ at point $P(r, \theta, z)$ in outer acoustic medium can be expressed as a sum of incident p^{inc} and scattered p^{sc} pressure fields

$$p = p^{inc} + p^{sc}. \tag{2.67}$$

The obliquely incident field at point $P(r, \theta, z)$ is given as

$$p^{inc} = \sum_{n=-\infty}^{\infty} A_n U_n^+(k_\perp \mathbf{x}) e^{ik_z z} \tag{2.68}$$

where $\mathbf{x}$ is a position vector of point P. The scattered field p^{sc} at point $P(r, \theta, z)$ can be expanded in the form:

$$p^{sc} = \sum_{n=-\infty}^{\infty} B_n V_n^+(k_\perp \mathbf{x}) e^{ik_z z}, \tag{2.69}$$

where B_n are the unknown coefficients, and the function $V_n^{\pm}(\mathbf{x})$ is defined by

$$V_n^{\pm}(\mathbf{x}) = H_n^{(1)}(|\mathbf{x}|) e^{\pm in \arg \mathbf{x}}, \tag{2.70}$$

where $H_n^{(1)}$ is the Hankel function of the first kind of order n. The functions $U_n^{\pm}(\mathbf{x})$ and $V_n^{\pm}(\mathbf{x})$ possess the properties

$$U_n^{\pm}(-\mathbf{x}) = (-1)^n U_n^{\pm}(\mathbf{x}), \;\; V_n^{\pm}(-\mathbf{x}) = (-1)^n V_n^{\pm}(\mathbf{x}), \;\; V_{-n}^{\pm}(\mathbf{x}) = (-1)^n V_n^{\mp}(\mathbf{x}), \tag{2.71}$$

and obey the generalized Graf's addition theorem [1, eq. (9.1.79)]:

$$V_l{}^+(\mathbf{x}-\mathbf{y}) = \sum_{n=-\infty}^{\infty} \begin{cases} V_n^+(\mathbf{x})\, U_{n-l}^-(\mathbf{y}), & |\mathbf{x}| > |\mathbf{y}|, \\ U_n^+(\mathbf{x})\, V_{n-l}^-(\mathbf{y}), & |\mathbf{x}| < |\mathbf{y}|. \end{cases} \tag{2.72}$$

Incident field: plane wave, cylindrical line source

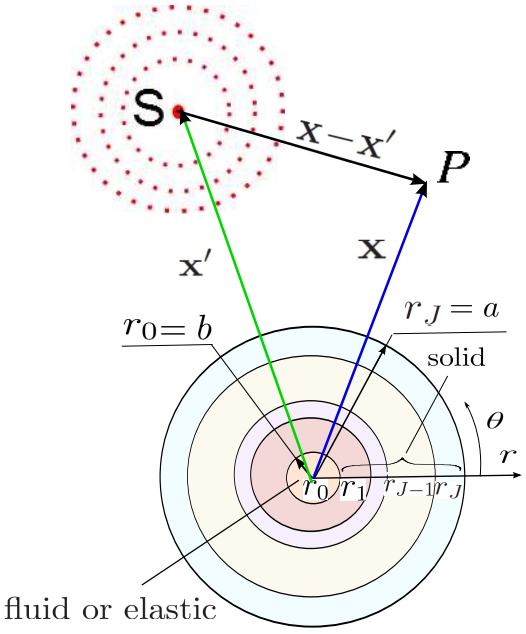

Figure 2.4: A point source impinging on an isotropic multilaminate cylinder submerged in a fluid medium or embedded in an elastic matrix.

In eq. (2.68), the unknown coefficients A_n for a plane wave incidence are derived assuming no source term: $p_s = 0$, and that the incident wave is the plane wave of amplitude A^{inc} in direction ψ, obliquely incident on cylinder at an angle α:

$$p^{inc} = A^{inc} e^{ik\mathbf{e}_\psi \cdot \mathbf{x}} e^{ik_z z} \quad \Rightarrow \quad A_n = A^{inc} i^n. \tag{2.73}$$

For a cylindrical line source, A_n can be derived considering a source at point S with a position vector $\mathbf{x}'$ with respect to origin, and assuming that [103]

$$p_s = \frac{\delta(r')}{2\pi r'} e^{ik_z z} \quad \Rightarrow \quad p^{inc} = \frac{1}{4i} H_0^{(1)}(k_\perp r') e^{ik_z z}, \tag{2.74}$$

where $\delta(r')$ is the Dirac delta function, (r', θ') is the polar coordinate system placed at the center of source S (see Figure 2.4). A point source normalized by its amplitude at

the origin is

$$p^{inc} = A_0 H_0^{(1)}(k_\perp r')e^{ik_z z} \quad \text{where} \quad A_0 = \frac{1}{H_0^{(1)}(k_\perp |\mathbf{x}'|)}, \tag{2.75}$$

and $r' = |\mathbf{x} - \mathbf{x}'|$. Thus, in the neighborhood of cylinder $\mathtt{S}_1$, we have

$$p^{inc} = A_0 \sum_{n=-\infty}^{\infty} U_n^+(k_\perp \mathbf{x}) V_n^-(k_\perp \mathbf{x}') e^{ik_z z} \quad \Rightarrow \quad A_n = A_0 V_n^-(k_\perp \mathbf{x}'), \tag{2.76}$$

for $n \in \mathbb{Z}$, where the Graf's addition theorem (2.72) is used for $|\mathbf{x}| < |\mathbf{x}'|$.

Response of cylinder

The response of cylinder $\mathtt{S}_1$ to the incident waves p^{inc} can be defined by the transition matrix $\mathbf{T}$. In general, for obstacles with no rotational symmetry, the $\mathbf{T}$ matrix is non-diagonal. For cylinders with a rotational symmetry, $\mathbf{T}$ is diagonal. Applying boundary conditions and evaluating the pressure field around a circular cylinder $\mathtt{S}_1$ yields T_{nq}, the components of transition matrix $\mathbf{T}$ of cylinder $\mathtt{S}_1$, such that

$$B_n = \sum_{q=-\infty}^{\infty} T_{nq} A_q, \tag{2.77}$$

where the components of transition matrix $\mathbf{T} = \left[T_{nq}\right]$ will be defined in the succeeding chapter.

2.3.2 P/SV in-plane wave propagation

Solid isotropic cylinder

Consider an isotropic homogeneous elastic cylinder $\mathtt{S}^{(1)}$ $(0 < b \leq r \leq a)$ illustrated in Figures 2.3 and 2.5 with the density ρ, Lamé parameters λ and μ, and total displacement field $\mathbf{u}$. The equation of motion of the elasticity theory is given by eq. (2.1). The general Hooke's law for an isotropic material follows from eq. (2.21) taking $C_{11} = C_{22} = C_{33} = \lambda + 2\mu$, $C_{12} = C_{13} = C_{23} = \lambda$, $C_{44} = C_{55} = C_{66} = \mu$. Incorporating eqs. (2.1), (2.21), and (2.3), yields the equilibrium equations of linear elastodynamics or Navier's equations for a displacement vector $\mathbf{u}$:

$$(\lambda + \mu)\boldsymbol{\nabla}\boldsymbol{\nabla} \cdot \mathbf{u} + \mu \nabla^2 \mathbf{u} = \rho \ddot{\mathbf{u}} + \mathbf{f}, \tag{2.78}$$

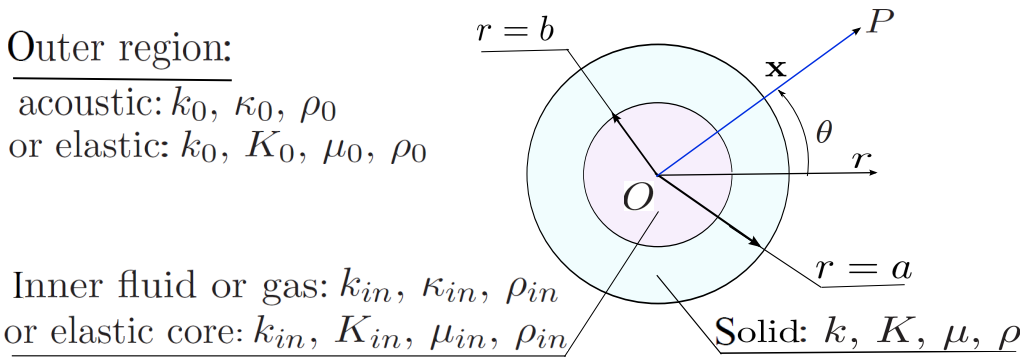

Figure 2.5: Schematics of a cylindrical layer of inner b and outer a radii in polar coordinates (r, θ). A cylindrical layer is an elastic solid; the medium inside the cylinder is either fluid, gas, or elastic core; the outer region is either acoustic medium or elastic matrix.

where ∇^2 is the Laplace operator, and $\mathbf{f}$ represents the forcing. We seek the total wave field $\mathbf{u}$ in the form of an incident wave, $\mathbf{u}^{inc}$, plus the scattered field, $\mathbf{u}^{sc}$, such that

$$\mathbf{u}(\mathbf{x}) = \mathbf{u}^{inc} + \mathbf{u}^{sc} \quad \Rightarrow \quad \varphi(\mathbf{x}) = \varphi^{inc} + \varphi^{sc}, \qquad \psi(\mathbf{x}) = \psi^{inc} + \psi^{sc}. \tag{2.79}$$

General solutions. We consider in-plane time harmonic solutions of Navier's equations (2.78). For a planar motion, in the absence of forcing $\mathbf{f}$ introducing the Helmholtz decomposition of a vector field $\mathbf{u}$, eq. (2.56), into eq. (2.78) yields the following uncoupled Helmholtz equations

$$\nabla^2\varphi + k^2\varphi = 0, \qquad \nabla^2\psi + K^2\psi = 0, \tag{2.80}$$

where k, K are the longitudinal (P) and shear (SV) wavenumbers, respectively: $k^2 = \omega^2\rho/(\lambda + 2\mu)$, $K^2 = \omega^2\rho/\mu$, ω is the frequency, the indices p and s stand for P and SV waves correspondingly. We also define, for later use, $\kappa \equiv k/K$, or equivalently $\kappa^2 = 2(1-\nu)/(1-2\nu)$ where ν is Poisson's ratio.

We expand any functions f of r and θ in Fourier series in θ as

$$f(r,\theta) = \sum_{n=-\infty}^{\infty} f_n(r)e^{in\theta}, \tag{2.81}$$

and seek solution of wave equations (2.80) in this form. Thus, the potentials can be written as

$$\varphi_n = \frac{1}{k}C_n^l f_n^l(kr), \qquad \psi_n = \frac{1}{K}D_n^l f_n^l(Kr), \tag{2.82}$$

where C_n^l and D_n^l are the unknowns, and $f_n^l(x)$ is associated with cylindrical wavefunctions and defined as

$$f_n^l(x) = \begin{cases} J_n(x), & l = 1, \\ Y_n(x), & l = 2, \\ H_n^{(1)}(x), & l = 3, \\ H_n^{(1)}(x), & l = 4, \end{cases} \tag{2.83}$$

where $f_n^1(x) = J_n(x)$ for solutions that are regular at $r = 0$, $f_n^2(x) = Y_n(x)$ for real valued irregular solutions at $r = 0$, $f_n^3(x) = H_n^{(1)}(x)$ for outgoing (radiating) solutions, $f_n^4(x) = H_n^{(2)}(x)$ for ingoing solutions, where $Y_n(x)$ is the Bessel function of the second kind; $H_n^{(2)}(x)$ is the Hankel functions of the second kind.

The stress-displacement relations for an isotropic elastic cylider follow from the Hooke's law (2.21), incorporating Cauchy relations (2.3) and Fourier expansion (2.81):

$$\sigma_{rrn} = (\lambda + 2\mu)\frac{\partial u_{rn}}{\partial r} + \lambda\left[\frac{u_{rn}}{r} + \frac{1}{r}\frac{\partial u_{\theta n}}{\partial \theta}\right], \quad \sigma_{r\theta n} = \mu\left[\frac{\partial u_{\theta n}}{\partial r} - \frac{u_{\theta n}}{r} + \frac{1}{r}\frac{\partial u_{rn}}{\partial \theta}\right]. \tag{2.84}$$

where σ_{rrn}, $\sigma_{r\theta n}$ and u_{rn}, $u_{\theta n}$ are the radial traction and displacement vector components of the cylinder $\mathtt{S}^{(1)}$ corresponding to circumferential mode $n = 0, 1, 2, ...$

Incorporating eqs. (2.82) and (2.57), and neglecting z dependence yields the displacements in the form

$$u_{rn} = \sum_{l=1,\,3}\Big\{C_n^l f_n^{l\prime}(kr) + D_n^l \frac{in}{Kr} f_n^l(Kr)\Big\}, \tag{2.85a}$$

$$u_{\theta n} = \sum_{l=1,\,3}\Big\{C_n^l \frac{in}{kr} f_n^l(kr) - D_n^l f_n^{l\prime}(Kr)\Big\}. \tag{2.85b}$$

The nth mode of stresses are found incorporating eqs. (2.84) and (2.85)

$$\sigma_{rrn} = \mu \sum_{l=1,\,3}\Big\{C_n^l k\Big[2f_n^{l\prime\prime}(kr) - \Big(\frac{K^2}{k^2} - 2\Big)f_n^l(kr)\Big] + D_n^l \frac{2in}{r}\Big[f_n^{l\prime}(Kr) - \frac{1}{Kr} f_n^l(Kr)\Big]\Big\}, \tag{2.86a}$$

$$\sigma_{r\theta n} = \mu \sum_{l=1,\,3}\Big\{C_n^{l\,\frac{2in}{r}}\Big[f_n^{l\prime}(kr) - \frac{1}{kr} f_n^l(kr)\Big] + D_n^l\Big[\frac{K^2r^2 - 2n^2}{Kr^2} f_n^l(Kr) + \frac{2}{r} f_n^{l\prime}(Kr)\Big]\Big\}. \tag{2.86b}$$

Let us define matrices such that

$$\mathbf{X}_n^l(r) = \mathbf{X}_n^l(r,\, k,\, K) = \begin{bmatrix} a_n^l(kr) & b_n^l(Kr) \\ c_n^l(kr) & d_n^l(Kr) \end{bmatrix} = \begin{bmatrix} f_n^{l\prime}(kr) & \frac{in}{Kr} f_n^l(Kr) \\ \frac{in}{kr} f_n^l(kr) & -f_n^{l\prime}(Kr) \end{bmatrix}, \tag{2.87a}$$

$$\mathbf{Y}_n^l(r) = \mathbf{Y}_n^l(r,\, k,\, K) = \begin{bmatrix} \alpha_n^l(r,k,\mu) & \beta_n^l(r,K,\mu) \\ \gamma_n^l(r,k,\mu) & \delta_n^l(r,K,\mu) \end{bmatrix}, \tag{2.87b}$$

where

$$\alpha_n^l(r,k,\mu) = \alpha_n^l(rk) = \mu k\Big[2f_n^{l\prime\prime}(kr) - \Big(\frac{K^2}{k^2} - 2\Big)f_n^l(kr)\Big], \tag{2.88a}$$

$$\beta_n^l(r,K,\mu) = \beta_n^l(rk) = \mu\frac{2in}{r}\Big[f_n^{l\prime}(Kr) - \frac{1}{Kr}f_n^l(Kr)\Big], \tag{2.88b}$$

$$\gamma_n^l(r,k,\mu) = \gamma_n^l(rk) = \mu\frac{2in}{r}\Big[f_n^{l\prime}(kr) - \frac{1}{kr}f_n^l(kr)\Big], \tag{2.88c}$$

$$\delta_n^l(r,K,\mu) = \delta_n^l(rk) = \mu\Big[\frac{K^2r^2 - 2n^2}{Kr^2}f_n^l(Kr) + \frac{2}{r}f_n^{l\prime}(Kr)\Big]. \tag{2.88d}$$

Then the displacements and traction in the cylinder can be written in the matrix form as:

$$\begin{pmatrix}\mathbf{U}_n\\ \boldsymbol{\Upsilon}_n\end{pmatrix} = \begin{pmatrix}u_{rn}(r)\\ u_{\theta n}(r)\\ \sigma_{rrn}(r)\\ \sigma_{r\theta n}(r)\end{pmatrix} = \begin{bmatrix}\mathbf{X}_n^1(r) & \mathbf{X}_n^3(r)\\ \mathbf{Y}_n^1(r) & \mathbf{Y}_n^3(r)\end{bmatrix}\begin{pmatrix}C_n^1\\ D_n^1\\ C_n^3\\ D_n^3\end{pmatrix}. \tag{2.89}$$

Green's tensor. Consider now a particular solution of Navier's equations (2.78) for displacements $\mathbf{u}$ due to a point force applied at $\mathbf{x} = \mathbf{x}'$:

$$\mathbf{f} = \mathbf{F}\delta(\mathbf{x} - \mathbf{x}'). \tag{2.90}$$

Let us define a Green's tensor such that

$$\mathbf{u} = \mathbf{G}\cdot\mathbf{F} \quad \text{or} \quad u_i = G_{ik}F_k, \tag{2.91}$$

where $\mathbf{G} = [G_{ik}]$ is the Green's tensor. Introducing eqs. (2.90) and (2.91) into (2.78) yields [108]

$$\Sigma_{ijk,j} + \rho\omega^2 G_{ik} = \delta_{ik}\delta(\mathbf{x} - \mathbf{x}'), \tag{2.92}$$

where

$$\Sigma_{ijk} = C_{ijpq}G_{pk,q}, \tag{2.93}$$

and the solution of eq. (2.92) has the form

$$G_{ik} = \big(\rho\omega^2\big)^{-1}\Big[\delta_{ik}\,K^2G_s + \partial_i\partial_k(G_s - G_p)\Big], \tag{2.94}$$

or in vector-tensor notation as

$$-(\rho\omega^2)\mathbf{G}(\mathbf{x} - \mathbf{x}') = \nabla\nabla G_p + (\mathbf{I}\nabla^2 - \nabla\nabla)G_s = \nabla\nabla G_p + (\nabla\times\mathbf{k})(\nabla\times\mathbf{k})G_s \ \text{ for } \mathbf{x}\neq\mathbf{x}', \tag{2.95}$$

where $(\nabla\times\mathbf{k})_i = e_{ij3}\partial_j$, $(i,j = \overline{1,2})$, ∂_j denotes partial derivatives, and G_s and G_p satisfy the identities

$$(\nabla^2 + K^2)G_s = \delta(\mathbf{x}-\mathbf{x}') \quad \text{and} \quad (\nabla^2 + k^2)G_p = \delta(\mathbf{x}-\mathbf{x}'), \tag{2.96}$$

respectively and have the form

$$G_s = \frac{1}{4i}V_0(K(\mathbf{x}-\mathbf{x}')), \quad G_p = \frac{1}{4i}V_0(k(\mathbf{x}-\mathbf{x}')), \tag{2.97}$$

where $V_0(\mathbf{x})$ is defined by eq. (2.70) where $n = 0$. Introducing (2.95) into (2.91) and incorporating with the Helmholtz decomposition (2.56) gives

$$\nabla\varphi + (\nabla\times\mathbf{k})\psi = \big(-\rho\omega^2\big)^{-1}\big[\nabla\nabla G_p\cdot\mathbf{F} + (\nabla\times\mathbf{k})(\nabla\times\mathbf{k})G_s\cdot\mathbf{F}\big], \quad \mathbf{x}\neq\mathbf{x}'. \tag{2.98}$$

Thus, a comparison of terms on the right hand of eq. (2.98) with ones on the left hand side produces

$$\begin{aligned} -\rho\omega^2\varphi &= \mathbf{F}\cdot\nabla G_p = F_1\partial_1 G_p + F_2\partial_2 G_p, \\ -\rho\omega^2\psi &= \mathbf{F}\cdot(\nabla\times\mathbf{k})G_s = F_1\partial_2 G_s - F_2\partial_1 G_s, \end{aligned} \qquad \mathbf{x}\neq\mathbf{x}'. \tag{2.99}$$

This makes it clear that for a standard point source, regardless of the choice of $\mathbf{F}$, both compressional and shear waves propagate away from the point source.

Inner region

Acoustic medium. In the interior fluid ($r < b$) (see Figure 2.5), the displacements and stresses are found allowing all shear terms to tend to zero, i.e. in eq. (2.87)

$$\gamma_n^l(r,k,\mu)\to 0, \quad \text{and} \quad \alpha_n^l(r,k,\mu)\to\hat{\alpha}_n^l(r,k_{in},\kappa_{in}) \equiv -\kappa_{in}k_{in}f_n^l(k_{in}r), \tag{2.100}$$

where ${f_n}^l(k_{in}r)$ is given by (2.83). Thus, the n-th mode of the displacements and traction in the interior fluid is of the form

$$\begin{pmatrix} u_{rn}^{in} \\ u_{\theta n}^{in} \\ \sigma_{rrn}^{in} \end{pmatrix} = \begin{pmatrix} a_n^1(k_{in}r) \\ c_n^1(k_{in}r) \\ \hat{\alpha}_n^1(r,k_{in},\kappa_{in}) \end{pmatrix} C_n^{1,\,in}, \tag{2.101}$$

where $C_n^{1,in}$ is the unknown coefficient, and

$$a_n^1(k_{in}r) = J_n{}'(k_{in}r), \qquad c_n^1(k_{in}r) = \frac{i\,n}{k_{in}r} J_n(k_{in}r). \tag{2.102}$$

Elastic core. Since the radius of the solid core is allowed to go to zero, we only use the regular solutions of wave equations, and the displacements and tractions reduce to the form

$$\begin{pmatrix} \mathbf{U}_n^{in} \\ \boldsymbol{\Upsilon}_n^{in} \end{pmatrix} = \begin{pmatrix} u_{rn}^{in} \\ u_{\theta n}^{in} \\ \sigma_{rrn}^{in} \\ \sigma_{r\theta n}^{in} \end{pmatrix} = \begin{pmatrix} \mathbf{X}_n^1(r) \\ \mathbf{Y}_n^1(r) \end{pmatrix} \begin{pmatrix} C_n^{1,in} \\ D_n^{1,in} \end{pmatrix} = \begin{pmatrix} a_n^1(k_{in}r) & b_n^1(K_{in}r) \\ c_n^1(k_{in}r) & d_n^1(K_{in}r) \\ \alpha_n^1(r,k_{in},\mu_{in}) & \beta_n^1(r,K_{in},\mu_{in}) \\ \gamma_n^1(r,k_{in},\mu_{in}) & \delta_n^1(r,K_{in},\mu_{in}) \end{pmatrix} \begin{pmatrix} C_n^{1,in} \\ D_n^{1,in} \end{pmatrix}, \tag{2.103}$$

where a_n^1, b_n^1, c_n^1 and d_n^1 are defined by (2.87) and $\alpha_n^1, \beta_n^1, \gamma_n^1$ and δ_n^1 by (2.88).

Rigid core and hollow region. A rigid inner core does not displace, and therefore

$$\mathbf{U}_n^{in} = \mathbf{0}, \quad (\mathbf{z}_n^{in})^{-1} = \mathbf{0}, \tag{2.104}$$

where $\mathbf{z}_n^{in}(r)$ is the impedance matrix on inner surface of cylinder. A hollow inner region is traction free, thus

$$\boldsymbol{\Upsilon}_n^{in} = \mathbf{0}, \quad \mathbf{z}_n^{in} = \mathbf{0}. \tag{2.105}$$

Outer medium

Displacement and stress in acoustic medium. For an acoustic medium allowing all shear terms to tend to zero, only the first columns of the matrices $\mathbf{X}_n^l$ and $\mathbf{Y}_n^l$ remain in eq. (2.87) with

$$\gamma_n^l(r,k,\mu) \to 0 \tag{2.106}$$

and

$$\alpha_n^l(r,k,\mu) \to \hat{\alpha}_n{}^l(r,k_0,\kappa_0) \equiv -\kappa_0 k_0 f_n^l(k_0 r), \quad \text{for the exterior fluid,} \tag{2.107}$$

where $f_n{}^e(k_0 r)$ is defined by (2.83).

Thus, the nth mode of the displacements and traction in the exterior fluid is of the form

$$\begin{pmatrix} u^0_{rn} \\ u^0_{\theta n} \\ \sigma^0_{rrn} \end{pmatrix} = \begin{pmatrix} a^1_n(k_0 r) & a^3_n(k_0 r) \\ c^1_n(k_0 r) & c^3_n(k_0 r) \\ \hat{\alpha}^1_n(r, k_0, \kappa_0) & \hat{\alpha}^3_n(r, k_0, \kappa_0) \end{pmatrix} \begin{pmatrix} A_n \\ B_n \end{pmatrix}, \tag{2.108}$$

where $\hat{\alpha}^l_n(r, k_0, \kappa_0)$ is given by (2.107)

$$a^l_n(k_0 r) = {f_n}^{l\prime}(k_0 r), \qquad c^l_n(k_0 r) = \frac{in}{k_0 r} {f_n}^l(k_0 r), \tag{2.109}$$

with ${f_n}^l(k_0 r)$ given by (2.83). Here A_n is the incident wave coefficient and defined in Section 2.3.1 for both plane wave and cylindrical line sources. The scattering coefficient B_n is to be determined.

Elastic matrix. In a solid elastic matrix, we consider a longitudinal (P) and transversal (SV) incidence separately. Then, for ***incident P waves***, the displacement and the traction in exterior solid elastic matrix are defined in matrix form as

$$\begin{pmatrix} \mathbf{U}^0_n \\ \mathbf{\Upsilon}^0_n \end{pmatrix} = \begin{pmatrix} u^0_{rn} \\ u^0_{\theta n} \\ \sigma^0_{rrn} \\ \sigma^0_{r\theta n} \end{pmatrix} = \begin{pmatrix} a^1_n(k_0 r) \\ c^1_n(k_0 r) \\ \alpha^1_n(r, k_0, \mu_0) \\ \gamma^1_n(r, k_0, \mu_0) \end{pmatrix} A_{p,n} + \begin{pmatrix} \mathbf{X}^3_n(r) \\ \mathbf{Y}^3_n(r) \end{pmatrix} \begin{pmatrix} B_{p,n} \\ B_{s,n} \end{pmatrix}, \tag{2.110}$$

where $\mathbf{X}^3_n(r)$ and $\mathbf{Y}^3_n(r)$ are defined by (2.87), the $B_{p,n}$ and $B_{s,n}$ are the unknown scattering coefficients to be found from boundary conditions, $A_{p,n}$ is the incident P wave coefficient derived at the end of this section for a plane wave and point force.

For ***incident SV waves***, the displacement and the traction in an exterior solid elastic matrix are of the form

$$\begin{pmatrix} \mathbf{U}^0_n \\ \mathbf{\Upsilon}^0_n \end{pmatrix} = \begin{pmatrix} u^0_{rn} \\ u^0_{\theta n} \\ \sigma^0_{rrn} \\ \sigma^0_{r\theta n} \end{pmatrix} = \begin{pmatrix} b^1_n(K_0 r) \\ d^1_n(K_0 r) \\ \beta^1_n(r, K_0, \mu_0) \\ \delta^1_n(r, K_0, \mu_0) \end{pmatrix} A_{s,n} + \begin{pmatrix} \mathbf{X}^3_n(r) \\ \mathbf{Y}^3_n(r) \end{pmatrix} \begin{pmatrix} B_{p,n} \\ B_{s,n} \end{pmatrix}, \tag{2.111}$$

where $\mathbf{X}^3_n(r)$ and $\mathbf{Y}^3_n(r)$ are defined by (2.87). Here, the scattering coefficients $B_{p,n}$ and $B_{s,n}$ can be determined from the boundary conditions. The incident P/SV wave coefficients $A_{p,n}$ and $A_{s,n}$ are derived next.

Incident elastic wave coefficients. For a plane P/SV wave incidence, the incident wave coefficients $A_{p,n}$ and $A_{s,n}$ in eqs. (2.110) and (2.111) are derived assuming no forcing term ($\mathbf{f} = 0$), and that the incident wave is the plane wave of amplitude A_{ς}^{inc} in direction Ψ and perpendicularly incident on cylinder ($\alpha = 0$), where $\varsigma = p$ for P wave incidence and $\varsigma = s$ for SV wave incidence:

$$\begin{pmatrix} \phi^{inc}(\mathbf{x}) \\ \psi^{inc}(\mathbf{x}) \end{pmatrix} = \begin{pmatrix} A_p^{inc} e^{ik\mathbf{e}_\psi \cdot \mathbf{x}} \\ A_s^{inc} e^{iK\mathbf{e}_\psi \cdot \mathbf{x}} \end{pmatrix} = \begin{pmatrix} A_p^{inc} e^{ikx} \\ A_s^{inc} e^{iKx} \end{pmatrix} \quad \Rightarrow \quad \begin{pmatrix} A_{p,n} \\ A_{s,n} \end{pmatrix} = \begin{pmatrix} A_p^{inc} i^n \\ A_s^{inc} i^n \end{pmatrix}. \tag{2.112}$$

For a point force $\mathbf{f} = \mathbf{F}\delta(\mathbf{x} - \mathbf{x}')$ applied at point S with a position vector $\mathbf{x}'$ with respect to the origin, the $A_{p,n}$ and $A_{s,n}$ can be derived from a particular solution of elasticity theory given by eqs. (2.91), (2.99):

$$\mathbf{u}^{inc} = \mathbf{G} \cdot \mathbf{F} \quad \Rightarrow \quad -\rho\omega^2 \begin{pmatrix} \phi^{inc}(\mathbf{x}) \\ \psi^{inc}(\mathbf{x}) \end{pmatrix} = \begin{pmatrix} F_1 \partial_1 G_p + F_2 \partial_2 G_p, \\ F_1 \partial_2 G_s - F_2 \partial_1 G_s, \end{pmatrix}, \qquad \mathbf{x} \neq \mathbf{x}'. \tag{2.113}$$

Introducing (2.97) into (2.113) leads to

$$\rho\omega^2 |\mathbf{x} - \mathbf{x}'| \begin{pmatrix} \phi^{inc}(\mathbf{x}) \\ \psi^{inc}(\mathbf{x}) \end{pmatrix} = \begin{pmatrix} k\left[F_1(x - x') + F_2(y - y')\right] V_1^+(k(\mathbf{x} - \mathbf{x}'))\, e^{-i \arg(\mathbf{x} - \mathbf{x}')} \\ K\left[F_1(y - y') - F_2(x - x')\right] V_1^+(K(\mathbf{x} - \mathbf{x}')) e^{-i \arg(\mathbf{x} - \mathbf{x}')} \end{pmatrix}. \tag{2.114}$$

Using the Graf's addition theorem (2.72) for $|\mathbf{x}| < |\mathbf{x}'|$, in the neighborhood of cylinder $\mathtt{S}_1$, we have

$$\begin{pmatrix} \phi^{inc}(\mathbf{x}) \\ \psi^{inc}(\mathbf{x}) \end{pmatrix} = \frac{e^{-i \arg(\mathbf{x} - \mathbf{x}')}}{\rho\omega^2 |\mathbf{x} - \mathbf{x}'|} \sum_{n=-\infty}^{\infty} \begin{pmatrix} k\left[F_1(x - x') + F_2(y - y')\right] U_n^+(k\mathbf{x})\, V_{n-1}^-(k\mathbf{x}') \\ K\left[F_1(y - y') - F_2(x - x')\right] U_n^+(K\mathbf{x})\, V_{n-1}^-(K\mathbf{x}') \end{pmatrix}. \tag{2.115}$$

Thus, a comparison of eqs. , (2.110), and (2.111) yields

$$\begin{pmatrix} A_{p,n} \\ A_{s,n} \end{pmatrix} = \frac{e^{-i \arg(\mathbf{x} - \mathbf{x}')}}{\rho\omega^2 |\mathbf{x} - \mathbf{x}'|} \begin{pmatrix} k\left[F_1(x - x') + F_2(y - y')\right] V_{n-1}^-(k\mathbf{x}') \\ K\left[F_1(y - y') - F_2(x - x')\right] V_{n-1}^-(K\mathbf{x}') \end{pmatrix} \quad \text{for } n \in \mathbb{Z}. \tag{2.116}$$

Chapter 3

Scattering from multilayered cylindrical and spherical structures

In this chapter, the mathematical model of acoustic and elastic wave scattering from multilayered cylindrical and spherical structures is developed. It begins with the impedance matrix method proposed in Section 3.1 for radially inhomogeneous anisotropic solids. Section 3.1.2 provides an explicit method for finding the impedance in piecewise uniform, transversely isotropic materials. The method described in this section also serves as a tool to compare with more general solution methods based on the Riccati matrix differential equation for the impedance matrix [114] for a cylindrically anisotropic medium. In section 3.2, acoustic and elastic wave scattering of incident waves from transversely-isotropic cylinder is investigated. Transformation from elastic to acoustic matricant is shown in Section 3.2.4 for acoustic SH wave propagation. A Global matrix method is described in Section 3.3 for isotropic multilayered elastic cylindrical structures. Section 3.3.1 considers acoustic scattering from a multilaminate cylinder immersed in fluid, and Section 3.3.2 describes elastic scattering of P/SV waves from a multilayered cylinder embedded in an elastic matrix.

3.1 Impedance matrix method

Wave propagation in layered elastic media has been widely studied resulting in a variety of solution approaches. These include the use of scalar and vector potentials [104], the transfer matrix method [23, 81, 152, 79], and the delta matrix method [159, 48]. Alternatively, computationally stable methods have also been developed, e.g. the stiffness matrix [137, 138], the global matrix [145], and the reflectivity method [136]. Such approaches are limited to isotropic or transversely-isotropic materials whereas we are

interested in general anisotropic solids in order to develop scattering solutions related to metamaterial devices such as acoustic cloaks [117, 111, 143] which can be modeled as radially inhomogeneous anisotropic solids. The goal of this Section is to provide a methodology for modeling such materials.

Consider a time harmonic wave motion in radially inhomogeneous anisotropic solids. The method proposed in this section is applicable for both cylindrically anisotropic and spherically anisotropic media. The associated equilibrium equations for linear elastodynamics in cylindrical coordinates are summarized in Section 2.1.1 and in spherical coordinates in Section 2.1.2. We seek solutions of equilibrium equations (2.19) in cylindrical coordinates in the form of time-harmonic cylindrical waves given by eqs. (2.15) (which includes the superscript n that is here omitted for simplicity), and solutions of equilibrium equations (2.29) in spherical coordinates in the form of eq. (2.31), in terms of the vector spherical harmonics $\mathbf{P}_{mn\sigma}, \mathbf{B}_{mn\sigma}, \mathbf{C}_{mn\sigma}$ given by eqs. (2.26). The $m \times m$ conditional impedance matrix $\mathbf{z}$ defined by (2.47) relates the m dimensional vectors $\mathbf{U}(r)$ and $\mathbf{V}(r)$ associated with displacement and traction, respectively, where m is either 3, 2 or 1.

We develop an approach suitable for radially inhomogeneous piecewise uniform anisotropic medium by explicit calculation of the global impedance matrix $\mathbf{Z}$ of (2.53), from which the conditional impedance can be found using (2.55). In particular, this method can be applied for piecewise uniform transversely isotropic (TI) cylinders for which the explicit formulas are available for the conditional impedance $\mathbf{z}$ [116] and the two point impedance matrix $\mathbf{Z}$ of a given TI layer that will be derived in Section 3.1.2. The approach is also suitable in spherical coordinates for a radially inhomogeneous sphere for which the material is piecewise uniform TI about $\mathbf{e}_r$ vector. However, the explicit formulas for impedance matrices $\mathbf{z}$ and $\mathbf{Z}$ for TI material in spherical coordinates are not available; we consider spherically anisotropic medium as radially inhomogeneous multilayered medium consisting of N isotropic layers, and derive the explicit formular for $\mathbf{Z}$ of a given isotropic layer in Section 3.1.4.

The approach is based on a recursive algorithm proposed by Rokhlin et al. [137]

called the stiffness matrix method. The analysis in [137] was restricted to multilayered media in Cartesian coordinates, whereas the present method is applicable to both cylindrically and spherically layered anisotropic medium. We will refer to Rokhlin and Wang [137] several times in this section to note the similarities and differences of the approaches.

Results of this section are published in [114] for a cylindrically anisotropic medium.

3.1.1 Calculating the global impedance matrix

Consider $J > 1$ layers of uniform anisotropic materials with the k-th layer $r_{k-1} < r < r_k$, $k \in \overline{1, J}$, see Figure 2.1. The local two point impedance matrix of the k-th layer is denoted by $\mathbf{Z}^k(r_k, r_{k-1})$:

$$\begin{pmatrix} \mathbf{V}_{k-1}(r_{k-1}) \\ -\mathbf{V}_k(r_k) \end{pmatrix} = -i\mathbf{Z}^k(r_k, r_{k-1}) \begin{pmatrix} \mathbf{U}(r_{k-1}) \\ \mathbf{U}(r_k) \end{pmatrix}, \quad \mathbf{Z}^k(r_k, r_{k-1}) = \begin{pmatrix} \mathbf{Z}_1^k & \mathbf{Z}_2^k \\ \mathbf{Z}_3^k & \mathbf{Z}_4^k \end{pmatrix}. \tag{3.1}$$

The explicit form of $\mathbf{Z}^k(r_k, r_{k-1})$ of the k-th cylindrical layer of TI material is defined by eq. (3.24) and derived in Section 3.1.2. The explicit form of $\mathbf{Z}^k(r_k, r_{k-1})$ of the k-th spherical layer of isotropic material is given by (3.37) in Section 3.1.4. Denote the global two point impedance matrix for the layer between r_0 and r_k by $\mathbf{Z}^{\mathbf{K}} = \mathbf{Z}^{\mathbf{K}}(r_k, r_0)$. Our objective is the global two point impedance matrix for the entire medium, $\mathbf{Z}(r_J, r_0) \equiv \mathbf{Z}^{\mathbf{J}}(r_J, r_0)$.

Consider first the two bordering layers between $r = r_0$ and $r = r_2$ and sharing the $r = r_1$ surface. Continuity of displacements and traction on the interface implies

$$\begin{pmatrix} \mathbf{V}_0 \\ -\mathbf{V}_1 \end{pmatrix} = -\mathrm{i} \begin{pmatrix} \mathbf{Z}_1^a & \mathbf{Z}_2^a \\ \mathbf{Z}_3^a & \mathbf{Z}_4^a \end{pmatrix} \begin{pmatrix} \mathbf{U}_0 \\ \mathbf{U}_1 \end{pmatrix}, \tag{3.2a}$$

$$\begin{pmatrix} \mathbf{V}_1 \\ -\mathbf{V}_2 \end{pmatrix} = -\mathrm{i} \begin{pmatrix} \mathbf{Z}_1^b & \mathbf{Z}_2^b \\ \mathbf{Z}_3^b & \mathbf{Z}_4^b \end{pmatrix} \begin{pmatrix} \mathbf{U}_1 \\ \mathbf{U}_2 \end{pmatrix}, \tag{3.2b}$$

where $\mathbf{Z}^a \equiv \mathbf{Z}^1(r_1, r_0)$, $\mathbf{Z}^b \equiv \mathbf{Z}^2(r_2, r_1)$. From the second row of eq. (3.2a) and the first row of eq. (3.2b), we have

$$\mathbf{U}_1 = -\big(\mathbf{Z}_4^a + \mathbf{Z}_1^b\big)^{-1}\big(\mathbf{Z}_3^a\,\mathbf{U}_0 + \mathbf{Z}_2^b\,\mathbf{U}_2\big). \tag{3.3}$$

Introducing eq. (3.3) into eqs. (3.2a) and (3.2b), we define the impedance matrix $\mathbf{Z^2}(r_2, r_0)$ that relates the traction vector to the displacement vector on the inner ($r = r_0$) and outer ($r = r_2$) surfaces of the bilayer,

$$\begin{pmatrix} \mathbf{V}_0 \\ -\mathbf{V}_2 \end{pmatrix} = -\mathrm{i}\,\mathbf{Z^2}(r_2, r_0) \begin{pmatrix} \mathbf{U}_0 \\ \mathbf{U}_2 \end{pmatrix}, \tag{3.4}$$

where

$$\mathbf{Z^2}(r_2, r_0) = \begin{pmatrix} \mathbf{Z}_1^a - \mathbf{Z}_2^a\big(\mathbf{Z}_4^a + \mathbf{Z}_1^b\big)^{-1}\mathbf{Z}_3^a & -\mathbf{Z}_2^a\big(\mathbf{Z}_4^a + \mathbf{Z}_1^b\big)^{-1}\mathbf{Z}_2^b \\ -\mathbf{Z}_3^b\big(\mathbf{Z}_4^a + \mathbf{Z}_1^b\big)^{-1}\mathbf{Z}_3^a & \mathbf{Z}_4^b - \mathbf{Z}_3^b\big(\mathbf{Z}_4^a + \mathbf{Z}_1^b\big)^{-1}\mathbf{Z}_2^b \end{pmatrix}, \tag{3.5}$$

$\mathbf{Z}_i^a = \mathbf{Z}_i^1$, $\mathbf{Z}_i^b = \mathbf{Z}_i^2$ and $\mathbf{Z}_i^k$ ($k = 1, 2$, $i = \overline{1,4}$) are given by eqs. (3.1). Note that eqs. (3.2a) and (3.2b) are similar, apart from a sign change, to eqs. (19) and (20) in [137].

Employing (3.4) recursively, the global impedance matrix $\mathbf{Z^K}(r_k, r_0)$ for the medium layer between r_0 and r_k is obtained with 3×3 components

$$\mathbf{Z^K} = \begin{pmatrix} \mathbf{Z_1^{K\text{-}1}} - \mathbf{Z_2^{K\text{-}1}}\big(\mathbf{Z}_1^k + \mathbf{Z_4^{K\text{-}1}}\big)^{-1}\mathbf{Z_3^{K\text{-}1}} & -\mathbf{Z_2^{K\text{-}1}}\big(\mathbf{Z}_1^k + \mathbf{Z_4^{K\text{-}1}}\big)^{-1}\mathbf{Z}_2^k \\ -\mathbf{Z}_3^k\big(\mathbf{Z}_1^k + \mathbf{Z_4^{K\text{-}1}}\big)^{-1}\mathbf{Z_3^{K\text{-}1}} & \mathbf{Z}_4^k - \mathbf{Z}_3^k\big(\mathbf{Z}_1^k + \mathbf{Z_4^{K\text{-}1}}\big)^{-1}\mathbf{Z}_2^k \end{pmatrix}, \tag{3.6}$$

where $\mathbf{Z_i^{K\text{-}1}}$, ($i = \overline{1,4}$) are the 3×3 sub-matrices of the matrix $\mathbf{Z^{K\text{-}1}}(r_{k-1}, r_0)$ for $k-1$ layers, $\mathbf{Z}_i^k$, ($i = \overline{1,4}$) are the 3×3 sub-matrices of the matrix $\mathbf{Z}^k(r_k, r_{k-1})$ for the k-th layer, defined by eq. (3.1). The global impedance matrix for the N-layered medium is obtained by using eq. (3.6) $(N-1)$ times.

The main differences between the present results and those of [137] are, first that by construction the local $\mathbf{Z}^k$ and global $\mathbf{Z^K}$ two point impedance matrices are Hermitian matrices. Secondly, the present results are valid for cylindrically and spherically layered structures, as compared with those of [137] which are for multilayered structures in Cartesian coordinates. Despite the differences, we note that the two point impedance matrix $\mathbf{Z}^k$ of eq. (3.1) and the global two point impedance matrix $\mathbf{Z^K}(r_k, r_0)$ are, apart from some sign differences, similar to the stiffness matrix $\mathbf{K}^m$ and global stiffness matrix $\mathbf{K}^M$ of Rokhlin and Wang [137].

3.1.2 Impedance for uniform transversely isotropic cylinders

We consider transversely isotropic (TI) solids with the symmetry axis in the z-direction. The general Hooke's law for an orthotropic material is given by eq. (2.21). A transversal

isotropy is a particular case of orthotropy. The general Hooke's law for a TI material follows from eq. (2.21) taking $C_{11} = C_{22}$, $C_{13} = C_{23}$, $C_{44} = C_{55}$, and $C_{66} = (C_{11} - C_{22})/2$. Incorporating Cauchy relations (2.8) and Hooke's law for TI material, the equilibrium equations (2.1) can be written in terms of displacements [78]

$$C_{44}\left(\frac{\partial^2 u_z}{\partial z \partial r} + \frac{\partial^2 u_r}{\partial z^2}\right) + C_{11}\left(\frac{\partial^2 u_r}{\partial r^2} + \frac{1}{r}\frac{\partial u_r}{\partial r} - \frac{3}{2r^2}\frac{\partial u_\theta}{\partial \theta} + \frac{1}{2r^2}\frac{\partial^2 u_r}{\partial \theta^2} - \frac{u_r}{r^2} + \frac{1}{2r}\frac{\partial^2 u_\theta}{\partial r \partial \theta}\right) + \frac{1}{2r}C_{12}\left[\frac{\partial}{\partial \theta}\left(\frac{\partial u_\theta}{\partial r} - \frac{1}{r}\frac{\partial u_r}{\partial \theta} + \frac{u_\theta}{r}\right)\right] + C_{13}\frac{\partial^2 u_z}{\partial z \partial r} = \rho \frac{\partial^2 u_r}{\partial t^2} \tag{3.7a}$$

$$C_{44}\left[\frac{\partial}{\partial z}\left(\frac{\partial u_\theta}{\partial z} + \frac{1}{r}\frac{\partial u_z}{\partial \theta}\right)\right] + C_{12}\left(-\frac{1}{2r}\frac{\partial u_\theta}{\partial r} + \frac{1}{2}\frac{u_\theta}{r^2} - \frac{1}{2}\frac{\partial^2 u_\theta}{\partial r^2} - \frac{1}{2r^2}\frac{\partial u_r}{\partial \theta} + \frac{1}{2r}\frac{\partial^2 u_r}{\partial \theta \partial r}\right) + C_{11}\left(\frac{1}{r^2}\frac{\partial^2 u_\theta}{\partial \theta^2} + \frac{1}{2r}\frac{\partial u_\theta}{\partial r} + \frac{1}{2}\frac{\partial^2 u_\theta}{\partial r^2} + \frac{3}{2r^2}\frac{\partial u_r}{\partial \theta} + \frac{1}{2r}\frac{\partial^2 u_r}{\partial r \partial \theta} - \frac{1}{2}\frac{u_\theta}{r^2}\right) + \frac{C_{13}}{r}\frac{\partial^2 u_z}{\partial z \partial \theta} = \rho \frac{\partial^2 u_\theta}{\partial t^2}, \tag{3.7b}$$

$$C_{44}\left(\frac{1}{r^2}\frac{\partial^2 u_z}{\partial \theta^2} + \frac{\partial^2 u_z}{\partial r^2} + \frac{1}{r}\frac{\partial^2 u_\theta}{\partial z \partial \theta} + \frac{1}{r}\frac{\partial u_z}{\partial r} + \frac{1}{r}\frac{\partial u_r}{\partial z} + \frac{\partial^2 u_r}{\partial z \partial r}\right) + C_{33}\frac{\partial^2 u_z}{\partial z^2} + C_{13}\left[\frac{\partial}{\partial z}\left(\frac{u_r}{r} + \frac{1}{r}\frac{\partial u_\theta}{\partial \theta} + \frac{\partial u_r}{\partial r}\right)\right] = \rho \frac{\partial^2 u_z}{\partial t^2}. \tag{3.7c}$$

General solutions for transverse isotropy

We seek solutions of equilibrium equations for transverse isotropy in the form of time-harmonic cylindrical waves. The displacement vector may be decomposed using Buchwald's scalar potentials [26], the functions φ, χ and ψ, given by eq. (2.58). Inserting eq. (2.58) into equations of motion in displacements (3.7) and modifying obtained equations, yields [32], [4]:

$$C_{11}\nabla_1^2\varphi + C_{44}\frac{\partial^2 \varphi}{\partial z^2} + (C_{13} + C_{44})\frac{\partial^2 \psi}{\partial z^2} - \rho\frac{\partial^2 \varphi}{\partial t^2} = 0, \tag{3.8a}$$

$$(C_{13} + C_{44})\nabla_1^2\varphi + C_{44}\nabla_1^2\psi + C_{33}\frac{\partial^2 \psi}{\partial z^2} - \rho\frac{\partial^2 \psi}{\partial t^2} = 0, \tag{3.8b}$$

$$C_{66}\nabla_1^2\chi + C_{44}\frac{\partial^2 \chi}{\partial z^2} - \rho\frac{\partial^2 \chi}{\partial t^2} = 0, \tag{3.8c}$$

where

$$C_{66} = \frac{1}{2}(C_{11} - C_{12}), \qquad \nabla_1^2 = \nabla^2 - \frac{\partial^2}{\partial z^2} = \frac{\partial^2}{\partial r^2} + \frac{1}{r}\frac{\partial}{\partial r} + \frac{1}{r^2}\frac{\partial^2}{\partial \theta^2}. \tag{3.9}$$

We assume solutions of the form:

$$\varphi = R_{on}^{l}\frac{1}{k}\,f_n^l(kr)\,e^{i(n\theta+k_z z-\omega t)}, \tag{3.10a}$$

$$\psi = S_{on}^{l}\frac{1}{k}\,f_n^l(kr)\,e^{i(n\theta+k_z z-\omega t)}, \tag{3.10b}$$

$$\chi = T_{on}^{l}\frac{1}{k_3}f_n^l(k_3 r)\,e^{i(n\theta+k_z z-\omega t)}, \tag{3.10c}$$

where $n = ...,\ -2,\ -1,\ 0,\ 1,\ 2,\ ...$ is the circumferential number, k_z is the wavenumber, and ω is the frequency, and $f_n^l(x)$ is associated with cylindrical wavefunctions and defined by (2.83). Introducing solutions (3.10) into eqs. (3.8), we obtain

$$\left[C_{11}k^2 - (\rho\omega^2 - C_{44}k_z^2\right] R_{on}^{l} + \left[(C_{13}+C_{44})k_z^2\right] S_{on}^{l} = 0, \tag{3.11a}$$

$$\left[(C_{13}+C_{44})k^2\right] R_{on}^{l} + \left[C_{44}k^2 - (\rho\omega^2 - C_{33}k_z^2)\right] S_{on}^{l} = 0, \tag{3.11b}$$

$$\left[C_{66}k_3^2 - \left(\rho\omega^2 - C_{44}k_z^2\right)\right] T_{on}^{l} = 0. \tag{3.11c}$$

Thus, for potential function χ eq. (3.11c) yields

$$k_3^2 = \frac{(\rho\,\omega^2 - C_{44}k_z^2)}{C_{66}}. \tag{3.12}$$

Equating the determinant of coefficients of R_{on}^{l} and T_{on}^{l} to zero in eqs. (3.11a)-(3.11b) for potentials φ and ψ, we obtain the following characteristic equation:

$$C_{11}\,C_{44}\,k^4 + k^2\,A + B = 0, \tag{3.13}$$

where

$$A \;=\; \left(C_{13} + \,C_{44}\right)k_z^2 + C_{11}\left(\rho\omega^2 - C_{33}k_z^2\right) + C_{44}\left(\rho\omega^2 - C_{44}k_z^2\right), \tag{3.14a}$$

$$B \;=\; \rho\omega^4 - \omega^2\left(C_{33} + \,C_{44}\right)k_z^2 + C_{33}\,C_{44}k_z^4. \tag{3.14b}$$

The roots of characteristic equation (3.13) are

$$k_{1,\,2}^2 = \frac{-A \mp \sqrt{A^2 - 4C_{11}\,C_{44}\,B}}{2\,C_{11}\,C_{44}}. \tag{3.15}$$

Thus, the general solution of the equilibrium equations for transverse isotropy are of the form

$$\{\varphi, \chi, \psi\} = \{\bar{\varphi}, \bar{\chi}, \bar{\psi}\}\mathrm{e}^{\mathrm{i}(n\theta+k_z z-\omega t)} \tag{3.16}$$

where

$$\bar{\varphi} = R^l_{on}\,\frac{1}{k_1} f^l_n(k_1 r) + \frac{1}{k_2} S^l_{on}\, f^l_n(k_2 r), \qquad \bar{\chi} = -\,T^l_{on}\,\frac{1}{k_3} f^l_n(k_3 r), \tag{3.17}$$
$$\bar{\psi} = \frac{\kappa_1}{k_1}\, R^l_{on}\, f^l_n(k_1 r) + S^l_{on}\frac{\kappa_2}{k_2}\, f^l_n(k_2 r),$$

and R^l_{on}, S^l_{on}, T^l_{on} are unknown coefficients, $f^l_n(x)$ are cylindrical functions defined by eq. (2.83). The displacement field can be represented as a linear combination of any two of the four types of cylindrical functions $f^l_n(x)$, $(l = \overline{1,4})$. The non-dimensional numbers κ_1, κ_2 are given by

$$\kappa_i = \frac{C_{66}\, k_3^2 - C_{11}\, k_i^2}{\big(C_{13} + C_{44}\big) k_z}, \quad (i = 1, 2). \tag{3.18}$$

For isotropic material wavenumbers k_i, κ_i reduce to $k_1^2 = \omega^2\rho/(\lambda + 2\mu) - k_z^2$, $k_2^2 = k_3^2 = \omega^2\rho/\mu - k_z^2$, $\kappa_1 = 1$, $\kappa_2 = -k_2^2/k_z^2$.

The displacement and traction vectors $\mathbf{U}$ and $\mathbf{V}$ are obtained in matrix form for each n as

$$\mathbf{U}(r) = \sum_l \mathbf{X}^l(r)\mathbf{w}^l, \quad \mathbf{V}(r) = \sum_l \mathbf{Y}^l(r)\mathbf{w}^l, \quad \mathbf{w}^l = \begin{pmatrix} R^l_{on} \\ S^l_{on} \\ T^l_{on} \end{pmatrix}, \tag{3.19}$$

where the summation on l is over any two of the possible $l = \overline{1,4}$, and

$$\mathbf{X}^l(r) = \begin{bmatrix} f_n^{l\prime}(k_1 r) & f_n^{l\prime}(k_2 r) & -\frac{\mathrm{i}n}{k_3 r} f^l_n(k_3 r) \\ \frac{\mathrm{i}n}{k_1 r} f^l_n(k_1 r) & \frac{\mathrm{i}n}{k_2 r} f^l_n(k_2 r) & f_n^{l\,\prime}(k_3 r) \\ \frac{\mathrm{i}\kappa_1}{k_1} f^l_n(k_1 r) & \frac{\mathrm{i}\kappa_2}{k_2} f^l_n(k_2 r) & 0 \end{bmatrix}, \tag{3.20}$$

$$\mathbf{Y}^l(r) = -\mathrm{i}\mathbf{z}^l(r)\mathbf{X}^l(r), \tag{3.21}$$

and $\mathbf{z}^l$, $l = \overline{1,4}$, follows from [116]:

$$\begin{aligned} \mathbf{z}^l(r) = &\begin{pmatrix} 2C_{66} & \mathrm{i}n2C_{66} & \mathrm{i}k_z r C_{44} \\ -\mathrm{i}n2C_{66} & 2C_{66} & 0 \\ -\mathrm{i}k_z r C_{44} & 0 & Z_z \end{pmatrix} \\ &+ c_0 \begin{pmatrix} \xi_3(y_1 - y_2) & \mathrm{i}n(y_1 - y_2) & \mathrm{i}\xi_3(\xi_1 - \xi_2) \\ -\mathrm{i}n(y_1 - y_2) & \xi_2 y_1 - \xi_1 y_2 & n(\xi_1 - \xi_2) \\ -\mathrm{i}\xi_3(\xi_1 - \xi_2) & n(\xi_1 - \xi_2) & 0 \end{pmatrix}, \end{aligned} \tag{3.22}$$

$$
\begin{aligned}
Z_z &= C_{44}\left(\frac{n^2(\xi_1 y_1 - \xi_2 y_2) - \xi_1\xi_2\xi_3(y_1 - y_2)}{\xi_3(\xi_2 y_1 - \xi_1 y_2) - n^2(y_1 - y_2)}\right), \quad y_i = \kappa_i r \quad (i = 1, 2), \\
c_0 &= \frac{C_{66}k_3^2 r^2}{\xi_3(\xi_2 y_1 - \xi_1 y_2) - n^2(y_1 - y_2)}, \quad \xi_j = k_j r \frac{f_n^{l\,\prime}(k_j r)}{f_n^l(k_j r)} \quad (j = 1, 2, 3),
\end{aligned}
\tag{3.23}
$$

where the cylindrical functions $f_n^l(x)$ are defined by eq. (2.83). The formula for $\mathbf{X}^l$ follows by substituting the potentials (3.17) into Eq. (2.58). The derivation of the matrix $\mathbf{z}^l(r)$ can be found in [116]. Note that $\mathbf{z}^1(r)$ ($l \equiv 1$) is the exact form of the conditional impedance of a solid cylinder, i.e. with material at $r = 0$ and hence bounded displacements there [116].

The explicit form of the two point impedance matrix (see eq. (3.1)) of a given transversely isotropic cylindrical layer is

$$
\mathbf{Z}^k(r_k, r_{k-1}) = \begin{pmatrix} \mathbf{Z}_1^k & \mathbf{Z}_2^k \\ \mathbf{Z}_3^k & \mathbf{Z}_4^k \end{pmatrix} = \begin{bmatrix} -\mathbf{Y}^1(r_{k-1}) & -\mathbf{Y}^3(r_{k-1}) \\ \mathbf{Y}^1(r_k) & \mathbf{Y}^3(r_k) \end{bmatrix} \begin{bmatrix} \mathbf{X}^1(r_{k-1}) & \mathbf{X}^3(r_{k-1}) \\ \mathbf{X}^1(r_k) & \mathbf{X}^3(r_k) \end{bmatrix}^{-1}.
\tag{3.24}
$$

Eq. (3.24), which defines the impedance matrix $\mathbf{Z}$, is similar to eq. (7) of [137] (for the stiffness matrix $\mathbf{K}$), and the first and the second matrices on the right hand side of eq. (3.24) are similar to the matrices $\mathbf{E}_m^\sigma$ and $(\mathbf{E}_m^u)^{-1}$ in [137, eqs. (5) and (3)]. One reason why we prefer to use the impedance matrix $\mathbf{Z}$ rather than the stiffness matrix as in [137] is that the impedance is always Hermitian: $\mathbf{Z} = \mathbf{Z}^+$.

3.1.3 Example: Acoustic scattering from an elastic cylinder in water

In this section, we explore the use of the impedance matrix by considering acoustic scattering from a fluid filled elastic cylinder immersed in water. Assume that the cylinder consists of J layers. Let the first innermost layer bordering with inner fluid be located between $r = r_0 = b$ and $r = r_1$ and the last outermost layer between $r = r_{J-1}$ and $r = r_J = a$, see Figure 3.1.

Consider a perpendicular wave incidence, i.e. $k_z = 0$, in a uniform exterior fluid. The total pressure p is defined as a sum of incident p^{inc} and scattered p^{sc} pressure fields, and satisfies the Helmholtz equation (2.62), and momentum balance equation (2.63). The incident field p^{inc} is given by (2.68), and the scattered field p^{sc} by (2.69). The total radial stress and displacement fields in the surrounding fluid are defined by (2.108) and

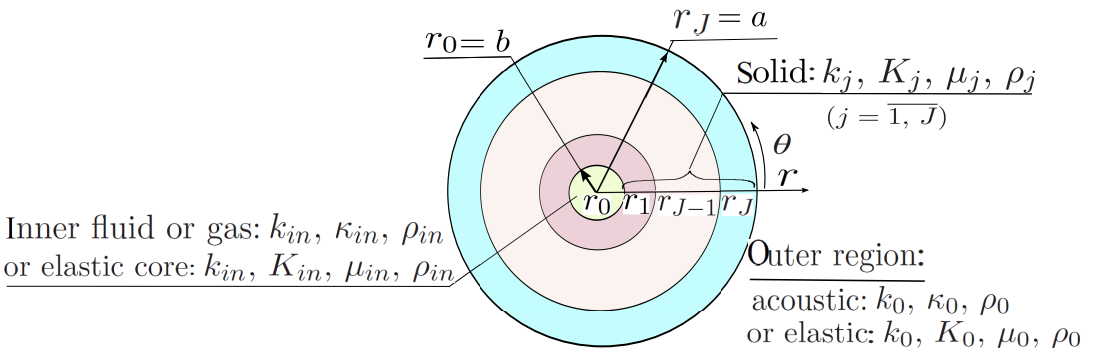

Figure 3.1: Schematic of elastic multilaminate cylinder of inner radius $r_0 = b$ and outer radius $r_J = a$ in polar coordinates $(r,\ \theta)$. The medium inside the multilaminate is either fluid, gas, or elastic core; the outer region is either acoustic medium or elastic matrix.

in the inner fluid region by (2.101). We assume a perfect interface between each layer of a multilayered cylinder which requires continuity of stresses and displacements at the interface. Thus, the boundary conditions at the interfaces of the solid and acoustic media are given on the inner surface of the cylinder at $r = r_0 = b$:

$$\sigma_{rr}^{in}(b) = \sigma_{rr}^{1}(b), \quad \sigma_{r\theta}^{in}(b) = \sigma_{r\theta}^{1}(b), \tag{3.25}$$

and on the outer surface at $r = r_J = a$:

$$\sigma_{rr}^{J}(a) = \sigma_{rr}^{0}(a), \quad \sigma_{r\theta}^{J}(a) = \sigma_{r\theta}^{0}(a). \tag{3.26}$$

We use the definition of the conditional impedance matrix, noted in eq. (2.47), and write this statement for the innermost radial coordinate at $r = r_0 = b$, for which we find the initial impedance matrix from eq. (3.22), and for the outer surface at $r = r_J = a$

$$\mathbf{V}(b) = -\mathrm{i}\mathbf{z}_1\mathbf{U}(b), \quad \mathbf{V}(a) = -\mathrm{i}\mathbf{z}_2\mathbf{U}(a). \tag{3.27}$$

Recall that the conditional impedance matrix $\mathbf{z}(r)$ satisfies a differential Riccati equation (2.48) with assumed initial condition $\mathbf{z}(r_0)$ at some specified $r = r_0$. The conditional impedance matrix, $\mathbf{z}_1 = \mathbf{z}(b)$, can be used as the initial impedance matrix on the inner surface of the cylinder to obtain the total impedance matrix $\mathbf{z}$. The conditional impedance matrix, $\mathbf{z}_2 = \mathbf{z}(a)$, can be obtained from the integration technique outlined in [114]. Considering acoustic fluid in the interior, we write eq. (3.27) for $r = b$ in detail

for which the shear stress, $\sigma_{r\theta}^{in}$, must be zero:

$$r\begin{pmatrix}\sigma_{rr}^{in}\\0\end{pmatrix}=-\mathbf{z}_1\begin{pmatrix}u_r^{in}\\u_\theta^{in}\end{pmatrix}=-\mathbf{z}^{in}\begin{pmatrix}u_r^{in}\\u_\theta^{in}\end{pmatrix}=-\begin{bmatrix}Z^{in}&0\\0&0\end{bmatrix}\begin{pmatrix}u_r^{in}\\u_\theta^{in}\end{pmatrix}. \tag{3.28}$$

Incorporating eqs. (3.43)-(3.46), and (3.47) yields scalar impedance in the form

$$Z^{in}=-r\frac{\sigma_{rr}^{in}}{u_r^{in}}=r\frac{\kappa_{in}k_{in}J_n(k_{in}r)}{J_n'(k_{in}r)}. \tag{3.29}$$

Similarly, for acoustic fluid in the exterior, the shear stress, $\sigma_{r\theta}^{0}$, is zero and evaluating eq. (3.27) at $r=a$ yields:

$$-a\begin{pmatrix}\sigma_{rr}^{0}\\0\end{pmatrix}=\mathbf{z}_2\begin{pmatrix}u_r^{0}\\u_\theta^{0}\end{pmatrix}=\begin{pmatrix}z_{11}&z_{12}\\z_{21}&z_{22}\end{pmatrix}\begin{pmatrix}u_r^{0}\\u_\theta^{0}\end{pmatrix}. \tag{3.30}$$

Eliminating u_θ using the second row of eq. (3.30) implies

$$a\sigma_{rr}^{0}=z_0u_r^{0},\quad\text{with}\quad z_0=\frac{z_{12}z_{21}-z_{22}z_{11}}{z_{22}}, \tag{3.31}$$

where z_0 is called the acoustical impedance. The stresses and displacements for the outer acoustic medium are given by (2.108). Incorporating eqs. (2.108) and (3.31) yields

$$-\kappa_0\,k_0a\,J_n(k_0a)\,A_n-\kappa_0\,k_0a\,H_n^{(1)}(k_0a)\,B_n=\,z_0\Big\{J_n'(k_0a)\,A_n+H_n^{(1)'}(k_0a)B_n\Big\}. \tag{3.32}$$

Thus, the scattering coefficients are found as

$$B_n=-\frac{A_n\big(\kappa_0k_0aJ_n(k_0a)+z_0J_n^{'}(k_0a)\big)}{\kappa_0k_0aH_n^{(1)}(k_0a)+z_0H_n^{(1)'}(k_0a)}, \tag{3.33}$$

where the incident wave coefficient A_n is defined by eq. (2.73) for a plane wave incidence and (2.76) for a point source. We will compare the result for B_n obtained in this section with the one that follows from the application of the Global matrix method to the solution of scattering of a multilayered cylindrical structure in the succeeding section.

For the "gas-solid-fluid" case, i.e. a gas-filled cylinder submerged in water, the inner surface of the cylinder is assumed to be traction-free. The stresses and displacements for the inner acoustic region are given by (2.101). The traction-free boundary conditions

are given by eq. (2.105), and at the interfaces of solid and acoustic media are given on the inner surface of cylinder at $r = b$:

$$\sigma_{rr}^{in}(b) = 0 = \sigma_{rr}^{1}(b), \quad \sigma_{r\theta}^{in}(b) = 0 = \sigma_{r\theta}^{1}(b), \tag{3.34}$$

and on the outer surface at $r = a$:

$$\sigma_{rr}^{J}(a) = \sigma_{rr}^{0}(a), \quad \sigma_{r\theta}^{J}(a) = \sigma_{r\theta}^{0}(a), \tag{3.35}$$

Then (3.27) and (3.34) yield:

$$\mathbf{z}^{in}(b) = 0 \tag{3.36}$$

that can be used as initial impedance matrix to find the total conditional impedance matrix $\mathbf{z}$.

3.1.4 Impedance for multilayered radially inhomogeneous sphere

In this section, we consider a radially inhomogeneous multilayered sphere consisting of J isotropic spherical layers. We derive an explicit formula for the impedance $\mathbf{Z}$ of a given isotropic layer, and find scattering coefficients using an acoustic impedance. We assume that each spherical layer satisfies the eqs. (2.40) - (2.44).

The two point impedance matrix

The two point impedance matrix $\mathbf{Z}^k(r_k, r_{k-1})$ relates the traction and displacement vectors on the inner, (r_{k-1}), and outer, $(r = r_k)$, surfaces of a given layer and can be defined as:

$$\mathbf{Z}^k(r_k, r_{k-1}) = -\widetilde{\boldsymbol{\Upsilon}}(r_{k-1}, r_k)\widetilde{\mathbf{U}}^{-1}(r_{k-1}, r_k), \tag{3.37}$$

where $\widetilde{\boldsymbol{\Upsilon}}$ and $\widetilde{\mathbf{U}}$ are given by

$$\widetilde{\mathbf{U}}(r_{k-1}, r_k) = \begin{bmatrix} \mathbf{U}^1(r_{k-1}) & \mathbf{U}^3(r_{k-1}) \\ \mathbf{U}^1(r_k) & \mathbf{U}^3(r_k) \end{bmatrix}, \qquad \widetilde{\boldsymbol{\Upsilon}}(r_{k-1}, r_k) = \begin{bmatrix} \boldsymbol{\Upsilon}^1(r_{k-1}) & \boldsymbol{\Upsilon}^3(r_{k-1}) \\ -\boldsymbol{\Upsilon}^1(r_k) & -\boldsymbol{\Upsilon}^3(r_k) \end{bmatrix}, \tag{3.38}$$

where $\mathbf{U}^l(r)$ and $\boldsymbol{\Upsilon}^l(r), (l = 1, 3)$ correspondingly are given by eqs. (2.40) and (2.44), and evaluated at $r = r_{k-1}$ and $r = r_k$ where $k = \overline{1,\, J}$, and index the n is dropped to simplify notation.

Transformation from elastic to acoustic impedance matrix

Consider scattering of an infinite normal plane acoustic incident wave from a fluid filled anisotropic layered elastic sphere immersed in an ideal fluid and comprised of J isotropic layers (see Figure 3.1). Assume a perfect interface between each layer in the multilayered sphere which requires continuity of stresses and displacements at the interface.

Outer acoustic region. The total pressure $p(\mathbf{x})$ is a sum of incident p^{inc} and scattered p^{sc} pressure fields, and satisfies the acoustic Helmholtz wave equation (2.62), and momentum equation (2.63). The incident pressure is taken as an obliquely traveling plane wave of unit amplitude and written in terms of regular solutions of eq. (2.62). The outgoing scattered wave pressure p^{sc} is taken in terms of irregular solutions of eq. (2.62) and unknown scattering coefficients R^3_{0n}. The displacement and the traction vectors in the outer acoustic medium ($r \geq a$) can be found using momentum balance equations (2.63) and are given by

$$\mathbf{u}(r) = \begin{pmatrix} \mathbf{P}_{0n} & \mathbf{B}_{0n} \end{pmatrix} \begin{pmatrix} a^1_n(k_0 r) & a^3_n(k_0 r) \\ c^1_n(k_0 r) & c^3_n(k_0 r) \end{pmatrix} \begin{pmatrix} R^{1,0}_{0n} \\ R^{3,0}_{0n} \end{pmatrix}, \tag{3.39}$$

$$\mathbf{t}(r) = \mathbf{P}_{0n} \begin{pmatrix} \bar{\alpha}^1_n(r, k_0, \kappa_0) & \bar{\alpha}^3_n(r, k_0, \kappa_0) \end{pmatrix} \begin{pmatrix} R^{1,0}_{0n} \\ R^{3,0}_{0n} \end{pmatrix}, \tag{3.40}$$

where

$$a^l_n(k_0 r) = g^{l\,\prime}_n(k_0 r), \quad c^l_n(k_0 r) = (\eta_n k_0 r)^{-1} g^l_n(k_0 r), \quad (l = 1, 3) \tag{3.41}$$

$$\bar{\alpha}^l_n(r, k_0, \kappa_0) = -\kappa_0 k_0 g^l_n(k_0 r), \quad (l = 1, 3) \tag{3.42}$$

and the spherical wavefunctions g^l_n are defined by eq. (2.41).

Inner acoustic region. In the inner fluid region ($r < b$) the displacement vector is given by

$$\boldsymbol{u}(r) = \mathbf{P}_{0n} \begin{pmatrix} a^1_n(k_{in} r) \\ c^1_n(k_{in} r) \end{pmatrix} R^{1,in}_{0n}, \tag{3.43}$$

where

$$a^1_n(k_{in} r) = j^{'}_n(k_{in} r), \quad c^1_n(k_{in} r) = \frac{j_n(k_{in} r)}{\eta_n k_{in} r}, \tag{3.44}$$

and the stresses are given as

$$\mathbf{t}(r) = \mathbf{P}_{0n}\, \bar{\alpha}_n^1(r, k_{in}, \kappa_{in})\, R_{0n}^{1,in}\,, \tag{3.45}$$

where

$$\bar{\alpha}_n^1(r, k_{in}, \kappa_{in}) = -\kappa_{in} k_{in} j_n(k_{in} r). \tag{3.46}$$

Acoustic impedance. Continuity of displacements and traction on the interface implies the boundary conditions (3.25) on the inner surface of sphere at $r = r_0 = b$, and (3.26) on the outer surface at $r = r_J = a$. Equation (2.47) yields

$$r \begin{pmatrix} \sigma_{rr}^{in} \\ 0 \end{pmatrix} = -\mathbf{z}^{in} \begin{pmatrix} u_r^{in} \\ u_\theta^{in} \end{pmatrix} = - \begin{bmatrix} Z^{in} & 0 \\ 0 & 0 \end{bmatrix} \begin{pmatrix} u_r^{in} \\ u_\theta^{in} \end{pmatrix}, \tag{3.47}$$

where we dropped index k for convenience. Incorporating eqs. (3.43)-(3.46), and (3.47) yields scalar impedance in the form

$$Z^{in} = -r \frac{\sigma_{rr}^{in}}{u_r^{in}} = r \frac{\kappa_{in} k_{in} j_n(k_{in} r)}{j_n'(k_{in} r)}. \tag{3.48}$$

Equation (3.48) evaluated at $r = b$ can be used as the initial impedance matrix on the inner surface of the sphere to obtain the total impedance matrix $\mathbf{z}$:

$$\mathbf{z}^1(b) = \mathbf{z}^{in}(b). \tag{3.49}$$

Equation (2.47) for an acoustic medium yields

$$a \begin{pmatrix} \sigma_{rr}^0 \\ 0 \end{pmatrix} = -\mathbf{z} \begin{pmatrix} u_r^0 \\ u_\theta^0 \end{pmatrix}. \tag{3.50}$$

Equation (3.50) can be written as

$$\boldsymbol{z}_{11} u_r^0 + \boldsymbol{z}_{12} u_\theta^0 = -a \sigma_{rr}^0, \tag{3.51}$$

$$\boldsymbol{z}_{21} u_r^0 + \boldsymbol{z}_{22} u_\theta^0 = 0. \tag{3.52}$$

Eliminating u_θ from equations (3.51) - (3.52), we obtain

$$a\, \sigma_{rr}^0 = z_0 u_r^0, \tag{3.53}$$

where Z_0 is the acoustic scalar impedance found as

$$z_0 = \frac{z_{12} z_{21} - z_{11} z_{22}}{z_{22}}. \tag{3.54}$$

The stresses and displacements for the outer acoustic medium are given by (3.39)-(3.40). Using (3.39)-(3.40) and equating with (3.53) yields

$$-\kappa_0\, k_0 a\, j_n(k_0 a)\, R_{0n}^{1,0} - \kappa_0\, k_0 a\, h_n^{(1)}(k_0 a)\, R_{0n}^{3,0} = z_0 \Big\{ j_n'(k_0 a)\, R_{0n}^{1,0} + h_n^{(1)\prime}(k_0 a) R_{0n}^{3,0} \Big\}, \tag{3.55}$$

where the incident plane wave coefficient $R_{0n}^{1,0} = i^n$. Thus scattering wave coefficient $R_{0n}^{3,0}$ found as

$$R_{0n}^{3,0} = -\frac{i^n \big[\kappa_0\, k_0 a\, j_n(k_0 a) + z_0\, j_n'(k_0 a)\big]}{z_0\, h_n^{(1)\prime}(k_0 a) + \kappa_0\, k_0 a\, h_n^{(1)}(k_0 a)}. \tag{3.56}$$

3.2 Elastic and acoustic scattering from TI cylinders

Although the solution for acoustic scattering from isotropic elastic cylinders has been known for more than half a century [55], it was not until 1996 that [78] provided the first complete theory applicable to a uniform TI-cylinder. Their original formulation was for a cylinder submerged in an acoustic, compressible, inviscid fluid, and was was generalized in [54] to the case of a cylinder embedded in an elastic matrix. [107] provides an alternative but similar formulation for the solid-solid case. [53] discuss physical characteristics displayed by the original general solution of [78]. Orthotropic cylindrical shells submerged in and filled with compressible ideal fluids were considered by [73] using a a state space formulation for the sequentially laminated piecewise homogeneous configuration. Piezoelectric hollow cylinders have been considered recently in two separate papers [130, 73].

In this section, the mathematical model of acoustic and elastic wave scattering from a submerged TI cylinder is developed. Both solid and hollow (shell) configurations are considered by combining an integral solution based on the Shuvalov formulation for a shell of non-zero interior radius with the impedance operator of a uniform core region. The impedance is expressed using the exact solution for a solid cylinder. The impedance is zero for a hollow cylinder.

In a cylindrical coordinate system (r, θ, z), consider an infinite perpendicular plane wave of circular frequency ω and $k_z = 0$ incident on submerged infinite cylinder of outer radius a shown in Figure 2.2. The material of the cylinder in $0 < b \leq r \leq a$ is

assumed to be TI. The general Hooke's law for a TI material follows from eq. (2.21) taking $C_{11} = C_{22}$, $C_{13} = C_{23}$, $C_{44} = C_{55}$, and $C_{66} = (C_{11} - C_{22})/2$. The equilibrium equations written in terms of displacements are given by eqs. (3.7). Substituting Cauchy's geometric relations (2.8) into Hooke's law (2.2) for TI material yields the following stress-displacement relations for in-plane displacements

$$\sigma_{rr} = C_{11}\frac{\partial u_r}{\partial r} + C_{12}\left[\frac{u_r}{r} + \frac{1}{r}\frac{\partial u_\theta}{\partial \theta}\right], \quad \sigma_{r\theta} = \frac{C_{11} - C_{12}}{2}\left[\frac{\partial u_\theta}{\partial r} - \frac{u_\theta}{r} + \frac{1}{r}\frac{\partial u_r}{\partial \theta}\right]. \tag{3.57}$$

We expand any functions f of r and θ in Fourier series in θ in the form of eq. (2.81). We seek an in-plane time harmonic solution of on equation of motion in the form (2.15) with no z dependence ($m = 2$) where $\mathbf{U}_n(r)$ and $\boldsymbol{\Upsilon}_n(r)$ are 2 dimensional vectors defined by eq. (2.16).

3.2.1 Elastic incident and scattered waves

Consider a plane harmonic elastic wave propagation impending on an infinite cylinder of outer radius a and inner radius b. At the outer surface of the cylinder $r \geq a$ the displacement field consists of 4 parts:

$$\mathbf{u} = \mathbf{u}_p^{inc} + \mathbf{u}_s^{inc} + \mathbf{u}_p^{sc} + \mathbf{u}_s^{sc}, \tag{3.58}$$

where the incident longitudinal $\mathbf{u}_p^{inc}$ and transversal $\mathbf{u}_s^{inc}$ displacements, and the scattered longitudinal $\mathbf{u}_p^{sc}$ and transversal $\mathbf{u}_s^{sc}$ displacements will be found in the subsequent sections below. Similarly, $\boldsymbol{\eta}(r)$ defined by eq. (2.17) also consists of 4 parts:

$$\boldsymbol{\eta}(r) = \boldsymbol{\eta}_p^{inc}(r) + \boldsymbol{\eta}_s^{inc}(r) + \boldsymbol{\eta}_p^{sc}(r) + \boldsymbol{\eta}_s^{sc}(r). \tag{3.59}$$

The form of $\boldsymbol{\eta}_p^{inc}(r)$, $\boldsymbol{\eta}_s^{inc}(r)$, $\boldsymbol{\eta}_p^{sc}(r)$ and $\boldsymbol{\eta}_s^{sc}(r)$ will be defined in the succeeding sections.

The incident displacement field for ***P waves*** is of the form

$$\mathbf{u}_p^{inc} = u_p^{inc}\mathbf{e}_x + 0\,\mathbf{e}_y + 0\,\mathbf{e}_z, \quad u_p^{inc} = A_p^{inc}\, e^{ikr\cos\theta}, \tag{3.60}$$

where $\mathbf{e}_x$, $\mathbf{e}_y$, $\mathbf{e}_z$ are unit vectors in Cartesian coordinates and $x = r\cos\theta$. We decompose the displacement vector $\mathbf{u}_p^{inc}$ using Helmholtz potentials (2.56)

$$\mathbf{u}_p^{inc} = \boldsymbol{\nabla}\varphi, \quad \text{where} \quad \varphi = \frac{1}{ik}A_p^{inc}\, e^{ikr\cos\theta} = \frac{1}{ik}\sum_{n=-\infty}^{\infty} i^n\, A_p^{inc}\, J_n(kr)e^{in\theta}. \tag{3.61}$$

Incorporating expressions for stresses and displacements for each circumferential mode n, we define $\boldsymbol{\eta}_p^{inc}$ as

$$\boldsymbol{\eta}_p^{inc} = \begin{pmatrix} \mathbf{U}_p^{inc}(r) \\ \mathbf{V}_p^{inc}(r) \end{pmatrix} = i^n \, A_p^{inc} \, \boldsymbol{\eta}_{pJ}(r), \qquad \boldsymbol{\eta}_{pJ} = \begin{pmatrix} \mathbf{U}_{pJ} \\ \mathbf{V}_{pJ} \end{pmatrix} = \big[\boldsymbol{\eta}_{pf}\big]_{f=J_n(kr)}, \tag{3.62}$$

where

$$\boldsymbol{\eta}_{pf} = \begin{pmatrix} -if'(kr) \\ \frac{n}{kr} f(kr) \\ C_{11} k_p r f''(kr) + C_{12}\Big(f'(kr) - \frac{n^2}{k_p r} f(kr)\Big) \\ in\big[C_{11} - C_{12}\big]\Big[f'(kr) - \frac{1}{k_p r} f(kr)\Big] \end{pmatrix}. \tag{3.63}$$

Incident displacement field for ***SV waves*** has the form

$$\mathbf{u}_s^{inc} = (0, u_s^{inc}, 0), \quad u_s^{inc} = A_s^{inc} e^{iKr\cos\theta}. \tag{3.64}$$

Let us define $\mathbf{u}_s^{inc} = -\boldsymbol{\nabla} \times \psi \, \mathbf{e}_z$ via Helmholtz decomposition (2.56), then

$$\psi = \frac{1}{i\,K} A_s^{inc} e^{iKr\cos\theta} = \frac{1}{iK} \sum_{n=-\infty}^{\infty} i^n A_s^{inc} J_n(Kr) e^{in\theta}. \tag{3.65}$$

Incorporating eqs. (3.65), and (3.57), we define $\boldsymbol{\eta}_s^{inc}$ as

$$\boldsymbol{\eta}_s^{inc} = \begin{pmatrix} \mathbf{U}_s^{inc}(r) \\ \mathbf{V}_s^{inc}(r) \end{pmatrix} = i^n A_s^{inc} \boldsymbol{\eta}_{sJ}(r), \quad \text{with} \quad \boldsymbol{\eta}_{sJ} = \begin{pmatrix} \mathbf{U}_{sJ} \\ \mathbf{V}_{sJ} \end{pmatrix} = \big[\boldsymbol{\eta}_{sf}\big]_{f=J_n(Kr)}, \tag{3.66}$$

where

$$\boldsymbol{\eta}_{sf} = \begin{pmatrix} -\frac{n}{Kr} f(Kr) \\ -if'(Kr) \\ in\big[C_{11} - C_{12}\big]\big[\frac{1}{rK} f(Kr) - f'(Kr)\big] \\ \big[C_{11} - C_{12}\big]\Big[\frac{2n^2 - K^2 r^2}{rK} f(Kr) - f'(Kr)\Big] \end{pmatrix}. \tag{3.67}$$

The scattered displacement vector $\mathbf{u}_p^{sc}$ for ***scattered P waves*** is decomposed using Helmholtz potentials (2.56)

$$\mathbf{u}_p^{sc} = \boldsymbol{\nabla}\varphi, \quad \text{where} \quad \varphi = \frac{1}{ik} \sum_{n=-\infty}^{\infty} B_{p,n} H_n^{(1)}(kr) e^{in\theta}. \tag{3.68}$$

Substituting Helmholtz decomposition (3.68) into eqs. (3.57), we define $\boldsymbol{\eta}_p^{sc}$ as

$$\boldsymbol{\eta}_p^{sc} = \begin{pmatrix} \mathbf{U}_p^{sc}(r) \\ \mathbf{V}_p^{sc}(r) \end{pmatrix} = B_{p,n} \boldsymbol{\eta}_{pH}(r), \quad \text{with} \quad \boldsymbol{\eta}_{pH} = \begin{pmatrix} \mathbf{U}_{pH} \\ \mathbf{V}_{pH} \end{pmatrix} = \big[\boldsymbol{\eta}_{pf}\big]_{f=H_n^{(1)}(kr)}, \tag{3.69}$$

where $\boldsymbol{\eta}_{pf}$ is defined by (3.63).

The scattered displacement for ***transversal SV waves*** is represented via Helmholtz potential ψ:

$$\mathbf{u}_s^{sc} = -\boldsymbol{\nabla} \times \psi \mathbf{e}_z = -\frac{1}{r}\frac{\partial \psi^T}{\partial \theta}\mathbf{e}_r + \frac{\partial \psi}{\partial r}\mathbf{e}_\theta, \qquad \psi = \frac{1}{iK}\sum_{n=-\infty}^{\infty} B_{s,n} H_n^{(1)}(Kr) e^{in\theta}. \tag{3.70}$$

Introducing (3.70) into (3.57) allows us to define $\boldsymbol{\eta}_s^{sc}$ as

$$\boldsymbol{\eta}_s^{sc} = \begin{pmatrix} \mathbf{U}_s^{sc}(r) \\ \mathbf{V}_s^{sc}(r) \end{pmatrix} = B_{s,n}\boldsymbol{\eta}_{sH}, \quad \text{with} \quad \boldsymbol{\eta}_{sH} = \begin{pmatrix} \mathbf{U}_{sH} \\ \mathbf{V}_{sH} \end{pmatrix} = \left[\boldsymbol{\eta}_{sf}\right]_{f=H_n^{(1)}(kr)}, \tag{3.71}$$

where $\boldsymbol{\eta}_{sf}$ is defined by (3.67).

3.2.2 Boundary Conditions

Recall that $\boldsymbol{\eta}$ is defined as:

$$\boldsymbol{\eta}(r) = \boldsymbol{\eta}_p^{inc}(r) + \boldsymbol{\eta}_s^{inc}(r) + \boldsymbol{\eta}_p^{sc}(r) + \boldsymbol{\eta}_s^{sc}(r) = i^n A_p^{inc}\boldsymbol{\eta}_{pJ} + i^n A_s^{inc}\boldsymbol{\eta}_{sJ} + B_{p,n}\boldsymbol{\eta}_{pH} + B_{s,n}\boldsymbol{\eta}_{sH}, \tag{3.72}$$

where $\boldsymbol{\eta}_{pJ}$, $\boldsymbol{\eta}_{sJ}$, $\boldsymbol{\eta}_{pH}$, and $\boldsymbol{\eta}_{sH}$ are defined by eqs. (3.62), (3.66), (3.69), and (3.71) correspondingly, and $B_{p,n}$ and $B_{s,n}$ are the unknown scattering coefficients.

Rigid inner surface. If the inner surface of cylinder is rigid, i.e. $\mathbf{u}(b) = \mathbf{0}$, the boundary conditions at $r = b$ will be

$$\boldsymbol{\eta}(b) = \begin{pmatrix} 0 & 0 & \eta_3(b) & \eta_4(b) \end{pmatrix}^T. \tag{3.73}$$

At the interface, the outer surface of cylinder, $r = a$:

$$\boldsymbol{\eta}(a) = \mathbf{M}\boldsymbol{\eta}(b) \quad \Leftrightarrow \quad \boldsymbol{\eta}_p^{inc}(a) + \boldsymbol{\eta}_s^{inc}(a) + B_{p,n}\boldsymbol{\eta}_{pH}(a) + B_{s,n}\boldsymbol{\eta}_{sH}(a) = \mathbf{M}\begin{pmatrix} 0 & 0 & \eta_3(b) & \eta_4(b) \end{pmatrix}^T, \tag{3.74}$$

where $\mathbf{M}$ is a 4×4 matricant given in Section 2.1.3 which can be obtained from ODE, eq. (2.49), when $b \to a$. In eq. (3.74), taking all unknown components to one side and all known components to other side, we obtain

$$\begin{bmatrix} M_{13} & M_{14} & -\eta_{pH1}(a) & -\eta_{sH1}(a) \\ M_{23} & M_{24} & -\eta_{pH2}(a) & -\eta_{sH2}(a) \\ M_{33} & M_{34} & -\eta_{pH3}(a) & -\eta_{sH3}(a) \\ M_{43} & M_{44} & -\eta_{pH4}(a) & -\eta_{sH4}(a) \end{bmatrix} \begin{pmatrix} \eta_3(b) \\ \eta_4(b) \\ B_{p,n} \\ B_{s,n} \end{pmatrix} = \begin{bmatrix} \boldsymbol{\eta}_{pH} & \boldsymbol{\eta}_{sH} \end{bmatrix} \begin{pmatrix} i^n A_p^{inc} \\ i^n A_s^{inc} \end{pmatrix}. \tag{3.75}$$

Traction free inner surface. If the inner surface of cylinder is traction free, i.e. $\mathbf{t}_r(b) = \mathbf{0}$, the boundary conditions at $r = b$ will be

$$\boldsymbol{\eta}(b) = \begin{pmatrix} \eta_1(b) & \eta_2(b) & 0 & 0 \end{pmatrix}^T. \tag{3.76}$$

At the interface $r = a$:

$$\boldsymbol{\eta}(a) = \boldsymbol{\eta}_p^{inc}(a) + \boldsymbol{\eta}_s^{inc}(a) + B_{p,n}\boldsymbol{\eta}_{pH}(a) + B_{s,n}\boldsymbol{\eta}_{sH}(a) = \mathbf{M}\begin{pmatrix}\eta_1(b) & \eta_2(b) & 0 & 0\end{pmatrix}^T, \tag{3.77}$$

which can be written as:

$$\begin{bmatrix} M_{11} & M_{12} & -\eta_{pH1}(a) & -\eta_{sH1}(a) \\ M_{21} & M_{22} & -\eta_{pH2}(a) & -\eta_{sH2}(a) \\ M_{31} & M_{32} & -\eta_{pH3}(a) & -\eta_{sH3}(a) \\ M_{41} & M_{42} & -\eta_{pH4}(a) & -\eta_{sH4}(a) \end{bmatrix} \begin{pmatrix} \eta_1(b) \\ \eta_2(b) \\ B_{p,n} \\ B_{s,n} \end{pmatrix} = \begin{bmatrix} \boldsymbol{\eta}_{LH} & \boldsymbol{\eta}_{TH} \end{bmatrix} \begin{pmatrix} i^n A_p^{inc} \\ i^n A_s^{inc} \end{pmatrix}. \tag{3.78}$$

3.2.3 Impedance matrix

We can relate the vectors $\mathbf{U}_n(r)$ and $\mathbf{V}_n(r)$ associated with displacement and traction using the conditional impedance matrix $\mathbf{z}(r)$ defined by eqs. (2.47). From eq. (2.47) we find conditions at inner surface $r = b$:

$$\mathbf{V}_n(b) = -i\mathbf{z}_1\mathbf{U}_n(b), \tag{3.79}$$

and outer surface at $r = a$:

$$\mathbf{V}_n(a) = -i\mathbf{z}_2\mathbf{U}_n(a), \tag{3.80}$$

where $\mathbf{z}_1$ and $\mathbf{z}_2$ are known quantities, and $\mathbf{U}_n(r)$ and $\mathbf{V}_n(r)$ are defined by eqs. (2.16) and (2.17) correspondingly. At the outer surface of cylinder $r = a$, taking into account (2.47), the interface condition (3.80) requires that

$$\mathbf{z}_2 = \mathbf{z}(a). \tag{3.81}$$

At inner surface of cylinder $r = b$:

$$\begin{pmatrix} \mathbf{U}_n(r) \\ \mathbf{V}_n(r) \end{pmatrix} = \begin{bmatrix} \mathbf{M}_1 & \mathbf{M}_2 \\ \mathbf{M}_3 & \mathbf{M}_4 \end{bmatrix} \begin{pmatrix} \mathbf{U}_n(b) \\ \mathbf{V}_n(b) \end{pmatrix}, \tag{3.82}$$

where $\mathbf{M}$, a 4×4 matricant, follows from the solution of elasticity equation (2.49) in the cylinder $0 < b \le r \le a$ given in Section 2.1.3.

Suppose $\mathbf{z}_1 = \mathbf{z}(b)$ is given conditional impedance at $r = b$, then using eq. (3.79) we obtain

$$\mathbf{U}_n(r) = (\mathbf{M}_1 - i\mathbf{M}_2\mathbf{z}_1)\mathbf{U}_n(b), \tag{3.83}$$

$$\mathbf{V}_n(r) = (\mathbf{M}_3 - i\mathbf{M}_4\mathbf{z}_1)\mathbf{U}_n(b). \tag{3.84}$$

Incorporating eqs. (2.47) and (3.83)-(3.84), we obtain

$$-i\mathbf{z}(r) = (\mathbf{M}_3 - i\mathbf{M}_4\mathbf{z}_1)(\mathbf{M}_1 - i\mathbf{M}_2\mathbf{z}_1)^{-1}. \tag{3.85}$$

Total fields at the inner and outer surface of the cylinder are related by the interface condition (3.74), based on the solution of the elasticity equations in the cylinder $0 < b \leq r \leq a$. Let us rearrange eq. (3.74) in the following form

$$\begin{pmatrix} \mathbf{U}_p^{inc}(a) \\ \mathbf{V}_p^{inc}(a) \end{pmatrix} + \begin{pmatrix} \mathbf{U}_s^{inc}(a) \\ \mathbf{V}_s^{inc}(a) \end{pmatrix} = - \begin{pmatrix} \mathbf{U}_p^{sc}(a) \\ \mathbf{V}_p^{sc}(a) \end{pmatrix} - \begin{pmatrix} \mathbf{U}_s^{sc}(a) \\ \mathbf{V}_s^{sc}(a) \end{pmatrix} + \begin{bmatrix} \mathbf{M}_1 & \mathbf{M}_2 \\ \mathbf{M}_3 & \mathbf{M}_4 \end{bmatrix} \begin{pmatrix} \boldsymbol{U}_n(b) \\ \boldsymbol{V}_n(b) \end{pmatrix}. \tag{3.86}$$

Using eqs. (3.83)-(3.84) and the definition of the $\mathbf{U}_j^{inc}$, $\mathbf{V}_j^{inc}$, $\mathbf{U}_j^{sc}$ and $\mathbf{V}_j^{sc}$ functions $(j = p, s)$, we obtain

$$\begin{aligned} i^n \left[\begin{pmatrix} \mathbf{U}_{pJ}(a) \\ \mathbf{V}_{pJ}(a) \end{pmatrix} A_p^{inc} + \begin{pmatrix} \mathbf{U}_{sJ}(a) \\ \mathbf{V}_{sJ}(a) \end{pmatrix} A_s^{inc} \right] \\ = - \begin{pmatrix} \mathbf{U}_{pH}(a) \\ \mathbf{V}_{pH}(a) \end{pmatrix} B_{p,n} - \begin{pmatrix} \mathbf{U}_{sH}(a) \\ \mathbf{V}_{sH}(a) \end{pmatrix} B_{s,n} a + \begin{pmatrix} \mathbf{M}_1 - i\mathbf{M}_2\mathbf{z}_1 \\ \mathbf{M}_3 - i\mathbf{M}_4\mathbf{z}_1 \end{pmatrix} \mathbf{U}_n(b), \end{aligned} \tag{3.87}$$

where $\mathbf{U}_{pJ}(a)$, $\mathbf{V}_{pJ}(a)$ are defined by (3.62), $\mathbf{U}_{sJ}(a)$, $\mathbf{V}_{sJ}(a)$ by (3.66), $\mathbf{U}_{pH}(a)$, $\mathbf{V}_{pH}(a)$ by (3.69) , $\mathbf{U}_{sH}(a)$, $\mathbf{V}_{sH}(a)$ by (3.71). Introducing 2×1 vectors: $\mathbf{W}_n = \begin{pmatrix} B_{p,n} & B_{s,n} \end{pmatrix}^T$ into eq. (3.87), we obtain

$$\begin{bmatrix} -\mathbf{M}_{s1}(a) & (\mathbf{M}_1 - i\mathbf{M}_2\mathbf{z}_1) \\ -\mathbf{M}_{s2}(a) & (\mathbf{M}_3 - i\mathbf{M}_4\mathbf{z}_1) \end{bmatrix} \begin{pmatrix} \mathbf{W}_n \\ \mathbf{U}_n(b) \end{pmatrix} = \begin{pmatrix} \mathbf{M}_{i1}(a) \\ \mathbf{M}_{i2}(a) \end{pmatrix} \begin{pmatrix} i^n A_p^{inc} \\ i^n A_s^{inc} \end{pmatrix}, \tag{3.88}$$

where

$$\mathbf{M}_{s1}(a) = \begin{bmatrix} \mathbf{U}_{LH}(a) & \mathbf{U}_{TH}(a) \end{bmatrix}, \quad \mathbf{M}_{s2}(a) = \begin{bmatrix} \mathbf{V}_{LH}(a) & \mathbf{V}_{TH}(a) \end{bmatrix}, \tag{3.89}$$

$$\mathbf{M}_{i1}(a) = \begin{bmatrix} \mathbf{U}_{LJ}(a) & \mathbf{U}_{TJ}(a) \end{bmatrix}, \quad \mathbf{M}_{i2}(a) = \begin{bmatrix} \mathbf{V}_{LJ}(a) & \mathbf{V}_{TJ}(a) \end{bmatrix}. \tag{3.90}$$

The second equation in system (3.88) yields

$$\mathbf{U}_n(b) = (\mathbf{M}_3 - i\mathbf{M}_4\mathbf{z}_1)^{-1} \left[\mathbf{M}_{s2}(a)\mathbf{W}_n + \mathbf{V}_{pJ}(a) i^n A_p^{inc} + \mathbf{V}_{sJ}(a) i^n A_s^{inc} \right]. \tag{3.91}$$

Substituting eq. (3.91) into the first equation of the system (3.88), and incorporating eqs. (3.85) and (3.81), produce

$$\mathbf{W}_n = \left[\mathbf{M}_{s2}(a) + i\mathbf{z}_2\mathbf{M}_{s1}(a) \right]^{-1} \left[-\mathbf{M}_{i2}(a) - i\boldsymbol{z}_2\mathbf{M}_{i1}(a) \right] \begin{pmatrix} i^n A_p^{inc} \\ i^n A_s^{inc} \end{pmatrix}, \tag{3.92}$$

or it can be written as

$$\begin{pmatrix} B_{p,n} \\ B_{s,n} \end{pmatrix} = \Big[\mathbf{V}_{pH}(a) + i\mathbf{z}_2\,\mathbf{U}_{pH}(a), \quad \mathbf{V}_{sH}(a) + i\mathbf{z}_2\,\mathbf{U}_{sH}(a) \Big]^{-1}$$
$$\cdot \Big[-\mathbf{V}_{pJ}(a) - i\mathbf{z}_2\,\mathbf{U}_{pJ}(a), \quad -\mathbf{V}_{sJ}(a) - i\mathbf{z}_2\,\mathbf{U}_{sJ}(a) \Big] \begin{pmatrix} i^n A_p^{inc} \\ i^n A_s^{inc} \end{pmatrix}. \qquad (3.93)$$

3.2.4 Acoustic SH wave

In cylindrical coordinate system (r, θ, z), an infinite plane acoustic wave of circular frequency ω incident at an angle α on submerged infinite TI cylinder of outer radius a illustrated in Figure 2.2 is considered. The total pressure field $p(\mathbf{x})$ is defined by eq. (2.67) as a sum of incident p^{inc} and scattered p^{sc} pressure fields, and satisfies the acoustic Helmholtz wave equation (2.62) and momentum balance equation (2.63). Subindex p is dropped hereunder for acoustic medium to simplify a notation. The incident pressure p^{inc} is taken as an obliquely traveling plane wave, with value at a point $P(r, \theta, z)$ of the form of eq. (2.68). The outgoing scattered wave pressure p^{sc} at point P has form (2.69). The scattering coefficients B_n are derived next.

The scattered field

Let

$$p^{inc} = \sum_{n=-\infty}^{\infty} p_n^{inc}(r) e^{i\,(n\theta + k_z z)}, \qquad p^{sc} = \sum_{n=-\infty}^{\infty} p_n^{sc}(r) e^{i\,(n\theta + k_z z)}, \qquad (3.94)$$

where the coefficients $p_n^{inc}(r)$ and $p_n^{sc}(r)$ follow from eqs. (2.68) and (2.69). The radial velocity components of the incident and scattered fields in the fluid, which follow from (2.63) as $v^{\,inc} = (i\omega\rho_f)^{-1}\partial p^{inc}/\partial r$ and $v^{\,sc} = (i\omega\rho_f)^{-1}\partial p^{sc}/\partial r$, can similarly be expanded as

$$v^{\,inc} = \sum_{n=-\infty}^{\infty} v_n^{inc}(r) e^{i\,(n\theta + k_z z)}, \qquad v^{\,sc} = \sum_{n=-\infty}^{\infty} v_n^{sc}(r) e^{i\,(n\theta + k_z z)}, \qquad (3.95)$$

According to the assumed forms of the incident and scattered fields, eqs. (2.68) and (2.69), we have

$$v_n^{sc}(a) = v_n^{inc}(a) B_n \frac{H_n^{(1)\prime}(k_\perp a)}{A^{inc} i^n J_n'(k_\perp a)}. \qquad (3.96)$$

The scattering coefficients B_n can therefore be determined if we can find a separate relation between $v_n^{sc}(a)$ and $v_n^{inc}(a)$. Such a relation follows from the continuity conditions.

Before considering the interface conditions it is useful to define some impedances for the surface $r = a$. The pressure and velocity coefficients for circumferential mode n at $r = a$ are related by

$$p_n^{inc}(a) = Z_n^{inc} v_n^{inc}(a), \qquad p_n^{sc}(a) = Z_n^{sc} v_n^{sc}(a), \tag{3.97}$$

where the impedance Z_n^{inc} follows from eqs. (2.63) and (2.68), and Z_n^{sc} follows from eqs. (2.63) and (2.69), as

$$Z_n^{inc} = \frac{i\omega\rho_f}{k_\perp} \frac{J_n(k_\perp a)}{J_n'(k_\perp a)}, \qquad Z_n^{sc} = \frac{i\omega\rho_f}{k_\perp} \frac{H_n^{(1)}(k_\perp a)}{H_n^{(1)\prime}(k_\perp a)}. \tag{3.98}$$

The continuity conditions at the outer surface $r = a$ require that the normal components of the traction and the velocity are continuous. Let $v_{0n}(b)$ and $p_{0n}(b)$ be the radial velocity and pressure at the inner surface of the cylinder for circumferential mode n. We assume that the inner surface at $r = b$ has zero shear traction and that the pressure and radial velocity are related by an impedance Z_{0n},

$$p_{0n}(b) = Z_{0n} v_{0n}(b). \tag{3.99}$$

For example: $Z_{0n} = 0$ if the inner boundary is traction free.

Based on the solution of the elasticity equations in the cylinder $0 < b \leq r \leq a$, we can then relate the total fields at the inner and outer surface of the cylinder:

$$\begin{pmatrix} v_n^{inc}(a) + v_n^{sc}(a) \\ p_n^{inc}(a) + p_n^{sc}(a) \end{pmatrix} = \begin{bmatrix} \tilde{M}_{11} & \tilde{M}_{12} \\ \tilde{M}_{21} & \tilde{M}_{22} \end{bmatrix} \begin{pmatrix} v_{0n}(b) \\ p_{0n}(b) \end{pmatrix}, \tag{3.100}$$

where $\tilde{\mathbf{M}}$ is 2×2 matrix is derived in the subsequent section. Expressing the system as a pair of equations for unknowns $v_{sn}(a)$ and $v_{0n}(b)$ gives

$$\begin{bmatrix} -1 & \tilde{M}_{11} + Z_{0n}\tilde{M}_{12} \\ -Z_n^{sc} & \tilde{M}_{21} + Z_{0n}\tilde{M}_{22} \end{bmatrix} \begin{pmatrix} v_n^{sc}(a) \\ v_{0n}(b) \end{pmatrix} = v_n^{inc}(a) \begin{pmatrix} 1 \\ Z_n^{inc} \end{pmatrix}, \tag{3.101}$$

and hence,

$$v_n^{sc}(a) = -v_n^{inc}(a) \left\{ \frac{\tilde{M}_{21} + Z_{0n}\tilde{M}_{22} - Z_n^{inc}(\tilde{M}_{11} + Z_{0n}\tilde{M}_{12})}{\tilde{M}_{21} + Z_{0n}\tilde{M}_{22} - Z_n^{sc}(\tilde{M}_{11} + Z_{0n}\tilde{M}_{12})} \right\}. \tag{3.102}$$

Therefore, comparison of eqs. (3.96) and (3.102) implies the scattering coefficient for circumferential mode n,

$$B_n = -\left(\frac{Z_n - Z_n^{inc}}{Z_n - Z_n^{sc}}\right)\frac{A^{inc} i^n J_n'(k_\perp a)}{H_n^{(1)'}(k_\perp a)}, \tag{3.103}$$

where Z_n depends only on the properties of the cylinder,

$$Z_n = \frac{\tilde{M}_{21} + Z_{0n}\tilde{M}_{22}}{\tilde{M}_{11} + Z_{0n}\tilde{M}_{12}}. \tag{3.104}$$

It remains to find the elements of the 2×2 matrix $\tilde{\mathbf{M}}$ which is derived next.

Transformation from elastic to acoustic matricant

Recall the interface condition (3.74), on the outer surface of cylinder

$$\boldsymbol{\eta}(a) = \mathbf{M}\boldsymbol{\eta}(b), \tag{3.105}$$

where $\boldsymbol{\eta}(r)$ is defined by (2.17), the elements of 4×4 matricant $\mathbf{M}(r, r_0)$

$$\mathbf{M}(r, r_0) = \begin{bmatrix} \mathbf{M}_1 & \mathbf{M}_2 \\ \mathbf{M}_3 & \mathbf{M}_4 \end{bmatrix} \tag{3.106}$$

follow from analysis in Section 2.1.3. Consider a two point impedance matrix $\mathbf{Z}(r, r_0)$ defined by eq. (2.53) and evaluate it at inner and outer surfaces of cylinder

$$\begin{pmatrix} \mathbf{V}_n(a) \\ -\mathbf{V}_n(b) \end{pmatrix} = -i\,\mathbf{Z}(b, a)\begin{pmatrix} \mathbf{U}_n(a) \\ \mathbf{U}_n(b) \end{pmatrix}, \tag{3.107}$$

where $\mathbf{Z}$ and $\mathbf{M}$ are related to each other by relations given in eqs. (2.54):

$$\mathbf{Z}(r, r_0) = \begin{bmatrix} \mathbf{Z}_1 & \mathbf{Z}_2 \\ \mathbf{Z}_3 & \mathbf{Z}_4 \end{bmatrix} = i\begin{bmatrix} -\mathbf{M}_2^{-1}\mathbf{M}_1 & \mathbf{M}_2^{-1} \\ \mathbf{M}_4\mathbf{M}_2^{-1}\mathbf{M}_1 - \mathbf{M}_3 & -\mathbf{M}_4\mathbf{M}_2^{-1} \end{bmatrix}, \tag{3.108}$$

$\mathbf{Z}_j = \mathbf{Z}_j(r, r_0)$, $\mathbf{M}_j = \mathbf{M}_j(r, r_0)$, $\mathbf{U}_n(r)$ and $\mathbf{V}_n(r)$ vectors are defined by (2.16) and (2.17) correspondingly, for acoustic medium $V_{2n}(r) = \sigma_{r\theta n}(r) = 0$.

Introducing matrix $\mathbf{K}$ such that

$$\mathbf{K} = \mathbf{K}^{-1} = \mathbf{K}^T = \begin{bmatrix} 1 & 0 & 0 & 0 \\ 0 & 0 & 1 & 0 \\ 0 & 1 & 0 & 0 \\ 0 & 0 & 0 & 1 \end{bmatrix}, \tag{3.109}$$

and applying (3.109) to both sides of eq. (3.107) yields

$$\begin{pmatrix} V_1(a) \\ -V_1(b) \\ 0 \\ 0 \end{pmatrix} = i\,\widetilde{\mathbf{Z}} \begin{pmatrix} U_1(a) \\ U_1(b) \\ U_2(a) \\ U_2(b) \end{pmatrix}, \tag{3.110}$$

where

$$\widetilde{\mathbf{Z}} = \mathbf{K}\,\mathbf{Z}\,\mathbf{K}^{-1} = \begin{bmatrix} \widetilde{\mathbf{z}}_1 & \widetilde{\mathbf{z}}_2 \\ \widetilde{\mathbf{z}}_3 & \widetilde{\mathbf{z}}_4 \end{bmatrix}, \tag{3.111}$$

$\widetilde{\mathbf{z}}_j$ ($j = \overline{1,4}$) are 2×2 block matrices.

Define vector $\widetilde{\boldsymbol{\eta}}(r)$ as

$$\widetilde{\boldsymbol{\eta}}(r) = \begin{pmatrix} U_{1n} \\ V_{1n} \end{pmatrix}. \tag{3.112}$$

The system of eqs. (3.110) enables us to find relation between $\widetilde{\boldsymbol{\eta}}(a)$ and $\widetilde{\boldsymbol{\eta}}(b)$ in the form

$$\widetilde{\boldsymbol{\eta}}(a) = \tilde{\mathbf{M}}\,\widetilde{\boldsymbol{\eta}}(b), \tag{3.113}$$

where

$$\tilde{\mathbf{M}} = \begin{bmatrix} \tilde{M}_{11} & \tilde{M}_{12} \\ \tilde{M}_{21} & \tilde{M}_{22} \end{bmatrix} = \begin{bmatrix} -\hat{z}_3^{-1}\hat{z}_4 & i\hat{z}_3^{-1} \\ i\hat{z}_2 - i\hat{z}_1\hat{z}_3^{-1}\hat{z}_4 & -\hat{z}_1\hat{z}_3^{-1} \end{bmatrix}, \tag{3.114}$$

$$\begin{bmatrix} \hat{z}_1 & \hat{z}_2 \\ \hat{z}_3 & \hat{z}_4 \end{bmatrix} = \widetilde{\mathbf{z}}_1 - \widetilde{\mathbf{z}}_2\widetilde{\mathbf{z}}_4^{-1}\widetilde{\mathbf{z}}_3. \tag{3.115}$$

3.3 Global matrix method for an isotropic multilayered elastic cylinder

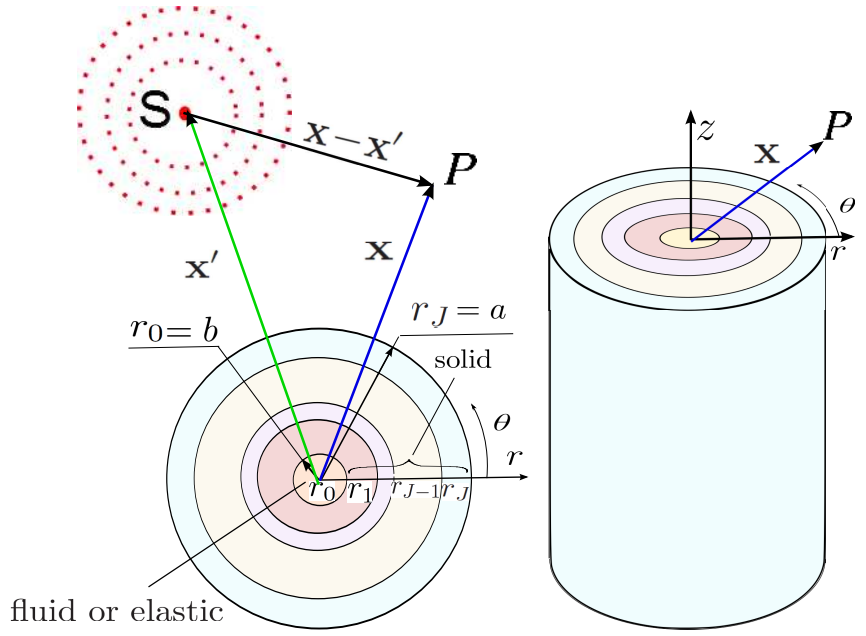

(a) A Source impinging on 2D Multilayer $\mathtt{S}_m$, outer region: fluid or elastic **(b)** Multilayer $\mathtt{S}_m$, 3D view

Figure 3.2: A point source impinging on an isotropic multilaminate cylinder submerged in a fluid medium or embedded in an elastic matrix.

Consider the scattering from sources impinging on a multilaminate cylinder in cylindrical coordinates (r, θ, z) illustrated in Figure 3.2. A point source located at point S has position vector $\mathbf{x}'$. Our goal is to find a field (pressure, velocity, displacement, stress) at an arbitrary point $\mathbf{P}(\mathbf{x})$, and investigate a far field response of cylinder to an excitation.

A scattering of plane incident waves ($\alpha = 0$) from a multilayered cylinder can be tackled analogously and will be considered in parallel. The material of the cylinder in $0 \leq b \leq r \leq a$ is assumed to be radially inhomogeneous and isotropic. We consider a planar motion and neglect z dependence, and assume that cylinder $\mathtt{S}_m$ is comprised of J isotropic layers; each layer in general may have different material properties: the density ρ_j, Lamé parameters λ_j and μ_j, and total displacement field $\mathbf{u}_j$ where the

subindex denotes the jth layer of cylinder $\mathtt{S}_m$ and $j = \overline{1,\ J}$, see Figures 3.1 and Figure 3.2.

First, we study the scattering of acoustic waves from an isotropic multilayered cylinder by considering a clad-rod consisting of an elastic isotropic core cladded with other isotropic materials, and a fluid filled cylinder submerged in water. Then, we investigate an elastic wave scattering from an infinite multilayered cylinder embedded in an elastic medium, considering the incidence of longitudinal and transverse waves seperately. A fluid-filled multilayered cylinder embedded in an elastic matrix will be studied as a particular case. We obtain the scattering coefficients for both acoustic and elastic waves, and relate them to the transition matrix $\mathbf{T}^{(m)}$ that is also called the T-matrix. We will use T-matrix $\mathbf{T}^{(m)}$ of cylinder $\mathtt{S}_m$ in isolation to study MS of acoustic and elastic waves from the cluster of cylinders in the proceeding chapters. In this section, we only investigate a scattering from a single scatterer, and drop super-index m for simplicity of notation hereinafter. We will validate our approach by comparing our results with finding available in literature and with COMSOL simulations.

3.3.1 Acoustic scattering from an isotropic multilayered cylinder

Acoustic scattering from a multilayered clad-rod

Consider scattering of acoustic incident waves from an elastic isotropic multilayered cylindrical clad-rod immersed in an ideal fluid as illustrated in Figure 3.1. For perpendicular acoustic incidence, i.e. $k_z = 0$, the axial dependence vanishes. The displacements and stress are defined by eq. (2.103) for an inner solid region, (2.89) for solid cladded regions, and (2.108) for an outer fluid region. Rod and claddings have correspondingly the densities ρ_{in}, ρ_1, ρ_2, $\cdots$, ρ_J, Lamé parameters λ_{in}, μ_{in}, λ_1, $\mu_1, \cdots$, λ_J, μ_J, and total displacement fields $\mathbf{u}_{in}$, $\mathbf{u}_1$, $\cdots \mathbf{u}_J$ (see Figure 3.1). The outer acoustic medium has the density ρ_0 and acoustic speed c_0. The total outer acoustic pressure $p(\mathbf{x})$ is a sum of incident p^{inc} and scattered p^{sc} pressure fields defined by (2.68) and (2.69). The outer pressure fields satisfies the acoustic Helmholtz equation (2.62) and the momentum balance equation (2.62). We assume that the metamaterial cladding

consists of J isotropic layers, and is perfectly attached to the rod. The configuration is solid core inside, $J \geq 1$ layers of solid, and water outside:

$$\text{inner solid,} \quad \rho_{in},\, \lambda_{in},\, \mu_{in} \quad 0 \leq r < b, \tag{3.116}$$

$$\text{solid "1",} \quad \rho_1,\, \lambda_1,\, \mu_1 \quad b \leq < r_1, \tag{3.117}$$

$$\vdots \qquad\qquad \vdots$$

$$\text{solid "J",} \quad \rho_J,\, \lambda_J,\, \mu_J \quad r_{J-1} \leq r < r_J \equiv a, \tag{3.118}$$

$$\text{liquid,} \quad \rho_o, \kappa_o = \rho_o c_o^2 \quad a \leq r < \infty. \tag{3.119}$$

A perfect interface condition between the rod and each layer of cladding as well as the outer fluid yields 3 boundary conditions at fluid-solid interfaces: the outermost $r = a$ surfaces, and 4 conditions at each of the J solid-solid interfaces. The complete set of $3 + 4\,J$ interface conditions yield the following linear system:

$$\begin{pmatrix} a_n^3(k_0 a) & \widehat{\mathbf{x}}_n^1(a,\, k_1,\, K_1) & \widehat{\mathbf{x}}_n^3(a,\, k_1,\, K_1) & \cdots & \mathbf{0}_{1\times 2} \\ \widehat{\mathbf{y}}_n^3(a, k_0, \kappa_0) & \mathbf{Y}_n^1(a,\, k_1,\, K_1) & \mathbf{Y}_n^3(a,\, k_1,\, K_1) & \cdots & \mathbf{0}_{2\times 2} \\ & \vdots & & \vdots & \\ \mathbf{0}_{2\times 1} & & 4(J-1)\,conditions & & \\ & \vdots & & \vdots & \mathbf{0}_{2\times 2} \\ \mathbf{0}_{2\times 1} & \cdots & \mathbf{X}_n^1(b,\, k_J,\, K_J) & \mathbf{X}_n^3(b,\, k_J,\, K_J) & \mathbf{X}_n^1(b,\, k_i,\, K_i) \\ \mathbf{0}_{2\times 1} & \cdots & \mathbf{Y}_n^1(b,\, k_J,\, K_J) & \mathbf{Y}_n^3(b,\, k_J,\, K_J) & \mathbf{Y}_n^1(b,\, k_i,\, K_i) \end{pmatrix} \begin{pmatrix} -B_n \\ C_n^{1,\,1} \\ D_n^{1,\,1} \\ C_n^{3,\,1} \\ D_n^{3,\,1} \\ \vdots \\ C_n^{1,\,J} \\ D_n^{1,\,J} \\ C_n^{3,\,J} \\ D_n^{3,\,J} \\ -C_n^{1,\,in} \\ -D_n^{1,\,in} \end{pmatrix}$$

$$= A_n \begin{pmatrix} a_n^1(k_0 a) \\ \widehat{\mathbf{y}}_n^1(a, k_0, \kappa_0) \\ \mathbf{0}_{2\times 1} \\ \vdots \\ \\ \vdots \\ \mathbf{0}_{2\times 1} \end{pmatrix}, \tag{3.120}$$

where A_n is given by (2.73) for a plane wave incidence and (2.76) for a point source, $\mathbf{X}_n^l(r,\, k_j,\, K_j)$ is defined by eq. (2.87a) and $\mathbf{Y}_n^l(r,\, k_j,\, K_j)$ by eq. (2.87b), and

$$\widehat{\mathbf{x}}_n^l(a,\, k_1,\, K_1) = \begin{pmatrix} a_n^l(k_1 a) & b_n^l(K_1 a) \end{pmatrix}, \tag{3.121}$$

$$\widehat{\mathbf{y}}_n^l(a_m,\, k_0,\, \kappa_0) = \begin{pmatrix} \hat{\alpha}_n^l(a, k_0, \kappa_0) & 0 \end{pmatrix}^T, \tag{3.122}$$

$$\mathbf{0}_{2\times 2} = \begin{pmatrix} 0 & 0 \\ 0 & 0 \end{pmatrix}, \quad \mathbf{0}_{2\times 1} = \begin{pmatrix} 0 \\ 0 \end{pmatrix}, \quad \mathbf{0}_{1\times 2} = \begin{pmatrix} 0 & 0 \end{pmatrix} \tag{3.123}$$

a_n^l, b_n^l are given by (2.87), and $\hat{\alpha}_n^l$ by (2.100) with ($l = 1, 3$).

Solving the system (3.120) for B_n yields

$$B_n = \sum_{q=-\infty}^{\infty} T_{nq} A_q \delta_{nq}, \tag{3.124}$$

where δ_{nq} is the Kronecker delta, the desired $\mathbf{T} = [T_{nn}]$ is a diagonal matrix, and its elements $T_{nn} = T_{nq}\delta_{nq}$ are obtained by Cramer's rule:

$$T_{nn} = -\frac{\overline{\Delta}_n}{\Delta_n}, \tag{3.125}$$

where Δ_n and $\overline{\Delta}_n$ are determinants of matrices defined as:

$$\Delta_n = \begin{vmatrix} a_n^3(k_0 a) & \widehat{\mathbf{x}}_n^1(a,\, k_1,\, K_1) & \widehat{\mathbf{x}}_n^3(a,\, k_1,\, K_1) & \cdots & \mathbf{0}_{1\times 2} \\ \widehat{\mathbf{y}}_n^3(a, k_0, \kappa_0) & \mathbf{Y}_n^1(a,\, k_1,\, K_1) & \mathbf{Y}_n^3(a,\, k_1,\, K_1) & \cdots & \mathbf{0}_{2\times 2} \\ & \vdots & & \vdots & \\ \mathbf{0}_{2\times 1} & \vdots & 4(J-1)\,conditions & \vdots & \\ & \vdots & & \vdots & \mathbf{0}_{2\times 2} \\ \mathbf{0}_{2\times 1} & \cdots & \mathbf{X}_n^1(b,\, k_J,\, K_J) & \mathbf{X}_n^3(b,\, k_J,\, K_J) & \mathbf{X}_n^1(b,\, k_i,\, K_i) \\ \mathbf{0}_{2\times 1} & \cdots & \mathbf{Y}_n^1(b,\, k_J,\, K_J) & \mathbf{Y}_n^3(b,\, k_J,\, K_J) & \mathbf{Y}_n^1(b,\, k_i,\, K_i) \end{vmatrix}, \tag{3.126}$$

$$\overline{\Delta}_n = \begin{vmatrix} a_n^1(k_0 a) & \widehat{\mathbf{x}}_n^1(a,\, k_1,\, K_1) & \widehat{\mathbf{x}}_n^3(a,\, k_1,\, K_1) & \cdots & \mathbf{0}_{1\times 2} \\ \widehat{\mathbf{y}}_n^1(a, k_0, \kappa_0) & \mathbf{Y}_n^1(a,\, k_1,\, K_1) & \mathbf{Y}_n^3(a,\, k_1,\, K_1) & \cdots & \mathbf{0}_{2\times 2} \\ & \vdots & & \vdots & \\ \mathbf{0}_{2\times 1} & \vdots & 4(J-1)\,conditions & \vdots & \\ & \vdots & & \vdots & \mathbf{0}_{2\times 2} \\ \mathbf{0}_{2\times 1} & \cdots & \mathbf{X}_n^1(b,\, k_J,\, K_J) & \mathbf{X}_n^3(b,\, k_J,\, K_J) & \mathbf{X}_n^1(b,\, k_i,\, K_i) \\ \mathbf{0}_{2\times 1} & \cdots & \mathbf{Y}_n^1(b,\, k_J,\, K_J) & \mathbf{Y}_n^3(b,\, k_J,\, K_J) & \mathbf{Y}_n^1(b,\, k_i,\, K_i) \end{vmatrix}. \tag{3.127}$$

Equivalently, T_{nn} can be modified as

$$T_{nn} = -\frac{\eta_n J_n{}'(k_0 a) + J_n(k_0 a)}{\eta_n H_n^{(1)'}(k_0 a) + H_n^{(1)}(k_0 a)}, \tag{3.128}$$

where

$$\eta_n = \frac{\Delta_n^1}{k_0 \kappa_0 \Delta_n^2}, \tag{3.129}$$

and

$$\Delta_n^1 = \begin{vmatrix} \alpha_n^1(a,k_1,\mu_1) & \beta_n^1(a,K_1,\mu_1) & \alpha_n^3(a,k_1,\mu_1) & \beta_n^3(a,K_1,\mu_1) & \cdots & 0 & 0 \\ \gamma_n^1(a,k_1,\mu_1) & \delta_n^1(a,K_1,\mu_1) & \gamma_n^3(a,k_1,\mu_1) & \delta_n^3(a,K_1,\mu_1) & \cdots & 0 & 0 \\ \vdots & & 4(J-1) & Conditions & \vdots & & \\ \vdots & & & & \vdots & & \\ \cdots & a_n^1(k_Jb) & b_n^1(K_Jb) & a_n^3(k_Jb) & b_n^3(K_Jb) & a_n^1(k_{in}b) & b_n^1(K_{in}b) \\ \cdots & c_n^1(k_Jb) & d_n^1(K_Jb) & c_n^3(k_Jb) & d_n^3(K_Jb) & c_n^1(k_{in}b) & d_n^1(K_{in}b) \\ \cdots & \alpha_n^1(b,k_J,\mu_J) & \beta_n^1(K_Jb) & \alpha_n^3(b,k_J,\mu_J) & \beta_n^3(b,K_J,\mu_J) & \alpha_n^1(b,k_{in},\mu_{in}) & \beta_n^1(b,K_{in},\mu_{in}) \\ \cdots & \gamma_n^1(b,k_J,\mu_J) & \delta_n^1(b,K_J,\mu_J) & \gamma_n^3(b,k_J,\mu_J) & \delta_n^3(b,K_J,\mu_J) & \gamma_n^1(b,k_{in},\mu_{in}) & \delta_n^1(b,K_{in},\mu_{in}) \end{vmatrix}, \tag{3.130}$$

$$\Delta_n^2 = \begin{vmatrix} a_n^1(k_1a) & b_n^1(K_1a) & a_n^3(k_1a) & b_n^3(K_1a) & \cdots & 0 & 0 \\ \gamma_n^1(a,k_1,\mu_1) & \delta_n^1(a,K_1,\mu_1) & \gamma_n^3(a,k_1,\mu_1) & \delta_n^3(a,K_1,\mu_1) & \cdots & 0 & 0 \\ \vdots & & 4(J-1) & Conditions & \vdots & & \\ \vdots & & & & \vdots & & \\ \cdots & a_n^1(k_Jb) & b_n^1(K_Jb) & a_n^3(k_Jb) & b_n^3(K_Jb) & a_n^1(k_{in}b) & b_n^1(K_{in}b) \\ \cdots & c_n^1(k_Jb) & d_n^1(K_Jb) & c_n^3(k_Jb) & d_n^3(K_Jb) & c_n^1(k_{in}b) & d_n^1(K_{in}b) \\ \cdots & \alpha_n^1(b,k_J,\mu_J) & \beta_n^1(K_Jb) & \alpha_n^3(b,k_J,\mu_J) & \beta_n^3(b,K_J,\mu_J) & \alpha_n^1(b,k_{in},\mu_{in}) & \beta_n^1(b,K_{in},\mu_{in}) \\ \cdots & \gamma_n^1(b,k_J,\mu_J) & \delta_n^1(b,K_J,\mu_J) & \gamma_n^3(b,k_J,\mu_J) & \delta_n^3(b,K_J,\mu_J) & \gamma_n^1(b,k_{in},\mu_{in}) & \delta_n^1(b,K_{in},\mu_{in}) \end{vmatrix}, \tag{3.131}$$

where a_n^l, b_n^l, c_n^l and d_n^l are given by (2.87), α_n^l, β_n^l, γ_n^l and δ_n^l by (2.88), and $\hat{\alpha}_n^l$ is given by (2.107) for inner fluid and (2.100) for outer fluid. For an acoustic single scattering, a diagonal matrix $\mathbf{T}$ has the form

$$\mathbf{T} = \begin{pmatrix} T_{-N,-N} & 0 & 0 & \cdots & 0 \\ 0 & T_{-N+1,-N+1} & 0 & \cdots & 0 \\ 0 & 0 & T_{-N+2,-N+2} & \cdots & 0 \\ \vdots & \vdots & \vdots & \ddots & \vdots \\ 0 & 0 & 0 & \cdots & T_{N,N} \end{pmatrix}, \quad (m = \overline{1,M}). \tag{3.132}$$

For an isotropic elastic rod cladded with one isotropic elastic layer, the system of equations (3.120) reduces to the system of 7 algebraic equations. For a solid elastic cylinder with no cladding, the scalar potentials, eq. (2.82), must be taken in the form of regular solutions of wave equation: $f_n^1(kr) = J_n(kr)$, because the irregular solution, $f_n^3(x) = H_n^{(1)}(x)$, has singularity at $x = 0$: $H_n^{(1)}(x) \to \infty$. The boundary conditions

reduce to 3 conditions at its outer surface leading to the system of 3 algebraic equations. For a solid elastic cylinder, the T-matrix components have simplified form, and eqs. (3.130)- (3.131) reduce to:

$$\Delta_n^1 = \begin{vmatrix} \alpha_n^1(k_1 a) & \beta_n^1(K_1 a) \\ \gamma_n^1(k_1 a) & \delta_n^1(K_1 a) \end{vmatrix}, \qquad \Delta_n^2 = \begin{vmatrix} a_n^1(k_1 a) & b_n^1(K_1 a) \\ \gamma_n^1(k_1 a) & \delta_n^1(K_1 a) \end{vmatrix}.$$

For rigid and hollow cylinders immersed in an acoustic medium, the boundary conditions are given correspondingly by eqs. (2.104) and (2.105). The density of rigid cylinder ρ_1 with respect to the density of outer acoustic medium ρ_0 tends to infinity: $\rho_1 \to \infty$. Consequently, both the impedance $\mathbf{z}^1$ defined by (2.47) and η_n given by (3.129) tend to infinity. Hence, for a rigid cylinder, eq. (3.128) reduces to the form

$$T_{nn} = -\frac{J_n{}'(k_0 a)}{H_n^{(1)'}(k_0 a)}. \tag{3.133}$$

As opposed to the rigid case, the density of hollow cylinder ρ_1 in relation to outer acoustic medium ρ_0 vanishes: $\rho_1 \to 0$, and the impedance $\mathbf{z}^1$ and η_n approach zero. Thus, for a hollow cylinder, the T-matrix components reduce to the form:

$$T_{nn} = -\frac{J_n(k_0 a)}{H_n^{(1)}(k_0 a)}. \tag{3.134}$$

These relations show the equivalence between the impedance $\mathbf{z}^1$ and η_n.

Acoustic scattering from a fluid filled cylinder

Consider scattering of acoustic incident waves from an anisotropic layered elastic cylinder immersed in an ideal fluid illustrated in Figure 2.2. For perpendicular acoustic incidence, i.e. $k_z = 0$, the axial dependence vanishes. The inner and outer pressure fields satisfy the acoustic Helmholtz equation (2.62) and the momentum balance equation (2.62). The total outer acoustic pressure $p(\mathbf{x})$ is a sum of incident p^{inc} and scattered p^{sc} pressure fields defined by (2.68) and (2.69). The displacements and stress are defined by eq. (2.101) for inner fluid region, (2.89) for solid region, and (2.108) for outer fluid region. The configuration is a gas or liquid inside, $J \geq 1$ layers of solid, and water

outside:

$$\text{gas or liquid,} \quad \rho_{in}, \kappa_{in} = \rho_{in} c_{in}^2 \quad 0 \le r < b, \tag{3.135}$$

$$\text{solid "1",} \quad \rho_1,\, \lambda_1,\, \mu_1 \quad b \le r < r_1, \tag{3.136}$$

$$\vdots \qquad\qquad \vdots$$

$$\text{solid "J",} \quad \rho_J,\, \lambda_J,\, \mu_J \quad r_{J-1} \le r < r_J \equiv a, \tag{3.137}$$

$$\text{liquid,} \quad \rho_0, \kappa_0 = \rho_0 c_0^2 \quad a \le r < \infty. \tag{3.138}$$

The boundary conditions are continuity of traction and continuity of normal displacements at the interface. For a fluid-filled isotropic cylinder submerged in water, there are 6 boundary conditions at fluid-solid interfaces: the innermost $r = b$ and the outermost $r = a$ surfaces, and 4 conditions at each of the $J-1$ solid-solid interfaces. The complete set of $2 + 4\,J$ interface conditions yields a system of linear algebraic equations which follows from the system (3.120) by removing its last column and third to last row, and changing in the second to last row $\alpha_n^1(k_{in}b) \to \hat{\alpha}_n^1(k_{in}b)$ where $\hat{\alpha}_n^l$ is defined by (2.100), and in the last row $\gamma_n^1(k_{in}b) \to \hat{\gamma}_n^1(k_{in}b) \equiv 0$ where k_{in} is the wave number in an inner fluid medium. The determinants in eqs. (3.126)-(3.127) will change accordingly, and simplify the T-matrix components given by (3.125).

Far-field radiated response

Consider now the far-field response, the scattered pressure field p^{sc} , when kr becomes very large: $kr >> 1$. For large values of argument kr, the asymptotic expansion of the Hankel function is

$$H_n^{(1)}(kr) = \sqrt{\frac{2}{\pi kr}} e^{-i(n\frac{\pi}{2}+\frac{\pi}{4})} e^{ikr} \Big[1 + O\Big(\frac{1}{kr}\Big)\Big]. \tag{3.139}$$

The scattered field p^{sc} is defined by eq. (2.69) as an infinite sum of multipoles. The far scattered field p^{sc} can be split into two parts, $g(k|\mathbf{x}|)$ and $f(\theta)$:

$$p^{sc} = g(k|\mathbf{x}|)\, f(\theta) \Big[1 + O\Big(\frac{1}{k|\mathbf{x}|}\Big)\Big], \quad k|\mathbf{x}| >> 1 \tag{3.140}$$

Material	ρ $[\frac{kg}{m^3}]$	λ $[GPa]$	μ $[GPa]$	c_p $[\frac{m}{s}]$	c_s $[\frac{m}{s}]$	E $[GPa]$	ν
Al, [57]	2711.8			6370	3136		
Water, [57]	998			1482			
Air, [89]	1.2			330			
Al, [89]	2790			6300	3100		
Water, [89]	1000			1470			
Al, [133]	2706	57.09	26.69	6389.4	3140.6	71.567	0.3407
Steel (St), [133]	7850	110.79	80.23	5878.1	3196.8	206.99	0.29
Zirconia(ZrO_2),[133]	5700	129	94.8	7476.3	4078.2	244.24	0.2882
Water, [133]	1000			1480			
Air, [133]	1.2			344			
Copper, [79]	8900			4600	2160		
Al, [79]	2694			6427	3112		

Table 3.1: Material properties used for comparison with literature

where the function $g(k|\mathbf{x}|)$ and the farfield amplitude function $f(\theta)$, $\theta = \arg(\mathbf{x})$, can be derived using the asymptotic form of the Hankel functions, eq. (3.139):

$$g(k|\mathbf{x}|) = \sqrt{\frac{1}{k|\mathbf{x}|}} e^{ik|\mathbf{x}|}, \quad |\mathbf{x}| \to \infty, \tag{3.141}$$

$$f(\theta) = \sum_{n=-\infty}^{\infty} f_n e^{in\theta}, \qquad f_n = \sqrt{\frac{2}{\pi}}\, e^{-i\left(\frac{\pi}{4}+\frac{n\pi}{2}\right)} B_n. \tag{3.142}$$

The normalized far-field scattering form function $\overline{f}_\infty$ is defined as

$$\left|\overline{f}_\infty(ka,\theta)\right| = \lim_{|\mathbf{x}|\to\infty} \sqrt{|\mathbf{x}|/a}\, \left|p^{sc}(r,\theta)/A^{inc}\right| = \frac{|f(\theta)|}{A^{inc}\sqrt{ka}}, \tag{3.143}$$

where A^{inc} is the amplitude of an incident plane wave. We evaluate eq. (3.143) at $\theta = \pi$ and multiply it by $\sqrt{2}$ to find a backscattering form function $f_\infty(ka)$ and keep a notation used in the literature [57, 89] for verification. Thus, for a plane wave of unit

amplitude, the backscattering form function has the form

$$|f_\infty(ka)| = \sqrt{2}\,|\overline{f}_\infty(ka,\theta=\pi)| = \sqrt{\frac{2}{ka}}\,|f(\pi)| = \frac{2}{\sqrt{\pi ka}}\left|\sum_{n=-\infty}^{\infty} B_n e^{in\pi/2}\right|. \qquad (3.144)$$

The total power radiated by the multilayered shell is measured by the non-negative far-field flux parameter

$$\sigma_r = \int_0^{2\pi} |f(\theta)|^2\,\mathrm{d}\,\theta = \int_0^{2\pi}\left|\sqrt{\frac{2}{\pi}}\sum_{n=-\infty}^{\infty} B_n e^{in(\theta-\pi/2)}\right|^2 \mathrm{d}\,\theta = 4\sum_{n=-\infty}^{\infty}|B_n|^2. \qquad (3.145)$$

The non-dimensional total scattering cross section(TSCS) is then given by:

$$Q = \int_0^{2\pi} |\overline{f}_\infty(ka,\theta)|^2\,\mathrm{d}\,\theta = \int_0^{2\pi}\left|\sqrt{\frac{2}{\pi ka}}\sum_{n=-\infty}^{\infty} B_n e^{in(\theta-\pi/2)}\right|^2 \mathrm{d}\,\theta = \frac{4}{ka}\sum_{n=-\infty}^{\infty}|B_n|^2, \qquad (3.146)$$

where Q is normalized by a, the outer radius of the cylinder.

Numerical results

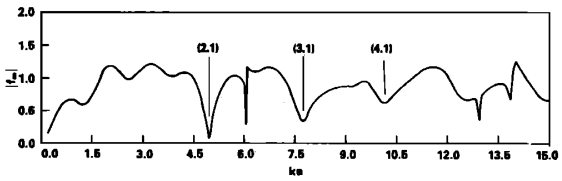

(a) Calculation performed by Flax et al. [57]

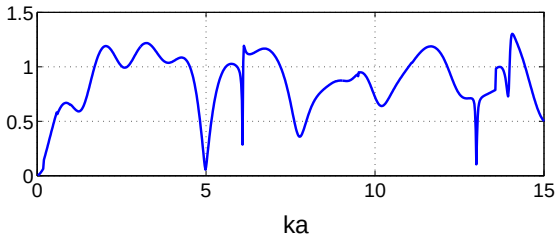

(b) 2D Elasticity solution, MATLAB computation

Figure 3.3: The variation of modulus of backscattering form function $|f_\infty|$ with dimensionless frequency ka for an isotropic cylinder submerged in fluid.

We computed the scattering coefficients as well as T-matrix components for perpendicular incidence $\alpha = 0$ to calculate the modulus of backscattered form function $|f_\infty|$,

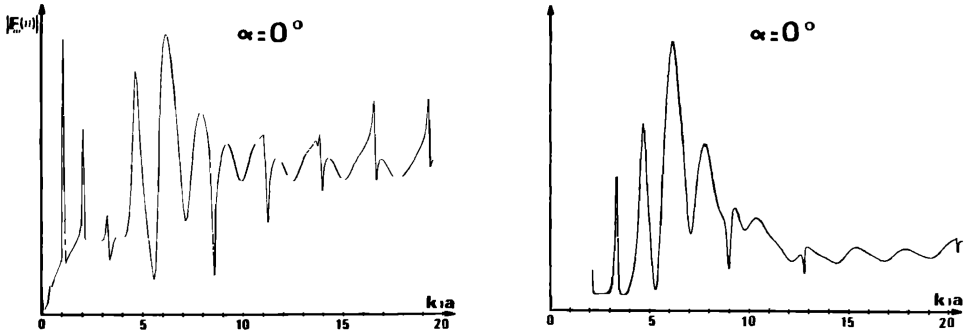

(a) Theoretical and experimental backscattered form function modulus [89].

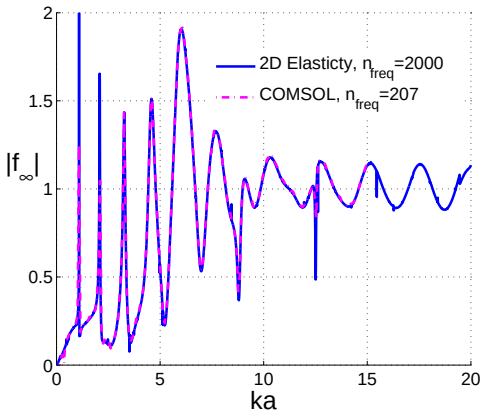

(b) $|f_\infty(ka)|$ vs. ka

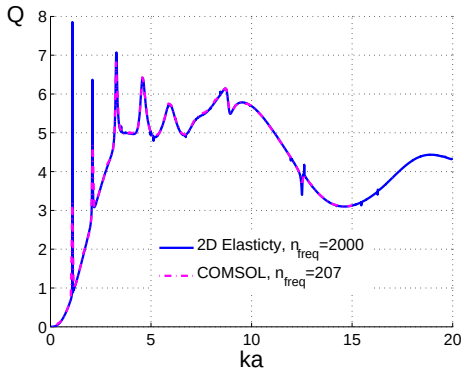

(c) Q vs. ka.

Figure 3.4: Variation of modulus of backscattering form function $|f_\infty|$ and TSCS with non-dimensional frequency ka for air filled thin shell submerged in water

total scattering cross section (TSCS) Q, as well as pressure field. We performed calculations on MATLAB and COMSOL to validate and compare our results with the existing literature. We created a MATLAB code to construct the global matrix and compute the scattering coefficients and transfer matrix. Properties of materials considered in this section are given Table 3.1.

Figure 3.3 shows the back-scattered form function modulus $|f_\infty(ka)|$ defined by eq. (3.144) with $\alpha = 0$ for an Aluminum (Al) solid cylinder submerged in fluid. In Figure 3.3, the graph on the top figure was obtained by Flax et al. [57] theoretically, and the bottom picture displays our MATLAB results using the Global matrix method for Al solid cylinder, which is in agreement with the top picture [57]. Figure 3.4 shows

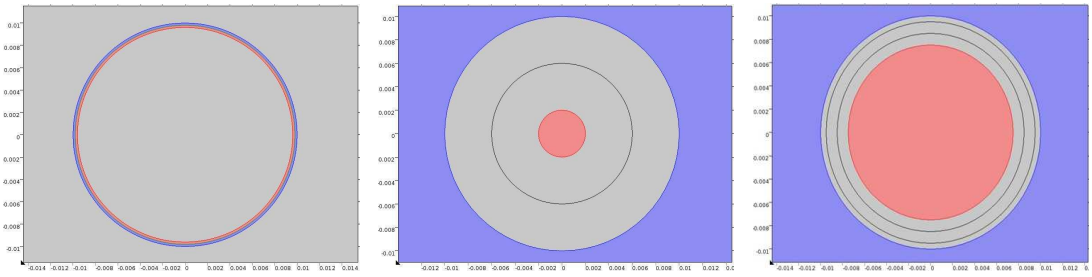

(a) Thin bi-laminate, $h/a = 0.04$, $h_1 = h_2 = 0.5h$ **(b)** Thick bi-laminate, $h/a = 0.8$, $h_1 = h_2 = 0.5h$ **(c)** Tri-laminate, $h/a = 0.25$, $h_1 = 0.2h$, $h_2 = h_3 = 0.4h$

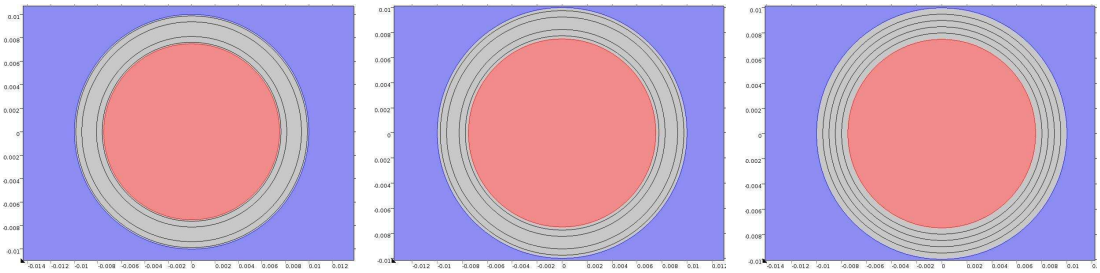

(d) $h/a = 0.25$, $h_3 = 0.5h$, $h_1{=}h_5 = 0.05h$, $h_2{=}h_4 = 0.2h$ **(e)** $h/a = 0.25$, $h_3 = 0.4h$, $h_1{=}h_5 = 0.1h$, $h_2{=}h_4 = 0.2h$, **(f)** $h/a = 0.25$, $h_1 = 0.1h$, $h_1 = h_2 = h_3 = h_4 = h_5$

Figure 3.5: Configurations of air-filled multilayered shells submerged in fluid used in MATLAB and COMSOL simulations.

the dependance of $|f_\infty(ka)|$ and Q on non-dimensional frequency ka for an air filled Al cylindrical thin shell of thickness $h = 0.04$cm and outer radius $a = 0.25$cm submerged in water. The graphs in Figure a were obtained by Leon et al. [89] both theoretically, and experimentally. Figure a on the left shows a theoretical backscattered form function modulus $|f_\infty(ka)|$, and on the right illustrates experimental backscattered spectrum for air filled shell submerged in water. Figures b and c display our results obtained on MATLAB and COMSOL. Variation of modulus $|f_\infty(ka)|$ with ka is shown in Figure b, and TSCS, Q versus ka, is given in Figure c, where Q is defined by eq. (3.146). The properties of shell taken from [89] are given in Table 3.1 for a comparison with findings of Leon et al. [89], Figure a. MATLAB computations are based on our Global matrix method, which uses a 2D Elasticity solution. COMSOL computations are performed with $n_{freq} = 207$ and $ka_{max} = 15$ and MATLAB results are given for $n_{freq} = 2000$

and $ka_{max} = 20$, where ka_{max}, the maximum value of ka, is divided into n_{freq} intervals (n_{freq} is the total number of frequency intervals). COMSOL results are shown for a lesser number of n_{freq} because of prohibitively long computation time. Figures b- c show a consistency between MATLAB and COMSOL simulation for both $|f_\infty(ka)|$ and Q except missed resonance picks caused by reduction of n_{freq} almost 10 times.

Variation of modulus of backscattering form function and TSCS with normalized frequency ka for air-filled multilayers submerged in water is depicted in Figures 3.6-3.9 to compare our results with findings in [133]. Computations are performed in MATLAB and COMSOL with material properties given in Table 3.1 for different multilaminate configurations shown in Figure 3.5 where a is the outer radius of the shell, h is the total thickness of the multilayered shell and h_j is the thickness of j^{th} layer. The following cases are considered: Figure a: $Steel - Al$ or $Al - Al$ thin bilaminate shell with $h/a = 0.04$, $h_1 = h_2 = 0.5h$; Figure b: $Steel - Al$ or $Al - Al$ thick bilaminate shell with $h/a = 0.8$, $h_1 = h_2 = 0.5h$; Figure c: $ZrO_2 - Steel - Al$ tri-laminate shell with $h/a = 0.25$, $h_1 = 0.2h$, $h_2 = h_3 = 0.4h$; Figures d - f: $ZrO_2 - Steel - Al - Steel - ZrO_2$ pento-laminate shell of total thickness $h = 0.25a$ with $h_1 = h_5 = 0.05h$, $h_2 = h_4 = 0.2h$, $h_3 = 0.5h$ in Figure d, with $h_1 = h_5 = 0.1h$, $h_2 = h_4 = 0.2h$, $h_3 = 0.4h$ in Figure e, and with $h_1 = h_2 = h_3 = h_4 = h_5 = 0.2h$ in Figure f.

Figure 3.6 shows the variations of $|f_\infty|$ with non-dimensional frequency ka for Al shell and Al bi-laminate shell depicted in Figure b. Figure a was given in [133]; Figure b shows our MATLAB calculations for a single Al shell of thickness $h = 0.4a$ (blue solid line) and Al bilayer with $h = 0.8a$ (red dash line) depicted in Figure b with properties given in Table 3.1. Graphs in Figure b show a full agreement with findings in [133] depicted in Figure a. Figure 3.7 displays the dependance of $|f_\infty|$ and Q on ka for a thin single and bi-laminate shell configuration shown in Figure a. Figure a shows calculations performed in [133]. Figures b - c illustrate correspondingly our MATLAB computation of $|f_\infty|$ and Q for a thin Al bilaminate shell of thickness $h = 0.04a$ (blue solid line) and single Al shell of thickness $h = 0.02a$ (red dash line). Graphs in Figures a - b are consistent. Figures d - e show comparison of MATLAB and COMSOL computations of $|f_\infty|$ and Q for single and bilaminate Al shells, and a bilaminate $Al - Steel$ shell of

total thickness $h = 0.04a$ submerged in fluid.

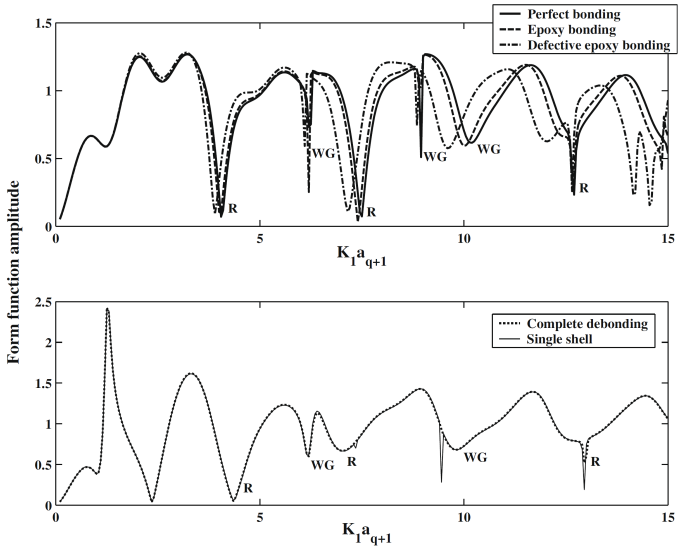

(a) Calculations of $|f_\infty|$ performed in [133] (Figure 6).

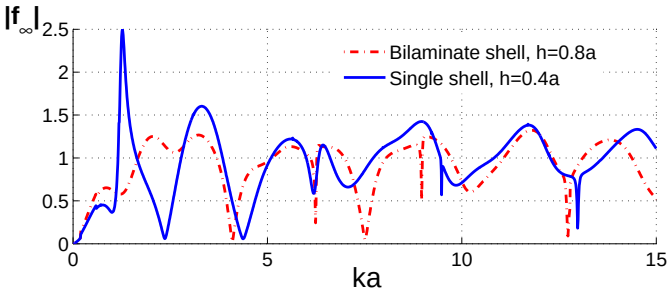

(b) MATLAB computation of amplitudes of $|f_\infty|$

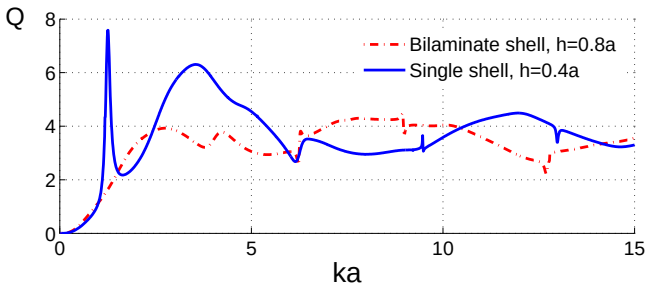

(c) MATLAB computation of amplitudes of Q

Figure 3.6: Variation of modulus of backscattering form function $|f_\infty|$ and TSCS with normalized frequency ka for an air filled Al thick shell and bi-layer submerged in fluid.

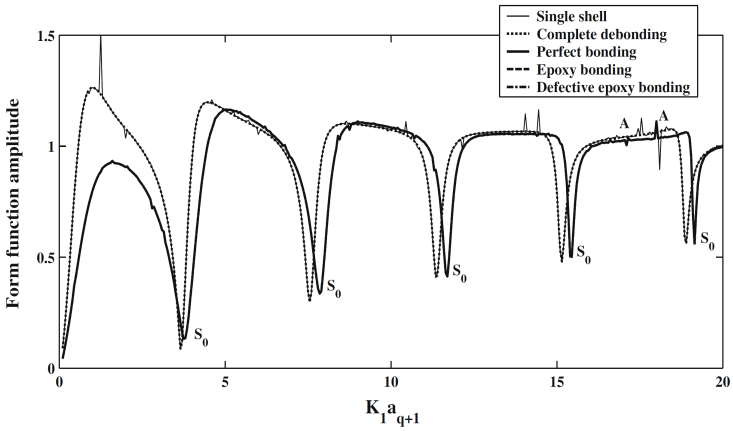

(a) Calculations of $|f_\infty|$ performed in [133] (Figure 2).

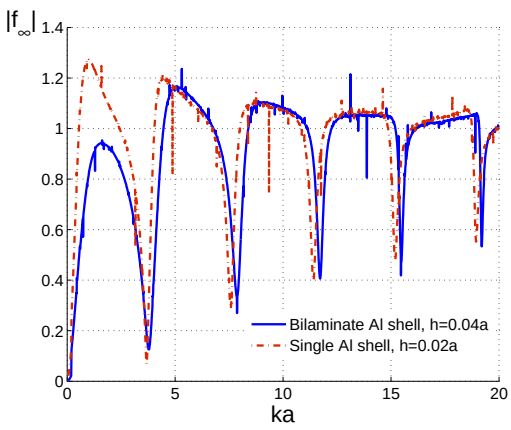

(b) MATLAB computation of $|f_\infty|$ for Al shell

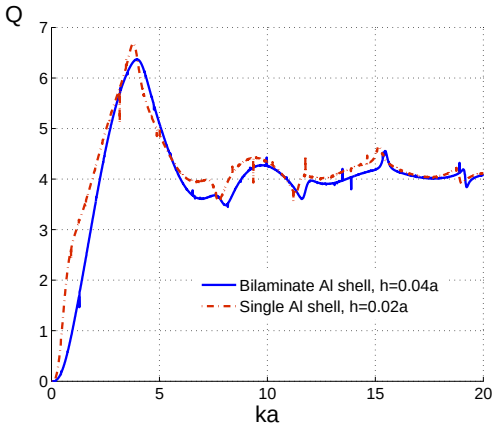

(c) MATLAB computation of Q for Al shell

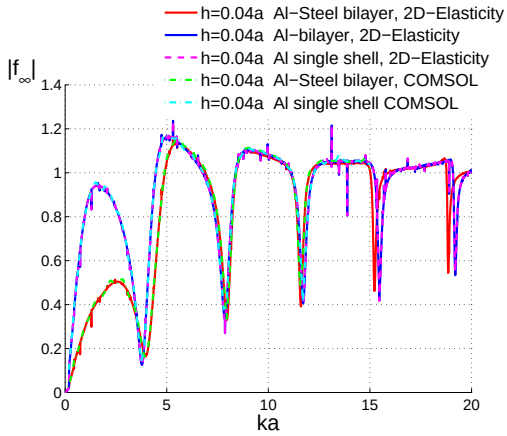

(d) MATLAB and COMSOL comparisons for $|f_\infty|$

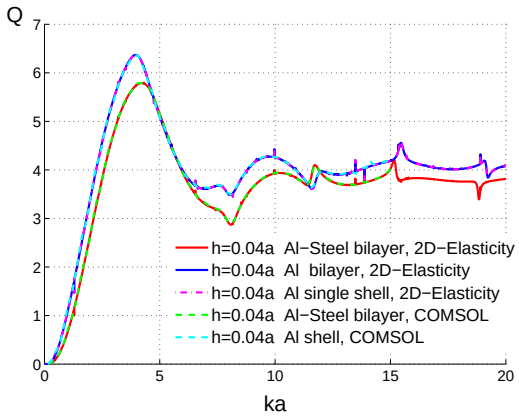

(e) MATLAB and COMSOL comparisons for Q

Figure 3.7: Variation of backscattering form function $|f_\infty|$ and TSCS Q with normalized frequency ka for bilaminate shell.

MATLAB computations are based on the Global matrix method using a 2D elasticity solution. COMSOL computations are performed with $n_{freq} = 100$ and MATLAB results are given for $n_{freq} = 1000$. Figures d - e show an agreement between MATLAB and COMSOL simulation for single and bilaminar shells.

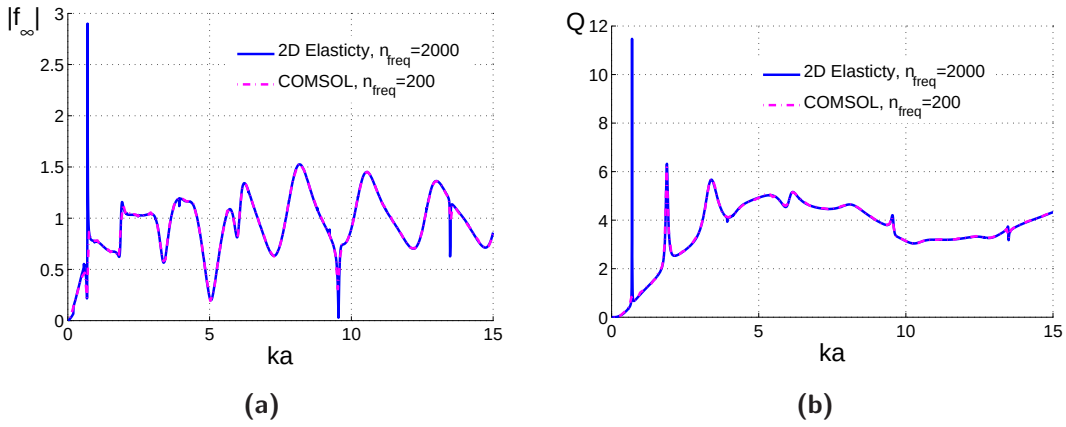

Figure 3.8: Variation of $|f_\infty|$ and Q with normalized frequency ka. Figures (a) and (b) show correspondingly our MATLAB and COMSOL computations of $|f_\infty|$ and Q for an isotropic trilaminate $(Al - Steel - ZrO_2)$ shell with $h/a = 0.25$.

Figure 3.8 illustrates $|f_\infty|$ and Q as a function of ka for an air filled isotropic trilaminate $(Al-Steel-ZrO_2)$ shell submerged in fluid; the innermost layer is made of Al. The total shell thickness is $h = 0.25a$, the trilaminate configuration is depicted in Figure c. Figures a - b show correspondingly our MATLAB and COMSOL computations of $|f_\infty|$ and Q, where $n_{freq} = 2000$ in MATLAB computations and $n_{freq} = 200$ in COMSOL simulation. The graphs display consistency between MATLAB and COMSOL simulations. Figure 3.9 exhibits MATLAB and COMSOL computations of amplitudes of $|f_\infty|$ and Q versus ka for the pentolaminate shell $(ZrO_2 - Steel - Al - Steel - ZrO_2)$ with $h/a = 0.25$ and $a = 0.01m$ with configurations depicted in Figures d, e, and f. MATLAB and COMSOL simulations are performed correspondingly with $n_{freq} = 2000$ (blue solid line) in the former case and $n_{freq} = 200$ (maroon dash-dot line) in the latter case. MATLAB and COMSOL results are consistent for all 3 pentolaminate configurations.

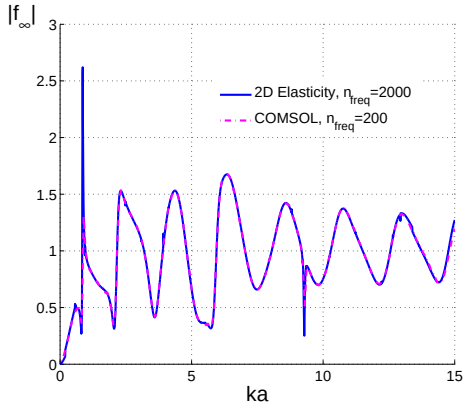

(a) $|f_\infty|$ vs. ka for pentolaminate in Fig. 3.5d.

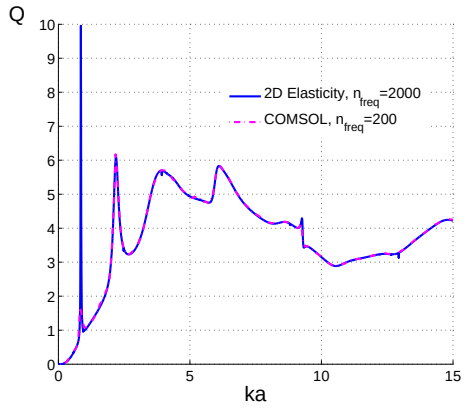

(b) Q vs. ka for pentolaminate in Fig. 3.5d.

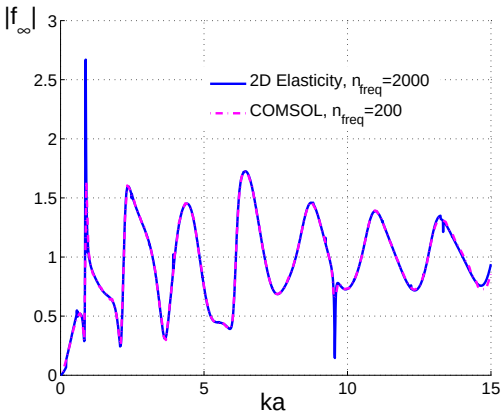

(c) $|f_\infty|$ vs. ka for pentolaminate in Fig. 3.5e.

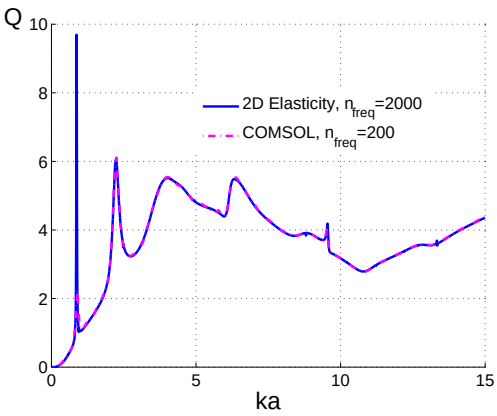

(d) Q vs. ka for pentolaminate in Fig. 3.5e.

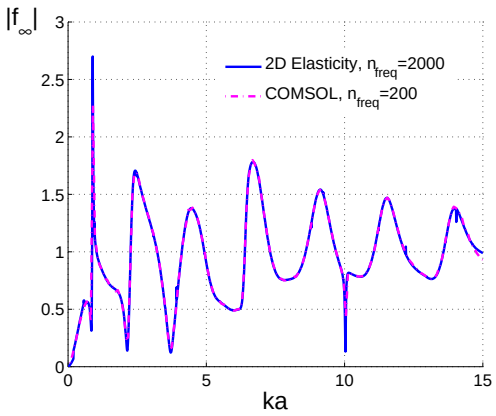

(e) $|f_\infty|$ vs. ka for pentolaminate in Fig. 3.5f.

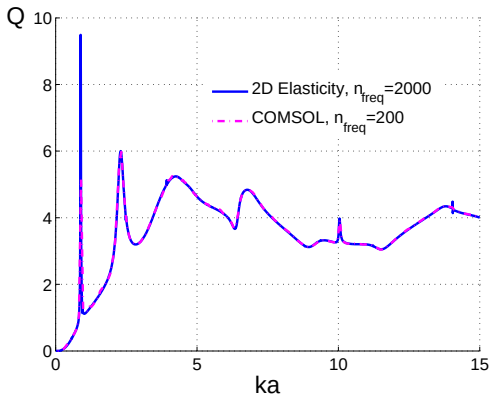

(f) Q vs. ka for pentolaminate in Fig. 3.5f.

Figure 3.9: Variation of $|f_\infty|$ and Q with normalized frequency ka for pento-laminate $(ZrO_2 - Steel - Al - Steel - ZrO_2)$ shell $(h = 0.25a)$ depicted in Figures 3.5d- 3.5f.

The amplitudes of $|f_\infty|$ and Q of 3 different configurations with different sublayer thicknesses are coincide for small values of ka (approximately $ka < 3.5$) and diverge with increase of ka. Figure 3.10 displays calculations performed in [133] for the pento-

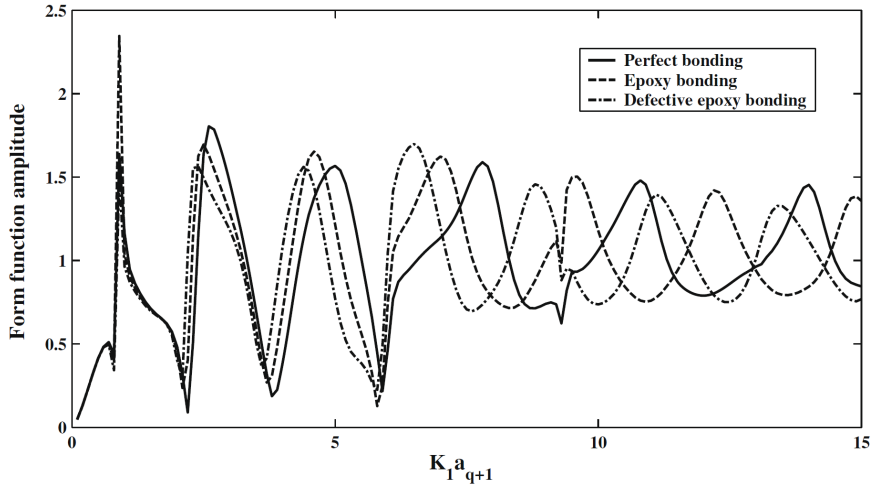

Figure 3.10: Variation of modulus of backscattering form function with normalized frequency for an pento-laminate ($Al-Steel-ZrO_2-Steel-Al$) shell with $h/a = 0.25$. Figure displays calculations performed in [133] .

layered shell shown in Figure d. Figure a illustrates our MATLAB and COMSOL computation of $|f_\infty|$ versus ka for the same configuration. Comparison of Figures a and 3.10 show that the Global matrix method used in MATLAB (blue solid line) matches with the COMSOL result (maroon dash-dot line) for all values of ka shown in the picture whereas the graph (solid line) in Figure 3.10 coincides with the COMSOL result (maroon dash-dot line in Figure a) only for small values of ka (approximately $ka < 2$).

Figure 3.11 displays variation of modulus of normal mode components of backscattering form function $|f_n(\theta = \pi, ka)|$ with ka for different values of mode number $n = \overline{0,7}$ for the pentolaminate shell ($ZrO_2 - Steel - Al - Steel - ZrO_2$) in water, the configurations are depicted in Figure d. Figure a shows calculations performed in Figure 8 [133]. Figures b - e display our computations for comparison. In [133], the coefficients f_n were obtained via Fourier sine and cosine series expansion, whereas here the form function coefficients f_n are defined by eq. (3.142) in exponential form.

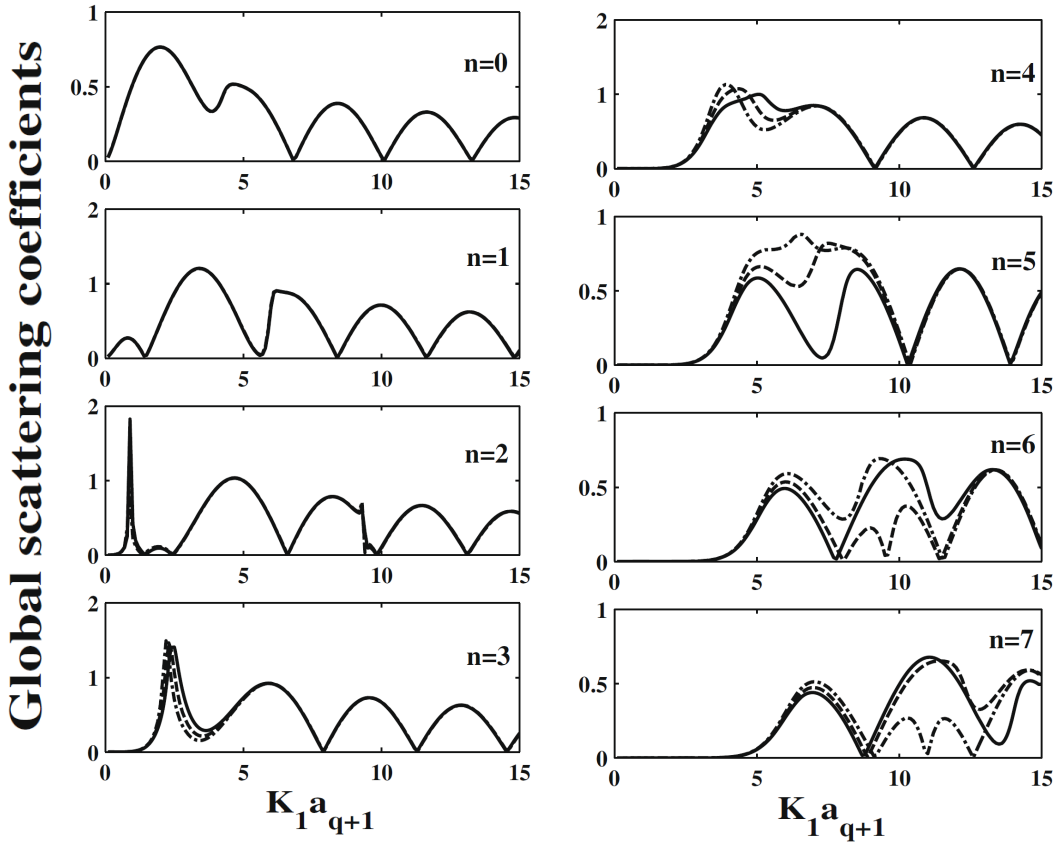

(a) The coefficients $|f_n|$ vs. dimensionless frequency $K_1 a_{q+1}$ for $n = \overline{0,\ 7}$, from Figure 8 in [133]

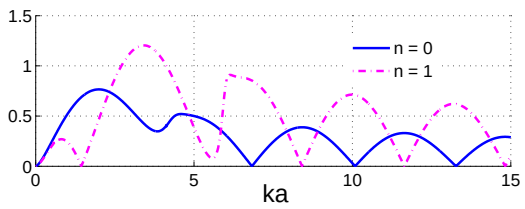

(b) $\sqrt{\frac{2}{ka}}|f_n + f_{-n}|$ vs. ka for $n = 0,\ 1$

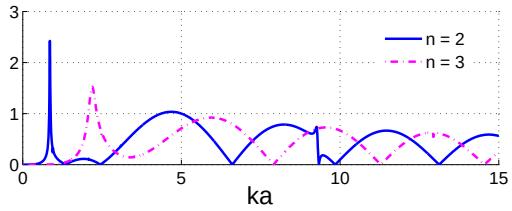

(c) $\sqrt{\frac{2}{ka}}|f_n + f_{-n}|$ vs. ka for $n = 2,\ 3$

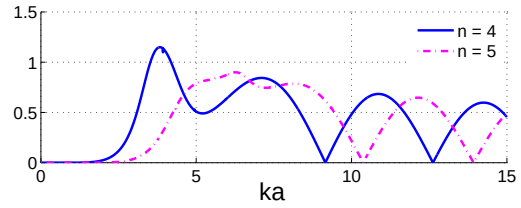

(d) $\sqrt{\frac{2}{ka}}|f_n + f_{-n}|$ vs. ka for $n = 4,\ 5$

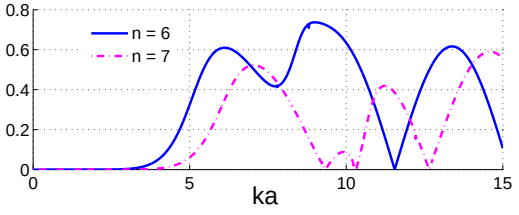

(e) $\sqrt{\frac{2}{ka}}|f_n + f_{-n}|$ vs. ka for $n = 6,\ 7$

Figure 3.11: Variation of modulus of normal mode coefficients of form function $\sqrt{\frac{2}{ka}}|f_n + f_{-n}|$ with dimensionless frequency for a pento-laminate ($ZrO_2 - Steel - Al - Steel - ZrO_2$) shell submerged in fluid for different values of $n = \overline{0,\ 7}$

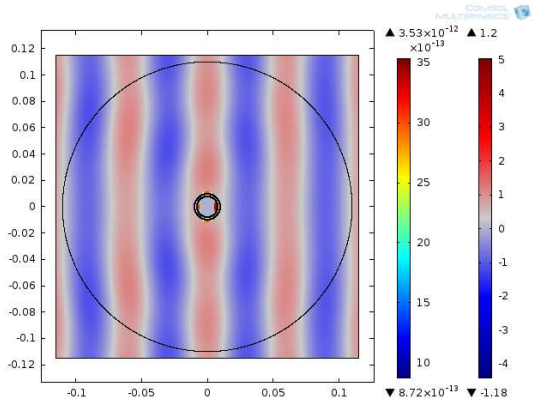

(a) Total field at $ka = 1.05$, zoomed out

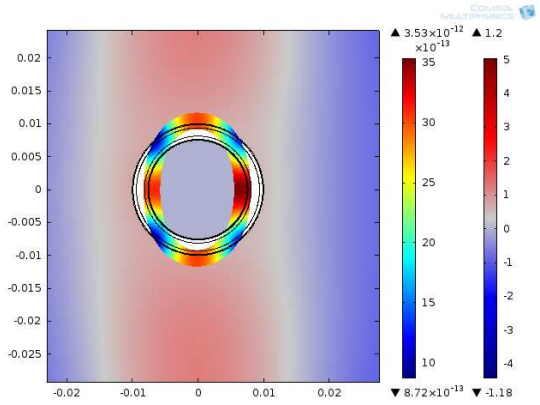

(b) Total field at $ka = 1.05$, zoomed in

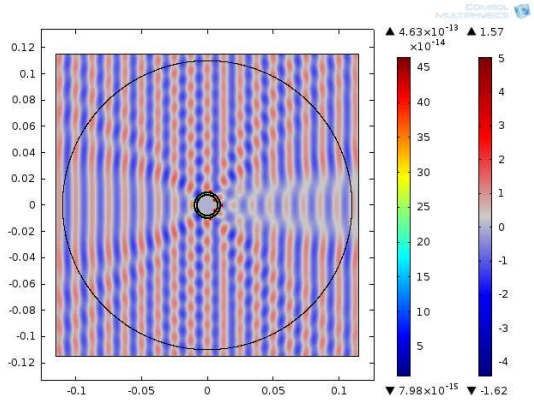

(c) Total field at $ka = 5.025$, zoomed out

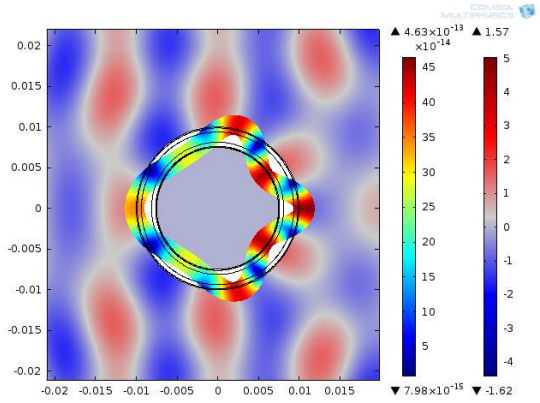

(d) Total field at $ka = 5.025$, zoomed in

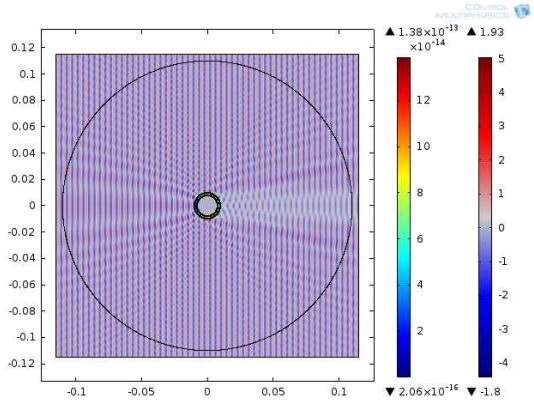

(e) Total field at $ka = 15$, zoomed out

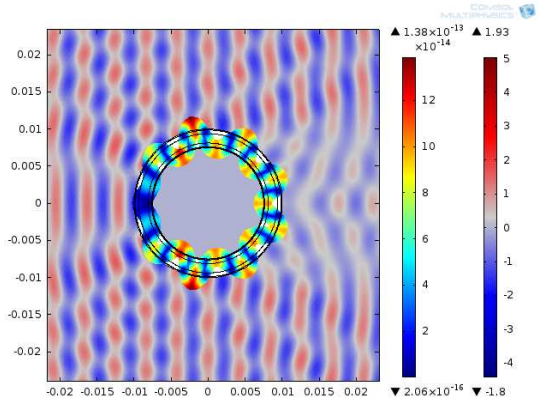

(f) Total field at $ka = 15$, zoomed in

Figure 3.12: Total acoustic pressure field and total displacement at fixed normalized frequency ka for an isotropic pentolaminate shell depicted in Figure 3.5d. Figures on the left display the total field zoomed out. Figures on the right show enlarged view of total field zoomed in.

Hence, we calculated $\sqrt{\frac{2}{ka}}|f_n + f_{-n}|$ to do comparison with $|f_n|$ in Figure a. As we can see, the graphs in Figures a, b, and c coincide for $n = 0, 1, 2, 3, 4$. For $n \geq 4$, results start deviating, the changes in graphs for higher modes ($n \geq 4$) contribute to differences in Figures 3.10 and a for approximately $ka \geq 2$.

Figure 3.12 illustrates the total acoustic pressure field and total displacement at fixed values of normalized frequency ka, $ka = 1.05, 5.025, 15$, for an isotropic pentolaminate shell depicted in Figure 3.5d. Figures on the left display a total field zoomed out. Figures on the right show an enlarged view, a total field zoomed in. Left color bars correspond to total displacement of the shell and right color bars correspond to total outer acoustic pressure field. In Figures a, c, e, a large circle of radius $r_{far} = 11a$ denotes a path over which integration was performed on COMSOL to calculate built-in function $pfar$ - the pressure in the far-field depicted in Figure a.

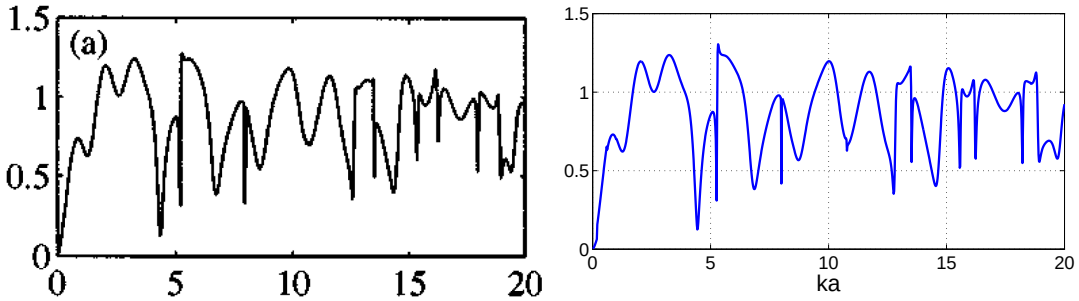

(a) $|f_\infty|$ vs. ka, calculations performed in [79] **(b)** our MATLAB computation of $|f_\infty|$ vs. ka

Figure 3.13: Variation of modulus of backscattering form function $|f_\infty|$ with normalized frequency ka for an isotropic clad-rod submerged in fluid.

Figure 3.13 displays a backscattered form function modulus $|f_\infty|$ with $\alpha = 0$ for a copper-clad aluminum rod submerged in fluid. The graph in Figure a was given by Honanvar and Sinclair [79], while Figure b illustrates our MATLAB calculation for comparison, the graphs are in a good agreement. The computation of $|f_\infty|$ was performed on MATLAB for an aluminum rod with copper-cladding with properties from [79] given in Table 3.1. The outer radius of the clad-rod is $a = 29.571mm$ and its core radius is $b = 29.35mm$. Graphs in Figures a-b exhibit a full agreement between

the theories.

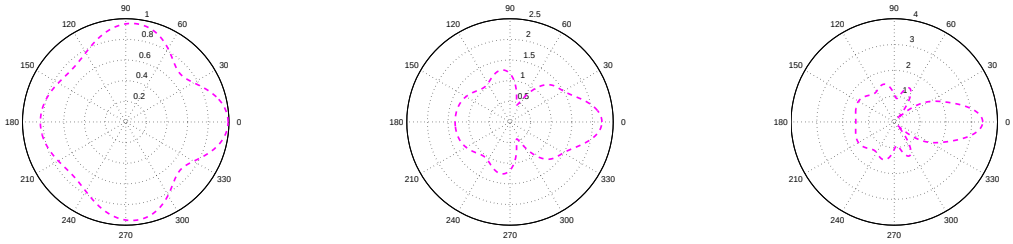

(a) $ka = 1.7$ **(b)** $ka = 3.4$ **(c)** $ka = 5$

Figure 3.14: Angular distribution of far-field amplitude function $|f(\theta)|$ with fixed values of ka for a rigid cylinder submerged in fluid

Figure 3.14 illustrates the angular distribution of the far-field amplitude function $|f(\theta)|$ defined by (3.142) for fixed vales of ka: $ka = 1.7, 3.4, 5$. Polar plots coincide with findings in [55]: Figures 5, 9, and 13 respectively.

3.3.2 Elastic scattering of P/SV waves from a multilayered cylinder embedded in elastic medium

In this section, we investigate an elastic scattering of in-plane P/SV waves from a multilayered clad-rod embedded in an elastic medium taking into account mode conversion of P and SV waves and obtain the transition matrix $\mathbf{T}$ of cylinder $\mathtt{S}_m$ in isolation to examine MS of elastic P/SV waves from the cluster of cylinders in the proceeding chapters. A scattering from a fluid-filled multilayered cylinder can be analyzed analogously and will be discussed in parallel. We consider perpendicular incidence of P/SV waves, i.e. $k_z = 0$. The displacements and stress are defined by eq. (2.103) for the inner elastic rod, eq. (2.89) for the cladding region, and eqs. (2.110) and (2.111) correspondingly for P and SV wave incidences in the outer elastic matrix. An anisotropic clad-rod consists of an elastic isotropic core cladded with anisotropic multilayered metamaterial. We assume that metamaterial cladding is comprised of J isotropic layers, and is perfectly attached to the rod (core), see Figure 3.1. The configuration is a solid core inside, $J \geq 1$ layers of solid, and an elastic matrix outside:

$$\text{inner solid,} \quad \rho_{in},\, \lambda_{in},\, \mu_{in} \quad 0 \leq r < b, \tag{3.147a}$$

$$\text{solid "1",} \quad \rho_1,\, \lambda_1,\, \mu_1 \quad b \leq r < r_1, \tag{3.147b}$$

$$\vdots \qquad\qquad \vdots \tag{3.147c}$$

$$\text{solid "J",} \quad \rho_J,\, \lambda_J,\, \mu_J \quad r_{J-1} \leq r < r_J \equiv a, \tag{3.147d}$$

$$\text{elastic matrix,} \quad \rho_0,\, \lambda_0,\, \mu_0 \quad a \leq r < \infty. \tag{3.147e}$$

For a fluid-filled multilayered cylinder configuration, the inner solid defined by eq. (3.147a) will be replaced with the properties of an inner fluid:

$$\text{gas or liquid,} \quad \rho_{in}, \kappa_{in} = \rho_{in} c_{in}^2 \quad 0 \leq r < b. \tag{3.148}$$

Applying boundary conditions and evaluating the displacement and stress field around cylinder $\mathtt{S}_m$ yields a solution for the scattering coefficients via the transition matrix $\mathbf{T}$ of cylinder $\mathtt{S}_m$ in isolation, such that

$$\begin{pmatrix} B_{p,\,n} \\ B_{s,\,n} \end{pmatrix} = \sum_{q=-\infty}^{\infty} \begin{pmatrix} T_{nq}^{pp} & T_{nq}^{ps} \\ T_{nq}^{sp} & T_{nq}^{ss} \end{pmatrix} \begin{pmatrix} A_{p,\,q} \\ A_{s,\,q} \end{pmatrix}, \tag{3.149}$$

where the submatrices of transition matrix $\mathbf{T}^{\varsigma\xi} = [T_{nq}^{\varsigma\xi}]$ $(\varsigma, \xi \equiv p, s)$, are obtained considering P and SV wave incidences separately as follows.

Scattering of incident P waves from a multilayered clad-rod

A perfect interface condition between a rod and cladding as well as each layer of cladding requires 4 conditions of continuity of stresses and displacements at each of the $J+1$ solid-solid interfaces. The complete set of $4\,J+4$ interface conditions yields the following system of linear algebraic equations for incident P waves:

$$\mathbb{G}\,\mathbf{b} \;=\; \widetilde{\mathbf{a}}_p \tag{3.150}$$

where $\mathbb{G}$ is a Global matrix, $\mathbf{b}$ is the vector of unknown coefficients, and the right hand side vector $\widetilde{\mathbf{a}}_p$ is known:

$$\mathbb{G} \;=\; \begin{pmatrix} \mathbf{X}_n^3(a,\,k_0,\,K_0) & \mathbf{X}_n^1(a,\,k_1,\,K_1) & \mathbf{X}_n^3(a,\,k_1,\,K_1) & \cdots & \mathbf{0}_{2\times 2} \\ \mathbf{Y}_n^3(a,\,k_0,\,K_0) & \mathbf{Y}_n^1(a,\,k_1,\,K_1) & \mathbf{Y}_n^3(a,\,k_1,\,K_1) & \cdots & \mathbf{0}_{2\times 2} \\ \mathbf{0}_{2\times 2} & \vdots & \overset{4(J-1)}{Conditions} & \vdots & \\ & \vdots & & \vdots & \mathbf{0}_{2\times 2} \\ \mathbf{0}_{2\times 2} & \cdots & \mathbf{X}_n^1(b,\,k_J,\,K_J) & \mathbf{X}_n^3(b,\,k_J,\,K_J) & \mathbf{X}_n^1(b,\,k_{in},\,K_{in}) \\ \mathbf{0}_{2\times 2} & \cdots & \mathbf{Y}_n^1(b,\,k_J,\,K_J) & \mathbf{Y}_n^3(b,\,k_J,\,K_J) & \mathbf{Y}_n^1(b,\,k_{in},\,K_{in}) \end{pmatrix}, \tag{3.151}$$

$$\mathbf{b} \;=\; \begin{pmatrix} -B_{p\,n} \\ -B_{s\,n} \\ C_n^{1,\,1} \\ D_n^{1,\,1} \\ C_n^{3,\,1} \\ D_n^{3,\,1} \\ \vdots \\ C_n^{1,\,J} \\ D_n^{1,\,J} \\ C_n^{3,\,J} \\ D_n^{3,\,J} \\ -C_n^{1,\,i} \\ -D_n^{1,\,i} \end{pmatrix}, \quad \widetilde{\mathbf{a}}_p \;=\; A_{p,n}\,\mathbf{a}_p, \quad \text{with} \quad \mathbf{a}_p \;=\; \begin{pmatrix} a_n^1(k_0 a) \\ c_n^1(k_0 a) \\ \alpha_n^1(a, k_0, \mu_0) \\ \gamma_n^1(a, k_0, \mu_0) \\ 0 \\ 0 \\ \vdots \\ \vdots \\ \vdots \\ 0 \\ 0 \end{pmatrix}, \tag{3.152}$$

where $A_{p,n}$ is the incident P wave coefficient defined by (2.112) for an incident plane wave and by (2.116) for a point force, the matrices $\mathbf{X}_n^l(r)$ and $\mathbf{Y}_n^l(r)$ are given by (2.87), a_n^l, b_n^l, c_n^l and d_n^l are given by (2.87), α_n^l, β_n^l, γ_n^l and δ_n^l by (2.88), and $\hat{\alpha}_n^l$ by (2.100).

Employing Cramer's rule in the system (3.150) allows us to find the scattering coefficients $B_{p,\,n}$ and $B_{s,\,n}$ as well as components of block matrices of desired T-matrix $\mathbf{T}$, i.e. $\mathbf{T}^{pp} = [T_{nq}^{pp}]$ and $\mathbf{T}^{sp} = [T_{nq}^{sp}]$ which have diagonal form in this case:

$$T_{nq}^{pp}\delta_{nq} = -\frac{|\mathbb{G}_{pp}|}{|\mathbb{G}|}, \qquad T_{nq}^{sp}\delta_{nq} = -\frac{|\mathbb{G}_{sp}|}{|\mathbb{G}|}, \tag{3.153}$$

where $\mathbb{G}_{pp}$ is constructed from matrix $\mathbb{G}$ by replacing its first column by vector $\mathbf{a}_p$ and $\mathbb{G}_{sp}$ by replacing the second column of $\mathbb{G}$ by vector $\mathbf{a}_p$.

Scattering of incident SV waves from a multilayered clad-rod

For incident SV waves, a perfect interface condition at the $J+1$ solid-solid interfaces of a multilayered clad-rod yields a complete set of $4\,J+4$ interface conditions that yields the following system of linear algebraic equations

$$\mathbb{G}\,\mathbf{b} \;=\; \widetilde{\mathbf{a}}_s \tag{3.154}$$

where $\mathbb{G}$ is a Global matrix defined by eq. (3.151), $\mathbf{b}$ is the vector of unknown coefficients given by (3.152), and the right hand side vector $\widetilde{\mathbf{a}}_s$ is known and has the form:

$$\widetilde{\mathbf{a}}_s \;=\; A_{s,n}\,\mathbf{a}_s, \tag{3.155}$$

with

$$\mathbf{a}_s \;=\; \Big(b_n^1(K_0a) \quad d_n^1(K_0a) \quad \beta_n^1(a,k_0,\mu_0) \quad \delta_n^1(a,k_0,\mu_0) \quad 0 \quad \cdots \quad 0\Big)^T, \tag{3.156}$$

where $A_{s,n}$ is the incident SV wave coefficient given by (2.112) for an incident plane wave and by (2.116) for a point force. The block matrices $\mathbf{T}^{ps} = [T_{nq}^{ps}]$ and $\mathbf{T}^{ss} = [T_{nq}^{ss}]$ of the desired T-matrix are obtained from the system (3.150) using Cramer's rule

$$T_{nq}^{ps}\delta_{nq} = -\frac{|\mathbb{G}_{ps}|}{|\mathbb{G}|}, \qquad T_{nq}^{ss}\delta_{nq} = -\frac{|\mathbb{G}_{ss}|}{|\mathbb{G}|}, \tag{3.157}$$

where $\mathbb{G}_{ps}$ is constructed from matrix $\mathbb{G}$ by replacing its first column by vector $\mathbf{a}_s$ and $\mathbb{G}_{ss}$ by replacing the second column of $\mathbb{G}$ by vector $\mathbf{a}_s$.

For a fluid-filled multilayered cylinder imbedded in elastic matrix, the complete set of $3 + 4\,J$ interface conditions yields a system of linear algebraic equations which follows from the system (3.150) for incident P waves and (3.154) for incident SV waves by removing the last column and third to last row of Global matrix $\mathbb{G}$, and changing its second to last row: $\alpha_n^1(k_{in}b) \to \hat{\alpha}_n^1(k_{in}b)$, where $\hat{\alpha}_n^l$ is defined by (2.100), and in the last row $\gamma_n^1(k_{in}b) \to \hat{\gamma}_n^1(k_{in}b) \equiv 0$.

Far-field elastic radiated response

A far-field elastic radiated response can be evaluated analogously to an acoustic case. The far scattered field amplitude function follows the asymptotic form of the Hankel function for large values of argument (see eq. (3.139)). For $k|\mathbf{x}| >> 1$ and $K|\mathbf{x}| >> 1$, the far scattered field can be split as:

$$\begin{pmatrix} \varphi^{sc}(\mathbf{x}) \\ \psi^{sc}(\mathbf{x}) \end{pmatrix} = \begin{pmatrix} \frac{1}{k}\, g(k|\mathbf{x}|) f_p(\theta) \left[1 + O\Big(\frac{1}{k|\mathbf{x}|}\Big)\right] \\ \frac{1}{K}\, g(K|\mathbf{x}|) f_s(\theta) \left[1 + O\Big(\frac{1}{K|\mathbf{x}|}\Big)\right] \end{pmatrix}, \tag{3.158}$$

where the function $g(x)$ is given by (3.141) and the farfield amplitude function $f_\zeta(\theta), (\zeta = p, s)$ is defined as

$$f_\zeta(\theta) = \sqrt{\frac{2}{\pi}} e^{-i\frac{\pi}{4}} \sum_{n=-\infty}^{\infty} e^{-i\frac{n\pi}{2}} B_{\zeta,n} e^{in\theta}, \quad (\zeta = p, s). \tag{3.159}$$

The far scattered field form functions $f_{\zeta,\infty}(ka, \theta)$ with $\zeta = p$ for compressional wave incidence and $\zeta = s$ for shear wave incidence are defined as follows:

$$\begin{pmatrix} f_{p,\infty}(ka, \theta) \\ f_{s,\infty}(ka, \theta) \end{pmatrix} = \lim_{|\mathbf{x}|\to\infty} \sqrt{2|\mathbf{x}|/a} \begin{pmatrix} \frac{1}{k}\, g(k|\mathbf{x}|) f_p(\theta)/A_p^{inc} \\ \frac{1}{K}\, g(K|\mathbf{x}|) f_s(\theta)/A_s^{inc} \end{pmatrix}, \tag{3.160}$$

where $f_{\zeta,\infty}$ is normalized by factor $\frac{\sqrt{2}}{aA_\zeta^{inc}}$, $(\zeta = p, s)$. Thus, for a plane wave of a unit amplitude, we have

$$\begin{pmatrix} f_{p,\infty}(ka, \theta) \\ f_{s,\infty}(ka, \theta) \end{pmatrix} = \begin{pmatrix} \frac{2}{\sqrt{k^3 a\pi}} \left| \sum_{n=-\infty}^{\infty} B_{p,n} e^{in(\theta-\pi/2)} \right| \\ \frac{2}{\sqrt{K^3 a\pi}} \left| \sum_{n=-\infty}^{\infty} B_{s,n} e^{in(\theta-\pi/2)} \right| \end{pmatrix}. \tag{3.161}$$

The total displacement $\mathbf{u}$ is the sum of incident $\mathbf{u}^{inc}$ and scattered $\mathbf{u}^{sc}$ fields, and the total stress tensor is $\boldsymbol{\sigma} = \boldsymbol{\sigma}^{inc} + \boldsymbol{\sigma}^{sc}$. In the far-field, the scattered field $\mathbf{u}^{sc}$ in terms of the Helmholtz potentials has the form

$$\mathbf{u}^{sc} = \begin{pmatrix} \boldsymbol{\nabla}\varphi^{sc}(\hat{\mathbf{x}}) \\ \boldsymbol{\nabla} \times (\mathbf{e}_z \psi^{sc}(\hat{\mathbf{x}})) \end{pmatrix} = \lim_{|\mathbf{x}|\to\infty} \begin{pmatrix} \sqrt{\frac{2}{i\pi}}\, g(k|\mathbf{x}|) \widetilde{f}_p(\theta) \\ -\sqrt{\frac{2}{i\pi}}\, g(K|\mathbf{x}|) \widetilde{f}_s(\theta) \end{pmatrix}, \tag{3.162}$$

with

$$\widetilde{f}_\zeta(\theta) = \sum_{n=-\infty}^{\infty} B_{\zeta,n}\, e^{in\theta}\, i^{-(n-1)} = \sqrt{\frac{\pi i^3}{2}} f_\zeta(\theta), \quad (\zeta = p, s), \tag{3.163}$$

where $f_\zeta(\theta)$ is defined by (3.159), $\hat{\mathbf{x}} = \frac{\mathbf{x}}{|\mathbf{x}|} = \mathbf{e}_r$ is the unit vector that defines the scattering direction, the angle θ is determined as the angle between the scattering direction $\hat{\mathbf{x}}$ and the incidence direction, with $\theta = 0$ associated with the direction of incidence.

The far-field stress tensor $\boldsymbol{\sigma}$ defined in terms of far-field amplitudes has the form

$$\boldsymbol{\sigma}^{sc}(\mathbf{x}) = \lim_{|\mathbf{x}|\to\infty} \Big[i\,k\big(\lambda\,\mathbf{I} + 2\,\mu\,\mathbf{e}_r\mathbf{e}_r\big)\sqrt{\frac{2}{i\pi}}\,g(k|\mathbf{x}|)\widetilde{f}_p(\theta) \\ - i\,K\,\mu\big(\mathbf{e}_r\mathbf{e}_\theta + \mathbf{e}_\theta\mathbf{e}_r\big)\sqrt{\frac{2}{i\pi}}\,g(k|\mathbf{x}|)\widetilde{f}_s(\theta)\Big]. \tag{3.164}$$

The total power radiated by the cylinder is:

$$\Sigma = \Sigma_p + \Sigma_s \tag{3.165}$$

where Σ_p and Σ_s are the compresional and shear far-field averaged radial flux vector components defined as

$$\Sigma_\zeta = \int_0^{2\pi} |f_\zeta(\theta)|^2\,\mathtt{d}\,\theta = 4\sum_{n=-\infty}^{\infty} |B_{\zeta,n}|^2, \quad (\zeta = p, s). \tag{3.166}$$

The average power radiated across the closed surface S' is zero due to the conservation of energy in an elastic solid [178]:

$$< \Sigma >= \frac{\omega}{2} Im\left(\int_{S'} \mathbf{u}(\mathbf{x})\cdot\boldsymbol{\sigma}^*(\mathbf{x})\cdot\mathbf{n}(\mathbf{x})dS\right) = 0, \tag{3.167}$$

where $\mathbf{n}$ is the unit normal of position vector $\mathbf{x}$. For a plane wave:

$$\int_{S'} \mathbf{u}^{inc}(\mathbf{x})\cdot\boldsymbol{\sigma}^{inc*}(\mathbf{x})\cdot\hat{\mathbf{x}}\,dS = 0. \tag{3.168}$$

Hence, eq. (3.167) yields

$$\frac{\omega}{2} Im\left(\int_{S'} \mathbf{u}^{sc}(\mathbf{x})\cdot\boldsymbol{\sigma}^{sc*}(\mathbf{x})\cdot\hat{\mathbf{x}}\,dS\right) \\ = -\frac{\omega}{2} Im\left(\int_{S'} (\mathbf{u}^{inc}(\mathbf{x})\cdot\boldsymbol{\sigma}^{sc*}(\mathbf{x}) + \mathbf{u}^{sc}(\mathbf{x})\cdot\boldsymbol{\sigma}^{inc*}(\mathbf{x}))\cdot\hat{\mathbf{x}}\,dS\right), \tag{3.169}$$

where "Im" denotes the imaginary part of the variable. The right-hand side of eq. (3.169) normalized with respect to the incident power P_0 is defined as the scattering cross-section of the scatterer Q [178], i.e.

$$Q = \frac{\omega}{2P_0} Im\left(\int_{S'} \mathbf{u}^{sc}\cdot\boldsymbol{\sigma}^{sc*}\cdot\mathbf{x}\,dS\right) \\ = -\frac{\omega}{2P_0} Im\left(\int_{S'} (\mathbf{u}^{inc}\cdot\boldsymbol{\sigma}^{sc*} + \mathbf{u}^{sc}\cdot\boldsymbol{\sigma}^{inc*})\cdot\hat{\mathbf{x}}\,dS\right). \tag{3.170}$$

The non-dimensional total scattering cross sections are

$$Q_p = Q_{pp} + Q_{sp}, \quad \text{for P wave incidence,} \tag{3.171}$$

$$Q_s = Q_{ps} + Q_{ss}, \quad \text{for SV wave incidence,} \tag{3.172}$$

where $Q_{\zeta\chi}$ (ζ, $\chi = p$, s) are given by [81]:

$$Q_{\zeta p} = \frac{4}{ka}\sum_{n=-\infty}^{\infty}|B_{\zeta,n}|^2, \quad Q_{\zeta s} = \frac{4}{Ka}\sum_{n=-\infty}^{\infty}|B_{\zeta,n}|^2, \quad (\zeta = p,\, s). \tag{3.173}$$

Hereinafter the double sub-index $\zeta\,\chi$ (ζ, $\chi = p$, s) means the following: the first sub-index ζ ($\zeta = p$, s) denotes the polarization of scattered a P or SV wave, and the second sub-index χ ($\chi = p$, s) denotes the polarization ofan incident P or SV wave.

"The forward scattering theorem", also called "Optical theorem", derived in [178] for elastic P and SV waves states that the total rate of energy transmitted through a closed surface by both scattered P and SV waves is proportional (in 2D) to the imaginary part of the amplitude of the scattered wave in the forward direction alone. This implies the following identities for the total scattering cross-sections Q_p and Q_s[178]:

$$Q_p = \frac{2(\lambda+2\mu)k_p\omega}{P_0} Im[\widetilde{f}_{pp}(\theta=0)], \quad \text{for P wave incidence,} \tag{3.174}$$

$$Q_s = \frac{2\,\mu k_s\omega}{P_0}\,\hat{\mathbf{u}}\cdot\hat{\boldsymbol{\theta}}_K\, Im[\widetilde{f}_{ss}(\theta=0)], \quad \text{for SV wave incidence,} \tag{3.175}$$

where $\hat{\mathbf{u}} = \hat{\mathbf{k}}\times\hat{\mathbf{e}}_z$ is the direction of polarization of the incident SV wave, $\hat{\boldsymbol{\theta}}_k$ is a vector perpendicular to $\hat{\mathbf{k}}$, $\hat{\mathbf{k}}$ is a unit vector along the direction of propagation, and $\widetilde{f}_{\zeta\zeta}(\theta)$, ($\zeta = p$, s) is defined by (3.163). In notation $\widetilde{f}_{\zeta\zeta}(\theta)$, the second sub-index ζ is included to indicate the direction of polarization of the incident wave, and $\theta = 0$ corresponds to the forward direction $\hat{\mathbf{k}}$ of both incident and scattered waves.

Numerical results

Numerical computations are performed for the scattering of P-waves for two types of scatterer: (a) a solid steel cylinder embedded in an Epoxy matrix, and (b) an empty Aluminum cylindrical shell embedded in an elastic polyethylene medium. The results are presented in Figures 3.15 - 3.16 for materials with properties given in Table 3.2. Figure 3.15 illustrates the variation of modulus of longitudinal backscattering form

Material	ρ $[kg/m^3]$	c_p $[m/s]$	c_s $[m/s]$
Steel (St) [17]	7800	5960	3235
Epoxy [17]	1129	2640	1339
Aluminum (Al)[183]	2800	6380	3100
Polyethylene [183]	1050	1950	540

Table 3.2: Material properties used for comparison with results in [17] and [183]

function $|f_{p,\infty}(ka,\pi)|$ with normalized frequency ka for an isotropic steel wire imbedded in an Epoxy matrix. The Figure on the left displays calculations performed in [17], both theoretically and experimentally. the Figure on the right represents our MATLAB computation of $|f_{p,\infty}(ka,\pi)|$ for a steel solid cylinder of radius $a = 0.37mm$. The graphs are in good agreement.

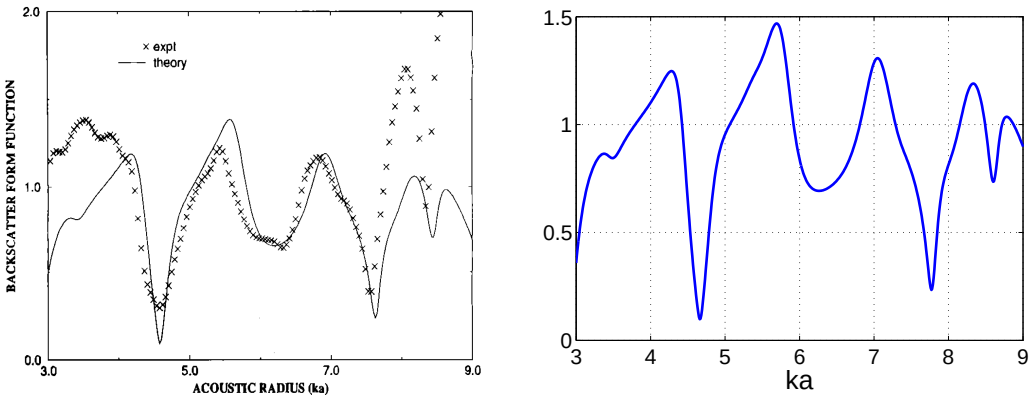

(a) $|f_{p,\infty}(ka,\pi)|$ vs ka [17] **(b)** $|f_{p,\infty}(ka,\pi)|$ vs ka, MATLAB computation

Figure 3.15: Variation of modulus of longitudinal backscattering form function $|f_{p,\infty}(ka,\pi)|$ with normalized frequency ka for isotropic wire embedded in Epoxy matrix. Figure (a) on the left displays calculations performed in [17]. Figure (b) on the right shows our MATLAB computation of $|f_{p,\infty}(ka,\pi)|$ for a steel wire of radius $a = 0.37mm$ in Epoxy matrix

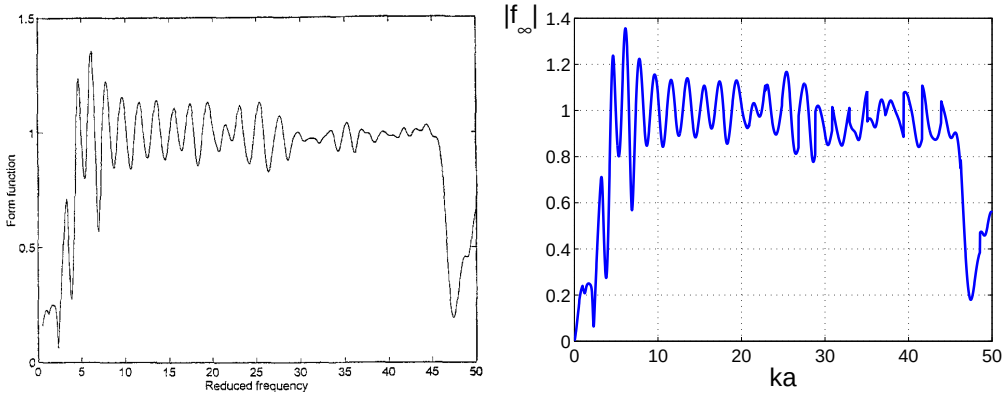

(a) h=0.2a, [183] **(b)** h=0.2a, MATLAB

Figure 3.16: Variation of modulus of longitudinal backscattered form function $|f_{p,\infty}(ka,\pi)|$ with normalized frequency ka for empty Al Shell embedded in polyethylene matrix.

Figures 3.16 exhibits the dependence of form function on non-dimensional frequency ka for an empty Al shell of thickness $h = 0.2a$ embedded in polyethylene matrix. Figure a on the right displays calculations performed in [183]. Figure b on the left shows our MATLAB computation of backscattered form function amplitudes.

Chapter 4

Acoustic and elastic multiple scattering and radiation from planar configuration of parallel cylindrical shells

In this chapter, we study multiple scattering and radiation from a cluster of cylinders situated in acoustic and elastic media including a full interaction between the cylinders. In Section 4.1.1, we review an acoustic multiple scattering theory (MST) and derive a linear system of equations to be solved. In Section 4.1.2, we present numerical results for angular distribution of form function, and absolute total and scattered pressure fields at small M and k; the results include the application of MST in designing waveguides and resonators using different configurations of active and empty shells. In Section 4.2, generalize the idea of acoustic MS to include the elastodynamical properties of media. In Section 4.2.1, we formulate the problem of elastic MS of SV/P waves from a configuration of parallel cylindrical shells, including the effect of a mode conversion in an MS. In Section 4.2.2, we illustrate some numerical simulations for a total displacement field.

4.1 Acoustic multiple scattering and radiation from planar configuration of parallel cylindrical shells

4.1.1 Multiple scattering theory

Formulation of problem

Consider an acoustic multiple scattering by an arbitrary grating of M obstacles $\mathtt{S}_m$, $(m = \overline{1, M})$ of cylindrical shape. In general, each obstacle may have no rotational symmetry. We will refer to obstacles simply as cylinders but may consider elastic solid, rigid,

or hollow cylinders of outer radii a_m, as well as thin, thick and multi-laminate cylindrical shells of outer a_m and inner b_m radii with and without attachments inside the shells. We consider a perpendicular incidence ($\alpha = 0$) on a planar configuration of cylinders and neglect z dependence, hence eq. (2.65) yields: $k_\perp = k$, $k_z = 0$, where k is an acoustic wavenumber. Let $\mathbf{x} = (x, y)$ be a position vector of a typical point in two-dimensional Cartesian coordinates with origin at O, and let us define plane polar coordinates (r_m, θ_m) at the centers O_m. An arbitrary planar configuration of shells is given in Fig. 4.1. Assume that the $\mathtt{S}_m, (m = \overline{1, M})$ cylinders have different physical properties and are located at the centers O_m, at $\mathbf{x} = \boldsymbol{l}_m$, the distance $|\boldsymbol{l}_m|$ from the origin O (see Fig. 4.1). Time harmonic dependence $e^{-i\omega t}$ is assumed but omitted in the following.

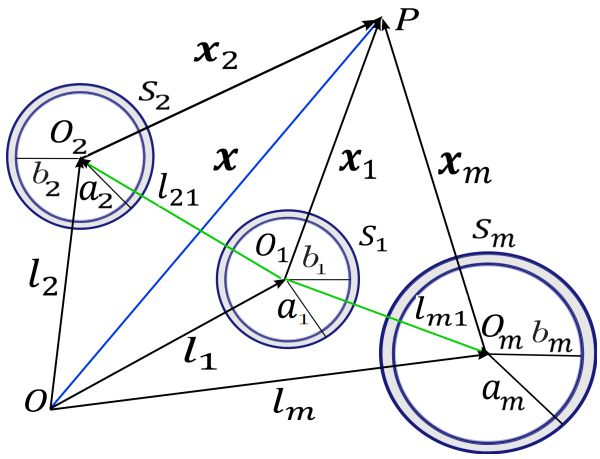

Figure 4.1: An arbitrary planar configuration of M cylindrical shells $\mathtt{S}_m$ with outer radius a_m and inner radius b_m, $m = \overline{1, M}$.

The total pressure field $p(\mathbf{x})$ is defined by (2.67) as the sum of incident p^{inc} and scattered p^{sc} pressure fields, and satisfies the acoustic Helmholtz wave equation (2.62) and the momentum equation(2.63). The incident field is scattered by cylinders, and in the neighborhood of cylinder $\mathtt{S}_m$ is given as

$$p_{inc}^{(m)} = \sum_{n=-\infty}^{\infty} A_n^{(m)} U_n^+(k\mathbf{x}_m), \tag{4.1}$$

where the function $U_n^{\pm}(\mathbf{x})$ is defined by eq. (2.66); $\mathbf{x}_m$ is a position vector of point P

with respect to the centers of multipoles at O_m (see Figure 4.1) and defined as:

$$\mathbf{x}_m = \mathbf{x} - \boldsymbol{l}_m, \tag{4.2}$$

where $\arg \mathbf{x} \in [0, 2\pi)$ and $\arg(-\mathbf{x}) = \big(\arg \mathbf{x} \pm \pi\big) \mod 2\pi$.

The total scattered field p^{sc} can be considered as a superposition of the scattered fields by all the cylinders in the configuration, and expanded as a sum of multipoles in the form:

$$p^{sc} = \sum_{m=1}^{M} p_{sc}^{(m)} = \sum_{m=1}^{M} \sum_{n=-\infty}^{\infty} B_n^{(m)} V_n^+(k\,\mathbf{x}_m), \tag{4.3}$$

where $B_n^{(m)}$ - the scattering coefficients, $p_{sc}^{(m)}$ is the wave scattered by cylinder $\mathtt{S}_m$:

$$p_{sc}^{(m)} = \sum_{n=-\infty}^{\infty} B_n^{(m)} V_n^+(k\,\mathbf{x}_m), \tag{4.4}$$

The scattered field p^{sc} can be expressed as the sum of multipoles at the origin using the generalized Graf's addition theorem (2.72).

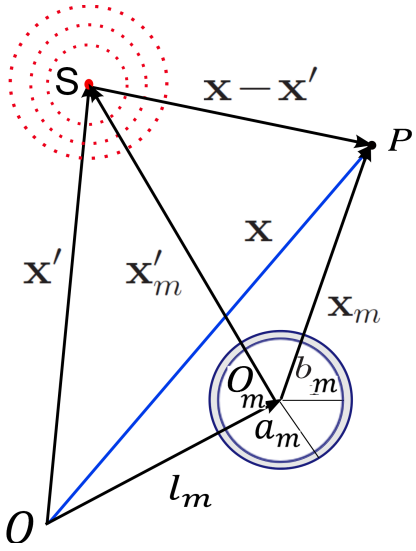

Figure 4.2: A point source impinging on an isotropic multilaminate cylinder submerged in a fluid medium or embedded in an elastic matrix

In eq. (4.1), the unknown coefficients $A_n^{(m)}$ for a plane wave incidence are derived assuming no source term: $p_S = 0$, and that the incident wave is the plane wave of unit amplitude in direction ψ:

$$p^{inc} = e^{ik\mathbf{e}_\psi \cdot \mathbf{x}} \quad \Rightarrow \quad A_n^{(m)} = e^{ik\hat{\mathbf{e}}(\psi)\cdot \boldsymbol{l}_\mathbf{m}} e^{in(\frac{\pi}{2}-\psi)} = e^{ik(x_m \cos\psi + y_m \sin\psi)} e^{in(\frac{\pi}{2}-\psi)}. \tag{4.5}$$

A point source normalized by its amplitude at the origin is defined by (2.75). For a source at point S depicted in Figure 4.2, the coefficients $A_n^{(m)}$ follow from eq. (2.75) noting that in the local coordinates of multipole centered at O_m:

$$r' = |\mathbf{x} - \mathbf{x}'| = |\mathbf{x}_m - \mathbf{x}'_m|,$$

where $\mathbf{x}'$ is the position vector of source at point S with respect to origin O, $\mathbf{x}_m$ and $\mathbf{x}'_m$ are correspondingly the position vectors of an arbitrary point P and a source S with respect to O_m. Thus, in the neighborhood of cylinders $\mathtt{S}_m$, $A_n^{(m)}$ can be derived as

$$p^{inc} = A_0 \sum_{n=-\infty}^{\infty} U_n^+(k\mathbf{x}_m)V_n^-(k\mathbf{x}'_m) \quad \Rightarrow \quad A_n^{(m)} = A_0 V_n^-(k\mathbf{x}'_m), \tag{4.6}$$

for $m = \overline{1, M}$, $n \in \mathbb{Z}$, where the Graf's addition theorem (2.72) is used for $|\mathbf{x}_m| < |\mathbf{x}'_m|$ (see Fig. 4.2).

Considering a scattering from a single cylinder in Section 2.3, the response of cylinder $\mathtt{S}_1$ to the incident waves p^{inc} was defined by eq. (2.77) via transition matrix $\mathbf{T}$. Following this procedure and applying the boundary conditions around each cylinder $\mathtt{S}_m$, $(m = \overline{1, M})$ yield $T_{nq}^{(m)}$, the components of transition matrix $\mathbf{T}^{(m)}$ of cylinder $\mathtt{S}_m$ in isolation such that

$$B_n^{(m)} = \sum_{q=-\infty}^{\infty} T_{nq}^{(m)} A_q^{(m)}, \tag{4.7}$$

with $T_{nq}^{(m)}$ defined in Section 3.3.1 by eqs. (3.128)-(3.129), (3.128) - (3.133), (3.133), and (3.134) for an elastic multilaminate cylindrical shell and solid cylinder, as well as rigid and hollow cylinders correspondingly. Below, we will consider MS from a grating of cylinders by taking into account the full interaction between the obstacles. We shall consider a grating of M obstacles, and in a particular case, MS from two cylinders.

MS by M cylinders

Consider now an arbitrary planar configuration of M cylinders as shown in Fig. 4.1. In order to use boundary conditions on the surface of each cylinder $\mathtt{S}_m$, we will express the total field in terms of r_m and θ_m using Graf's theorem (2.72). Let $\boldsymbol{l}_{mj} = \boldsymbol{l}_m - \boldsymbol{l}_j$ be a position vector of multipole O_m with respect to multipole O_j. Since $\mathbf{x} = \boldsymbol{l}_m + \mathbf{x}_m =$

$\boldsymbol{l}_j + \mathbf{x}_j \to \mathbf{x}_m = \mathbf{x}_j + (\boldsymbol{l}_j - \boldsymbol{l}_m)$, the total field p in the neighborhood of cylinder $\mathtt{S}_j$ can be written as

$$p = \sum_{n=-\infty}^{\infty} \left\{ A_n^{(j)} U_n^+(k\mathbf{x}_j) + B_n^{(j)} V_n^+(k\mathbf{x}_j) + \sum_{\substack{m=1 \\ m\neq j}}^{M} B_n^{(m)} V_n^+\big(k(\mathbf{x}_j + \boldsymbol{l}_{jm})\big) \right\}, \tag{4.8}$$

where $\boldsymbol{l}_{jm} = \boldsymbol{l}_j - \boldsymbol{l}_m = -\boldsymbol{l}_{mj}$. Then noting the properties of $V_n^+(\mathbf{x})$, eq. (2.71), and using Graf's theorem (2.72), we obtain for $|\mathbf{x}_j| < l_j$, where $l_j = \min|\boldsymbol{l}_{jm}|$:

$$\begin{aligned}
p &= \sum_{n=-\infty}^{\infty} \left[A_n^{(j)} U_n^+(k\mathbf{x}_j) + B_n^{(j)} V_n^+(k\mathbf{x}_j) + \sum_{\substack{m=1 \\ m\neq j}}^{M} B_n^{(m)} \sum_{l=-\infty}^{\infty} U_l^+(k\mathbf{x}_j) V_{l-n}^-(k\boldsymbol{l}_{mj}) \right] \\
&= \sum_{n=-\infty}^{\infty} \left[A_n^{(j)} U_n^+(k\mathbf{x}_j) + B_n^{(j)} V_n^+(k\mathbf{x}_j) + U_n^+(k\mathbf{x}_j) \sum_{\substack{m=1 \\ m\neq j}}^{M} \sum_{l=-\infty}^{\infty} B_l^{(m)} V_{n-l}^-\big(k\boldsymbol{l}_{mj}\big) \right] \\
&= \sum_{n=-\infty}^{\infty} \left[A_n^{(j)} U_n^+(k\mathbf{x}_j) + B_n^{(j)} V_n^+(k\mathbf{x}_j) + U_n^+(k\mathbf{x}_j) \sum_{\substack{m=1 \\ m\neq j}}^{M} \sum_{l=-\infty}^{\infty} B_l^{(m)} (-1)^{n-l} V_{n-l}^-(k\boldsymbol{l}_{jm}) \right] \\
&= \sum_{n=-\infty}^{\infty} \left[A_n^{(j)} U_n^+(k\mathbf{x}_j) + B_n^{(j)} V_n^+(k\mathbf{x}_j) + U_n^+(k\mathbf{x}_j) \sum_{\substack{m=1 \\ m\neq j}}^{M} \sum_{l=-\infty}^{\infty} B_l^{(m)} V_{l-n}^+(k\boldsymbol{l}_{jm}) \right] \\
&= \sum_{n=-\infty}^{\infty} \left[B_n^{(j)} V_n^+(k\mathbf{x}_j) + A_n^{(j)} U_n^+(k\mathbf{x}_j) + U_n^+(k\mathbf{x}_j) \sum_{\substack{m=1 \\ m\neq j}}^{M} \sum_{l=-\infty}^{\infty} P_{nl}(k\boldsymbol{l}_{jm}) B_l^{(m)} \right],
\end{aligned} \tag{4.9}$$

where

$$P_{nl}(\mathbf{x}) \equiv V_{l-n}^+(\mathbf{x}). \tag{4.10}$$

Here the matrix $\mathbf{P} = [P_{nl}]$ is equal to the transpose of Martin's $\mathbf{S} = [S_{nl}]$ matrix [98], $\mathbf{P} = \mathbf{S}^T$. The total incident field impinging on the cylinder $\mathtt{S}_j$ is a sum of the last two terms on the right hand side of eq. (4.9), i.e.

$$p_{inc}^{(j)} + \sum_{\substack{m=1 \\ m\neq j}}^{M} p_{sc}^{(m)} = \sum_{n=-\infty}^{\infty} \left[A_n^{(j)} + \sum_{\substack{m=1 \\ m\neq j}}^{M} \sum_{l=-\infty}^{\infty} P_{nl}(k\boldsymbol{l}_{jm}) B_l^{(m)} \right] U_n^+(k\mathbf{x}_j). \tag{4.11}$$

The response of shell $\mathtt{S}_j$ to the incident field (4.11) can be obtained by incorporating the boundary conditions at the interface and the transition matrix elements $T_{nq}^{(j)}$ of cylinder $\mathtt{S}_j$ [177]:

$$p_{sc}^{(j)} = \sum_{n=-\infty}^{\infty} \sum_{q=-\infty}^{\infty} T_{nq}^{(j)} \left[A_q^{(j)} + \sum_{\substack{m=1 \\ m\neq j}}^{M} \sum_{l=-\infty}^{\infty} P_{ql}(k\boldsymbol{l}_{jm}) B_l^{(m)} \right] V_n^+(k\mathbf{x}_j). \tag{4.12}$$

Thus, eqs. (4.4) and (4.12) yield a linear system of equations

$$B_n^{(j)} - \sum_{q=-\infty}^{\infty} T_{nq}^{(j)} \sum_{\substack{m=1 \\ m\neq j}}^{M} \sum_{l=-\infty}^{\infty} P_{ql}(k\boldsymbol{l}_{jm}) B_l^{(m)} = \sum_{q=-\infty}^{\infty} T_{nq}^{(j)} A_q^{(j)}, \quad n \in \mathbb{Z}, \tag{4.13}$$

where $T_{nq}^{(j)}$ is the component of the transition matrix of cylinder $\mathtt{S}_j$ in isolation defined in Section 3.3.1.

Equivalently,

$$\sum_{m=1}^{M} \sum_{l=-\infty}^{\infty} X_{jnml} B_l^{(m)} = \sum_{q=-\infty}^{\infty} T_{nq}^{(j)} A_q^{(j)}, \quad j = \overline{1, M}, \quad n \in \mathbb{Z}, \tag{4.14a}$$

$$X_{jnml} = \begin{cases} \delta_{nl}, & m = j, \\ -\sum\limits_{q=-\infty}^{\infty} T_{nq}^{(j)} P_{ql}(k\boldsymbol{l}_{jm}), & m \neq j. \end{cases} \tag{4.14b}$$

Consider now a truncated version of the infinite sum in equation (4.14a) that yields an algebraic system of equations with finite dimensions :

$$\sum_{m=1}^{M} \sum_{l=-N}^{N} X_{jnml} B_l^{(m)} = \sum_{q=-N}^{N} T_{nq}^{(j)} A_q^{(j)}, \quad j = \overline{1, M}, \quad n \in \mathbb{Z}, \tag{4.15}$$

or in a matrix form

$$\mathbb{X}\,\mathbf{b} = \mathbf{d}, \tag{4.16}$$

where

$$\mathbb{X} = \begin{bmatrix} \mathbf{I} & -\mathbf{T}^{(1)}\mathbf{P}^{1,2} & -\mathbf{T}^{(1)}\mathbf{P}^{1,3} & \dots & -\mathbf{T}^{(1)}\mathbf{P}^{1,M} \\ -\mathbf{T}^{(2)}\mathbf{P}^{2,1} & \mathbf{I} & -\mathbf{T}^{(2)}\mathbf{P}^{2,3} & \dots & -\mathbf{T}^{(2)}\mathbf{P}^{2,M} \\ \vdots & \vdots & \vdots & \ddots & \vdots \\ -\mathbf{T}^{(M)}\mathbf{P}^{M,1} & -\mathbf{T}^{(M)}\mathbf{P}^{M,2} & -\mathbf{T}^{(M)}\mathbf{P}^{M,3} & \dots & \mathbf{I} \end{bmatrix}, \tag{4.17}$$

and $\mathbf{b}$ is a vector of unknown coefficients:

$$\mathbf{b} = \begin{pmatrix} \mathbf{b}^{(1)} \\ \mathbf{b}^{(2)} \\ \vdots \\ \mathbf{b}^{(M)} \end{pmatrix}, \quad \mathbf{b}^{(j)} = \begin{pmatrix} B_{-N}^{(j)} \\ B_{-N+1}^{(j)} \\ \vdots \\ B_{N}^{(j)} \end{pmatrix}, \quad (j = \overline{1, M}) \tag{4.18}$$

$$\mathbf{d} = \begin{pmatrix} \mathbf{d}^{(1)} \\ \mathbf{d}^{(2)} \\ \vdots \\ \mathbf{d}^{(M)} \end{pmatrix} = \begin{pmatrix} \mathbf{T}^{(1)}\mathbf{a}^{(1)} \\ \mathbf{T}^{(2)}\mathbf{a}^{(2)} \\ \vdots \\ \mathbf{T}^{(M)}\mathbf{a}^{(M)} \end{pmatrix}, \quad \mathbf{a}^{(j)} = \begin{pmatrix} A_{-N}^{(j)} \\ A_{-N+1}^{(j)} \\ \vdots \\ A_{N}^{(j)} \end{pmatrix}, (j = \overline{1, M}) \tag{4.19}$$

where $\mathbf{T}^{(j)}$ is defined in Section 3.3.1. In eq. (4.17), $\mathbf{P}^{j,m} = \left[\mathbf{P}_{ql}^{j,m}\right]$, $(q, l \in \mathbb{Z})$ where $\mathbf{P}_{ql}^{j,m} = V_{l-q}^{+}(k\boldsymbol{l}_{jm}), (q = -\overline{N_j, N_j}, l = -\overline{N_m, N_m}),\ (j, m = \overline{1, M}, j \neq m)$.

Example: MS from two cylinders

Consider two arbitrarily located cylinders $\mathtt{S}_1$ and $\mathtt{S}_2$, in this case $M = 2$. Using Graf's theorem (2.72) and the components of transition matrix $\mathbf{T}^{(m)}$ of cylinder $\mathtt{S}_m, (m = 1, 2)$ in isolation, we find the response of each cylinder to incident field:

$$p_{sc}^{(1)} = \sum_{n=-\infty}^{\infty} \sum_{q=-\infty}^{\infty} T_{nq}^{(1)} \left[A_q^{(1)} + \sum_{l=-\infty}^{\infty} P_{ql}(k\boldsymbol{l}_{12}) B_l^{(2)} \right] V_n^{+}(k\mathbf{x}_1), \tag{4.20a}$$

$$p_{sc}^{(2)} = \sum_{n=-\infty}^{\infty} \sum_{q=-\infty}^{\infty} T_{nq}^{(2)} \left[A_q^{(2)} + \sum_{l=-\infty}^{\infty} P_{ql}(k\boldsymbol{l}_{21}) B_l^{(1)} \right] V_n^{+}(k\mathbf{x}_2), \tag{4.20b}$$

where $\boldsymbol{l}_{12} = \boldsymbol{l}_1 - \boldsymbol{l}_2 = -\boldsymbol{l}_{21}$ is the position vector of multipole O_1 with respect to O_2, and $P_{ql}(\mathbf{r})$ is defined by eq. (4.10). Thus, the system of equations (4.13) now reduces to:

$$B_n^{(1)} = \sum_{q=-\infty}^{\infty} T_{nq}^{(1)} \left[A_q^{(1)} + \sum_{l=-\infty}^{\infty} P_{ql}(k\boldsymbol{l}_{12}) B_l^{(2)} \right], \tag{4.21a}$$

$$B_n^{(2)} = \sum_{q=-\infty}^{\infty} T_{nq}^{(2)} \left[A_q^{(2)} + \sum_{l=-\infty}^{\infty} P_{ql}(k\boldsymbol{l}_{21}) B_l^{(1)} \right]. \tag{4.21b}$$

where $T_{nq}^{(m)}, (m = 1, 2)$ is defined in Section 3.3.1 for different cylindrical structures.

Far-field radiated response

Consider now farfield response, the scattered pressure field p^{sc} , when kr becomes very large: $kr >> 1$. The scattered field p^{sc} is defined by eq. (4.3) as an infinite sum at the center of multipoles, $\mathbf{x}_m$. To find far-field behavior of p^{sc}, we will write it in terms of position vector $\mathbf{x}$. Introducing eqs. (4.2), (2.70) and (3.139) into eq. (4.3) and incorporating the Graf's theorem (2.72) for $|\mathbf{x}| >> |\boldsymbol{l}_m|$ yields

$$p^{sc} = \sum_{m=1}^{M} \sum_{n=-\infty}^{\infty} B_n^{(m)} V_n^{+}\big(k(\mathbf{x}-\boldsymbol{l}_m)\big) = \sum_{m=1}^{M} \sum_{n=-\infty}^{\infty} B_n^{(m)} \sum_{l=-\infty}^{\infty} V_l^{+}(k\mathbf{x}) U_{l-n}^{-}(k\boldsymbol{l}_m), \text{ or} \tag{4.22}$$

$$p^{sc} = \sum_{m=1}^{M} \sum_{n=-\infty}^{\infty} B_n^{(m)} V_n^{+}\big(k(\mathbf{x}-\boldsymbol{l}_m)\big) = \sum_{n=-\infty}^{\infty} F_n V_n^{+}(k\mathbf{x}), \tag{4.23}$$

where

$$F_n = \sum_{m=1}^{M} \sum_{l=-\infty}^{\infty} B_l^{(m)} U_{n-l}^{-}(k\boldsymbol{l}_m). \tag{4.24}$$

Using the asymptotic expansion of the Hankel function for large values of argument, eq. (3.139), the far scattered field p^{sc} can be split into two parts, $g(k|\mathbf{x}|)$ and $f^M(\theta)$:

$$p^{sc} = g(k|\mathbf{x}|) f^M(\theta)\Big[1 + O\Big(\frac{1}{k|\mathbf{x}|}\Big)\Big], \tag{4.25}$$

where the function $g(k|\mathbf{x}|)$ is defined by eq. (3.141) and the far-field amplitude function $f^M(\theta)$, has the form :

$$f^M(\theta) = \sqrt{\frac{2}{\pi}} e^{-i\frac{\pi}{4}} \sum_{n=-\infty}^{\infty} \sum_{m=1}^{M} B_n^{(m)} \sum_{l=-\infty}^{\infty} J_{l-n}(k|\boldsymbol{l}_m|) e^{il\left(\theta - \arg \boldsymbol{l}_m - \frac{\pi}{2}\right)} e^{in \arg \boldsymbol{l}_m}, \text{ or} \tag{4.26}$$

$$f^M(\theta) = \sum_{n=-\infty}^{\infty} f_n e^{in\theta}, \qquad f_n = \sqrt{\frac{2}{\pi}} e^{-i\left(\frac{\pi}{4} + \frac{n\pi}{2}\right)} F_n, \tag{4.27}$$

with $\theta = \arg(\mathbf{x})$.

The total power radiated by the grating of cylinders is measured by the non-negative far-field flux parameter

$$\sigma_r = \int_0^{2\pi} |f^M(\theta)|^2 \, \mathrm{d}\, \theta = 4 \sum_{n=-\infty}^{\infty} |F_n|^2. \tag{4.28}$$

Then, for a configuration of cylinders with the radii $a_m = a$, the non-dimensional total scattering cross section is given by:

$$Q = \frac{4}{k\,a} \sum_{n=-\infty}^{\infty} |F_n|^2. \tag{4.29}$$

4.1.2 Numerical results: small M and k

In this section, we illustrate our numerical results based on MST. The computations are performed on Matlab for different configurations depicted in Figures 4.3 and 4.7 at small M and k. In Figure 4.3, d denotes the distance between the centers of two cylinders, which we also call the cylinder center-to-center spacing. The far-field amplitude function $f^M(\theta)$ is defined by eq. (4.27). Figure 4.4 illustrates the angular distribution of form function for 2 soft cylinders in water at the angle of wave incidence $\psi = -90\,^\circ$; the configuration is depicted in Figure a. Figure a represents Scharstein's results [144]. Figure b is our Matlab result based on the MST and given for comparison with findings in [144]. Plots in Figures a and b show a full correspondence and confirm our theoretical prediction.

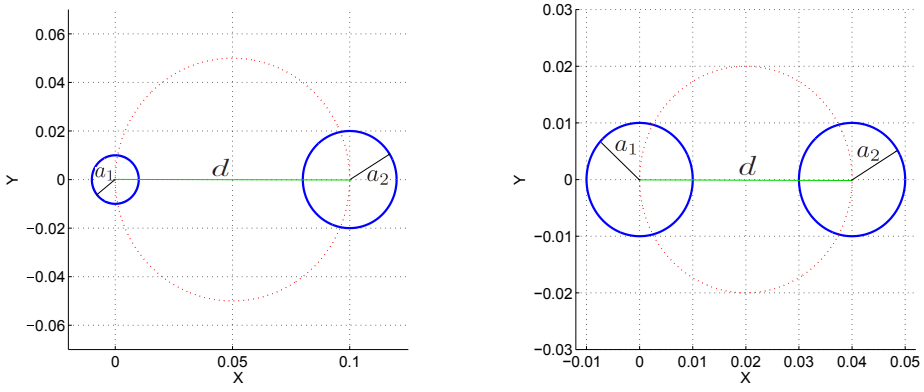

(a) $a_2 = 2a_1$, $d = 10a_1$ [144] **(b)** $a_1 = a_2$, $d = 4a_1$ [71]

Figure 4.3: Configuration of 2 cylinders on the ring. The left-hand side and the right-hand side pictures illustrate configurations considered in [144] and [71] correspondingly. Here d is the distance between the centers of the two cylinders.

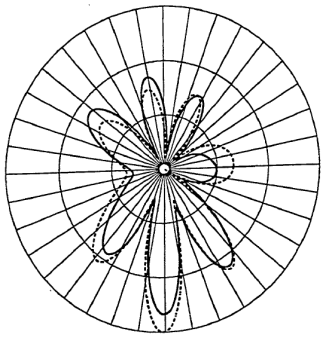

(a) solid line-accurate, dashed line-uncoupled, results provided in [144]

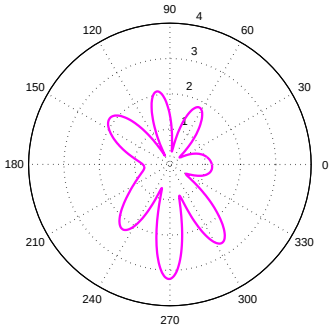

(b) Our result, 2D Elasticity solution

Figure 4.4: The angular distribution of the form function for 2 soft cylinders, $ka_1 = 1$, $ka_2 = 2$, $kd = 10$

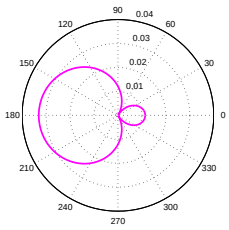

(a) $ka = 0.1$, $\psi = 0^o$

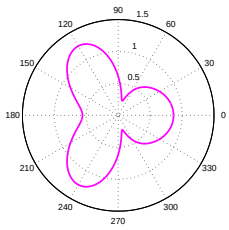

(b) $ka = 1$, $\psi = 0^o$

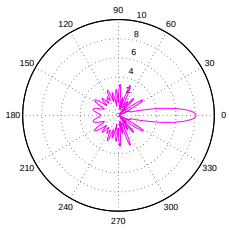

(c) $ka = 10$, $\psi = 0^o$

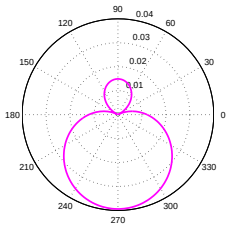

(d) $ka = 0.1$, $\psi = 90^o$

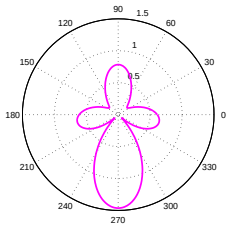

(e) $ka = 1$, $\psi = 90^o$

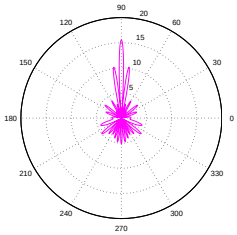

(f) $ka = 10$, $\psi = 90^o$

Figure 4.5: The angular distribution of the far-field amplitude function $|f(\theta)|$ at fixed values of ka for a rigid cylinder submerged in fluid

Figures 4.5 and 4.6 display the angular distribution of the far-field form function $|f(\theta)|$at fixed values of $ka = 0.1, 1, 10$ for the configuration of two rigid cylinders immersed in water (see Figure b). The polar plots show a good agreement between our theoretical predictions depicted in Figure 4.5 and findings given in [71], shown in

Figure 4.6.

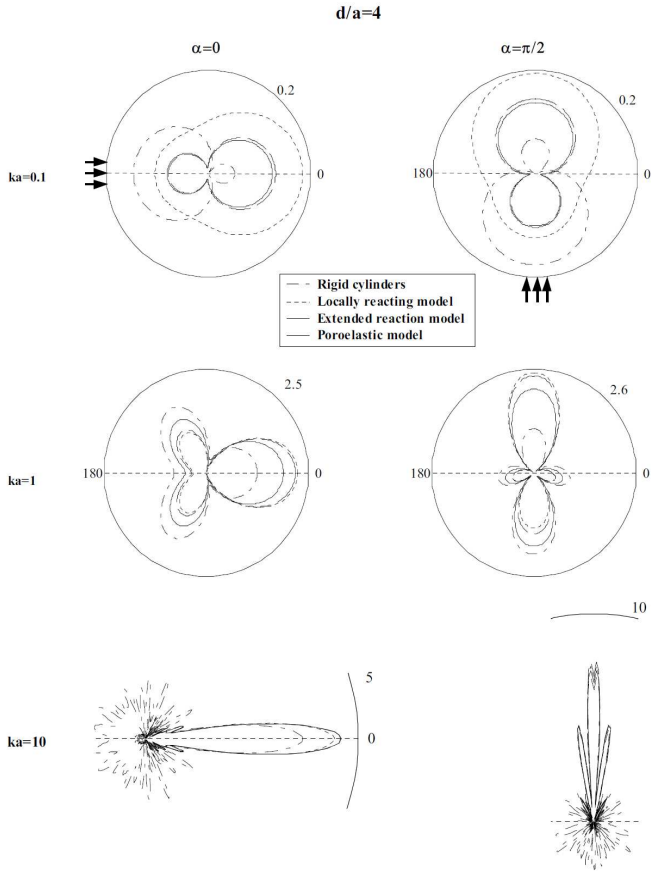

Figure 4.6: The angular distribution of the form function amplitude for end-on and broadside incidence upon a pair of cylinders with $d = 4a_1$ at selected non-dimensional frequencies given in [71].

Material	ρ $[kg/m^3]$	c_p $[m/s]$
Aluminum (Al)	2700	6420

Table 4.1: Material properties used for comparison.

Now let us consider some applications of MST. Specifically, we design waveguides and resonators as an arrangement of empty thin aluminum shells and active tuned shells [162, 163]. Shells have mechanical properties depicted in Table 4.1 In our calculations, an active shell is a thin shell with 16 springs and a mass attached inside. Figure 4.8

depicts an active thin shell with 2 springs and mass attached. It can be tuned by selecting the shell thickness, spring stiffness and added mass, and matching its impedance to the impedance of water. The T matrix for an active shell is derived in [163]. Figures 4.9 and 4.10 illustrate the absolute pressure field for a planar configuration of cylinders at selected values of nondimensional frequency $ka = 0.2, 0.3, 0.4, 0.5$. White colored cylinders correspond to empty thin aluminum shells of thickness $h = 0.025a$, and pink colored cylinders correspond to the impedance matched shells of the same thickness with 16 springs and a mass attached inside. Figures a, b, a and b correspond to case $M = 104$, when devices are inactive, Figures c, d, c and d show active devices ($M = 104$), and Figures e, f, e and f show the total field for a waveguide ($M = 80$). Analyzing the total field around the configuration, we can notice that active shells act as water. Pictures for a total field around a waveguide and a configuration with active shells are almost identical. Thus, by switching "ON" certain shells in the slab, the configuration becomes effectively open and acts as a waveguide.

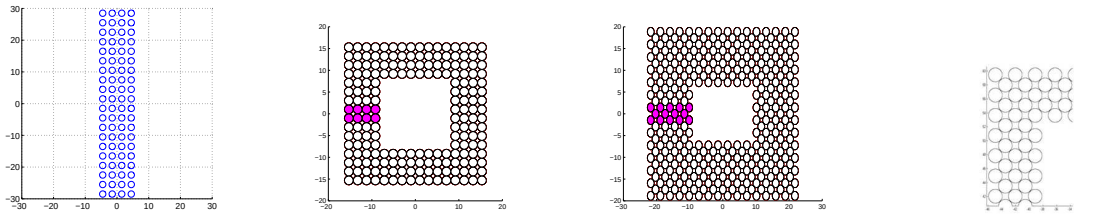

(a) M=80 **(b)** M=192 **(c)** M=360 **(d)** Sublayers

Figure 4.7: The configurations of cylinders: a waveguide slab and Helmholtz resonator.

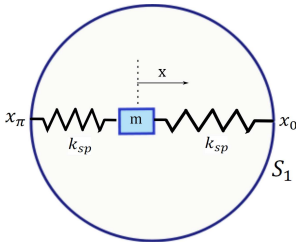

Figure 4.8: A schematic of a shell-spring-mass configuration S_1 with 2 springs and mass attached inside the thin shell.

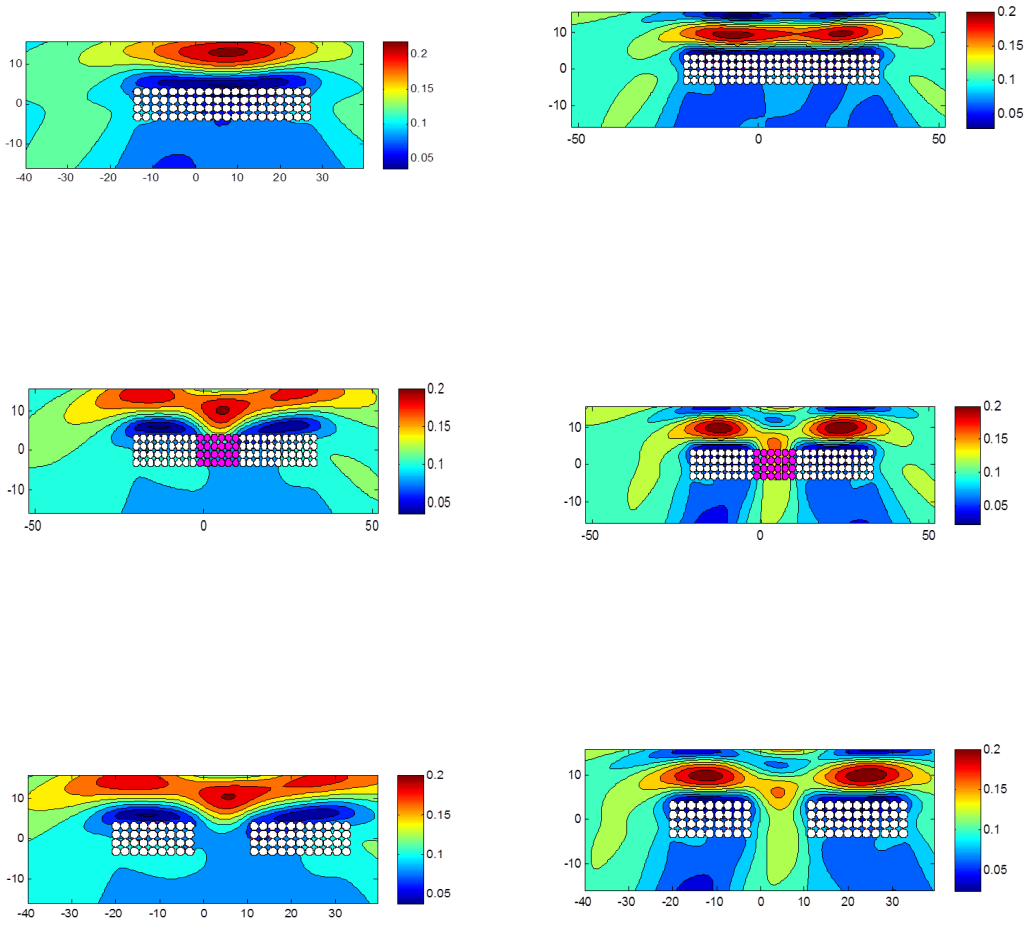

(e) Waveguide, $M = 80$, $ka = 0.2$ **(f)** Waveguide, $M = 80, ka = 0.3$

Figure 4.9: The absolute value of the pressure field for $N = 3$ at selected values of $ka = 0.2, 0.3$ when devices are inactive (a) and (b), and active (c) and (d), and for waveguide (e) and (f). White colored cylinders correspond to empty thin aluminum shells of thickness $h = 0.025a$, and pink colored cylinders correspond to tuned active shells

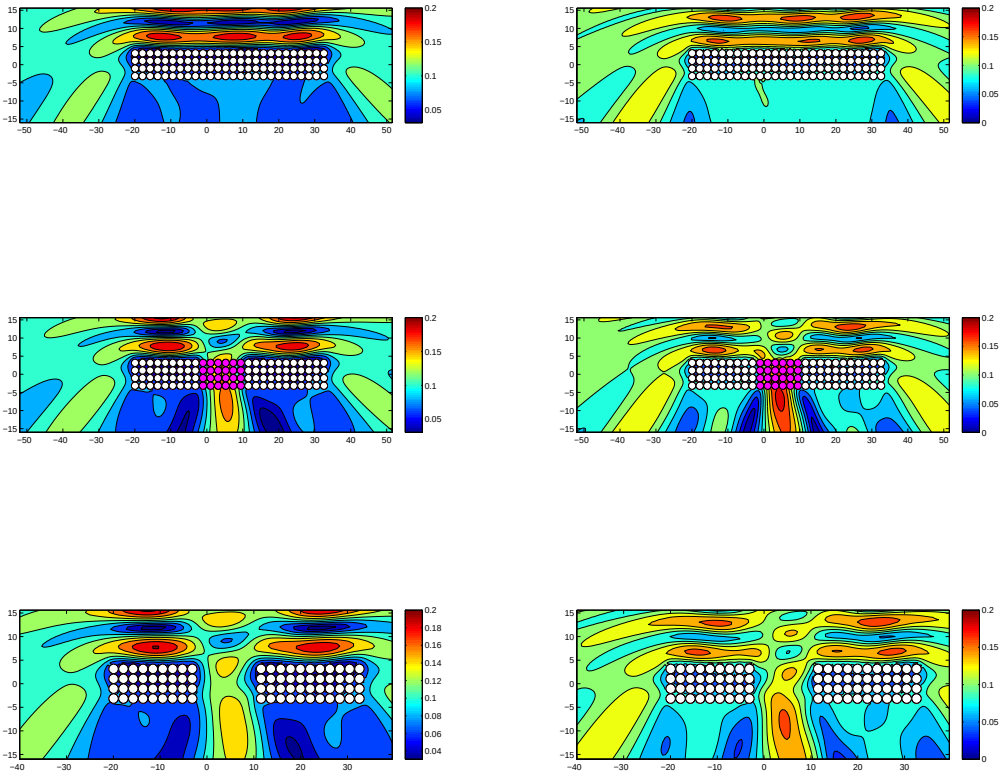

(e) Waveguide, $M = 80$ **(f)** Waveguide, $M = 80$

Figure 4.10: The absolute value of the pressure field for $N = 3$ for selected values of $ka = 0.4, 0.5$ when devices are inactive (a) and (b), and active (c) and (d), and for waveguide (e) and (f). White colored cylinders correspond to empty thin aluminum shells of thickness $h = 0.025a$, and pink colored cylinders correspond to tuned active shells.

Consider now another planar configuration of shells arranged in a closed rectangular frame shown in Figures b-c. The individual shells of these arrangements can be hidden in water by optimizing the spring-mass parameters. By switching "ON" certain shells in a rectangular frame, the frame can be effectively open and produce an effect of the Helmholtz resonator. Figures 4.11 and 4.12 illustrate the absolute total pressure field for a such configuration at $ka = 0.2$. The pressure field is excited by the source located at $(X_p, Y_p) = (-500, 500)$. White colored cylinders correspond to empty thin

aluminum shells of thickness $h = 0.025a$, and pink colored cylinders correspond to the impedance matched shells of the same thickness with 16 springs and a mass attached inside. Figures a and b illustrate correspondingly a resonator implemented with $M = 96$ thin shells and a resonator-like device constructed with $M = 104$ shells.

Figures a and b show identical behavior, similarly Figures a and b are alike and have a full correspondence. An arrangement of active and passive (empty) shells produces equal total field amplitudes. When all shells are active, i.e. the device is switched "ON" (see Figure c), the scattering amplitude is very low and equivalent to the amplitude of the incident field excited by the source p_s. When the switch is "OFF" (see Figure c), the amplitude is high.

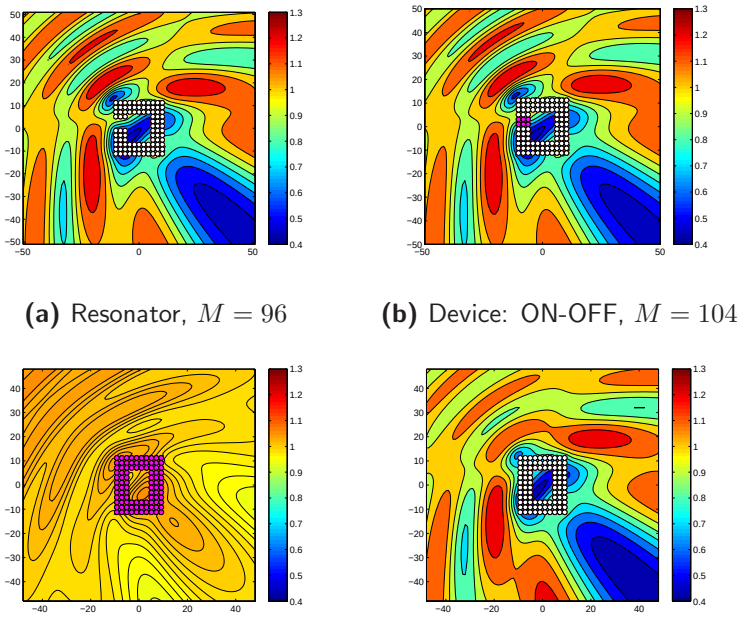

(a) Resonator, $M = 96$ **(b)** Device: ON-OFF, $M = 104$

(c) Device: all ON, $M = 104$ **(d)** Device: all OFF, $M = 104$

Figure 4.11: The absolute value of the normalized total pressure field amplitude $\left|\frac{p(\mathbf{x})}{p_s(\mathbf{0})}\right|$ at $ka = 0.2$ with $N = 2$, for a planar configuration of $M = 96$ and $M = 104$ shells excited by the source located at $(X_p, Y_p) = (-500, 500)$. White colored cylinders correspond to empty thin aluminum shells of thickness $h = 0.025a$, and pink colored cylinders correspond to tuned active shells.

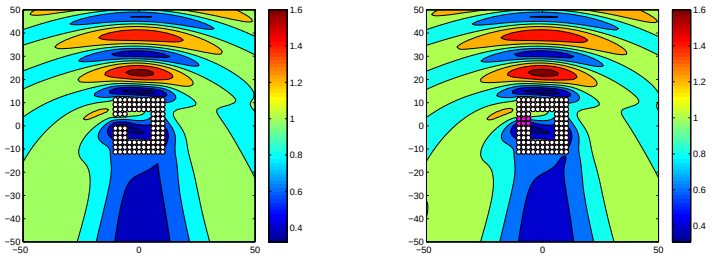

(a) Resonator, $M = 96$ **(b)** Device ON-OFF, $M = 104$

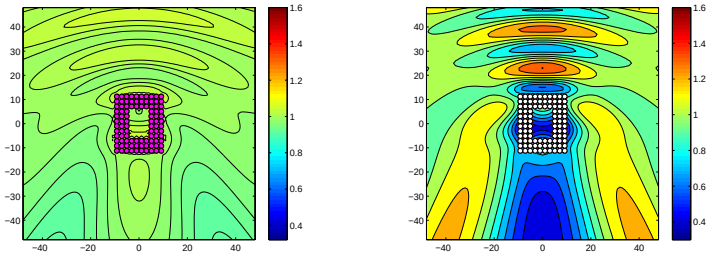

(c) Device ON, $M = 104$ **(d)** Device OFF, $M = 104$

Figure 4.12: The absolute value of the normalized total pressure field amplitude $\left|\frac{p(\mathbf{x})}{p_s(\mathbf{0})}\right|$ at $ka = 0.2$ with $N = 2$, for a planar configuration of $M = 96$ and $M = 104$ shells excited by the source located at $(X_p, Y_p) = (-1, 500)$. White colored cylinders correspond to empty thin aluminum shells of thickness $h = 0.025a$, and pink colored cylinders correspond to tuned active shells.

The total pressure field around the configurations given in Figures a - b

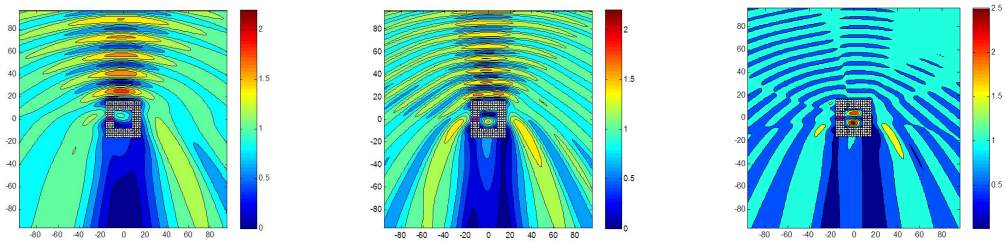

(a) $ka = 0.2$, $M = 192$ **(b)** $ka = 0.3$, $M = 192$ **(c)** $ka = 0.4$, $M = 192$

Figure 4.13: The absolute value of the normalized total pressure field amplitude $\left|\frac{p(\mathbf{x})}{p_s(\mathbf{0})}\right|$ for $N = 3$ and at selected nondimensional frequencies $ka = 0.2$, 0.3, 0.4, for a resonator, an arrangement of empty and active shells ($M = 192$).

Figure 4.13 illustrates the absolute value of the normalized total pressure field amplitude $\left|\frac{p(\mathbf{x})}{p_s(\mathbf{0})}\right|$ for a configuration of $M = 192$ shells at selected frequencies $ka = 0.2, 0.3, 0.4$ with $N = 3$. At $ka = 0.4$, the total field amplitude inside the frame is much higher than the field outside the frame.

To find the resonance frequencies at which the arrangement acts as resonator, the variation of the backscattering form function and the total scattering cross-section with wavenumber ka is evaluated for an arrangement of active and empty shells ($M = 360$, $N = 3$) and shown in Figure 4.14. Calculations are performed for the configuration, shown in Figure c, with $M = 360$, $N = 3$. The field around and inside the frame is excited by the source p_s located at the point $(-1000a, 1000a)$.

Figure 4.15 represents the absolute value and real part of the normalized scattered pressure field $\frac{p_{sc}(\mathbf{x})}{p_s(\mathbf{0})}$ for an arrangement shown in Figure c at selected resonance frequencies depicted in Figure 4.12. In Figure 4.15, the gray color corresponds to the field amplitude greater than 1, and the black color to the amplitude smaller than -1. Figures show that at resonance frequencies, the frame acts as a resonator resembling the dynamical behavior of two interacting dipoles.

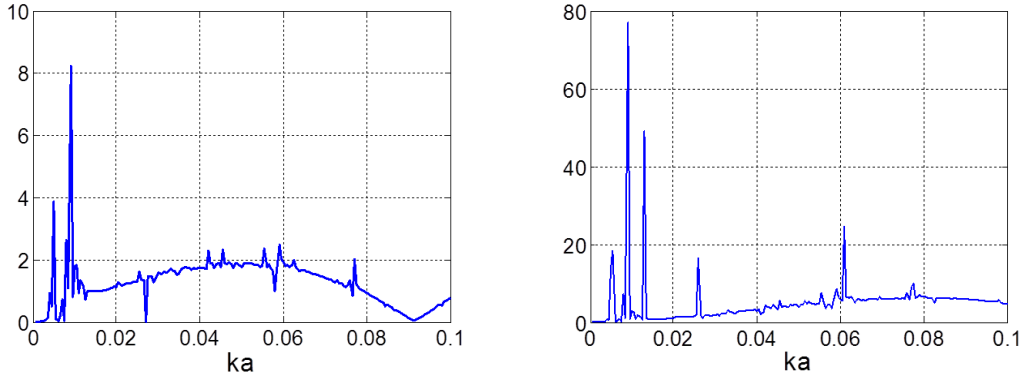

(a) Form function vs. ka **(b)** TSCS vs. ka

Figure 4.14: The backscattering form function and the total scattering cross-section versus wavenumber ka for a planar configuration of $M = 360$ aluminum cylinders of radius a, excited by the source p_s located at $(X_p, Y_p) = (-1000a, 1000a)$.

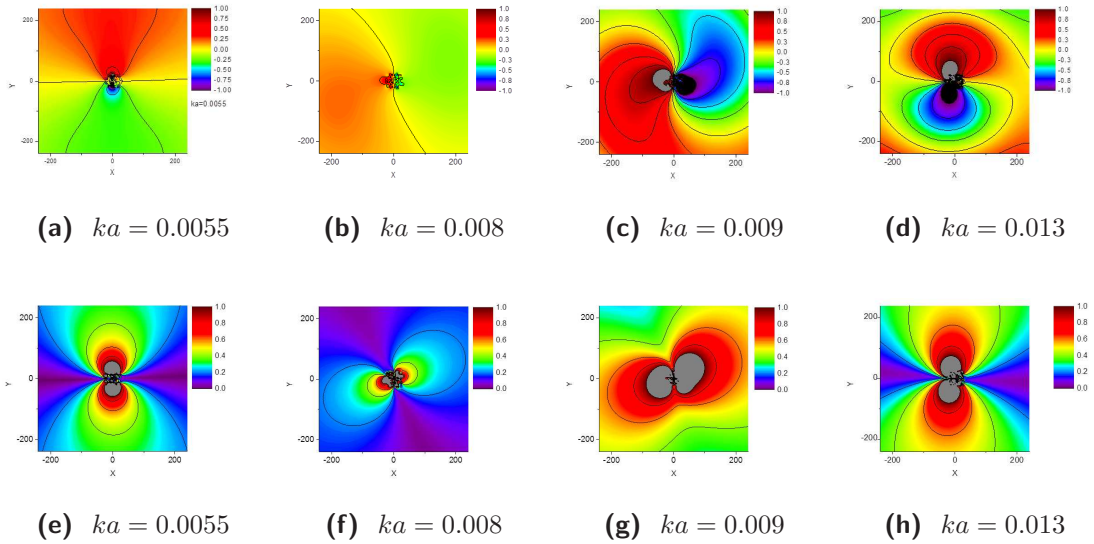

(a) $ka = 0.0055$ **(b)** $ka = 0.008$ **(c)** $ka = 0.009$ **(d)** $ka = 0.013$

(e) $ka = 0.0055$ **(f)** $ka = 0.008$ **(g)** $ka = 0.009$ **(h)** $ka = 0.013$

Figure 4.15: The absolute value and real part of the normalized scattered pressure field amplitudes at selected resonance frequencies with $N = 3$ for a resonator, a planar configuration of $M = 360$ shells excited by the source located at $(X_p, Y_p) = (-1000, 1000)$. The top row figures represent $Re\left(\frac{p_{sc}(\mathbf{x})}{p_s(0)}\right)$, and the bottom row figures depict $\left|\frac{p_{sc}(\mathbf{x})}{p_s(0)}\right|$.

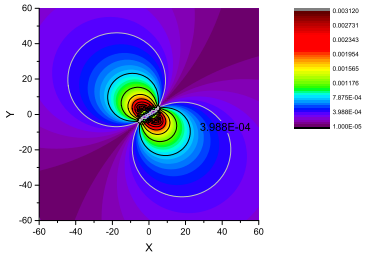

Figure 4.16: The absolute value of the normalized total pressure field amplitude $\left|\frac{p(\mathbf{x})}{p_s(\mathbf{0})}\right|$ for $N = 2$ and at the resonance frequency $ka = 0.007$, for a planar configuration of 4 rows and 5 columns of shells ($M = 20$).

Figure 4.16 illustrates the absolute value of the normalized total pressure field amplitude $\left|\frac{p(\mathbf{x})}{p_s(\mathbf{0})}\right|$ at the resonance frequency $ka = 0.007$ and $N = 2$, for a planar configuration of 4 rows and 5 columns of shells ($M = 20$). The dipole behavior of the structure is noticed again. The structure acts as a dipole oscillating in the direction of the source (45° from the origin).

4.2 Elastic Multiple Scattering and Radiation from Planar Configuration of Parallel Cylindrical Shells

In this section, we study elastic multiple scattering and radiation from a cluster of cylinders situated in elastic media, including wave mode conversion and a full interaction between the cylinders.

4.2.1 Elastic multiple scattering theory

Formulation of problem: P/SV in-plane wave propagation

Consider an elastic multiple scattering by an arbitrary grating of M obstacles $\mathtt{S}_m, (m = \overline{1, M})$ of cylindrical shape. In general, each obstacle may have no rotational symmetry. We will refer to obstacles simply as cylinders, but this may include hollow, rigid, and elastic solid cylinders of outer radii a_m, as well as thin and thick cylindrical shells of outer a_m and inner b_m radii with and without attachments inside the shells. Let $\mathbf{x} = (x, y)$ be a position vector of a typical point in two-dimensional Cartesian coordinates with origin at O, and let us define plane polar coordinates (r_m, θ_m) at the centers O_m. An arbitrary planar configuration of shells is given in Fig. 4.1. Assume that the $\mathtt{S}_m, (m = \overline{1, M})$ cylinders have different physical properties and are located at the centers O_m, at $\mathbf{x} = \boldsymbol{l}_m$, the distance $|\boldsymbol{l}_m|$ from the origin O (see Fig. 4.1).

The governing equations are Navier's equations (2.78) in two dimensions for the displacement $\mathbf{u} = (u_1, u_2)$, $u_j = u_j(x_1, x_2)$. The Helmholtz decomposition (2.56) for the displacement $\mathbf{u}$ leads to separate Helmholtz equations (2.80) for the scalar potentials φ and ψ. We decompose the total displacement field $\mathbf{u}$ as a sum of incident field $\mathbf{u}^{inc}$ and scattered field $\mathbf{u}^{sc}$ such that eq. (2.79) holds. We assume the general form of incident field potentials ϕ^{inc}, ψ^{inc} in the regular basis. The total scattered field potentials ϕ^{sc}, ψ^{sc} can be found as a superposition of the scattered fields by all obstacles

in the configuration, and hence, in the neighbourhood of each cylinder, we have

$$\begin{pmatrix} \phi^{inc} \\ \psi^{inc} \end{pmatrix} = \sum_{n=-\infty}^{\infty} \begin{pmatrix} A_{p,\,n}^{(m)} U_n^+(k\mathbf{x}_m) \\ A_{s,\,n}^{(m)} U_n^+(K\mathbf{x}_m) \end{pmatrix}, \tag{4.30a}$$

$$\begin{pmatrix} \phi^{sc} \\ \psi^{sc} \end{pmatrix} = \sum_{m=1}^{M} \begin{pmatrix} \Phi_{sc}^{(m)} \\ \Psi_{sc}^{(m)} \end{pmatrix} = \sum_{m=1}^{M} \sum_{n=-\infty}^{\infty} \begin{pmatrix} B_{p,\,n}^{(m)} V_n^+(k\mathbf{x}_m) \\ B_{s,\,n}^{(m)} V_n^+(K\mathbf{x}_m) \end{pmatrix}, \tag{4.30b}$$

where $\mathbf{x}_m$ is a position vector of point P with respect to the centers of multipoles at O_m (see Figure 4.1) and given by eq. (4.2); the functions $U_n^{\pm}(\mathbf{z})$ and $V_n^{\pm}(\mathbf{z})$ are defined by eqs. (2.66) and (2.70) respectively. The scattered field potentials Φ^{sc} and Ψ^{sc} can be expressed as the sum of multipoles at the origin using the generalized Graf's addition theorem given by eq. (2.66).

The response of each cylinder $\mathtt{S}_m$ to incident elastic waves can be defined by its transition matrix $\mathbf{T}^{(m)}$. Applying boundary conditions and evaluating the displacement and stress field around cylinder $\mathtt{S}_m$ yields the transition matrix $\mathbf{T}^{(m)}$ of cylinder $\mathtt{S}_m$ in isolation, such that

$$\begin{pmatrix} B_{p,\,n}^{(m)} \\ B_{s,\,n}^{(m)} \end{pmatrix} = \sum_{q=-\infty}^{\infty} \begin{pmatrix} T_{nq}^{pp(m)} & T_{nq}^{ps(m)} \\ T_{nq}^{sp(m)} & T_{nq}^{ss(m)} \end{pmatrix} \begin{pmatrix} A_{p,\,q}^{(m)} \\ A_{s,\,q}^{(m)} \end{pmatrix}, \tag{4.31}$$

where the submatrices of the transition matrix, $T_{nq}^{\varsigma\xi(m)}$ $(\varsigma, \xi \equiv p, s)$, are obtained considering P and SV wave incidences separately and given in Section 3.3.2 for cylindrical multilaminate structure, and can be reduced to use for a solid cylinder, or thin or thick shell. In general, for obstacles with no rotational symmetry, the blocks $T_{nq}^{\varsigma\xi(m)}$ $(\varsigma, \xi \equiv p, s)$ are nondiagonal; for cylinders with a rotational symmetry, $T_{nq}^{\varsigma\xi(m)}$ are diagonal.

MS by M cylinders

Consider now an arbitrary planar configuration of M cylinders as shown in Fig. 4.1. In order to use boundary conditions on the surface of each cylinder $\mathtt{S}_m$, we will express the total field in terms of r_m and θ_m using Graf's theorem (2.72). Let $\boldsymbol{l}_{mj} = \boldsymbol{l}_m - \boldsymbol{l}_j$ be a position vector of multipole O_m with respect to multipole O_j. Since $\mathbf{x} = \boldsymbol{l}_m + \mathbf{x}_m =$

$\boldsymbol{l}_j + \mathbf{x}_j \rightarrow \mathbf{x}_m = \mathbf{x}_j + (\boldsymbol{l}_j - \boldsymbol{l}_m)$, in the neighborhood of cylinder $\mathtt{S}_j$ the total field potentials ϕ and ψ can be written as

$$\begin{pmatrix}\phi\\ \psi\end{pmatrix} = \sum_{n=-\infty}^{\infty}\left\{\begin{pmatrix}A_{p,n}^{(j)}U_n^+(k\mathbf{x}_j)\delta_{ip} + B_{p,n}^{(j)}V_n^+(k\mathbf{x}_j)\\ A_{s,n}^{(j)}U_n^+(K\mathbf{x}_j)\delta_{is} + B_{s,n}^{(j)}V_n^+(K\mathbf{x}_j)\end{pmatrix} + \sum_{\substack{m=1\\ m\neq j}}^{M}\begin{pmatrix}B_{p,n}^{(m)}V_n^+(k(\mathbf{x}_j+\boldsymbol{l}_{jm}))\\ B_{s,n}^{(m)}V_n^+(K(\mathbf{x}_j+\boldsymbol{l}_{jm}))\end{pmatrix}\right\}, \tag{4.32}$$

where δ_{ip} and δ_{is} are the Kronecker deltas, with $i = p$ for P wave incidence and $i = s$ for SV wave incidence, and $\boldsymbol{l}_{jm} = \boldsymbol{l}_j - \boldsymbol{l}_m = -\boldsymbol{l}_{mj}$. Then noting the properties of $V_n^+(\mathbf{x})$, eq. (2.71), and using Graf's theorem, we obtain for $|\mathbf{x}_j| < l_j$, where $l_j = \min|\boldsymbol{l}_{jm}|$:

$$\begin{aligned}\begin{pmatrix}\phi\\ \psi\end{pmatrix} &= \sum_{n=-\infty}^{\infty}\left\{\begin{pmatrix}A_{p,n}^{(j)}U_n^+(k\mathbf{x}_j)\delta_{ip} + B_{p,n}^{(j)}V_n^+(k\mathbf{x}_j)\\ A_{s,n}^{(j)}U_n^+(K\mathbf{x}_j)\delta_{is} + B_{s,n}^{(j)}V_n^+(K\mathbf{x}_j)\end{pmatrix}\right.\\ &\quad\left. + \sum_{\substack{m=1\\ m\neq j}}^{M}\begin{pmatrix}B_{p,n}^{(m)}\sum_{l=-\infty}^{\infty}U_l^+(k\,\mathbf{x}_j)V_{l-n}^-(k\boldsymbol{l}_{jm}))\\ B_{s,n}^{(m)}\sum_{l=-\infty}^{\infty}U_l^+(K\,\mathbf{x}_j)V_{l-n}^-(K\boldsymbol{l}_{jm}))\end{pmatrix}\right\}\\ &= \sum_{n=-\infty}^{\infty}\left\{\begin{pmatrix}A_{p,n}^{(j)}U_n^+(k\mathbf{x}_j)\delta_{ip} + B_{p,n}^{(j)}V_n^+(k\mathbf{x}_j)\\ A_{s,n}^{(j)}U_n^+(K\mathbf{x}_j)\delta_{is} + B_{s,n}^{(j)}V_n^+(K\mathbf{x}_j)\end{pmatrix}\right.\\ &\quad\left. + \begin{pmatrix}U_n^+(k\mathbf{x}_j)\sum_{\substack{m=1\\ m\neq j}}^{M}\sum_{l=-\infty}^{\infty}B_{p,l}^{(m)}V_{n-l}^-(k\boldsymbol{l}_{mj})\\ U_n^+(K\mathbf{x}_j)\sum_{\substack{m=1\\ m\neq j}}^{M}\sum_{l=-\infty}^{\infty}B_{s,l}^{(m)}V_{n-l}^-(K\boldsymbol{l}_{mj})\end{pmatrix}\right\}\\ &= \sum_{n=-\infty}^{\infty}\left\{\begin{pmatrix}B_{p,n}^{(j)}V_n^+(k\mathbf{x}_j)\\ B_{s,n}^{(j)}V_n^+(K\mathbf{x}_j)\end{pmatrix}\right.\\ &\quad\left. + \begin{pmatrix}A_{p,n}^{(j)}U_n^+(k\mathbf{x}_j)\delta_{ip} + U_n^+(k\mathbf{x}_j)\sum_{\substack{m=1\\ m\neq j}}^{M}\sum_{l=-\infty}^{\infty}P_{nl}(k\boldsymbol{l}_{jm})B_{p,l}^{(m)}\\ A_{s,n}^{(j)}U_n^+(K\mathbf{x}_j)\delta_{is} + U_n^+(K\mathbf{x}_j)\sum_{\substack{m=1\\ m\neq j}}^{M}\sum_{l=-\infty}^{\infty}P_{nl}(K\boldsymbol{l}_{jm})B_{s,l}^{(m)}\end{pmatrix}\right\},\end{aligned} \tag{4.33}$$

where

$$P_{nl}(\mathbf{x}) \equiv V_{l-n}^+(\mathbf{x}). \tag{4.34}$$

Here the matrix $\mathbf{P} = [P_{nl}]$ is equal to the transpose of Martin's $\mathbf{S} = [S_{nl}]$ matrix [98], $\mathbf{P} = \mathbf{S}^T$. The total incident field impinging on cylinder $\mathtt{S}_j$ is a sum of the last two terms on the right hand side of eq. (4.32), i.e.

$$\begin{pmatrix}\phi_{inc}^{(j)} + \sum_{\substack{m=1\\ m\neq j}}^{M}\phi_{sc}^{(m)}\\ \psi_{inc}^{(j)} + \sum_{\substack{m=1\\ m\neq j}}^{M}\psi_{sc}^{(m)}\end{pmatrix} = \sum_{n=-\infty}^{\infty}\begin{pmatrix}\left[A_{p,n}^{(j)}\delta_{ip} + \sum_{\substack{m=1\\ m\neq j}}^{M}\sum_{l=-\infty}^{\infty}P_{nl}(k\boldsymbol{l}_{jm})B_{p,l}^{(m)}\right]U_n^+(k\mathbf{x}_j)\\ \left[A_{s,n}^{(j)}\delta_{is} + \sum_{\substack{m=1\\ m\neq j}}^{M}\sum_{l=-\infty}^{\infty}P_{nl}(K\boldsymbol{l}_{jm})B_{s,l}^{(m)}\right]U_n^+(K\mathbf{x}_j)\end{pmatrix}. \tag{4.35}$$

The response of shell $\mathtt{S}_j$ to the incident field (4.35) can be obtained by incorporating the boundary conditions at the interface and the transition matrix $\mathbf{T}^{(j)}$ of cylinder $\mathtt{S}_j$

in isolation [177]:

$$\begin{pmatrix}\phi_{sc}^{(j)}\\ \psi_{sc}^{(j)}\end{pmatrix} = \sum_{n=-\infty}^{\infty}\begin{pmatrix}T_{nq}^{pp(j)} & T_{nq}^{ps(j)}\\ T_{nq}^{sp(j)} & T_{nq}^{ss(j)}\end{pmatrix} \tag{4.36}$$

$$\times\begin{pmatrix}\left[A_{p,\,n}^{(j)}\delta_{ip} + \sum_{\substack{m=1\\ m\neq j}}^{M}\sum_{l=-\infty}^{\infty} P_{nl}(k\boldsymbol{l}_{jm})B_{p,l}^{(m)}\right]V_n^{+}(k\mathbf{x}_j)\\ \left[A_{s,\,n}^{(j)}\delta_{is} + \sum_{\substack{m=1\\ m\neq j}}^{M}\sum_{l=-\infty}^{\infty} P_{nl}(K\boldsymbol{l}_{jm})B_{s,l}^{(m)}\right]V_n^{+}(K\mathbf{x}_j)\end{pmatrix}. \tag{4.37}$$

Thus, eqs. (4.30b) and (4.36) yield a linear system of equations

$$\begin{pmatrix}B_{p,\,n}^{(j)}\\ B_{s,\,n}^{(j)}\end{pmatrix} - \sum_{q=-\infty}^{\infty}\begin{pmatrix}T_{nq}^{pp(j)} & T_{nq}^{ps(j)}\\ T_{nq}^{sp(j)} & T_{nq}^{ss(j)}\end{pmatrix}\sum_{\substack{m=1\\ m\neq j}}^{M}\sum_{l=-\infty}^{\infty}\begin{pmatrix}P_{ql}(k\boldsymbol{l}_{jm})B_{p,l}^{(m)}\\ P_{ql}(K\boldsymbol{l}_{jm})B_{s,l}^{(m)}\end{pmatrix}$$

$$= \sum_{q=-\infty}^{\infty}\begin{pmatrix}T_{nq}^{pp(j)} & T_{nq}^{ps(j)}\\ T_{nq}^{sp(j)} & T_{nq}^{ss(j)}\end{pmatrix}\begin{pmatrix}A_{p,\,n}^{(j)}\delta_{ip}\\ A_{s,\,n}^{(j)}\delta_{is}\end{pmatrix}, \quad n\in\mathbb{Z}. \tag{4.38}$$

Equivalently,

$$\sum_{m=1}^{M}\sum_{l=-\infty}^{\infty} X_{jnml}\begin{pmatrix}B_{p,\,l}^{(m)}\\ B_{s,\,l}^{(m)}\end{pmatrix} = \sum_{q=-\infty}^{\infty}\begin{pmatrix}T_{nq}^{pp(j)} & T_{nq}^{ps(j)}\\ T_{nq}^{sp(j)} & T_{nq}^{ss(j)}\end{pmatrix}\begin{pmatrix}A_{p,\,n}^{(j)}\delta_{ip}\\ A_{s,\,n}^{(j)}\delta_{is}\end{pmatrix}, \quad j=\overline{1,M}, \quad n\in\mathbb{Z} \tag{4.39a}$$

$$X_{jnml} = \begin{cases}\delta_{nl}, & m=j,\\ -\sum_{q=-\infty}^{\infty}\begin{pmatrix}T_{nq}^{pp(j)} & T_{nq}^{ps(j)}\\ T_{nq}^{sp(j)} & T_{nq}^{ss(j)}\end{pmatrix}\begin{pmatrix}P_{ql}(k\boldsymbol{l}_{jm})\\ P_{ql}(K\boldsymbol{l}_{jm})\end{pmatrix}, & m\neq j.\end{cases} \tag{4.39b}$$

Truncating the infinite sums in eq. (4.39) yields an algebraic system of equations with finite dimensions:

$$\sum_{m=1}^{M}\sum_{l=-N}^{N} X_{jnml}\begin{pmatrix}B_{p,\,l}^{(m)}\\ B_{s,\,l}^{(m)}\end{pmatrix} = \sum_{q=-N}^{N}\begin{pmatrix}T_{nq}^{pp(j)} & T_{nq}^{ps(j)}\\ T_{nq}^{sp(j)} & T_{nq}^{ss(j)}\end{pmatrix}\begin{pmatrix}A_{p,\,n}^{(j)}\delta_{ip}\\ A_{s,\,n}^{(j)}\delta_{is}\end{pmatrix}, \quad j=\overline{1,M}, \quad n\in\mathbb{Z} \tag{4.40}$$

or in matrix form

$$\mathbb{X}\,\mathbf{b} = \mathbf{d}, \tag{4.41}$$

where

$$\mathbb{X} = \begin{bmatrix}\mathbf{I} & -\mathbf{T}^{(1)}\mathbf{P}^{1,2} & -\mathbf{T}^{(1)}\mathbf{P}^{1,3} & \dots & -\mathbf{T}^{(1)}\mathbf{P}^{1,M}\\ -\mathbf{T}^{(2)}\mathbf{P}^{2,1} & \mathbf{I} & -\mathbf{T}^{(2)}\mathbf{P}^{2,3} & \dots & -\mathbf{T}^{(2)}\mathbf{P}^{2,M}\\ \vdots & \vdots & \vdots & \ddots & \vdots\\ -\mathbf{T}^{(M)}\mathbf{P}^{M,1} & -\mathbf{T}^{(M)}\mathbf{P}^{M,2} & -\mathbf{T}^{(M)}\mathbf{P}^{M,3} & \dots & \mathbf{I}\end{bmatrix}, \tag{4.42}$$

$\mathbf{b}$ is a vector of unknown coefficients:

$$\mathbf{b} = \begin{pmatrix} \mathbf{B}_p \\ \mathbf{B}_s \end{pmatrix}, \quad \mathbf{B}_\epsilon = \begin{pmatrix} \mathbf{b}_\epsilon^{(1)} \\ \mathbf{b}_\epsilon^{(2)} \\ \vdots \\ \mathbf{b}_\epsilon^{(M)} \end{pmatrix}, \quad \mathbf{b}_\epsilon^{(j)} = \begin{pmatrix} B_{\epsilon,-N}^{(j)} \\ B_{\epsilon,-N+1}^{(j)} \\ \vdots \\ B_{\epsilon,N}^{(j)} \end{pmatrix}, \epsilon = p, s, \quad j = \overline{1, M}, \quad (4.43)$$

$$\mathbf{d} = \begin{cases} \begin{pmatrix} \mathbf{d}_p & \mathbf{0} \end{pmatrix}^T, & \text{for } P \text{ wave incidence,} \\ \begin{pmatrix} \mathbf{0} & \mathbf{d}_s \end{pmatrix}^T, & \text{for } SV \text{ wave incidence,} \end{cases} \quad \mathbf{d}_\epsilon = \begin{pmatrix} \mathbf{d}_\epsilon^{(1)} \\ \mathbf{d}_\epsilon^{(2)} \\ \vdots \\ \mathbf{d}_\epsilon^{(M)} \end{pmatrix} = \begin{pmatrix} \mathbf{T}_\epsilon^{(1)} \mathbf{a}_\epsilon^{(1)} \\ \mathbf{T}_\epsilon^{(2)} \mathbf{a}_\epsilon^{(2)} \\ \vdots \\ \mathbf{T}_\epsilon^{(M)} \mathbf{a}_\epsilon^{(M)} \end{pmatrix}, \epsilon = p, s, \quad (4.44)$$

$$\mathbf{a}_\epsilon^{(j)} = \begin{pmatrix} A_{\epsilon,-N}^{(j)} \\ A_{\epsilon,-N+1}^{(j)} \\ \vdots \\ A_{\epsilon,N}^{(j)} \end{pmatrix}, \quad \mathbf{P}^{j,m} = \begin{pmatrix} \mathbf{P}_{ql}^{j,m}(k\boldsymbol{l}_{jm}) \\ \mathbf{P}_{ql}^{j,m}(K\boldsymbol{l}_{jm}) \end{pmatrix}, \epsilon = p, s, \ j, m = \overline{1, M}, j \neq m, \quad (4.45)$$

where index p stands for P waves and s for SV waves, $\mathbf{T}_\epsilon^{(j)}$ is defined by eq. (3.149), and its components $T_{nq}^{\epsilon\epsilon}(j)$, $\epsilon = p, s$ are given in Section 3.3.2. In eq. (4.45) $\mathbf{P}_{ql}^{j,m}(\tilde{\kappa}\,\boldsymbol{l}_{jm}) = V_{l-q}^{+}(\tilde{\kappa}\,\boldsymbol{l}_{jm}), (\tilde{\kappa} = k, K, \ q = -\overline{N_j, N_j}, l = -\overline{N_m, N_m}, \ j, m = \overline{1, M}, j \neq m)$.

4.2.2 Numerical results

In this section, we present the implementation of COMSOL simulations for a planar configuration of two aluminum cylinders of radii a embedded in a titanium matrix. The cylinders are positioned at points $O_1(0, 1.5a)$ and $O_2(0, -1.5a)$. Properties of considered material are given in Table 4.2. The field around the cylinders is excited by the point force $\mathbf{f}_p = (0, 100)$ applied at $(X_p, Y_p) = (-10a, 0)$. Figure 4.17 depicts a total displacement field, and Figure 4.18 illustrates the distribution of the stress tensor components at $ka = 2.5$ and $ka = 5$. Since the force applied is in the vertical upward direction, the normal stresses σ_{xx} and σ_{yy} are the reflections of one another across the x-axis. The shear stress σ_{xy} is symmetric around the x axis.

Material	Density, ρ $[kg/m^3]$	Young's modulus, E $[GPa]$	Poisson's ratio, ν
Aluminum 3003-H18, (Al)	2730	69	0.33
Titanium beta-21S, (Ti)	4940	105	0.33

Table 4.2: Material properties used for computation in COMSOL.

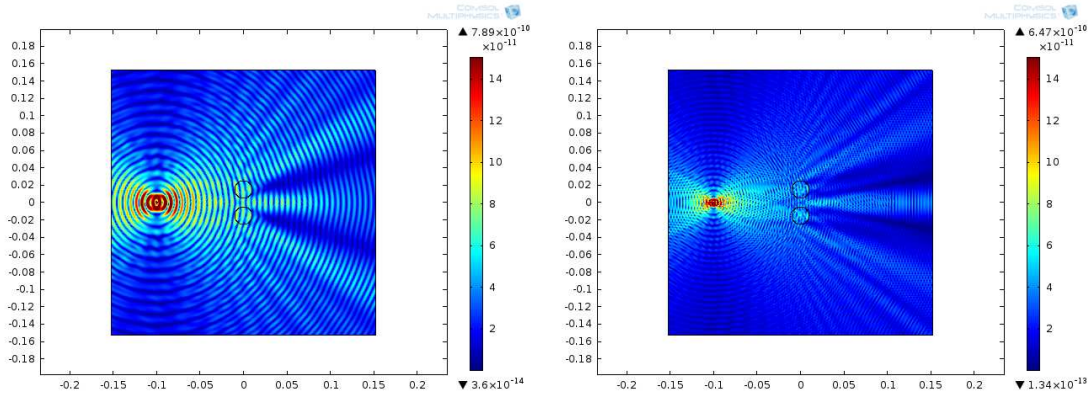

(a) $ka = 2.5$, $M = 2$ **(b)** $ka = 5$, $M = 2$

Figure 4.17: The total displacement field amplitude $\mathbf{u}$ at $ka = 2.5$ and $ka = 5$, for a planar configuration of two aluminum cylinders of radius a, excited by the point force $\mathbf{f}_p = (0, 100)$ located at $(X_p, Y_p) = (-10a, 0)$.

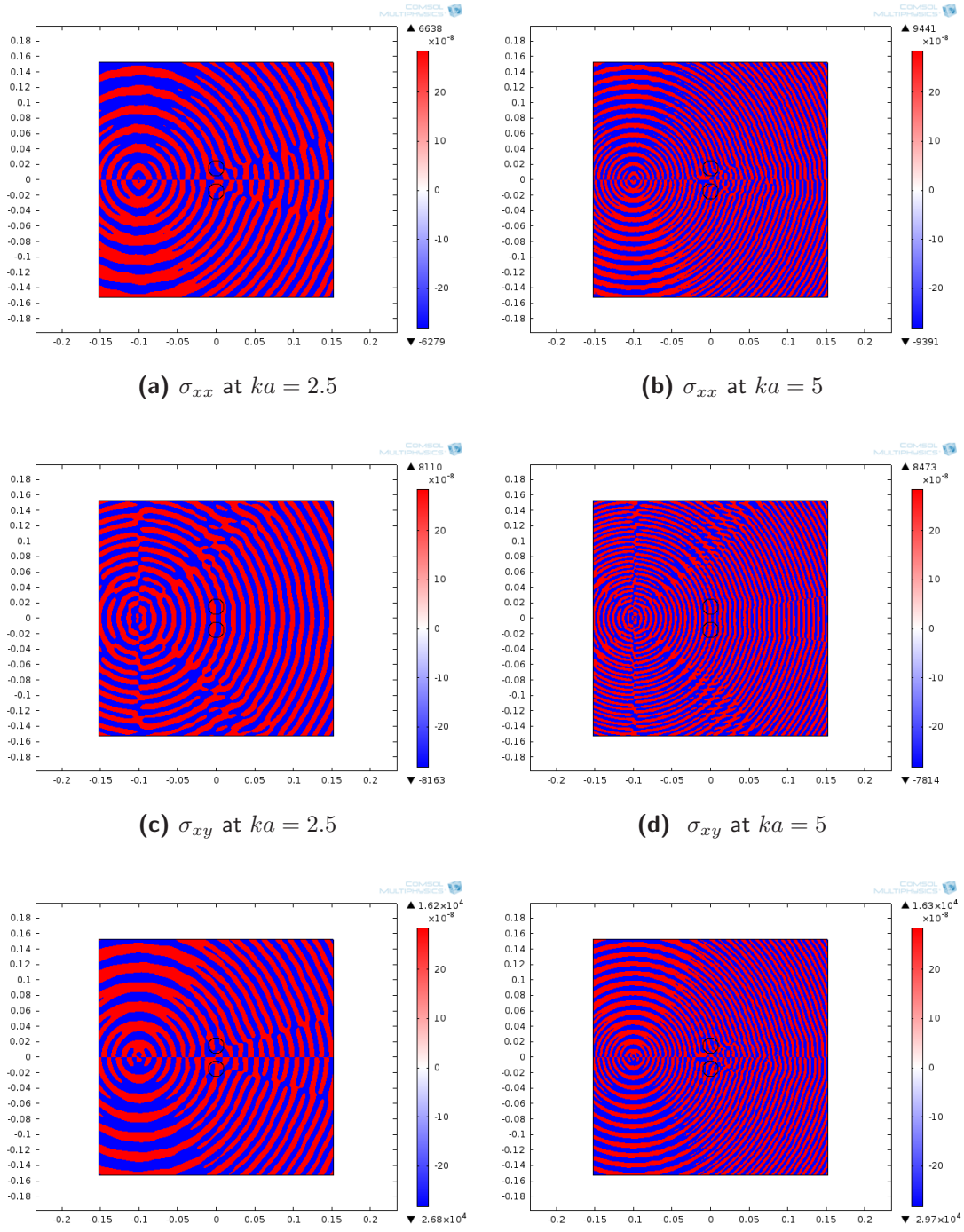

(a) σ_{xx} at $ka = 2.5$ **(b)** σ_{xx} at $ka = 5$

(c) σ_{xy} at $ka = 2.5$ **(d)** σ_{xy} at $ka = 5$

(e) σ_{yy} at $ka = 2.5$ **(f)** σ_{yy} at $ka = 5$

Figure 4.18: The amplitudes of components of stress tensor $\boldsymbol{\sigma}$ at $ka = 2.5$ and $ka = 5$, for a planar configuration of two aluminum cylinders of radius a, excited by the point force $\mathbf{f}_p = (0, 100)$ located at $(X_p, Y_p) = (-10a, 0)$.

Chapter 5

Iterative methods for solution of multiple scattering problems

The multiple scattering and radiation problems studied in Chapter 4 lead to the system of linear algebraic equations given by (4.16). The complexity of the system grows with the number of scatterers and frequency. A direct solution of the system leads to an excessive simulation run time. Therefore, in this chapter, we develop and provide iterative approaches suitable for a parallel computation of linear systems and applicable in many different areas of science and engineering. For example, these iterative techniques can be used in acoustics, elastodynamics, electrodynamics, probability and mathematical statistics, algebra, numerical solution of integral equations, random walk, theory of stationary time series and signals, etc. [185, 9, 66, 6, 184, 154, 46, 38, 134, 22].

We start in Section 5.1 with a definition of Toeplitz matrices, and categorize some matrix types. Specifically, we study the structure of multilevel matrices and consider some examples. In Section 5.2.2, we review biorthogonal and orthogonal polynomials, and investigate their properties and applications in a matrix inversion. The iterative methods for a solution of linear systems are described in Section 5.3. For an arbitrary planar configuration of scatterers, one of the iterative approaches uses a Neumann series expansion to invert the matrix $\mathbb{X}$ and solve a linear system. This approach is presented in Section 5.3.1 for a fixed value of frequency. The generalization of this iterative approach for a band of frequencies is provided in Section 5.3.2. Section 5.3.3 studies the fast preconditioned iterative methods. Particularly, the application of the matrix vector product method and Fast Fourier Transform is presented. Another iterative approach is proposed for an evenly distributed cluster of scatterers using the Block Toeplitz structure of the system. The iterative methods for Block Toeplitz matrices of

level 1 and 2 are described in Section 5.3.4. Numerical results are illustrated in Section 5.4. They include the Neumann expansion study given in Section 5.4.1, and the results obtained using the iterative method for Block Toeplitz matrix of level 1 illustrated in Section 5.4.2. The theoretical predictions implemented in Matlab and FORTRAN are compared to those obtained by COMSOL Multiphysics software. The spectral radius of the matrix is investigated as a function of wavenumber and the validity of the Neumann series solution is shown by modifying the number of scatterers M and the distance between the cylinders d. Numerical results are also presented for the CPU time taken to solve the linear system by varying values of M and d.

5.1 Matrix types

5.1.1 Toeplitz matrices

Toeplitz matrices or Toeplitz forms are named after O. Toeplitz [164], honoring his early work from 1911 on bilinear L-forms in relation to Laurent series. A Toeplitz matrix has a specific structure such that its each descending diagonal from the left to the right is constant. In the early 1920s, Szegö [66] studied the distribution of eigenvalues of Toeplitz forms and introduced a new class of polynomials that are closely related to these forms. As we will see further, the special features of the Toeplitz matrix will allow us to apply the Krylov subspace methods [140] that are nowadays considered among the most powerful iterative techniques available for large scale linear systems.

Toeplitz and Circulant matrices

The Toeplitz matrix $\mathbf{P}^{j,m} = \left[\mathbf{P}_{ql}^{j,m}\right] = \left[P_{q-l}^{j,m}\right]$ has such a structure that each of its subdiagonals, which are parallel to the main diagonal, is constant:

$$\mathbf{P} = \left[P_{q-l}\right] = \begin{bmatrix} P_0 & P_{-1} & P_{-2} & \dots & P_{-2N} \\ P_1 & P_0 & P_{-1} & \dots & P_{-2N+1} \\ P_2 & P_1 & P_0 & \dots & P_{-2N+2} \\ \dots & \dots & \dots & \ddots & \dots \\ P_{2N} & P_{2N-1} & P_{2N-2} & \dots & P_0 \end{bmatrix}, \tag{5.1}$$

where $1 \leq q, l \leq 2N+1$, $N = N_j = N_m$. Here we dropped upper indices j and m of matrix $\mathbf{P}^{j,m}$ for simplicity of notation. Matrix $\mathbf{P}$ of order $2N+1$ with elements P_{ql} will have Toeplitz structure if and only if [185]:

$$P_{q_1 l_1} = P_{q_2 l_2}, \quad \text{with } q_1 - l_1 = q_2 - l_2. \tag{5.2}$$

A special form of Toeplitz matrix where each column vector is rotated one element upward relative to the preceding column vector is called a Circulant matrix. In particular, if [185]

$$P_{q_1 l_1} = P_{q_2 l_2}, \quad \text{with} \quad q_1 - l_1 = \big(q_2 - l_2\big) \mod (2N+1), \tag{5.3}$$

then such a matrix will have Circulant structure, and will be called a Circulant matrix of order $2N+1$ and denoted by $\mathbf{C}$:

$$\mathbf{C} = \begin{bmatrix} P_0 & P_{-1} & P_{-2} & \ddots & P_{-2N} \\ P_{-2N} & P_0 & P_{-1} & \ddots & P_{-2N+1} \\ P_{-2N+1} & P_{-2N} & P_0 & \ddots & P_{-2N+2} \\ \ddots & \ddots & \ddots & \ddots & \ddots \\ P_{-1} & P_{-2} & P_{-3} & \ddots & P_0 \end{bmatrix}. \tag{5.4}$$

The Circulant matrices that have upper triangular or lower triangular form are called semicirculant matrices. For example, the elements of upper triangular semicirculant matrix $\mathbf{C}^U$ can be formed from elements of matrix $\mathbf{P}$ of order $2N+1$:

$$C^U_{q\,l} = \begin{cases} P_{q-l}, & q \leq l, \\ 0, & q > l, \end{cases} \quad \text{for} \quad 1 \leq q\,, l \leq 2N+1. \tag{5.5}$$

If [129]

$$P_{q_1 l_1} = -P_{q_2 l_2}, \quad \text{with} \quad q_1 - l_1 = \big(q_2 - l_2 + (2N+1)\big), \tag{5.6}$$

then such a matrix will be called a Skewcirculant matrix $\mathbf{S}$ of order $2N+1$. A Skewcirculant matrix $\mathbf{S}$ differs from Circulant matrix $\mathbf{C}$ by a sign change in all elements below

the main diagonal and has the form:

$$\mathbf{S} = \begin{bmatrix} P_0 & P_{-1} & P_{-2} & \ddots & P_{-2N} \\ -P_{-2N} & P_0 & P_{-1} & \ddots & P_{-2N+1} \\ -P_{-2N+1} & -P_{-2N} & P_0 & \ddots & P_{-2N+2} \\ \ddots & \ddots & \ddots & \ddots & \ddots \\ -P_{-1} & -P_{-2} & -P_{-3} & \ddots & P_0 \end{bmatrix}. \tag{5.7}$$

The Toeplitz matrix $\mathbf{P}$ of order $2N+1$ can be defined by its first row and first column and can be generated by the root vector

$$\mathbf{p} = \big(P_{-2N}, P_{-2N+1}, \ldots, P_{-1}, P_0, P_1, \ldots, P_{2N-1}, P_{2N}\big)^T, \tag{5.8}$$

whereas the Circulant matrix $\mathbf{C}$ of order $2N+1$ can be generated by its first column:

$$\mathbf{c} = \big(P_0, P_{-2N}, P_{-2N+1}, \ldots, P_{-1}\big)^T, \tag{5.9}$$

or its first row:

$$\mathbf{c}' = \big(P_0, P_{-1}, \ldots, P_{-2N+1}, P_{-2N}\big). \tag{5.10}$$

As we can see, the Circulant matrix $\mathbf{C}$ requires fewer elements to store than the Toeplitz matrix does.

The Toeplitz matrix $\mathbf{P} = \big[P_{ql}\big] = \big[P_{q-l}\big]$ of order $2N+1$ can be split into Circulant $\mathbf{C}$ and Skewcirculant $\mathbf{S}$ parts [129]:

$$\mathbf{P} = \mathbf{C} + \mathbf{S}, \tag{5.11}$$

where the top row elements of Circulant matrix $\mathbf{C} = [C_{q\,l}]$ of order $2N+1$ can be defined as:

$$C_{1\,1} = P_{11}, \quad C_{1\,l} = \frac{1}{2}(P_{1\,l} + P_{2N+2-l,\,1}) \quad \text{for} \quad l = 2, \ldots, 2N+1, \tag{5.12}$$

and the top row elements of Skewcirculant matrix $\mathbf{S} = [S_{q\,l}]$ of order $2N+1$ have the form:

$$S_{1\,1} = 0, \quad S_{1\,l} = \frac{1}{2}(P_{1\,l} - P_{2N+2-l,\,1}) \quad \text{for} \quad l = 2, \ldots, 2N+1, \tag{5.13}$$

In some cases P_i elements of Toeplitz matrix $\mathbf{P}$, eq. (5.1), can be treated as square matrices that can have a Toeplitz structure. These block matrices can also consist of blocks of Toeplitz structure leading to the construction of multilevel block matrices that will be addressed further.

Toeplitz matrices generated by the Laurent series

In his early work [164] from 1911, Toeplitz studied infinite Toeplitz matrices in relation to Laurent series:

$$f(\mathbf{z}) = \sum_{k=-\infty}^{\infty} P_k \, \mathbf{z}^k, \tag{5.14}$$

where P_k are elements of an infinite Toeplitz matrix $\mathbf{F} = \left[P_{q-l}\right]_{q,\, l=-\infty}^{\infty}$:

$$\mathbf{F} = \begin{bmatrix} . & . & . & . & . & . \\ . & P_0 & P_{-1} & P_{-2} & P_{-3} & . \\ . & P_1 & P_0 & P_{-1} & P_{-2} & . \\ . & P_2 & P_1 & P_0 & P_{-1} & . \\ . & P_3 & P_2 & P_1 & P_0 & . \\ . & . & . & . & . & . \end{bmatrix}. \tag{5.15}$$

Toeplitz [164] showed that the spectrum of matrix $\mathbf{F}$ overlaps with the set of values of $f(\mathbf{z})$ at $|\mathbf{z}| = 1$, if $f(\mathbf{z})$ is convergent in the ring that includes a unit circle $|\mathbf{z}| = 1$. The inverse of an infinite Toeplitz matrix has also infinite Toeplitz structure. Any infinite Toeplitz matrix $\mathbf{F}$ and its inverse $\mathbf{F}^{-1}$ can be decomposed as multiplication of two infinite upper and lower triangular Toeplitz matrices [170]:

$$\mathbf{F} = \mathbf{F}_- \, \mathbf{F}_+ = \mathbf{F}_+ \, \mathbf{F}_-, \qquad \mathbf{F}^{-1} = \mathbf{F}_-^{-1} \, \mathbf{F}_+^{-1} = \mathbf{F}_+^{-1} \, \mathbf{F}_-^{-1}. \tag{5.16}$$

The Laurent series (5.14) can also be associated with semi-infinite Toeplitz matrix $\mathbf{F}_{\overline{0,\infty}} = \left[P_{q-l}\right]_{q,\, l=0}^{\infty}$:

$$\mathbf{F}_{\overline{0,\infty}} = \begin{bmatrix} P_0 & P_{-1} & P_{-2} & . \\ P_1 & P_0 & P_{-1} & . \\ P_2 & P_1 & P_0 & . \\ . & . & . & . \end{bmatrix}. \tag{5.17}$$

The semi-infinite Toeplitz matrix $\mathbf{F}_{\overline{0,\infty}}$ may consist of some families of matrices of the form:

$$\mathbf{P}_n = \left[P_{q-l}\right]_{q,\,l=0}^{n}, \quad n = 0,\, 1,\, 2, \ldots 2N, \tag{5.18}$$

where $N = N_j = N_m$ is the truncation number and

$$\left[P_{q-l}\right]_{q,\,l=0}^{n} = \begin{bmatrix} P_0 & P_{-1} & P_{-2} & \cdots & P_{-n} \\ P_1 & P_0 & P_{-1} & \cdots & P_{-n+1} \\ \cdots & \cdots & \cdots & \cdots & \cdots \\ P_{n-1} & P_{n-2} & P_{n-3} & \cdots & P_{-1} \\ P_n & P_{n-1} & P_{n-2} & \cdots & P_0 \end{bmatrix}. \tag{5.19}$$

Multilevel block matrices will be addressed next.

5.1.2 Multilevel matrices

The idea of multilevel matrix was proposed by Voevodin and Tyrtyshnikov [185]. Considering different classes of matrices, it is assumed that one class contains matrices of the same size that form a linear manifold in the space of matrices of the same size. Such a class of matrices can be given by fixing some values of $\alpha_{ij}^{(q)}$ and $\gamma^{(q)}$ $(1 \le i \le m,\, 1 \le j \le n,\, 1 \le q \le Q)$ and requiring that it contains only matrices of size $m \times n$ with elements a_{ij} that satisfy the condition [185]:

$$\sum_{i,\,j} \alpha_{ij}^{(q)} a_{ij} = \gamma^{(q)}, \quad 1 \le q \le Q. \tag{5.20}$$

If `K` is one of such matrix classes and $\mathbf{A} \in$ `K` then the matrix $\mathbf{A} = [a_{ij}]$ is called `K` type. We will denote a general type of matrices by symbol `G`, Toeplitz matrices by `T`, and Circulant matrices by `C`. The general type of matrices `G` can be defined by eq. (5.20) only when $\alpha_{ij}^{(q)}$ and $\gamma^{(q)}$ take zero values.

Let matrices of `K` type be defined by eq.(5.20). If the matrix of size $mp \times nr$ is partitioned into blocks a_{ij} of size $m \times n$ that satisfy the relation

$$\sum_{i,\,j} \alpha_{ij}^{(q)} a_{ij} = \gamma^{(q)} \mathbf{E}, \tag{5.21}$$

then the $mp \times nr$ matrix has a block type K, or more precisely a composite type KG that we will discuss further; here $\mathbf{E}$ is $m \times n$ matrix with all entries equal to 1:

$$\mathbf{E} = \begin{bmatrix} 1 & 1 & 1 & \dots & 1 \\ 1 & 1 & 1 & \dots & 1 \\ 1 & 1 & 1 & \dots & 1 \\ \vdots & \vdots & \vdots & \ddots & \vdots \\ 1 & 1 & 1 & \dots & 1 \end{bmatrix}. \tag{5.22}$$

The block matrix of size $mp \times nr$ can be defined as the Kronecker product of two matrices: $m \times n$ matrix $\mathbf{A}$ and $p \times r$ matrix $\mathbf{B}$

$$\mathbf{A} \otimes \mathbf{B} = \begin{bmatrix} a_{11}\mathbf{B} & a_{12}\mathbf{B} & \dots & a_{1n}\mathbf{B} \\ a_{21}\mathbf{B} & a_{22}\mathbf{B} & \dots & a_{2n}\mathbf{B} \\ \vdots & \vdots & \ddots & \vdots \\ a_{m1}\mathbf{B} & a_{m2}\mathbf{B} & \dots & a_{mn}\mathbf{B} \end{bmatrix}. \tag{5.23}$$

Equation (5.20) is a linear system with respect to the elements of matrix $\mathbf{A} = [a_{ij}]$. This system can be written in a matrix form as:

$$\boldsymbol{\alpha}\ \mathbf{vec}\big(\mathbf{A}\big) = \boldsymbol{\gamma}, \tag{5.24}$$

where

$$\boldsymbol{\alpha} = \begin{pmatrix} \mathbf{vec}\big(\boldsymbol{\alpha}^{(1)}\big)^T \\ \mathbf{vec}\big(\boldsymbol{\alpha}^{(2)}\big)^T \\ \vdots \\ \mathbf{vec}\big(\boldsymbol{\alpha}^{(Q)}\big)^T \end{pmatrix}, \quad \boldsymbol{\gamma} = \begin{pmatrix} \boldsymbol{\gamma}^{(1)} \\ \boldsymbol{\gamma}^{(2)} \\ \vdots \\ \boldsymbol{\gamma}^{(Q)} \end{pmatrix}, \tag{5.25}$$

where $\boldsymbol{\alpha}^{(q)} = [\alpha_{ij}^{(q)}]$ is $m \times n$ matrix, and $\boldsymbol{\gamma}^{(q)}$ is $m \times 1$ vector ($1 \le i \le m$, $1 \le j \le n$, $1 \le q \le Q$); $\mathbf{vec}\big(\mathbf{A}\big)$ defines the vectorization of matrix $\mathbf{A}$ that is constructed by packing consecutively the columns of matrix $\mathbf{A}$ into a single column vector:

$$\mathbf{vec}\big(\mathbf{A}\big) = [a_{11} \dots a_{m1} a_{12} \dots a_{m2} a_{13} \dots \dots a_{mn-1} a_{1n} \dots a_{mn}]^T. \tag{5.26}$$

Similarly, $\mathbf{vec}\big(\boldsymbol{\alpha}^{(q)}\big)$ is formed by stacking the columns of matrix $\boldsymbol{\alpha}^{(q)}$. Let K type satisfy the system (5.21), then the block type $\mathtt{KG}_{kl}$ is defined by the following system:

$$\big(\mathbf{I}_l \otimes \boldsymbol{\alpha} \otimes \mathbf{I}_k\big)\mathbf{vec}\big(\mathbf{A}\big) = \mathbf{g}_l \otimes \boldsymbol{\gamma} \otimes \mathbf{g}_k, \tag{5.27}$$

where $\mathbf{I}$ is the identity matrix, $\mathbf{g}$ is the vector with all entries equal to 1, the subindices denote the order of matrix or vector, and $\otimes$ symbolizes the Kronecker product that is a special case of the tensor product and defined by eq. (5.23); the Kronecker product is associative.

Let $\mathtt{K}_1, \ldots, \mathtt{K}_s$ be different classes of matrices admitting such classification. We can construct new composite types based on these types, e.g. $\mathtt{K}_1 \cdots \mathtt{K}_s$. The matrices of composite types are called multilevel matrices and characterized by block partitioning of different levels. We will denote blocks as follows. The matrix $\mathbf{A}$ itself is a single block of level 0. If the matrix $\mathbf{A}$ has a composite type $\mathtt{K}_1 \ldots \mathtt{K}_s$ and class $\mathtt{K}_k$ consists of matrices of sizes $m_k \times n_k \, (1 \le k \le s)$ then the matrix $\mathbf{A}$ comprises $m_1 \times n_1$ blocks $a_{i_1 j_1}$ of size $m_2 \cdots m_k \times n_2 \cdots n_k$ that form the level 1 ($1 \le i_1 \le m_1, 1 \le j_1 \le n_1$). Next, $\forall a_{i_1 j_1}$ blocks consist of $m_2 \times n_2$ blocks $a_{i_1 j_1, i_2 j_2}$ that construct the level 2. For $1 \le k < s$, each of $a_{i_1 j_1, \ldots i_k j_k}$ blocks of level k consists of $m_k \times n_k$ blocks of level $k+1$. The last level s is formed by the elements that cannot be partitioned, and assumed to contain only complex numbers. In general, if the matrix is the s level block matrix, it has a composite type $\mathtt{G}_{m_1 n_1} \cdots \mathtt{G}_{m_s n_s}$. When each block is square, we can use one index: $\mathtt{G}_{m_1} \cdots \mathtt{G}_{m_s}$. Multilevel partitioning is of interest if the level blocks have some structure. In the proceeding section, we will consider the matrices of composite types $\mathtt{T}_{m_1}\mathtt{G}_{m_2}$ and $\mathtt{T}_{m_1, m_2}\mathtt{G}_{m_3}$. The former defines a two-level block matrix, i.e. a block Toeplitz (BT) matrix of level 1 with general type subblocks of order m_2 embedded in Toeplitz blocks of order m_1; the latter type characterizes a three-level block matrix with level orders m_1, m_2 and m_3 that is a BT matrix of level 2 with general type subblocks, here the general type subblocks of order m_3 are embedded in Toeplitz blocks of order m_2 that are nested inside of another Toeplitz block of order m_1.

Examples of multilevel matrices

Consider a planar configuration consisting of M_y rows and M_x columns of cylinders with a total number of cylinders: $M = M_x M_y$. Let each cylinder have the same physical properties and radius and satisfy the condition of continuity of normal stresses and displacements at the interfaces. This will yield the same T-matrix for each cylinder,

i.e. $\mathbf{T}^{(j)} = \tilde{\mathbf{T}}, (j = \overline{1, M})$. Then for a configuration with M_y rows and M_x columns of cylinders, the matrix $\mathbb{X}$ defined by eq. (4.17) has a BT structure. Figure 5.1 illustrates some examples of such configurations.

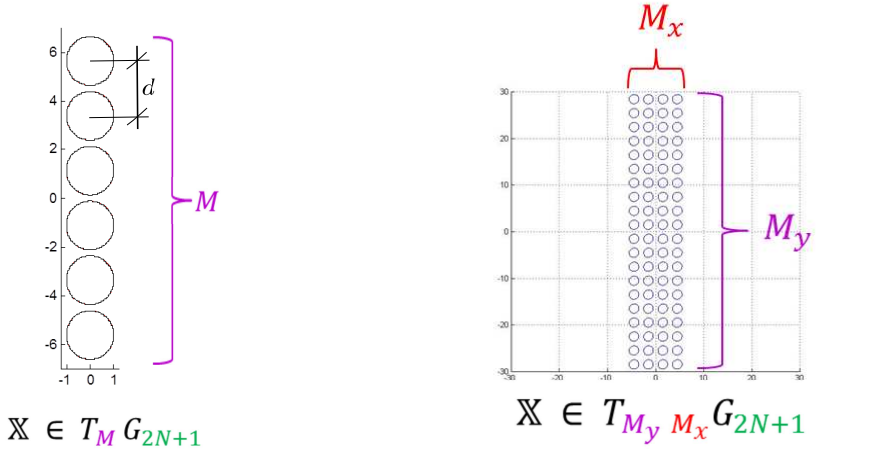

(a) $\mathbb{X}$ is a Block Toeplitz matrix of level 1 **(b)** $\mathbb{X}$ is a Block Toeplitz matrix of level 2

Figure 5.1: Examples of configurations that lead to Block Toeplitz matrices of level 1, $\mathbb{X} \in T_M G_{2N+1}$, and level 2, $\mathbb{X} \in T_{M_y,\, M_x} G_{2N+1}$, where $M_x \cdot M_y = M$. On the right picture, d is the distance between the centers of two cylinders.

Example of BT matrix of level 1. For a configuration with one row ($M_y = 1$) or one column ($M_x = 1$) of cylinders, the matrix $\mathbb{X} \in T_M G_{2N+1}$ becomes a BT matrix of level 1 with $M = M_x$ for one row of cylinders and $M = M_y$ for one column of cylinders (see Figure a). The matrix $\mathbb{X}$ has order $M(2N+1)$, where N is the mode number. As a two-level block matrix, the BT matrix $\mathbb{X}$ has order M and consists of square blocks $\boldsymbol{X}^1_{ij} = \boldsymbol{X}^1_{i-j}$ where $1 \le i, j \le M$, and in general, every block can be a non-symmetric complex valued matrix of order $(2N+1)$:

$$\mathbb{X} = \begin{bmatrix} \boldsymbol{X}^1_0 & \boldsymbol{X}^1_{-1} & \boldsymbol{X}^1_{-2} & \ddots & \boldsymbol{X}^1_{-M+1} \\ \boldsymbol{X}^1_1 & \boldsymbol{X}^1_0 & \boldsymbol{X}^1_{-1} & \ddots & \boldsymbol{X}^1_{-M+2} \\ \boldsymbol{X}^1_2 & \boldsymbol{X}^1_1 & \boldsymbol{X}^1_0 & \ddots & \boldsymbol{X}^1_{-M+3} \\ \ddots & \ddots & \ddots & \ddots & \ddots \\ \boldsymbol{X}^1_{M-1} & \boldsymbol{X}^1_{M-2} & \boldsymbol{X}^1_{M-3} & \ddots & \boldsymbol{X}^1_0 \end{bmatrix}, \tag{5.28}$$

Here $\boldsymbol{X}_0^1$ is the block identity matrix of order $2N+1$.

Example of BT matrix of level 2. Consider a planar configuration shown in Figure b with M_y rows and M_x columns of cylinders that have identical mechanical properties and transition matrices $\mathbf{T}^{(j)} = \tilde{\mathbf{T}}, (j = \overline{1, M})$. In this case, the matrix $\mathbb{X}$ is the three-level block matrix, i.e. $\mathbb{X} \in T_{M_y,\, M_x} G_{2N+1}$, and has a BT structure of level 2. Again, the matrix $\mathbb{X}$ is of order $M(2N+1)$. At the same time, as a BT matrix, the matrix $\mathbb{X}$ has order M_y (see eq. (5.29)). Each block $\boldsymbol{X}_{i-j}^1$ has order $M_x(2N+1)$ and appears in the matrix $\mathbb{X}$ again in a BT form (5.30). The block entries $\boldsymbol{X}_{i-j}^1 \in T_{M_x} G_{2N+1}$, $(1 \le i, j \le M_y)$ are the BT matrices of order M_x with individual entries $\boldsymbol{X}_{i-j}^2 \in G_{2N+1}$, $(1 \le i, j \le M_x)$. Each block $\boldsymbol{X}_{i-j}^2$ is of general type and has order $2N+1$. In other words, a general type matrix $\boldsymbol{X}_{i-j}^2$ of order $(2N+1)$ is embedded in a Toeplitz block $\boldsymbol{X}_{i-j}^1$ of order M_x that is nested inside of another Toeplitz block of order M_y, i.e. the matrix $\mathbb{X}$:

$$\mathbb{X} = \begin{bmatrix} \boldsymbol{X}_0^1 & \boldsymbol{X}_{-1}^1 & \boldsymbol{X}_{-2}^1 & \ddots & \boldsymbol{X}_{-M_y+1}^1 \\ \boldsymbol{X}_1^1 & \boldsymbol{X}_0^1 & \boldsymbol{X}_{-1}^1 & \ddots & \boldsymbol{X}_{-M_y+2}^1 \\ \boldsymbol{X}_2^1 & \boldsymbol{X}_1^1 & \boldsymbol{X}_0^1 & \ddots & \boldsymbol{X}_{-M_y+3}^1 \\ \ddots & \ddots & \ddots & \ddots & \ddots \\ \boldsymbol{X}_{M_y-1}^1 & \boldsymbol{X}_{M_y-2}^1 & \boldsymbol{X}_{M_y-3}^1 & \ddots & \boldsymbol{X}_0^1 \end{bmatrix}, \tag{5.29}$$

where

$$\boldsymbol{X}_{ij}^1 = \boldsymbol{X}_{i-j}^1 = \begin{bmatrix} \boldsymbol{X}_0^2 & \boldsymbol{X}_{-1}^2 & \boldsymbol{X}_{-2}^2 & \ddots & \boldsymbol{X}_{-M_x+1}^2 \\ \boldsymbol{X}_1^2 & \boldsymbol{X}_0^2 & \boldsymbol{X}_{-1}^2 & \ddots & \boldsymbol{X}_{-M_x+2}^2 \\ \boldsymbol{X}_2^2 & \boldsymbol{X}_1^2 & \boldsymbol{X}_0^2 & \ddots & \boldsymbol{X}_{-M_x+3}^2 \\ \ddots & \ddots & \ddots & \ddots & \ddots \\ \boldsymbol{X}_{M_x-1}^2 & \boldsymbol{X}_{M_x-2}^2 & \boldsymbol{X}_{M_x-3}^2 & \ddots & \boldsymbol{X}_0^2 \end{bmatrix}, \tag{5.30}$$

with $\boldsymbol{X}_{i-j}^2 \in G_{2N+1}$; here $\boldsymbol{X}_0^2$ is the block identity matrix of order $2N+1$.

5.2 Biorthogonal polynomials

A sequence of orthogonal polynomials in one variable is defined such that any two different polynomials in the sequence are orthogonal to each other under the particular

version of the L^2 inner product. Biorthogonal polynomials are a generalization of orthogonal polynomials and defined as polynomials that are orthogonal to several different measures. Biorthogonal polynomials share some properties of orthogonal polynomials.

The basics of the theory of orthogonal polynomials were established by Chebyshev [158], and further developed by A.A. Markov and T.J. Stieltjes. The properties of classical orthogonal polynomials such as Chebyshev, Jacobi, Legendre, Hermite, Laguerre and others were fully described by Szegö in his monograph [157] where he has contributed significantly to the further development of the general theory and developed a fundamentally new approach. In the 1920s, Szegö [156], [66], [157] studied the spectrum of Hermitian Toeplitz matrices of the form (5.18), introduced the theory of orthogonal polynomials on a unit circle, and found asymptotic formulae for these polynomials using precise considerations of functional analysis. Hermitian Toeplitz matrices and operators and associated orthogonal polynomials on a unit circle were also studied by Geronimus [64], Krein [87], and others [151], [128], [59]. The idea of orthogonality can be extended to the notion of biorthogonality [10]. Generalizations to biorthogonal polynomials that correspond to non-Hermitian Toeplitz matrices and operators were investigated by Baxter [14],[15], [16], Trench [167], Gohberg and Semencul [65], Kailath et al. [83], Voevodin and Tyrtyshnikov [185], Tyrtyshnikov [170], Brezinski [24], Heinig and Rost [74], Freund et al. [60], etc.

5.2.1 Orthogonal polynomials

Following Szegö [157], consider polynomials of the form:

$$g(\varsigma) = c_0 + c_1\varsigma + \cdots + c_m\varsigma^m, \tag{5.31}$$

where c_0, $c_1, \cdots, c_m$ are complex coefficients and ς a complex variable. If $c_m \neq 0$, m is called the precise degree of $g(\varsigma)$. We will denote an arbitrary polynomial of degree m by π_m. Every π_m can be represented as a linear combination of arbitrary polynomials $g_0(\varsigma)$, $g_1(\varsigma)$, $\cdots, g_m(\varsigma)$ with uniquely defined coefficients. The reciprocal or reverse Szegö polynomial is defined as:

$$g^*(\varsigma) = \overline{c}_m + \overline{c}_{m-1}\varsigma + \cdots + \overline{c}_0\varsigma^m = \varsigma^m\overline{g}(\varsigma^{-1}). \tag{5.32}$$

If $\varsigma_1, \varsigma_2, \ldots, \varsigma_m$ are zeros of $g(\varsigma)$, then $\varsigma_1^*, \varsigma_2^*, \ldots, \varsigma_m^*$ are zeros of $g^*(\varsigma)$ with $\varsigma_k^* = \varsigma_k^{-1}$.

Let $f(\theta) \geq 0$ be a function of period 2π, integrable in $[-\pi, \pi]$, and

$$\int_{-\pi}^{+\pi} f(\theta) d\theta > 0. \tag{5.33}$$

Consider the Fourier coefficients

$$P_n = \frac{1}{2\pi} \int_{-\pi}^{+\pi} f(\theta) e^{-i\,n\theta} d\theta, \quad n = 0, \pm 1, \pm 2, \ldots . \tag{5.34}$$

where $P_{-n} = \overline{P}_n$ are elements of Hermitian Toeplitz matrix $\mathbf{P}_n = \left[P_{q-l}\right]_{q,\,l=0}^{n}$. Let the polynomials $\varphi_n(\varsigma)$ satisfy the conditions:

$$\varphi_n(\varsigma) = \varphi_{0\,n} + \varphi_{1\,n}\varsigma + \cdots + \varphi_{n\,n}\varsigma^n, \quad \varphi_{n\,n} > 0, \quad \varphi_{n\,n} \in \Re; \tag{5.35}$$

$$\frac{1}{2\pi} \int_{-\pi}^{+\pi} \varphi_n(\varsigma)\overline{\varphi_m(\varsigma)} f(\theta) d\theta = \delta_{nm}, \quad \varsigma = e^{i\,\theta}. \tag{5.36}$$

As stated by Szegö [157], such defined system of polynomials $\{\varphi_n(\varsigma)\}$ is orthogonal with respect to $f(\theta)$ on interval $[-\pi, \pi]$, i.e. on unit circle $|\varsigma| = 1$, and uniquely determined. The orthogonality condition (5.36) yields

$$\sum_{q=0}^{m} \overline{\varphi_{qm}} \sum_{l=0}^{n} P_{q-l}\varphi_{ln} = \delta_{nm}, \tag{5.37}$$

that is equivalent to the inverse form of Cholesky decomposition of Hermitian positive definite Toeplitz matrix [170]

$$\begin{bmatrix} \overline{\varphi}_{00} & & & & \\ \overline{\varphi}_{01} & \overline{\varphi}_{11} & & \mathbf{0} & \\ \overline{\varphi}_{02} & \overline{\varphi}_{12} & \overline{\varphi}_{22} & & \\ \vdots & \vdots & \vdots & \ddots & \\ \overline{\varphi}_{0n} & \overline{\varphi}_{1n} & \overline{\varphi}_{2n} & \cdots & \overline{\varphi}_{nn} \end{bmatrix} \mathbf{P}_n \begin{bmatrix} \varphi_{00} & \varphi_{01} & \varphi_{02} & \cdots & \varphi_{0n} \\ & \varphi_{11} & \varphi_{12} & \cdots & \varphi_{1n} \\ & & \varphi_{22} & \cdots & \varphi_{2n} \\ & \mathbf{0} & & \ddots & \vdots \\ & & & & \varphi_{nn} \end{bmatrix} = \mathbf{I}. \tag{5.38}$$

The last column of the upper triangular matrix multiplied by $\overline{\varphi}_{nn}$ is the last column of $\mathbf{P}_n^{-1}$. The polynomials $\varphi_n(\varsigma)$ can be written explicitly as the determinant of Toeplitz

matrix [66]:

$$\varphi_n(\boldsymbol{\varsigma}) = \kappa_n \begin{vmatrix} P_0 & P_{-1} & P_{-2} & \cdots & P_{-n} \\ P_1 & P_0 & P_{-1} & \cdots & P_{-n+1} \\ \cdots & \cdots & \cdots & \cdots & \cdots \\ P_{n-1} & P_{n-2} & P_{n-3} & \cdots & P_{-1} \\ 1 & \boldsymbol{\varsigma} & \boldsymbol{\varsigma}^2 & \cdots & \boldsymbol{\varsigma}^n \end{vmatrix}, \quad \varphi_0(\boldsymbol{\varsigma}) = D_0^{-\frac{1}{2}} = P_0^{-\frac{1}{2}}, \tag{5.39}$$

where

$$\kappa_n = \left(D_{n-1}\, D_n\right)^{-\frac{1}{2}}, \tag{5.40}$$

$D_n = det(P_{q-l})_0^n$ is the determinant of Toeplitz matrix $\mathbf{P}_n = \left[P_{q-l}\right]_{q,\,l=0}^{n}$.

Consider the following important polynomials of $\boldsymbol{\varsigma}$ and $\overline{\mathbf{w}}$ [83]:

$$s_n(\boldsymbol{\varsigma}, \mathbf{w}) = \left[1 \;\boldsymbol{\varsigma}\; \boldsymbol{\varsigma}^2 \;\ldots\; \boldsymbol{\varsigma}^n\right] \mathbf{P}_n^{-1} \begin{bmatrix} 1 \\ \overline{\mathbf{w}} \\ \vdots \\ \overline{\mathbf{w}}^{\,n} \end{bmatrix}, \tag{5.41}$$

The polynomials $s_n(\boldsymbol{\varsigma}, \mathbf{w})$ are called kernel polynomials, which reproduce the inverse of matrices $\mathbf{P}_n$. More importantly, using eq. (5.38), the kernel polynomials $s_n(\boldsymbol{\varsigma}, \mathbf{w})$ can be written as the Cholesky decomposition

$$s_n(\boldsymbol{\varsigma}, \mathbf{w}) = \sum_{k=0}^{n} \varphi_k(\boldsymbol{\varsigma}) \overline{\varphi_k(\mathbf{w})}. \tag{5.42}$$

The following identity holds for any polynomial $g(\boldsymbol{\varsigma})$ of degree not greater than n, i.e. when $g(\boldsymbol{\varsigma})$ is an arbitrary π_n [83]:

$$\frac{1}{2\pi i} \int_{|\boldsymbol{\varsigma}|=1} s_n(\boldsymbol{\varsigma}, \mathbf{w}) \overline{g(\boldsymbol{\varsigma})} f(\boldsymbol{\varsigma}) \frac{d\boldsymbol{\varsigma}}{\boldsymbol{\varsigma}} = \overline{g(\mathbf{w})}. \tag{5.43}$$

If we represent $g(\boldsymbol{\varsigma})$ in the form:

$$g(\boldsymbol{\varsigma}) = v_0 \varphi_0(\boldsymbol{\varsigma}) + v_1 \varphi_1(\boldsymbol{\varsigma}) + \cdots + v_n \varphi_n(\boldsymbol{\varsigma}), \tag{5.44}$$

where $v_0,\ v_1,\ \ldots,\ v_n$ are complex variables, then eq. (5.43) will be

$$\sum_{k=0}^{n} \overline{v}_k \overline{\varphi_k(\mathbf{w})} = \overline{g(\mathbf{w})}. \tag{5.45}$$

Thus, $s_n(\varsigma, \mathbf{w})$ is the only polynomial of degree n in ς that satisfies eq. (5.43).

Let us assume that $\overline{\varphi_n^*(0)} = \varphi_{nn} = \kappa_n$ where κ_n is defined by eq. (5.40). The polynomials $\varphi_n(\varsigma)$, orthogonal on unit circle, satisfy the relations:

$$\kappa_n \varsigma \varphi_n(\varsigma) = \kappa_{n+1}\varphi_{n+1}(\varsigma) - \varphi_{n+1}(0)\varphi_{n+1}^*(\varsigma), \tag{5.46a}$$

$$\kappa_n \varphi_{n+1}(\varsigma) = \kappa_{n+1}\, \varsigma\, \varphi_n(\varsigma) \,+\, \varphi_{n+1}(0)\varphi_n^*(\varsigma), \tag{5.46b}$$

where $\varphi_{n+1}(0) = \varphi_{0\,n+1}$, and Christoffel-Darboux formulae:

$$s_n(\varsigma, \mathbf{w}) = \frac{\varphi_{n+1}^*(\varsigma)\,\overline{\varphi_{n+1}^*(\mathbf{w})} - \,\varphi_{n+1}(\varsigma)\,\overline{\varphi_{n+1}(\mathbf{w})}}{1 - \varsigma\,\overline{\mathbf{w}}}, \tag{5.47a}$$

$$s_n(\varsigma, \mathbf{w}) = \frac{\varphi_n^*(\varsigma)\,\overline{\varphi_n^*(\mathbf{w})} - \,\varsigma\,\overline{\mathbf{w}}\,\varphi_n(\varsigma)\,\overline{\varphi_n(\mathbf{w})}}{1 - \varsigma\,\overline{\mathbf{w}}}. \tag{5.47b}$$

Szegö [157] gave the proof of eq. (5.46) and (5.47) using the orthogonality conditions and Geronimus [64] showed the proof by induction; we will show both of them below. To distiguish between eqs. (5.42) and (5.47a), let $\widetilde{s}_n(\varsigma, \mathbf{w})$ denote a formula given by eq. (5.47a):

$$\widetilde{s}_n(\varsigma, \mathbf{w}) = \frac{\varphi_{n+1}^*(\varsigma)\overline{\varphi_{n+1}^*(\mathbf{w})} - \varphi_{n+1}(\varsigma)\overline{\varphi_{n+1}(\mathbf{w})}}{1 - \varsigma\overline{\mathbf{w}}}, \tag{5.48}$$

We want to show that eqs. (5.42) and (5.48) are equal. Introducing eq. (5.48) into eq. (5.43) yields

$$\begin{aligned} &\frac{1}{2\pi i}\int_{|\varsigma|=1} \widetilde{s}_n(\varsigma, \mathbf{w})\overline{g(\varsigma)}f(\varsigma)\frac{d\varsigma}{\varsigma} \qquad (5.49)\\ =&\frac{1}{2\pi i}\int_{|\varsigma|=1} \frac{\varphi_{n+1}^*(\varsigma)\overline{\varphi_{n+1}^*(\mathbf{w})} - \varphi_{n+1}(\varsigma)\overline{\varphi_{n+1}(\mathbf{w})}}{1 - \varsigma\overline{\mathbf{w}}}\overline{g(\varsigma)}f(\varsigma)\frac{d\varsigma}{\varsigma} \end{aligned}$$

$$=\overline{g(\mathbf{w})}\frac{1}{2\pi i}\int_{|\varsigma|=1} \frac{\varphi_{n+1}^*(\varsigma)\overline{\varphi_{n+1}^*(\mathbf{w})} - \varphi_{n+1}(\mathbf{z})\overline{\varphi_{n+1}(\mathbf{w})}}{1 - \varsigma\overline{\mathbf{w}}}f(\varsigma)\frac{d\varsigma}{\varsigma} \tag{5.50}$$

$$+\frac{1}{2\pi i}\int_{|\varsigma|=1} \{\varphi_{n+1}^*(\varsigma)\overline{\varphi_{n+1}^*(\mathbf{w})} - \varphi_{n+1}(\varsigma)\overline{\varphi_{n+1}(\mathbf{w})}\}\frac{\overline{g(\varsigma)} - \overline{g(\mathbf{w})}}{1 - \varsigma\overline{\mathbf{w}}}f(\varsigma)\frac{d\varsigma}{\varsigma}.$$

Assume that $g(\varsigma) - g(\mathbf{w}) = (\mathbf{z} - \mathbf{w})r(\varsigma)$, where $r(\varsigma)$ is a polynomial of degree $n-1$. Then

$$\frac{\overline{g(\varsigma)} - \overline{g(\mathbf{w})}}{1 - \varsigma\,\overline{\mathbf{w}}} = \frac{\overline{r(\varsigma)}(\overline{\varsigma} - \overline{\mathbf{w}})}{\varsigma\,(\overline{\varsigma} - \overline{\mathbf{w}})} = \overline{\varsigma}\,\overline{r(\varsigma)}. \tag{5.51}$$

Taking into account eq. (5.51) and the orthogonality condition, eq. (5.74), the last integral in eq. (5.49) vanishes, since

$$\frac{1}{2\pi i}\int_{|\varsigma|=1} \varphi^*_{n+1}(\varsigma)\overline{\varsigma}\,\overline{r(\varsigma)}f(\varsigma)\frac{d\varsigma}{\varsigma} = \frac{1}{2\pi}\int_{-\pi}^{+\pi} \varphi^*_{n+1}(\varsigma)\overline{\varsigma}\,\overline{r(\varsigma)}f(\theta)d\theta = 0, \quad \varsigma = e^{i\,\theta}, \tag{5.52}$$

$$\frac{1}{2\pi i}\int_{|\varsigma|=1} \varphi_{n+1}(\varsigma)\overline{\varsigma}\,\overline{r(\varsigma)}f(\varsigma)\frac{d\varsigma}{\varsigma} = \frac{1}{2\pi}\int_{-\pi}^{+\pi} \varphi_{n+1}(\varsigma)\overline{\varsigma}\,\overline{r(\varsigma)}f(\theta)d\theta = 0, \quad \varsigma = e^{i\,\theta}. \tag{5.53}$$

Thus,

$$\frac{1}{2\pi i}\int_{|\varsigma|=1} \widetilde{s}_n(\varsigma, \mathbf{w})\overline{g(\varsigma)}f(\varsigma)\frac{d\varsigma}{\varsigma} = \overline{g(\mathbf{w})}c(\mathbf{w}) \tag{5.54}$$

where $c(\mathbf{w})$ is independent of ς:

$$c(\mathbf{w}) = \frac{1}{2\pi i}\int_{|\varsigma|=1} \frac{\overline{\varphi^*_{n+1}(\mathbf{w})}\varphi^*_{n+1}(\varsigma) - \varphi_{n+1}(\varsigma)\overline{\varphi_{n+1}(\mathbf{w})}}{1 - \varsigma\overline{\mathbf{w}}} f(\varsigma)\frac{d\varsigma}{\varsigma}. \tag{5.55}$$

Comparison of eq. (5.43) and (5.54) yields

$$s(\varsigma, \mathbf{w}) = \frac{\widetilde{s}(\varsigma, \mathbf{w})}{c(\mathbf{w})}, \tag{5.56}$$

or

$$\widetilde{s}(\varsigma, \mathbf{w}) = c(\mathbf{w})s(\varsigma, \mathbf{w}). \tag{5.57}$$

Swapping the variables ς and $\mathbf{w}$, and taking the conjugate-complex values of both sides of eq. (5.57) yields

$$\overline{\widetilde{s}(\mathbf{w}, \varsigma)} = \overline{c(\varsigma)}\,\overline{s(\mathbf{w}, \varsigma)}, \tag{5.58}$$

or

$$\frac{\overline{\varphi^*_{n+1}(\mathbf{w})}\varphi^*_{n+1}(\varsigma) - \overline{\varphi_{n+1}(\mathbf{w})}\varphi_{n+1}(\varsigma)}{1 - \overline{\mathbf{w}}\varsigma} = \overline{c(\varsigma)}\sum_{k=0}^{n}\overline{\varphi_k(\mathbf{w})}\varphi_k(\varsigma). \tag{5.59}$$

Since we already know that c is independent of $\boldsymbol{\varsigma}$, $\overline{c}$ does not depend on $\overline{\boldsymbol{\varsigma}}$; therefore, c defined by eq. (5.55) is independent of $\mathbf{w}$ too. Moreover, if we take $\boldsymbol{\varsigma} = \mathbf{w} = 0$ in eq. (5.57), we have

$$\text{RHS}: \quad \overline{\varphi^*_{n+1}(0)}\varphi^*_{n+1}(0) - \varphi_{n+1}(0)\overline{\varphi_{n+1}(0)} = \kappa^2_{n+1} - |\varphi_{n+1}(0)|^2 = \kappa^2_n \tag{5.60a}$$

$$\text{LHS}: \quad c\sum_{k=0}^{n}\overline{\varphi_k(0)}\varphi_k(0) = c\sum_{k=0}^{n}|\varphi_k(0)|^2 = c\,\kappa^2_n \tag{5.60b}$$

$$\text{RHS} = \text{LHS}: \quad \text{if} \quad c = 1, \tag{5.60c}$$

In eq. (5.60c), the right hand side (RHS) is equal to the left hand side (LHS) only if $c = 1$. Thus,

$$\widetilde{s}(\boldsymbol{\varsigma}, \mathbf{w}) = s(\boldsymbol{\varsigma}, \mathbf{w}). \tag{5.61}$$

Let us now give Geronimus' [64] proof of the Christoffel-Darboux formulae (5.47a)-(5.47b) by induction. To show the proof, let us find the sum

$$s_{n+1}(\boldsymbol{\varsigma}, \mathbf{w}) = \sum_{k=0}^{n+1}\varphi_k(\boldsymbol{\varsigma})\overline{\varphi_k(\mathbf{w})} = s_n(\boldsymbol{\varsigma}, \mathbf{w}) + \varphi_{n+1}(\boldsymbol{\varsigma})\overline{\varphi_{n+1}(\mathbf{w})}. \tag{5.62}$$

Introducing one of Christoffel-Darboux formulas, eq. (5.47b) into (5.62) yields

$$s_{n+1}(\boldsymbol{\varsigma}, \mathbf{w})\big(1 - \boldsymbol{\varsigma}\,\overline{\mathbf{w}}\big) = \varphi^*_n(\boldsymbol{\varsigma})\,\overline{\varphi^*_n(\mathbf{w})} - \boldsymbol{\varsigma}\,\overline{\mathbf{w}}\,\varphi_n(\boldsymbol{\varsigma})\,\overline{\varphi_n(\mathbf{w})} + \big(1 - \boldsymbol{\varsigma}\,\overline{\mathbf{w}}\big)\varphi_{n+1}(\boldsymbol{\varsigma})\overline{\varphi_{n+1}(\mathbf{w})}. \tag{5.63}$$

The recursive relations (5.46a) and (5.46b) yield

$$\boldsymbol{\varsigma}\varphi_n(\boldsymbol{\varsigma}) = \frac{\kappa_{n+1}}{\kappa_n}\varphi_{n+1}(\boldsymbol{\varsigma}) - \frac{\varphi_{n+1}(0)}{\kappa_n}\varphi^*_{n+1}(\boldsymbol{\varsigma}), \tag{5.64a}$$

$$\varphi^*_n(\boldsymbol{\varsigma}) = \frac{\kappa_n}{\varphi_{n+1}(0)}\varphi_{n+1}(\boldsymbol{\varsigma}) - \frac{\kappa_{n+1}}{\varphi_{n+1}(0)}\,\boldsymbol{\varsigma}\,\varphi_n(\boldsymbol{\varsigma}), \tag{5.64b}$$

where $\varphi_{n+1}(0) = \varphi_{0\,n+1}$. Plugging eq. (5.64a) into eq. (5.64b), and taking into account the last equality in eq. (5.60a) lead to

$$\varphi^*_n(\boldsymbol{\varsigma}) = \frac{\overline{\varphi_{n+1}(0)}}{\kappa_n}\varphi_{n+1}(\boldsymbol{\varsigma}) - \frac{\kappa_{n+1}}{\kappa_n}\,\boldsymbol{\varsigma}\,\varphi_n(\boldsymbol{\varsigma}). \tag{5.65}$$

Introducing eqs. (5.64a) and (5.65) into (5.63), and incorporating again the last equality

in eq. (5.60a), complete the proof by induction:

$$\begin{aligned}
s_{n+1}(\varsigma,\mathbf{w})\big(1-\varsigma\,\overline{\mathbf{w}}\big) &= \big(1-\varsigma\,\overline{\mathbf{w}}\big)\varphi_{n+1}(\varsigma)\overline{\varphi_{n+1}(\mathbf{w})} \\
&+ \Big[\frac{\overline{\varphi_{n+1}(0)}}{\kappa_n}\varphi_{n+1}(\varsigma) - \frac{\kappa_{n+1}}{\kappa_n}\,\varsigma\,\varphi_n(\varsigma)\Big]\Big[\frac{\varphi_{n+1}(0)}{\kappa_n}\overline{\varphi_{n+1}(\mathbf{w})} - \frac{\kappa_{n+1}}{\kappa_n}\,\overline{\mathbf{w}}\,\overline{\varphi_n(\mathbf{w})}\Big] \\
&+ \Big[\frac{\kappa_{n+1}}{\kappa_n}\varphi_{n+1}(\varsigma) - \frac{\varphi_{n+1}(0)}{\kappa_n}\varphi^*_{n+1}(\varsigma)\Big]\Big[\frac{\kappa_{n+1}}{\kappa_n}\overline{\varphi_{n+1}(\mathbf{w})} - \frac{\overline{\varphi_{n+1}(0)}}{\kappa_n}\overline{\varphi^*_{n+1}(\mathbf{w})}\Big] \\
&= \big(1-\varsigma\,\overline{\mathbf{w}}\big)\varphi_{n+1}(\varsigma)\overline{\varphi_{n+1}(\mathbf{w})} + \varphi^*_{n+1}(\varsigma)\,\overline{\varphi^*_{n+1}(\mathbf{w})} - \varphi_{n+1}(\varsigma)\,\overline{\varphi_{n+1}(\mathbf{w})} \\
&= \varphi^*_{n+1}(\varsigma)\,\overline{\varphi^*_{n+1}(\mathbf{w})} - \varsigma\,\overline{\mathbf{w}}\varphi_{n+1}(\varsigma)\overline{\varphi_{n+1}(\mathbf{w})}, \qquad (5.66)
\end{aligned}$$

or

$$s_{n+1}(\varsigma,\mathbf{w}) = \frac{\varphi^*_{n+1}(\varsigma)\,\overline{\varphi^*_{n+1}(\mathbf{w})} - \varsigma\,\overline{\mathbf{w}}\varphi_{n+1}(\varsigma)\overline{\varphi_{n+1}(\mathbf{w})}}{1-\varsigma\,\overline{\mathbf{w}}}. \qquad (5.67)$$

The equivalence of Christoffel-Darboux formulas (5.47a) and (5.47b) can be shown incorporating eqs. (5.62) and (5.67) :

$$\begin{aligned}
s_n(\varsigma,\mathbf{w}) &= \frac{\varphi^*_n(\varsigma)\,\overline{\varphi^*_n(\mathbf{w})} - \varsigma\,\overline{\mathbf{w}}\,\varphi_n(\varsigma)\,\overline{\varphi_n(\mathbf{w})}}{1-\varsigma\,\overline{\mathbf{w}}} \\
&= s_{n+1}(\varsigma,\mathbf{w}) - \varphi_{n+1}(\varsigma)\overline{\varphi_{n+1}(\mathbf{w})} \\
&= \frac{\varphi^*_{n+1}(\varsigma)\,\overline{\varphi^*_{n+1}(\mathbf{w})} - \varsigma\,\overline{\mathbf{w}}\varphi_{n+1}(\mathbf{z})\overline{\varphi_{n+1}(\mathbf{w})} - (1-\varsigma\,\overline{\mathbf{w}})\varphi_{n+1}(\varsigma)\overline{\varphi_{n+1}(\mathbf{w})}}{1-\varsigma\,\overline{\mathbf{w}}} \\
&= \frac{\varphi^*_{n+1}(\varsigma)\,\overline{\varphi^*_{n+1}(\mathbf{w})} - \varphi_{n+1}(\varsigma)\overline{\varphi_{n+1}(\mathbf{w})}}{1-\varsigma\,\overline{\mathbf{w}}}. \qquad (5.68)
\end{aligned}$$

Let us write the Christoffel-Darboux formula (5.47a) as

$$s_n(\varsigma,\mathbf{w}) = \sum_{k=0}^{n-1}\varphi_k(\varsigma)\overline{\varphi_k(\mathbf{w})} + \varphi_n(\varsigma)\overline{\varphi}_{nn}\,\overline{\mathbf{w}}^n \qquad (5.69)$$

$$= \frac{\varphi^*_{n+1}(\varsigma)\,\varphi_{0\,n+1}\overline{\mathbf{w}}^{\,n+1} - \varphi_{n+1}(\varsigma)\,\overline{\varphi}_{n+1\,n+1}\overline{\mathbf{w}}^{\,n+1}}{(\mathbf{w}-\varsigma)\,\overline{\mathbf{w}}}. \qquad (5.70)$$

A comparison of coefficients of $\overline{\mathbf{w}}^n$ yields

$$-\varsigma\,\overline{\varphi}_{nn}\varphi_n(\varsigma) = \varphi_{0\,n+1}\varphi^*_{n+1}(\varsigma) - \overline{\varphi}_{n+1\,n+1}\,\varphi_{n+1}(\varsigma) \qquad (5.71)$$

or since $\overline{\varphi}_{nn} = \varphi_{nn} = \overline{\kappa}_n = \kappa_n$

$$\varsigma\,\kappa_n\varphi_n(\varsigma) = \kappa_{\,n+1}\,\varphi_{n+1}(\varsigma) - \varphi_{0\,n+1}\varphi^*_{n+1}(\varsigma), \qquad (5.72)$$

which is the same as eq. (5.46a).

5.2.2 Biorthogonal polynomials

Baxter [14] generalized the findings for orthogonal polynomials and introduced biorthogonal Szegö polynomials. Let the function $f(\varsigma)$ be expanded into series (5.14) that absolutely converges at $|\varsigma| = 1$. Note that $\overline{\varsigma} = \frac{1}{\varsigma}$ at $|\varsigma| = 1$. Two polynomial sequences

$$\varphi_n(\varsigma) = \varphi_{0\,n} + \varphi_{1\,n}\varsigma + \cdots + \varphi_{n\,n}\varsigma^n, \tag{5.73a}$$

$$\psi_m(\varsigma) = \psi_{0\,m} + \psi_{1\,m}\varsigma + \cdots + \psi_{m\,m}\varsigma^m, \quad \varphi_{n\,n} = \psi_{n\,n} = c_n, \tag{5.73b}$$

are called biorthogonal and define a biorthogonal system of Szegö on a unit circle with respect to the function $f(\varsigma)$, if they satisfy the relation [14]

$$\frac{1}{2\pi}\int_{|\varsigma|=1} \varphi_n(\varsigma)\psi_m(\overline{\varsigma})f(\varsigma)\frac{d\varsigma}{i\,\varsigma} = \delta_{nm}, \tag{5.74}$$

or equivalently,[170]

$$\sum_{q=0}^{m}\psi_{qm}\sum_{l=0}^{n}P_{q-l}\varphi_{ln} = \delta_{nm}, \tag{5.75}$$

or

$$\begin{bmatrix} \psi_{00} & & & & \\ \psi_{01} & \psi_{11} & & \mathbf{0} & \\ \psi_{02} & \psi_{12} & \psi_{22} & & \\ \vdots & \vdots & \vdots & \ddots & \\ \psi_{0n} & \psi_{1n} & \psi_{2n} & \cdots & \psi_{nn} \end{bmatrix} \mathbf{P}_n \begin{bmatrix} \varphi_{00} & \varphi_{01} & \varphi_{02} & \cdots & \varphi_{0n} \\ & \varphi_{11} & \varphi_{12} & \cdots & \varphi_{1n} \\ & & \varphi_{22} & \cdots & \varphi_{2n} \\ & \mathbf{0} & & \ddots & \vdots \\ & & & & \varphi_{nn} \end{bmatrix} = \mathbf{I}. \tag{5.76}$$

Here the φ_{nn} multiplied by the last row of the lower triangular matrix defines the last row of inverse matrix $\mathbf{P}_n^{-1}$, and the last column of the upper triangular matrix multiplied by ψ_{nn} is the last column of $\mathbf{P}_n^{-1}$. Note the equality of coefficients $\varphi_{n\,n} = \psi_{n\,n} = c_n$ in eq. (5.73) that is required to uniquely determine (to within a plus or minus sign) $\varphi_n(\varsigma)$ and $\psi_n(\varsigma)$ [14].

Using eq. (5.76), the kernel polynomials $s_n(\varsigma, \mathbf{w})$ can be decomposed as

$$s_n(\varsigma, \mathbf{w}) = \sum_{k=0}^{n}\varphi_k(\varsigma)\psi_k(\overline{\mathbf{w}}) \tag{5.77}$$

by analogy to Cholesky decomposition. In a biorthogonal system of Szegö, the biorthogonal polynomials satisfy the following three term recurrence relations [170]:

$$c_{n+1}\begin{bmatrix}\varphi_{n+1}(\varsigma)\\ \\ \overline{\psi^*_{n+1}}(\varsigma)\end{bmatrix} = c_n\begin{bmatrix}\varsigma & \varphi_{0n+1}\\ \\ \varsigma\psi_{0n+1} & 1\end{bmatrix}\begin{bmatrix}\varphi_n(\varsigma)\\ \\ \overline{\psi^*_n}(\varsigma)\end{bmatrix} \tag{5.78}$$

and Christoffel-Darboux formulae:

$$s_n(\varsigma,\mathbf{w}) = \frac{\overline{\varphi^*_{n+1}(\mathbf{w})}\overline{\psi^*_{n+1}}(\varsigma) - \varphi_{n+1}(\varsigma)\psi_{n+1}(\overline{\mathbf{w}})}{1-\varsigma\overline{\mathbf{w}}}, \tag{5.79a}$$

$$s_n(\varsigma,\mathbf{w}) = \frac{\overline{\varphi^*_n(\mathbf{w})}\overline{\psi^*_n}(\varsigma) - \varsigma\overline{\mathbf{w}}\varphi_n(\varsigma)\psi_n(\overline{\mathbf{w}})}{1-\varsigma\overline{\mathbf{w}}}, \tag{5.79b}$$

where

$$\overline{\varphi^*_n(\mathbf{w})} = \varphi_{n\,n} + \varphi_{n-1\,n}\overline{\mathbf{w}} + \cdots + \varphi_{0\,n}\overline{\mathbf{w}}^{\,n} = \varsigma^n\varphi_{\,n}(\overline{\mathbf{w}}^{\,-1}). \tag{5.80a}$$

$$\overline{\psi^*_n}\,(\varsigma) = \psi_{n\,n} + \psi_{n-1\,n}\,\varsigma + \cdots + \psi_{0\,n}\,\varsigma^{\,n} = \varsigma^{\,n}\psi_{\,n}(\varsigma^{-1}). \tag{5.80b}$$

If the leading principal minors of matrix $\mathbf{P}_n$ are nonzero then, the inverse matrix $\mathbf{P}_n^{-1}$ can be reproduced using Christoffel-Darboux formulae. For example, introducing eq. (5.41) into eq. (5.79b) leads to:

$$(1-\varsigma\overline{\mathbf{w}})s_n(\varsigma,\mathbf{w}) = (1-\varsigma\overline{\mathbf{w}})\big[1\ \varsigma\ \varsigma^2\ \ldots\ \varsigma^n\big]\mathbf{P}_n^{-1}\begin{bmatrix}1\\ \overline{\mathbf{w}}\\ \vdots\\ \overline{\mathbf{w}}^{\,n}\end{bmatrix}$$

$$= \big[1\ \varsigma\ \varsigma^2\ \ldots\ \varsigma^{n+1}\big]\left\{\begin{bmatrix}\mathbf{P}_n^{-1} & 0\\ 0 & 0\end{bmatrix} - \begin{bmatrix}0 & 0\\ 0 & \mathbf{P}_n^{-1}\end{bmatrix}\right\}\begin{bmatrix}1\\ \overline{\mathbf{w}}\\ \vdots\\ \overline{\mathbf{w}}^{\,n+1}\end{bmatrix}$$

$$
\begin{aligned}
=&\left[1\ \varsigma\ \varsigma^2\ \dots\ \varsigma^{n+1}\right]\Bigg\{\begin{bmatrix}\psi_{nn}\\ \psi_{n-1\,n}\\ \vdots\\ \psi_{0\,n}\\ 0\end{bmatrix}\left[\varphi_{n\,n}\ \varphi_{n-1\,n}\ \dots\ \varphi_{0\,n}\,0\right]\\
&-\begin{bmatrix}0\\ \varphi_{0n}\\ \varphi_{1\,n}\\ \vdots\\ \varphi_{n\,n}\end{bmatrix}\left[0\ \psi_{0\,n}\ \psi_{1\,n}\ \dots\ \psi_{n\,n}\right]\Bigg\}\begin{bmatrix}1\\ \overline{\mathbf{w}}\\ \vdots\\ \overline{\mathbf{w}}^{\,n+1}\end{bmatrix}. \qquad (5.81)
\end{aligned}
$$

Thus, the elements of inverse matrix $[\mathbf{P}_n^{-1}]$ have the form

$$
[\mathbf{P}_n^{-1}]_{ql} = [\mathbf{P}_n^{-1}]_{q-1\,l-1} + \psi_{n-q\,n}\varphi_{n-l\,n} - \varphi_{q-1\,n}\psi_{l-1\,n}, \quad (0 \le q,\, l \le n). \qquad (5.82)
$$

This formula is analogous to Trench's [167] inversion formula for $\mathbf{P}_n$ matrix, the Levinson-type recursion algorithm. Summing up the increments $[\mathbf{P}_n^{-1}]_{ql} - [\mathbf{P}_n^{-1}]_{q-1\,l-1}$, the inverse matrix $[\mathbf{P}_n^{-1}]$ can be written explicitly in the matrix form:

$$
\mathbf{P}_n^{-1} = \begin{bmatrix}
\varphi_{nn}\psi_{nn} & \varphi_{n-1\,n}\psi_{nn} & \cdots & \varphi_{1n}\psi_{nn} & \varphi_{0n}\psi_{nn}\\
\varphi_{nn}\psi_{n-1\,n} & \cdots & \cdots & \cdots & \varphi_{1n}\psi_{nn}\\
\vdots & \cdots & \cdots & \cdots & \vdots\\
\varphi_{nn}\psi_{1\,n} & \cdots & \cdots & \cdots & \varphi_{n-1\,n}\psi_{nn}\\
\varphi_{nn}\psi_{0\,n} & \varphi_{nn}\psi_{1n} & \cdots & \varphi_{nn}\psi_{n-1\,n} & \varphi_{nn}\psi_{nn}
\end{bmatrix}
$$

$$= \begin{bmatrix} \psi_{nn} & & & 0 \\ \psi_{n-1\,n} & \psi_{nn} & & \\ \vdots & \vdots & \ddots & \\ \psi_{0\,n} & \psi_{1n} & \cdots & \psi_{nn} \end{bmatrix} \begin{bmatrix} \varphi_{nn} & \varphi_{n-1\,n} & \cdots & \varphi_{0n} \\ & \varphi_{n\,n} & \cdots & \varphi_{1n} \\ & & \ddots & \vdots \\ 0 & & & \varphi_{n\,n} \end{bmatrix}$$

$$- \begin{bmatrix} 0 & & & 0 \\ \varphi_{0n} & 0 & & \\ \vdots & \ddots & \ddots & \\ \varphi_{n-1\,n} & \cdots & \varphi_{0n} & 0 \end{bmatrix} \begin{bmatrix} 0 & \psi_{0n} & \cdots & \psi_{n-1\,n} \\ & \ddots & \ddots & \vdots \\ & & 0 & \psi_{0n} \\ 0 & & & 0 \end{bmatrix}. \tag{5.83}$$

Here, the inverse of Toeplitz matrix $\mathbf{P}_n^{-1}$ is represented as the difference of multiplications of two semicurculant matrices, i.e. the lower and upper triangular Toeplitz matrices. Alternative derivation of matrix inverse was given by Baxter and Hirschman [16], they showed that the inverse of $\mathbf{P}_n$ can be uniquely defined by the solutions of the system [65]

$$\sum_{l=0}^{n} P_{q-l}\, x_l = \delta_{q\,0}, \qquad \sum_{l=0}^{n} P_{q-l}\, y_{l-n} = \delta_{q\,n}, \qquad (q = 0, 1, \ldots n) \tag{5.84}$$

if the polynomials

$$\chi(\varsigma) = \sum_{q=0}^{n} x_q\, \varsigma^q, \quad \gamma(\varsigma) = \sum_{q=0}^{n} y_{-q}\, \varsigma^q \tag{5.85}$$

are not zero in $|\varsigma| \le 1$. For $x_0 \neq 0$, Gohberg and Semencul [65] showed that if the system (5.84) has solutions then the matrix $\mathbf{P}_n$ is nondegenerate, and derived an explicit formula for its inverse:

$$\mathbf{P}_n^{-1} = x_0^{-1} \left\{ \begin{bmatrix} x_0 & 0 & \cdots & 0 \\ x_1 & x_0 & \cdots & 0 \\ \cdots & \cdots & \cdots & 0 \\ x_n & x_{n-1} & \cdots & x_0 \end{bmatrix} \begin{bmatrix} y_0 & y_{-1} & \cdots & y_{-n} \\ 0 & y_0 & \cdots & y_{-n+1} \\ \cdots & \cdots & \cdots & \cdots \\ 0 & 0 & \cdots & y_0 \end{bmatrix} \right.$$

$$\left. - \begin{bmatrix} 0 & 0 & 0 & \cdots & 0 & 0 \\ y_{-n} & 0 & 0 & \cdots & 0 & 0 \\ y_{-n+1} & y_{-n} & 0 & \cdots & 0 & 0 \\ \cdots & \cdots & \cdots & \cdots & \cdots & \cdots \\ y_{-1} & y_{-2} & y_{-3} & \cdots & y_{-n} & 0 \end{bmatrix} \begin{bmatrix} 0 & x_n & x_{n-1} & \cdots & x_1 \\ 0 & 0 & x_n & \cdots & x_2 \\ \cdots & \cdots & \cdots & \cdots & \cdots \\ 0 & 0 & 0 & \cdots & x_n \\ 0 & 0 & 0 & \cdots & 0 \end{bmatrix} \right\}. \tag{5.86}$$

If the matrix $\mathbf{P}_n$ has a block Toeplitz structure, its inverse $\mathbf{P}_n^{-1}$ can be formed analogously by elements of its first and last block columns, and first and last block rows [185]. See Section 5.3.4 for more details.

5.3 Iterative methods for solution of a linear system of equations

In this section, we deal with the numerical resolution of a complex-valued linear system of equations (4.16). In eq. (4.16), the matrix $\mathbb{X}$ has some interesting features. Its block diagonals are identity matrices, and off-diagonal blocks are obtained by multiplying the matrix $\mathbf{T}^{(j)}$ by $\mathbf{P}^{j,m}$, which allows us to solve eq. (4.16) using direct linear solvers. Nonetheless, for a large number of scatterers, especially for high frequencies, eq. (4.16) becomes a large-scale complex-valued linear system. Its complexity grows as the number of scatterers and frequency increase, and its solution by direct method requires excessive computational time and memory to store the system, requiring the development of iterative algorithms. To solve this system, we consider next some iterative approaches suitable for parallel computing.

5.3.1 A Neumann series expansion at a fixed value of frequency

The matrix $\mathbb{X}$ can be decomposed into two parts:

$$\mathbb{X} = \mathbb{I} - \mathbb{T}\,\mathbb{P}, \tag{5.87}$$

where

$$\mathbb{T} = \begin{bmatrix} \mathbf{T}^{(1)} & \mathbf{0} & \mathbf{0} & \cdots & \mathbf{0} \\ \mathbf{0} & \mathbf{T}^{(2)} & \mathbf{0} & \cdots & \mathbf{0} \\ \vdots & \vdots & \vdots & \ddots & \vdots \\ \mathbf{0} & \mathbf{0} & \mathbf{0} & \cdots & \mathbf{T}^{(M)} \end{bmatrix}, \quad \mathbb{I} = \begin{bmatrix} \mathbf{I} & \mathbf{0} & \mathbf{0} & \cdots & \mathbf{0} \\ \mathbf{0} & \mathbf{I} & \mathbf{0} & \cdots & \mathbf{0} \\ \vdots & \vdots & \vdots & \ddots & \vdots \\ \mathbf{0} & \mathbf{0} & \mathbf{0} & \cdots & \mathbf{I} \end{bmatrix}, \tag{5.88}$$

$$\mathbb{P} = \begin{bmatrix} \mathbf{0} & \mathbf{P}^{1,2} & \mathbf{P}^{1,3} & \cdots & \mathbf{P}^{1,M} \\ \mathbf{P}^{2,1} & \mathbf{0} & \mathbf{P}^{2,3} & \cdots & \mathbf{P}^{2,M} \\ \vdots & \vdots & \vdots & \ddots & \vdots \\ \mathbf{P}^{M,1} & \mathbf{P}^{M,2} & \mathbf{P}^{M,3} & \cdots & \mathbf{0} \end{bmatrix}. \tag{5.89}$$

In eq. (4.17), the purely geometrical part $\mathbb{P}$ depends on the position vector $\boldsymbol{l}_{jm}$ and takes into account the interaction between the scatterers, whereas the purely physical part $\mathbb{T}$ depends on the shape and the physical properties of the shell material, as well as the boundary conditions on the interfaces. Moreover, the matrix $\mathbb{P}$ has an interesting structure, each of its off diagonal block elements $\mathbf{P}^{j,m}$ is a Toeplitz matrix. The advantage of this structure will be studied and taken into account in the subsequent sections.

Plugging eq. (5.87) into eq. (4.16) yields

$$\big[\mathbb{I} - \mathbb{T}\,\mathbb{P}\big]\,\mathbf{b} = \mathbb{T}\mathbf{a}, \tag{5.90}$$

where

$$\mathbf{a} = \begin{pmatrix} \mathbf{a}^{(1)} \\ \mathbf{a}^{(2)} \\ \vdots \\ \mathbf{a}^{(M)} \end{pmatrix}, \tag{5.91}$$

where $\mathbf{a}^{(j)}, (j = \overline{1, M})$ vectors are defined by eq. (4.19). Solving eq. (5.90) for $\mathbf{b}$, and using Neumann expansion, we obtain, formally at least,

$$\begin{aligned} \mathbf{b} &= \sum_{i=0}^{\infty} \widetilde{\boldsymbol{b}}^{(i)} = \big[\mathbb{I} - \mathbb{T}\,\mathbb{P}\big]^{-1}\mathbb{T}\mathbf{a} = \big[\mathbb{I} + \mathbb{T}\,\mathbb{P} + \mathbb{T}\,\mathbb{P}\,\mathbb{T}\,\mathbb{P} + \cdots\big]\mathbb{T}\mathbf{a} \\ &= \big[\mathbb{T} + \mathbb{T}\,\mathbb{P}\mathbb{T} + \mathbb{T}\,\mathbb{P}\,\mathbb{T}\,\mathbb{P}\mathbb{T} + \cdots\big]\mathbf{a} \\ &= \mathbb{T}\big[\mathbb{T}^{-1} + \mathbb{P} + \mathbb{P}\mathbb{T}\,\mathbb{P} + \mathbb{P}\mathbb{T}\mathbb{P}\mathbb{T}\,\mathbb{P} + \cdots\big]\,\mathbb{T}\mathbf{a} \\ &= \mathbb{T}\big[\mathbb{I} + \mathbb{P}\,\mathbb{T} + \mathbb{P}\,\mathbb{T}\,\mathbb{P}\mathbb{T} + \cdots\big]\mathbf{a}, \end{aligned} \tag{5.92}$$

where the $\widetilde{\boldsymbol{b}}^{(i)}$ terms can be defined iteratively

$$\widetilde{\boldsymbol{b}}^{(0)} = \mathbb{T}\mathbf{a} \tag{5.93}$$

and

$$\widetilde{\boldsymbol{b}}^{(i)} = \mathbb{T}\,\mathbb{P}\widetilde{\boldsymbol{b}}^{(i-1)}, \quad \text{for} \quad i \geq 1. \tag{5.94}$$

Note that this solution is convergent if the norm of matrix $\mathbb{T}\,\mathbb{P}$ is less than one: $||\mathbb{T}\,\mathbb{P}|| = |\lambda^{TP}_{max}| < 1$, where $|\lambda^{TP}_{max}|$ is the absolute value of the maximum eigenvalue of matrix $\mathbb{T}\,\mathbb{P}$.

We truncate the Neumann series (5.92) solution

$$\bar{\boldsymbol{b}}^{(I)} = \sum_{i=0}^{I} \widetilde{\boldsymbol{b}}^{(i)}, \tag{5.95}$$

and calculate the error

$$\Delta_{err}^{(I)} = max|\mathbf{b} - \bar{\boldsymbol{b}}^{(I)}|, \tag{5.96}$$

to study a validity of solution and a convergence rate of series.

5.3.2 An iterative approach for a band of frequencies

The approximation (5.92) is only valid for a fixed value of frequency ω. Considering some frequency band, we need to use an iterative approach as follows. We may start with some initial value of frequency $\omega = \omega_0$ and calculate the inverse of matrix $\mathbb{X}$ at this fixed value of frequency to find $\mathbf{b}$

$$\mathbb{X}(\omega_0)\,\mathbf{b} = \mathbf{d} \quad \Rightarrow \quad \mathbf{b} = \mathbb{X}^{-1}(\omega_0)\mathbf{d}. \tag{5.97}$$

Now we change the frequency by small amount $\Delta\omega$ and define matrix $\mathbb{Y}$ such that

$$\mathbb{X}(\omega_0 + \Delta\omega) = \mathbb{X}(\omega_0) - \mathbb{Y} = \mathbb{X}(\omega_0)[\mathbb{I} - \mathbb{X}^{-1}(\omega_0)\mathbb{Y}], \tag{5.98}$$

where

$$\mathbb{Y} = \mathbb{X}(\omega_0) - \mathbb{X}(\omega_0 + \Delta\omega). \tag{5.99}$$

The inverse of matrix $\mathbb{X}(\omega_0 + \Delta\omega)$ can be obtained by means of Neumann series expansion

$$\begin{aligned} \mathbb{X}^{-1}(\omega_0 + \Delta\omega) &= [\mathbb{I} - \mathbb{X}^{-1}(\omega_0)\mathbb{Y}]^{-1}\mathbb{X}^{-1}(\omega_0) \\ &= [\mathbb{I} + \mathbb{W} + \mathbb{W}^2 + \mathbb{W}^3 + \cdots]\mathbb{X}^{-1}(\omega_0), \end{aligned} \tag{5.100}$$

where

$$\mathbb{W}(\omega_0) = \mathbb{X}^{-1}(\omega_0)\mathbb{Y}. \tag{5.101}$$

In eq. (5.100), the series expansion will converge if the norm of matrix $\mathbb{W}$ is less than one: $||\mathbb{W}|| = |\lambda_{max}^{W}| < 1$, where $|\lambda_{max}^{W}|$ is the absolute maximum eigenvalue of matrix $\mathbb{W}$. Continuing these steps iteratively allows us to find the inverse of matrix $\mathbb{X}$ at frequencies $\omega = \omega_0 + n \cdot \Delta\omega\,(n = 1, 2, ...N)$.

5.3.3 Fast preconditioned iterative methods

Background

Antoine et al. [7] studied an acoustic multiple scattering by circular obstacles at high frequencies and large number of obstacles and proposed fast iterative numerical methods for solving a large complex-valued dense linear system using its Toeplitz block structure. These methods yield a large memory saving; the efficiency of methods is shown for several general configurations by studying the convergence rate with respect to different geometrical parameters. They performed calculations considering GMRES and BICGSTAB iterative solvers and GMRES(η) with a restart parameter η.

Antoine et al. [8] studied numerically the solution of integral equations of multiple scattering by circular cylinders for a large band of frequencies and large number of obstacles. They proposed a method of robust and efficient solution of integral equations obtained via projection method on the base of Fourier series using an iterative solver (GMRES) with preconditioners, and presented examples of numerical simulation for multiple scattering at high frequency for a random configuration of cylinders. They took advantage of the Toeplitz structure of off-diagonal blocks of the linear system and stored a compressed version of the system using a root vector for the Toeplitz matrix. Two preconditioners were proposed to increase the convergence. The first preconditioner consists of diagonal terms including effects of single scattering, and leads to a matrix of the form: $\widehat{\mathbb{L}} = \mathbb{I} + \widehat{\mathbb{F}}$, where $\mathbb{I}$ is an identity matrix, and $\widehat{\mathbb{F}}$ contains off-diagonal blocks of system $\widehat{\mathbb{L}}$ with single scattering effects. This matrix representation is similar to our matrix $\mathbb{X}$ given by eq. (5.87). The second preconditioner is obtained by two successive approximations: first, keeping two terms in Neumann series expansion, and second, storing the blocks corresponding to interactions. A dependence of CPU time that was necessary for a construction of the system versus a number of cylinders M and wavenumber k, and a comparison of number of stored coefficients as function of M and k were presented for a full storage, and compressed storage with and without preconditioners.

Authors of [7] and [8] studied sound hard and sound soft cylinders considering

Dirichlet and Neumann boundary conditions. We will extend this approach presenting results for a different planar configuration of elastic cylinders and shells, and thin shells with internal structures.

Matrix vector product method

Consider a planar configuration with a large number of cylinders at high frequencies leading to a large scale complex valued linear system, eq. (4.16), where $\mathbb{X}$ is a complex valued, full, non-symmetric matrix of order $(2N+1)\cdot M$ with $N = N_j = N_m$. Here, each cylinder may have different physical properties and radii, i.e. the transition matrices $\mathbf{T}^{(j)}$, $(j = \overline{1, M})$ can be different and non-symmetric. We can take advantage of structure of matrix $\mathbb{X}$, defining it by eq. (5.87). As noted in Section 5.3.1, each of the block elements $\mathbf{P}^{j,m}$ of matrix $\mathbb{P}$ is a Toeplitz matrix. Using root vector $\mathbf{p}^{j,m}$ given by eq. (5.7) and the fast algorithm given in [36] for an MVP involving Toeplitz matrices, we can optimize a matrix vector product: $\mathbf{P}^{j,m}\mathbf{b}^{(m)}, (j, m = 1, 2, ..., M, j \neq m)$. This can be done by constructing circulant matrices [185] and applying a Fast Fourier Transform (FFT)-based MVP algorithm [36]. For example, it can be performed on Matlab with further use of iterative solvers such as GMRES or BICGStab [139].

The main cost of the GMRES algorithm is due to one matrix vector multiplication at each iteration.The multiplication (or MVP) $\mathbb{X}\mathbf{b}$ can be computed directly, according to the block structure of $\mathbb{X}$ and $\mathbf{b}$ given correspondingly by eq. (4.17) and (4.18), as follows:

$$\mathbb{X}\,\mathbf{b} = \begin{pmatrix} \mathbf{b}^{(1)} - \mathbf{T}^{(1)} \sum\limits_{m=2}^{M} \mathbf{P}^{1,m}\mathbf{b}^{(m)} \\ \vdots \\ \mathbf{b}^{(j)} - \mathbf{T}^{(j)} \sum\limits_{m=1, m\neq j}^{M} \mathbf{P}^{j,m}\mathbf{b}^{(m)} \\ \vdots \\ \mathbf{b}^{(M)} - \mathbf{T}^{(M)} \sum\limits_{m=1}^{M-1} \mathbf{P}^{M,m}\mathbf{b}^{(m)} \end{pmatrix}, \quad (j = \overline{1, M}). \tag{5.102}$$

FFT tricks

To accelerate the computation of MVP, eq. (5.102), we evaluate its components, i.e. the Toeplitz MVP: $\mathbf{P}^{j,m}\mathbf{b}^{(m)}$, using the root vector $\mathbf{p}^{j,m}$. The multiplication $\mathbf{P}^{j,m}\mathbf{b}^{(m)}$ cannot be directly computed by FFT; therefore, we associated a Toeplitz matrix with a Circulant matrix. A fast algorithm of computation of Circulant MVP, $\mathbf{f} = \mathbf{C}_i \cdot \mathbf{g}$, can be implemented using Matlab FFT and IFFT functions [36]

$$\mathbf{f} = IFFT[FFT(\mathbf{c}_i). * FFT(\mathbf{g})], \tag{5.103}$$

where $\mathbf{c}_i$ the first column of $\mathbf{C}_i$, generates the Circulant matrix $\mathbf{C}_i$ of order i.

The Circulant matrix associated with Toeplitz MVP can be constructed by embedding the Toeplitz matrix $\mathbf{P}^{j,m}$ of order $\widetilde{n} = 2N + 1$ into a larger Circulant matrix $\mathbf{C}_i$ of twice the order: $i = 2\widetilde{n}$. On Matlab, the first column $\mathbf{c}_i$ of the Circulant matrix $\mathbf{C}_i$ can be obtained from the root vector $\mathbf{p}^{j,m}$ defined by eq. (5.100):

$$\mathbf{p} = [\mathbf{P}(1, \widetilde{n} : -1 : 1) \ \text{transpose}(\mathbf{P}(2 : \widetilde{n}, 1))], \tag{5.104}$$

$$\mathbf{c}_i = [\text{transpose}([\mathbf{p}(\widetilde{n} : 2 * \widetilde{n} - 1) \ 0 \ \mathbf{p}(1 : \widetilde{n} - 1)])], \tag{5.105}$$

where $\mathbf{P} = \mathbf{P}^{j,m}_{lq}$, $\mathbf{p} = \mathbf{p}^{j,m}$ vector is of dimensions $(2\widetilde{n} - 1) \times 1$.

To compute $\mathbf{f} = \mathbf{P}^{j,m}_{ql} \cdot \mathbf{b}^{(j)}$, we introduce a new vector $\hat{\mathbf{b}} = [\mathbf{b}^{(j)} \, \mathbf{0}_{\widetilde{n}}]^T$ of length $2\widetilde{n}$ to match with the dimensions of the $\mathbf{C}_i$ matrix. Thus,

$$\tilde{\mathbf{f}} = \mathbf{C}_i\hat{\mathbf{b}} = \begin{pmatrix} \mathbf{P} & \mathbf{P}_1 \\ \mathbf{P}_1 & \mathbf{P} \end{pmatrix} \begin{pmatrix} \mathbf{b}^{(j)} \\ \mathbf{0}_n \end{pmatrix} = \begin{pmatrix} \mathbf{f} \\ \mathbf{P}_1\mathbf{b}^{(j)} \end{pmatrix}$$

$$= IFFT[FFT(\mathbf{c}_q). * FFT(\hat{\mathbf{b}})], \tag{5.106}$$

where $\mathbf{b}^{(j)}$ defined by eq. (4.18).

5.3.4 Iterative methods for a Block Toeplitz systems

Iterative method for BT matrix of level 1

For a configuration of one row or column of cylinders, the matrix $\mathbb{X}$ given by eq. (5.28) is a BT matrix of level one, i.e. $\mathbb{X} \in T_M G_{2N+1}$. Finding the inverse of a matrix that

has a specific structure does not always require finding of all elements of the inverse matrix. Instead it requires the development of algorithms that ensure the compact form of the inverse matrix and allow its fast multiplication on an arbitrary vector. Such an approach was proposed by Voevodin and Tyrtyshnikov [185] for BT matrix of level 1. We will use this method to find the inverse of $\mathbb{X}$ and solve the system (4.16) by adapting their notation.

For $0 \le m \le M-1$, let us denote by $\mathbb{X}_m$ the leading submatrix consisting of blocks $\boldsymbol{X}^1_{i-j}$ where $1 \le i, j \le m+1$; particularly $\mathbb{X}_{M-1} = \mathbb{X}$ and $\mathbb{X}^{-1} = \mathbb{X}^{-1}_{M-1}$. If all leading submatrices are nondegenerate, then according to Theorem 5.7 given in [185], for $\forall m$, the matrix $\mathbb{X}^{-1}_m$ can be restored using its first and last block columns, and first and last block rows. We will denote these block column and row vectors correspondingly by $\boldsymbol{x}^{(m)}_i$, $\boldsymbol{y}^{(m)}_i$, $\boldsymbol{z}^{(m)}_i$, $\boldsymbol{w}^{(m)}_i$ $(0 \le i \le m)$. Importantly, these block vectors can be calculated recursively, changing the index m from 0 to $M-1$.

Let $\mathbb{X}$ be a nondegenerate complex valued BT matrix of order M with blocks of order $2N+1$. Assume that the block vectors $\boldsymbol{x} = [\boldsymbol{x}_0\, \boldsymbol{x}_1\, \cdots\, \boldsymbol{x}_{M-1}]^T$ and $\boldsymbol{y} = [\boldsymbol{y}_0\, \boldsymbol{y}_1\, \cdots\, \boldsymbol{y}_{M-1}]^T$ satisfy equations:

$$\mathbb{X}\boldsymbol{x} = \boldsymbol{e}, \quad \mathbb{X}\boldsymbol{y} = \mathbb{J}\boldsymbol{e}, \tag{5.107}$$

and correspond to the first and the last block columns of inverse matrix $\mathbb{X}^{-1}$, and $\boldsymbol{z} = [\boldsymbol{z}_0\, \boldsymbol{z}_1\, \cdots\, \boldsymbol{z}_{M-1}]$ and $\boldsymbol{w} = [\boldsymbol{w}_0\, \boldsymbol{w}_1\, \cdots\, \boldsymbol{w}_{M-1}]$ satisfy equations:

$$\boldsymbol{z}\,\mathbb{X} = \boldsymbol{e}^T, \quad \boldsymbol{w}\,\mathbb{X} = \big(\mathbb{J}\boldsymbol{e}\big)^T, \tag{5.108}$$

and correspond to the first and the last block rows of inverse matrix $\mathbb{X}^{-1}$, where $\boldsymbol{e}$ is the unit block vector, and $\mathbb{J}$ is the permutation matrix:

$$\boldsymbol{e} = \begin{bmatrix} \mathbf{I} \\ \mathbf{0} \\ \vdots \\ \mathbf{0} \\ \mathbf{0} \end{bmatrix}, \quad \mathbb{J} = \begin{bmatrix} \mathbf{0} & \mathbf{0} & \cdots & \mathbf{0} & \mathbf{I} \\ \mathbf{0} & \mathbf{0} & \cdots & \mathbf{I} & \mathbf{0} \\ \vdots & \vdots & \vdots\vdots\vdots & \vdots & \vdots \\ \mathbf{0} & \mathbf{I} & \cdots & \mathbf{0} & \mathbf{0} \\ \mathbf{I} & \mathbf{0} & \cdots & \mathbf{0} & \mathbf{0} \end{bmatrix}, \tag{5.109}$$

where $\mathbf{I}$ is the block identity matrix of order $2N+1$. Then, if the blocks $\boldsymbol{x}_0$ and $\boldsymbol{y}_{M-1}$ are nondegenerate, and $\boldsymbol{x}_0 = \boldsymbol{z}_0$, $\boldsymbol{y}_{M-1} = \boldsymbol{w}_{M-1}$, the inverse of matrix $\mathbb{X}$ can be obtained

by:

$$\mathbb{X}^{-1} = \mathbb{X}_{M-1}^{-1} = \begin{bmatrix} \boldsymbol{x}_0 & & & & \mathbf{0} \\ \boldsymbol{x}_1 & \boldsymbol{x}_0 & & & \\ \cdots & \cdots & \cdots & & \\ \boldsymbol{x}_{M-1} & \boldsymbol{x}_{M-2} & \cdots & \cdots & \boldsymbol{x}_0 \end{bmatrix} \mathbb{D}_{\boldsymbol{x}_0^{-1}} \begin{bmatrix} \boldsymbol{z}_0 & \boldsymbol{z}_1 & \cdots & \boldsymbol{z}_{M-1} \\ & \boldsymbol{z}_0 & \boldsymbol{z}_1 & \boldsymbol{z}_{M-2} \\ & & \cdots & \cdots \\ \mathbf{0} & & & \boldsymbol{z}_0 \end{bmatrix}$$
$$- \begin{bmatrix} \mathbf{0} & & & \mathbf{0} \\ \boldsymbol{y}_0 & & & \\ \cdots & \cdots & \cdots & \\ \boldsymbol{y}_{M-2} & \boldsymbol{y}_{M-3} & \cdots & \mathbf{0} \end{bmatrix} \mathbb{D}_{\boldsymbol{y}_{M-1}^{-1}} \begin{bmatrix} \mathbf{0} & \boldsymbol{w}_0 & \cdots & \boldsymbol{w}_{M-2} \\ & & \cdots & \cdots \\ & & \mathbf{0} & \boldsymbol{w}_0 \\ \mathbf{0} & & & \mathbf{0} \end{bmatrix} \tag{5.110}$$

or

$$\mathbb{X}^{-1} = \begin{bmatrix} \boldsymbol{y}_{M-1} & \boldsymbol{y}_{M-2} & \cdots & \cdots & \boldsymbol{y}_0 \\ & \boldsymbol{y}_{M-1} & \boldsymbol{y}_{M-2} & \cdots & \boldsymbol{y}_1 \\ & & \cdots & \cdots & \cdots \\ \mathbf{0} & & & & \boldsymbol{y}_{M-1} \end{bmatrix} \mathbb{D}_{\boldsymbol{y}_{M-1}^{-1}} \begin{bmatrix} \boldsymbol{w}_{M-1} & & \mathbf{0} & \\ \boldsymbol{w}_{M-2} & \boldsymbol{w}_{M-1} & & \\ & & \cdots & \\ \boldsymbol{w}_0 & \boldsymbol{w}_1 & \cdots & \boldsymbol{w}_{M-1} \end{bmatrix}$$
$$- \begin{bmatrix} \mathbf{0} & \boldsymbol{x}_{M-1} & \cdots & \boldsymbol{x}_1 \\ & & \cdots & \cdots \\ & & \mathbf{0} & \boldsymbol{x}_{M-1} \\ \mathbf{0} & & & \mathbf{0} \end{bmatrix} \mathbb{D}_{\boldsymbol{x}_0^{-1}} \begin{bmatrix} \mathbf{0} & & \mathbf{0} & \\ \boldsymbol{z}_{M-1} & \mathbf{0} & & \\ \cdots & \cdots & \cdots & \\ \boldsymbol{z}_1 & \boldsymbol{z}_2 & \cdots & \mathbf{0} \end{bmatrix}, \tag{5.111}$$

where

$$\mathbb{D}_{\boldsymbol{x}_0^{-1}} = \begin{bmatrix} \boldsymbol{x}_0^{-1} & & & \mathbf{0} \\ & \boldsymbol{x}_0^{-1} & & \\ & & \ddots & \\ \mathbf{0} & & & \boldsymbol{x}_0^{-1} \end{bmatrix}, \quad \mathbb{D}_{\boldsymbol{y}_{M-1}^{-1}} = \begin{bmatrix} \boldsymbol{y}_{M-1}^{-1} & & & \mathbf{0} \\ & \boldsymbol{y}_{M-1}^{-1} & & \\ & & \ddots & \\ \mathbf{0} & & & \boldsymbol{y}_{M-1}^{-1} \end{bmatrix}. \tag{5.112}$$

Here the upper indices of blocks are dropped for convenience: $\boldsymbol{x}_i = \boldsymbol{x}_i^{M-1}$, $\boldsymbol{y}_i = \boldsymbol{y}_i^{M-1}$, $\boldsymbol{z}_i = \boldsymbol{z}_i^{M-1}$, $\boldsymbol{w}_i = \boldsymbol{w}_i^{M-1}$ for $i = 0, 1, ..., M-1$. Thus, the inverse of BT matrix, $\mathbb{X}^{-1}$, is presented as the difference of multiplication of semi-circulant matrices.

We will compute the block vectors recursively using the recurrent block algorithms given in [185] for calculation of block vectors $\boldsymbol{x}_i^{(m)}$, $\boldsymbol{y}_i^{(m)}$ and $\boldsymbol{z}_i^{(m)}$, $\boldsymbol{w}_i^{(m)}$ and changing

the index m from 0 to $M-1$. To reduce the number of operations used, instead of computing these blocks directly each block was normalized such that:

$$\boldsymbol{x}_i^{(m)} = \widetilde{\boldsymbol{x}}_i^{(m)} \boldsymbol{p}_m, \quad \boldsymbol{y}_i^{(m)} = \widetilde{\boldsymbol{y}}_i^{(m)} \boldsymbol{q}_m, \;\; 0 \le i \le m, \tag{5.113}$$

for column blocks, or

$$\boldsymbol{z}_i^{(m)} = \widehat{\boldsymbol{p}}_m \widetilde{\boldsymbol{z}}_i^{(m)}, \quad \boldsymbol{w}_i^{(m)} = \widetilde{\boldsymbol{w}}_i^{(m)} \widehat{\boldsymbol{q}}_m, \;\; 0 \le i \le m \tag{5.114}$$

for row blocks. Here $\widetilde{\boldsymbol{x}}_i^{(m)}$, $\widetilde{\boldsymbol{y}}_i^{(m)}$, $\widetilde{\boldsymbol{z}}_i^{(m)}$ and $\widetilde{\boldsymbol{w}}_i^{(m)}$ are normalized blocks, and $\boldsymbol{p}_m, \boldsymbol{q}_m, \widehat{\boldsymbol{p}}_m$ and $\widehat{\boldsymbol{q}}_m$ are non-degenerate blocks acting as normalizing multipliers.

The recurrent algorithm for normalized column blocks $\widetilde{\boldsymbol{x}}_i^{(m)}$, $\widetilde{\boldsymbol{y}}_i^{(m)}$ is formulated as follows [185]:

$$\begin{aligned}
&\mathbf{m} = 0 : \boldsymbol{p}_0, \boldsymbol{q}_0 - \text{any non-degenerate blocks} \\
&\quad \widetilde{\boldsymbol{x}}_0^{(0)} = \boldsymbol{X}_0^{-1} \boldsymbol{p}_0^{-1}, \quad \widetilde{\boldsymbol{y}}_0^{(0)} = \boldsymbol{X}_0^{-1} \boldsymbol{q}_0^{-1}; \qquad (5.115) \\
&\mathbf{m} = 1, ..., M-1 : \\
&\quad \widetilde{\boldsymbol{F}}_m = \boldsymbol{X}_m \widetilde{\boldsymbol{x}}_0^{(m-1)} + \boldsymbol{X}_{m-1} \widetilde{\boldsymbol{x}}_1^{(m-1)} + \ldots + \boldsymbol{X}_1 \widetilde{\boldsymbol{x}}_{m-1}^{(m-1)}, \\
&\quad \widetilde{\boldsymbol{G}}_m = \boldsymbol{X}_{-m} \widetilde{\boldsymbol{y}}_0^{(m-1)} + \boldsymbol{X}_{-2} \widetilde{\boldsymbol{y}}_1^{(m-1)} + \ldots + \boldsymbol{X}_{-m} \widetilde{\boldsymbol{y}}_{m-1}^{(m-1)}, \\
&\quad \boldsymbol{s}_m = -\boldsymbol{q}_{m-1} \widetilde{\boldsymbol{F}}_m, \quad \boldsymbol{t}_m = -\boldsymbol{p}_{m-1} \widetilde{\boldsymbol{G}}_m, \qquad (5.116) \\
&\quad \boldsymbol{p}_m = \left(\boldsymbol{I} - \boldsymbol{t}_m \boldsymbol{s}_m\right)^{-1} \boldsymbol{p}_{m-1}, \quad \boldsymbol{q}_m = \left(\boldsymbol{I} - \boldsymbol{s}_m \boldsymbol{t}_m\right)^{-1} \boldsymbol{q}_{m-1}, \\
&\quad \left[\widetilde{\boldsymbol{x}}_0^{(m)} \, \widetilde{\boldsymbol{x}}_1^{(m)} \, \cdots \, \widetilde{\boldsymbol{x}}_m^{(m)}\right]^T = \left[\widetilde{\boldsymbol{x}}_0^{(m-1)} \, \widetilde{\boldsymbol{x}}_1^{(m-1)} \, \cdots \, \widetilde{\boldsymbol{x}}_{m-1}^{(m-1)} \, 0\right]^T \\
&\qquad\qquad + \left[0 \, \widetilde{\boldsymbol{y}}_0^{(m-1)} \, \widetilde{\boldsymbol{y}}_1^{(m-1)} \, \cdots \, \widetilde{\boldsymbol{y}}_{m-1}^{(m-1)}\right]^T \boldsymbol{s}_m, \\
&\quad \left[\widetilde{\boldsymbol{y}}_0^{(m)} \, \widetilde{\boldsymbol{y}}_1^{(m)} \, \cdots \, \widetilde{\boldsymbol{y}}_m^{(m)}\right]^T = \left[\widetilde{\boldsymbol{x}}_0^{(m-1)} \, \widetilde{\boldsymbol{x}}_1^{(m-1)} \, \cdots \, \widetilde{\boldsymbol{x}}_{m-1}^{(m-1)} \, 0\right]^T \boldsymbol{t}_m \\
&\qquad\qquad + \left[0 \, \widetilde{\boldsymbol{y}}_0^{(m-1)} \, \widetilde{\boldsymbol{y}}_1^{(m-1)} \, \cdots \, \widetilde{\boldsymbol{y}}_{m-1}^{(m-1)}\right]^T.
\end{aligned}$$

The algorithm for normalized row blocks $\widetilde{\boldsymbol{z}}_i^{(m)}$, $\widetilde{\boldsymbol{w}}_i^{(m)}$ is of the following form [185]:

$$
\begin{aligned}
&\mathbf{m}=0:\widehat{\boldsymbol{p}}_0,\widehat{\boldsymbol{q}}_0-\text{any nondegenarate blocks}\\
&\quad\widetilde{\boldsymbol{z}}_0^{(0)}=\boldsymbol{X}_0^{-1}\widehat{\boldsymbol{p}}_0^{-1},\quad \widetilde{\boldsymbol{w}}_0^{(0)}=\boldsymbol{X}_0^{-1}\widehat{\boldsymbol{q}}_0^{-1};\\
&\mathbf{m}=1,...,M-1:\\
&\quad\widetilde{\widehat{\boldsymbol{F}}}_m=\widetilde{\boldsymbol{z}}_0^{(m-1)}\boldsymbol{X}_{-m}+\widetilde{\boldsymbol{z}}_1^{(m-1)}\boldsymbol{X}_{-k+1}+\ldots+\widetilde{\boldsymbol{z}}_{m-1}^{(m-1)}\boldsymbol{X}_{-1},\\
&\quad\widetilde{\widehat{\boldsymbol{G}}}_m=\widetilde{\boldsymbol{w}}_0^{(m-1)}\boldsymbol{X}_1+\widetilde{\boldsymbol{w}}_1^{(m-1)}\boldsymbol{X}_2+\ldots+\widetilde{\boldsymbol{x}}_{m-1}^{(m-1)}\boldsymbol{X}_m,\\
&\quad\widehat{\boldsymbol{s}}_m=-\widetilde{\widehat{\boldsymbol{F}}}_m\,\widehat{\boldsymbol{q}}_{m-1},\quad \widehat{\boldsymbol{t}}_m=-\widetilde{\widehat{\boldsymbol{G}}}_m\,\widehat{\boldsymbol{p}}_{m-1},
\end{aligned}
\tag{5.117}
$$

$$
\begin{aligned}
&\widehat{\boldsymbol{p}}_m=\widehat{\boldsymbol{p}}_{m-1}\big(\boldsymbol{I}-\widehat{\boldsymbol{s}}_m\widehat{\boldsymbol{t}}_m\big)^{-1},\quad \widehat{\boldsymbol{q}}_m=\widehat{\boldsymbol{q}}_{m-1}\big(\boldsymbol{I}-\widehat{\boldsymbol{t}}_m\widehat{\boldsymbol{s}}_m\big)^{-1},\\
&\big[\widetilde{\boldsymbol{z}}_0^{(m)}\,\widetilde{\boldsymbol{z}}_1^{(m)}\,\cdots\,\widetilde{\boldsymbol{z}}_m^{(m)}\big]=\big[\widetilde{\boldsymbol{z}}_0^{(m-1)}\,\widetilde{\boldsymbol{z}}_1^{(m-1)}\,\cdots\,\widetilde{\boldsymbol{z}}_{m-1}^{(m-1)}\,0\big]\\
&\qquad\qquad+\widehat{\boldsymbol{s}}_m\big[0\;\widetilde{\boldsymbol{w}}_0^{(m-1)}\,\widetilde{\boldsymbol{w}}_1^{(m-1)}\,\cdots\,\widetilde{\boldsymbol{w}}_{m-1}^{(m-1)}\big],\\
&\big[\widetilde{\boldsymbol{w}}_0^{(m)}\,\widetilde{\boldsymbol{w}}_1^{(m)}\,\cdots\,\widetilde{\boldsymbol{w}}_m^{(m)}\big]=\widehat{\boldsymbol{t}}_m\big[\widetilde{\boldsymbol{z}}_0^{(m-1)}\,\widetilde{\boldsymbol{z}}_1^{(m-1)}\,\cdots\,\widetilde{\boldsymbol{z}}_{m-1}^{(m-1)}\,0\big]\\
&\qquad\qquad+\big[0\;\widetilde{\boldsymbol{w}}_0^{(m-1)}\,\widetilde{\boldsymbol{w}}_1^{(m-1)}\,\cdots\,\widetilde{\boldsymbol{w}}_{m-1}^{(m-1)}\big].
\end{aligned}
\tag{5.118}
$$

Each of the algorithms require $2(2N+1)^3M^2$ operations of multiplication and the same number of operations of addition and subtraction.

Iterative method for BT matrix of level 2

We cannot directly apply eq. (5.111) to BT matrices of level 2, $\mathbb{X}\in T_{M_y,\,M_x}G_{2N+1}$. However, block matrix $\mathbb{X}\in T_{M_y,\,M_x}G_{2N+1}$ can also be written as BT matrix of level 1: $\mathbb{X}\in T_{M_y}G_{M_x(2N+1)}$, i.e. the block matrix $\mathbb{X}$ can be written in the form of eq. (5.29) with $\boldsymbol{X}_{ij}^1=\boldsymbol{X}_{i-j}^1\in G_{M_x(2N+1)}$ and $\boldsymbol{X}_0^1$ - identity matrix of order $M_x(2N+1)$. Therefore, we can still use eq. (5.111) to solve a linear system with $\mathbb{X}\in T_{M_y}G_{M_x(2N+1)}$ for configuration of M_x rows and M_y columns of cylinders.

Another possibility to solve a linear system (4.16) with $\mathbb{X}\in T_{M_y,\,M_x}G_{2N+1}$ - BT matrix of level 2, is to use GMRES solver with a fast algorithm for MVP proposed by Barrowes et al. [12], [11] for multilevel BT matrices. The method is based on a Fast Fourier Transform and expedites MVP involving multilevel BT matrices with minimal memory requirements and computational cost. The method was applied to solve an

electromagnetic 3D scattering problem [12]. A fast algorithm for MVP: $\mathbb{X}\,\mathbf{b}$, can be applied as follows [12]: For a large number number of obstacles and high frequencies, a full matrix $\mathbb{X}$ may become too large to store. Taking advantage of the Block Toeplitz structure, we assign nonreduntant entries of $\mathbb{X}$ to an associate vector $\boldsymbol{\chi}_u$ by assigning only the left column and top row of each block in analogy to a root vector (5.7) defined earlier for the Toeplitz matrix. The final blocks $\boldsymbol{X}_i^2 \in G_{2N+1}, (i = \overline{0, 2N})$ are of a general type, and will be assigned from left to right and from bottom to top. In the next step, we insert zeros at appropriate locations into $\mathbf{b}$ to obtain a vector $\mathbf{b}_z = \zeta_p(\mathbf{b})$ suitable for convolution with $\boldsymbol{\chi}_u$. The vector $\mathbf{b}_z$ has to be zero padded such that its entries coincide with proper terms in $\boldsymbol{\chi}_u$ during convolution in the Fourier domain to obtain $\tilde{\boldsymbol{\beta}}_z = \tilde{\boldsymbol{\chi}}_u \cdot \tilde{\mathbf{b}}_z$. In the last step, $\mathbb{X}\,\mathbf{b}$ is reconstructed from $\boldsymbol{\beta}_z = IFFT(\tilde{\boldsymbol{\chi}}_u \cdot \tilde{\mathbf{b}}_z)$. Denoting the last operation by ζ_a^{-1}, the fast MVP can be obtained as [12]:

$$\mathbb{X}\,\mathbf{b} = \boldsymbol{\beta} = \zeta_a^{-1}\big[IFFT\big(\tilde{\boldsymbol{\chi}}_u \cdot \widetilde{\zeta_p(\boldsymbol{\beta})}\big)\big]. \tag{5.119}$$

5.4 Numerical results

5.4.1 Neumann expansion study

In this section, we present numerical results for the Neumann series expansion method. Computations are performed on MATLAB for a configuration of rigid cylinders and empty thin elastic aluminum cylindrical shells of thickness $h = 0.025a$ with mechanical properties: $\rho = 2700kg/m^3$, $c_p = 6420m/s$, where a is the outer radius of a shell. The pressure field is excited by the source located at point $P_s(-1000a, 1000a)$. The configuration consists of one column of uniformly distributed cylinders and depicted in Figure 5.1a for $M = 6$ case. The distance between two cylinders is d which we also call the cylinder center to center spacing (see Figure 5.1a). The scattering coefficients can be obtained using the truncated Neumann expansion given by eq. (5.95).

To investigate the validity of this method, we measure the spectral radius of matrix $\mathbb{T}\,\mathbb{P}$, where the matrices $\mathbb{T}$ and $\mathbb{P}$ are defined by eqs. (5.88) and (5.89) correspondingly. As it was noted earlier, the method works if the spectral radius of matrix $\mathbb{T}\,\mathbb{P}$ is less than one: $\rho(\mathbb{P}\mathbb{T}) = ||\mathbb{T}\,\mathbb{P}|| < 1$. Therefore, we evaluate the spectral radii of matrices

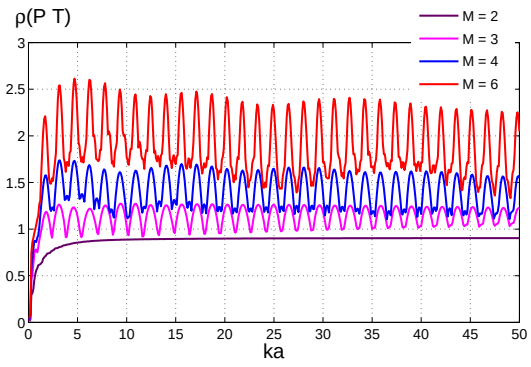

(a) $\rho(\mathbb{PT})$ vs. ka for $\frac{d}{2a} = 1.01$

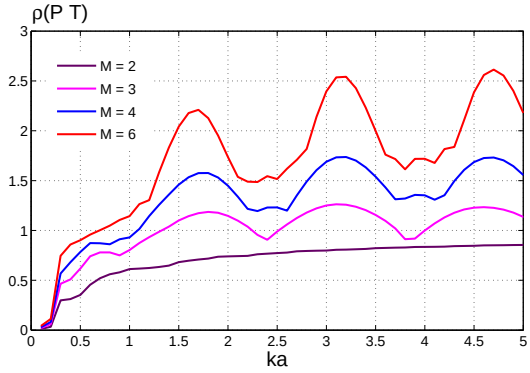

(b) $\frac{d}{2a} = 1.01$, enlarged view

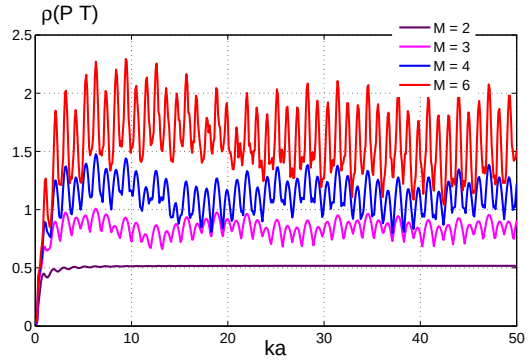

(c) $\rho(\mathbb{PT})$ vs. ka for $\frac{d}{2a} = 1.5$

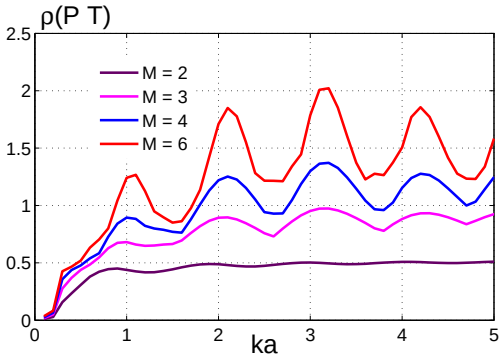

(d) $\frac{d}{2a} = 1.5$, enlarged view

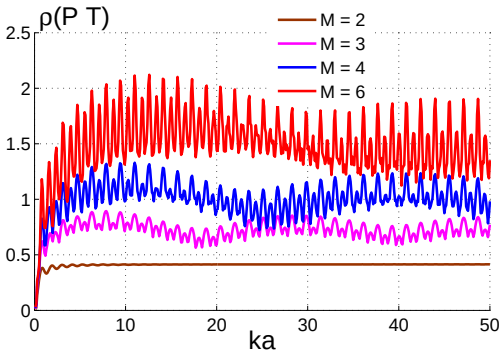

(e) $\rho(\mathbb{PT})$ vs. ka for $\frac{d}{2a} = 2$

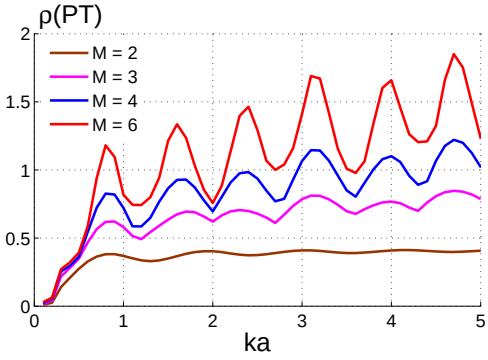

(f) $\frac{d}{2a} = 2$, enlarged view

Figure 5.2: Variation of spectral radius of matrix $\rho(\mathbb{PT})$ with a nondimensional frequency ka for a selected number M of rigid cylinders and distance between cylinder centers d.

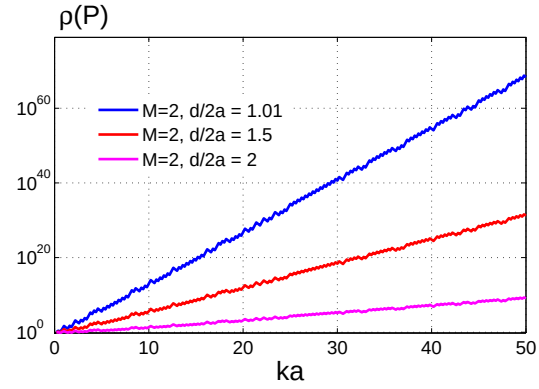

(a) $\rho(\mathbb{P})$ vs. ka for $M = 2$

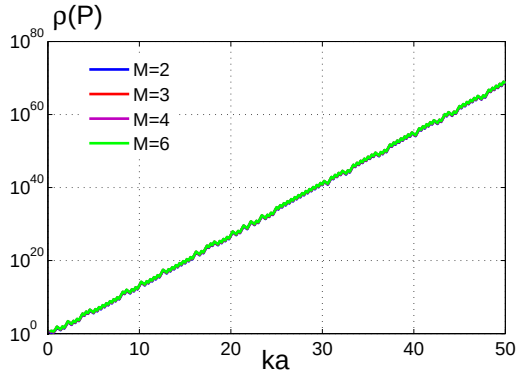

(b) $\rho(\mathbb{P})$ vs. ka for $\frac{d}{2a} = 1.01$

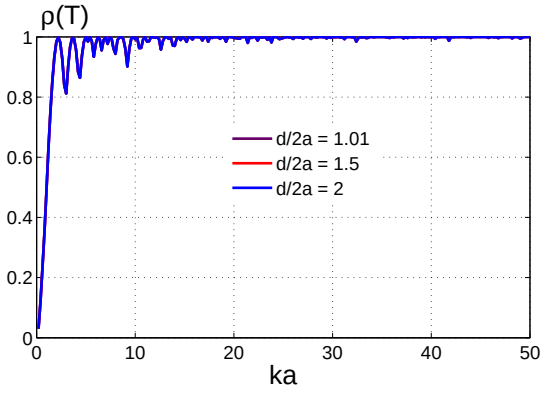

(c) $\rho(\mathbb{T})$ vs. ka for $M = 2$

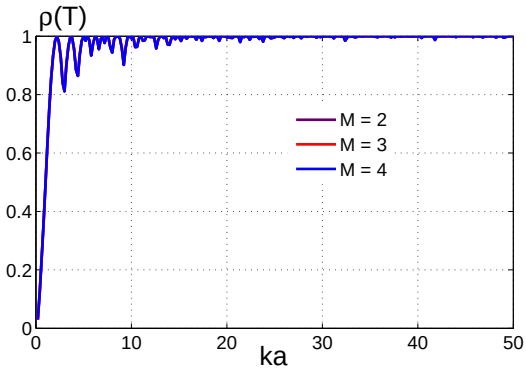

(d) $\rho(\mathbb{T})$ vs. ka for $\frac{d}{2a} = 1.01$

Figure 5.3: Variation of spectral radii of matrices $\rho(\mathbb{P})$ and $\rho(\mathbb{T})$ with a nondimensional frequency ka for a fixed number M of rigid cylinders varying the distances between the centers of cylinders $\frac{d}{2a} = 1.01,\ 1.15,\ 2$.

$\rho(\mathbb{T}\,\mathbb{P})$, $\rho(\,\mathbb{P})$, and $\rho(\mathbb{T})$ as functions of nondimensional frequency ka varying the number of scatterers M and the distance between two cylinders d. Our goal here is to find "the magic numbers" M, d, and ka for which the Neumann expansion method works, i.e. $\rho(\mathbb{T}\,\mathbb{P}) < 1$. The plots in Figures 5.2 - 5.5 are obtained keeping 4 terms in the Neumann expansion (5.95).

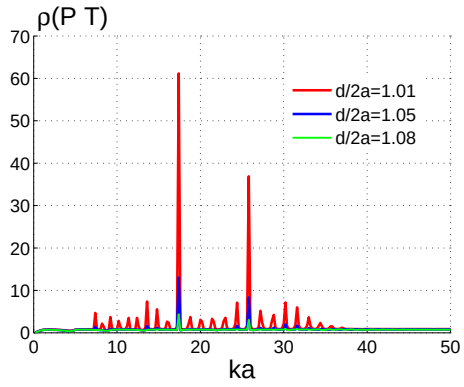

(a) $\rho(\mathbb{PT})$ vs. ka for $M = 2$

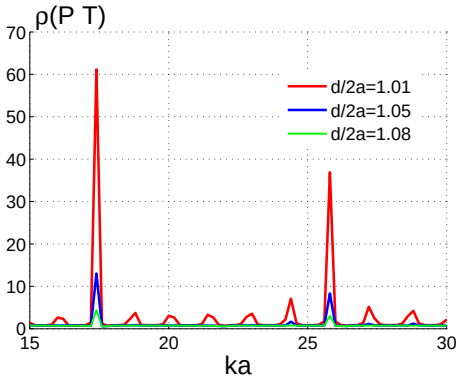

(b) $M = 2$, enlarged view

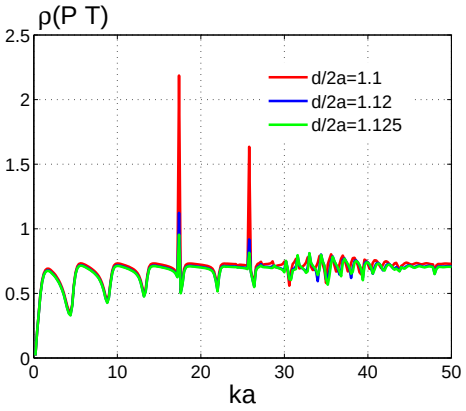

(c) $\rho(\mathbb{PT})$ vs. ka for $M = 2$

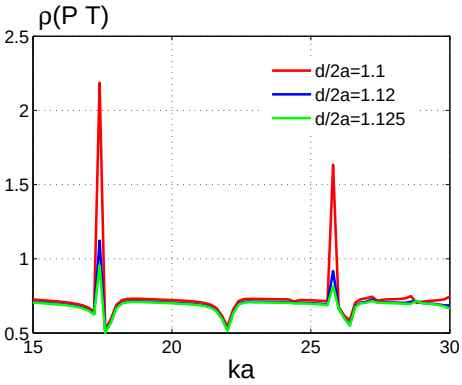

(d) $M = 2$, enlarged view

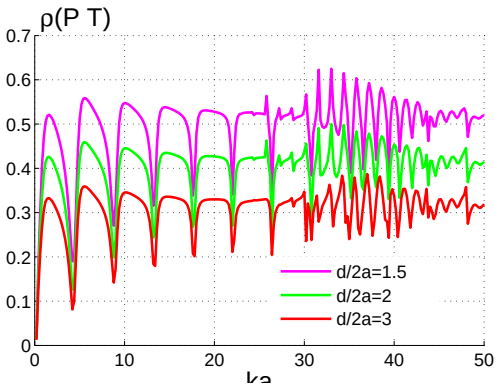

(e) $\rho(\mathbb{PT})$ vs. ka for $M = 2$

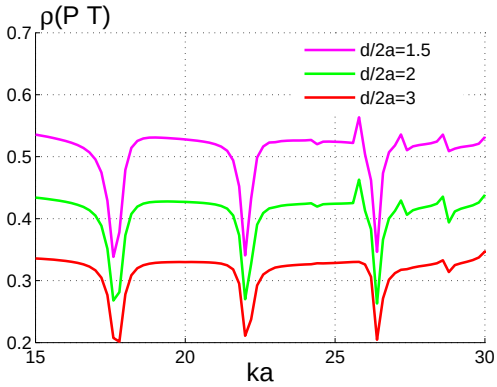

(f) $M = 2$, enlarged view

Figure 5.4: Variation of spectral radii of matrices $\rho(\mathbb{PT})$ with ka for $M = 2$: two empty thin elastic shells, modifying the values of the normalized distance $d/2a = \overline{1.01,\ 3}$.

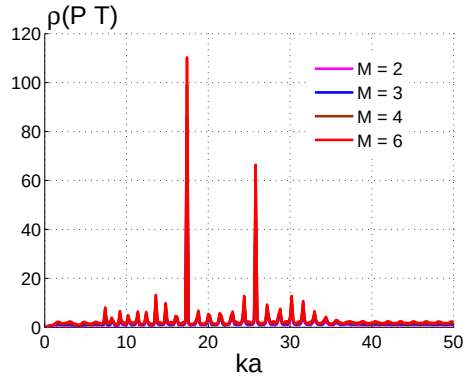

(a) $\rho(\mathbb{PT})$ vs. ka for $\frac{d}{2a} = 1.01$

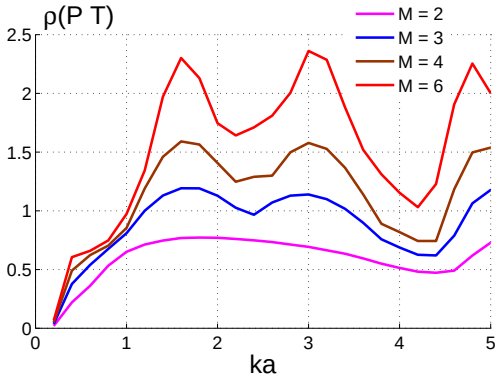

(b) $\frac{d}{2a} = 1.01$, enlarged view

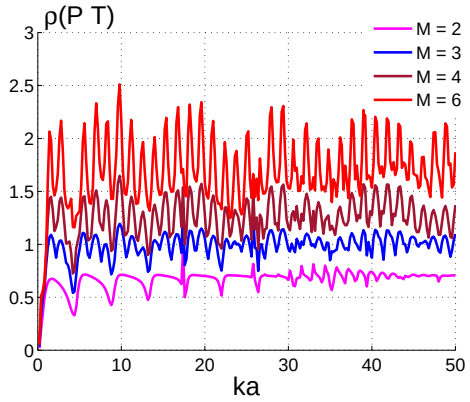

(c) $\rho(\mathbb{PT})$ vs. ka for $\frac{d}{2a} = 1.125$

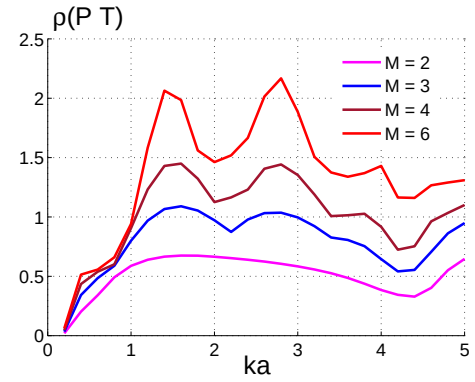

(d) $\frac{d}{2a} = 1.125$, enlarged view

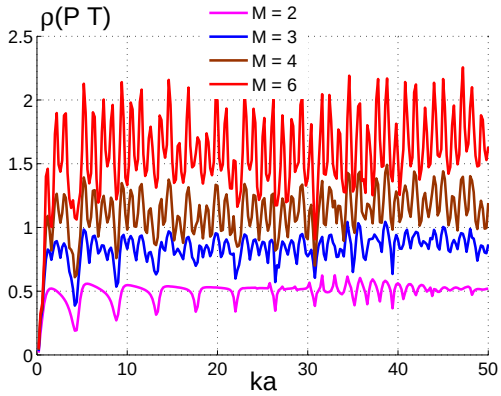

(e) $\rho(\mathbb{PT})$ vs. ka for $\frac{d}{2a} = 1.5$

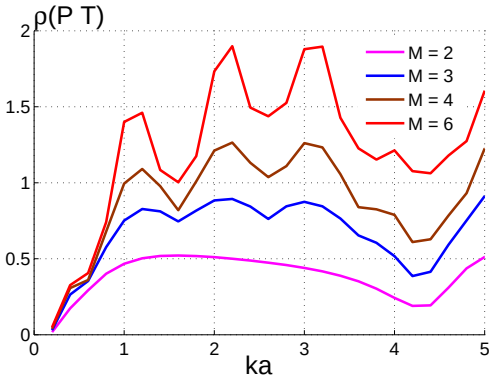

(f) $\frac{d}{2a} = 1.5$, enlarged view

Figure 5.5: Variation of spectral radii of matrices $\rho(\mathbb{PT})$ with a nondimensional frequency ka for a selected number M of empty thin elastic shells and distances between the centers of shells $\frac{d}{2a} = 1.01, 1.125, 1.5$.

Figure 5.2 illustrates a variation of spectral radius of matrix $\rho(\mathbb{PT})$ with a non-dimensional frequency ka for a selected number M of rigid cylinders submerged in a fluid medium with the normalized distances between the centers of cylinders $\frac{d}{2a} =$ 1.01, 1.15, 2, where a is the outer radius of a cylinder. Interestingly, the graphs in each subplot do not cross or overlap. The results show that the Neumann expansion method gives satisfactory results for a configuration of 2 rigid cylinders, $M = 2$, and works well for any considered values of $\frac{d}{2a} = 1.01, 1.15, 2$. For $M = 2$, $\rho(\mathbb{T}\,\mathbb{P}) < 1$ is satisfied for $\forall\, ka \in \overline{0,\, 50}$. For larger values of M, results differ and depend on values of d and ka. For low frequencies, i.e. $ka \leq 0.7$, the method works well for any considered values of M and d. The increase of d decreases the spectral radius $\rho(\mathbb{T}\,\mathbb{P})$ whereas the growth of M enlarges it as expected. Particularly for $\frac{d}{2a} = 2$, the condition $\rho(\mathbb{T}\,\mathbb{P}) < 1$ is valid at $M = 2, 3$ and $\forall\, ka \in \overline{0,\, 50}$. As expected, for closely located cylinders, the influence of interaction between each cylinder is high, and the increase in number of scatterers leads to more complex coupling, which consequently leads to an increase of the spectral radius.

The spectral radius of matrix $\rho(\mathbb{T}\,\mathbb{P})$ as a function of nondimensional frequency ka is illustrated in Figures 5.4 and 5.5 for a configuration of aluminum thin cylindrical shells of thickness $h = 0.025a$. Figure 5.4 depicts a variation of spectral radius of matrix $\rho(\mathbb{T}\,\mathbb{P})$ with a nondimensional frequency ka for two thin shells, $M = 2$, modifying the distance between the centers of shells, d. Unlike the rigid case, for a configuration of very closely located thin elastic shells, i.e. $\frac{d}{2a} = 1.01$, the graph of $\rho(\mathbb{PT})$ has sharp peaks and changes abruptly. The graphs in Figure 5.4 identify "the magic number" d to be $\frac{d}{2a} = 1.125$ and show that the approach is valid, i.e. $\rho(\mathbb{T}\,\mathbb{P}) < 1$, for two thin shells located at the distance $\frac{d}{2a} \geq 1.125$ and $\forall\, ka \in \overline{0,\, 50}$. Figure 5.5 illustrates a variation of spectral radius of matrix $\rho(\mathbb{PT})$ with ka for a selected number M of shells located at distances $\frac{d}{2a} = 1.01, 1.125, 1.5$. Again as in rigid case, the spectral radius $\rho(\mathbb{PT})$ grows with the rise of M and the decrease of d. At low frequencies we can notice that with the increase of distance d the first pick of the graphs shifts from the right to the left. Graphs at $M = 6$ show that for $\frac{d}{2a} = 1.01, 1.125$, $\rho(\mathbb{T}\,\mathbb{P}) < 1$ is satisfied for $ka \leq 1$; for $\frac{d}{2a} = 1.5$, it is valid at $ka \leq 0.8$.

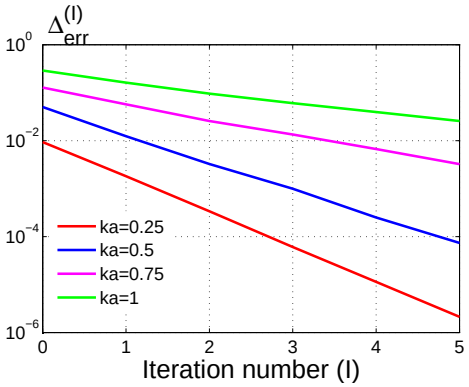

(a) $M = 2,\ \frac{d}{2a} = 1.01$

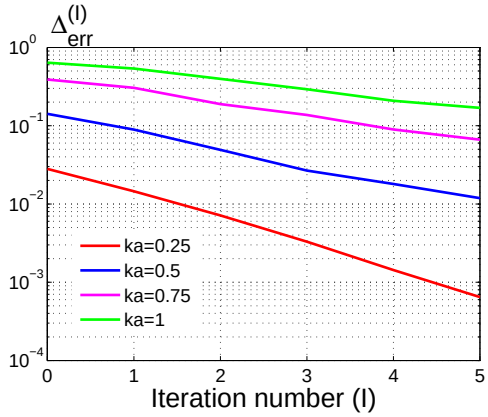

(b) $M = 6,\ \frac{d}{2a} = 1.01$

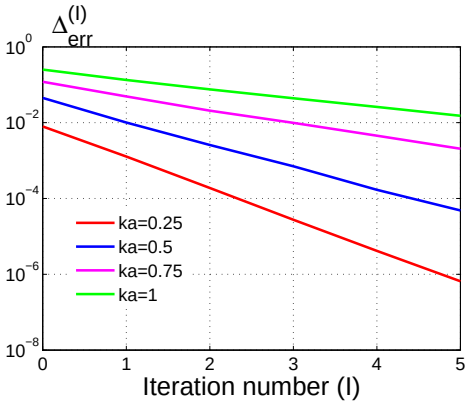

(c) $M = 2,\ \frac{d}{2a} = 1.125$

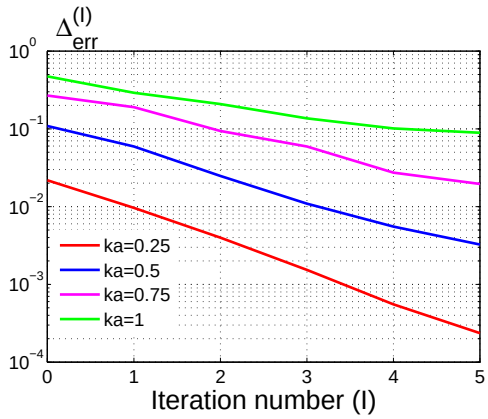

(d) $M = 6,\ \frac{d}{2a} = 1.125$

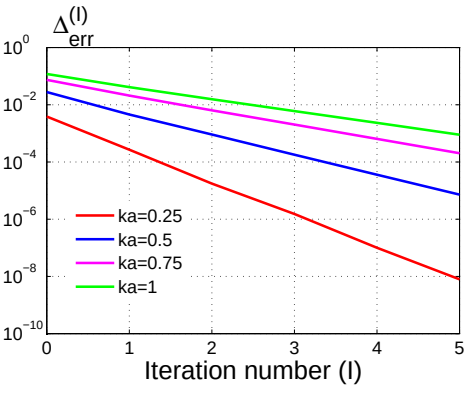

(e) $M = 2,\ \frac{d}{2a} = 2$

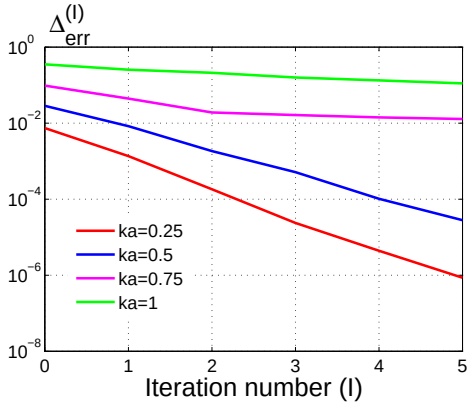

(f) $M = 6,\ \frac{d}{2a} = 2$

Figure 5.6: The error $\Delta_{err}^{(I)}$ versus the iteration number at selected numbers of ka, M, and $\frac{d}{2a}$ for empty thin elastic shells submerged in fluid.

Figure 5.6 illustrates the convergence rate of Neumann series solution (5.95) for a column of empty thin shells (see Figure a). Here the error $\Delta_{err}^{(I)}$ defined by (5.96) is evaluated with respect to the number of iterations I. A rapid convergence is observed with the increase of the distance $\frac{d}{2a}$ and the decrease of the number of scatterers M and the wave number ka. For closely located scatterers, i.e. $\frac{d}{2a} = 1.01$, and for configuration of large number of scatterers at high frequencies, a larger number of terms in the summation (5.95) is required.

5.4.2 Numerical results using an iterative method for Block Toeplitz matrix of level 1

In this section, we present the results produced using the iterative method for BT matrix of level 1 described in Section 5.3.4. This iterative technique is included in the TOEPLITZ package, a library which implements Toeplitz matrix system solver. The TOEPLITZ package solves a variety of Toeplitz and Circulant linear systems, their block analogs, and some other more complicated forms. The TOEPLITZ package was written in Fortran77 by a joint working group of American and Soviet mathematicians in the early 1980's [9]. The original version TOEPLITZ library is available in the TOEPLITZ subdirectory of the NETLIB web site:

`http://www.netlib.org/.`

The modified version of the TOEPLITZ package, converted to Fortran90, is provided at:

`http://people.sc.fsu.edu/~jburkardt/f_src/toeplitz/toeplitz.html.`

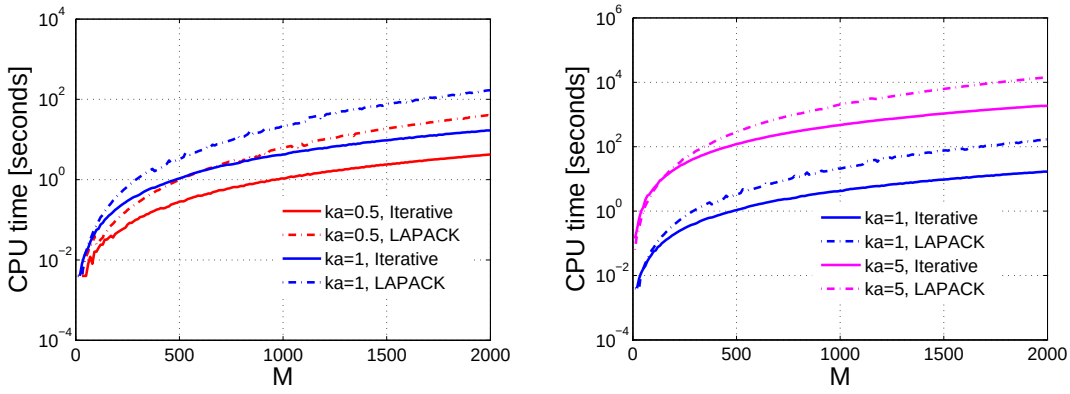

(a) CPU Time vs. M **(b)** CPU time vs. M

Figure 5.7: Variation of CPU time taken to calculate the scattering coefficients $B_n^{(m)}$ with a number of cylinders M for selected values of ka for a cluster of rigid cylinders submerged in fluid medium using two solvers: LAPACK and iterative algorithm described in Section 5.3.4.

We use the TOEPLITZ package [9] to solve our MS problem. Here, we consider an acoustic MS but the approach can be applied to both elastodynamic and electromagnetic MS problems. For verification and comparison, we compare the results for the iterative method with the direct method solutions which are implemented on Intel Fortran using LAPACK (Intel MKL) library. The computations are performed in Intel FORTRAN on SOE HPC Cluster of Rutgers University. The cluster hardware is based on Intel Sandy Bridge 2670 CPUs, 16 cores and 128 GB of RAM per node.

We calculated the CPU time taken to calculate the scattering coefficients $B_n^{(m)}$ for a cluster of rigid cylinders submerged in fluid medium using two solvers: LAPACK and TOEPLITZ libraries. The graphs in Figure 5.7 and Figure 5.8 are computed in a sequence in one core (thread). Figure 5.7 illustrates a variation of CPU time taken to calculate the $B_n^{(m)}$ coefficients with a number of cylinders M for selected values of $ka = 0.5,\ 1,\ 5$. The graphs show the efficiency of the iterative approach over the direct method. The iterative technique took less time to find the coefficients.

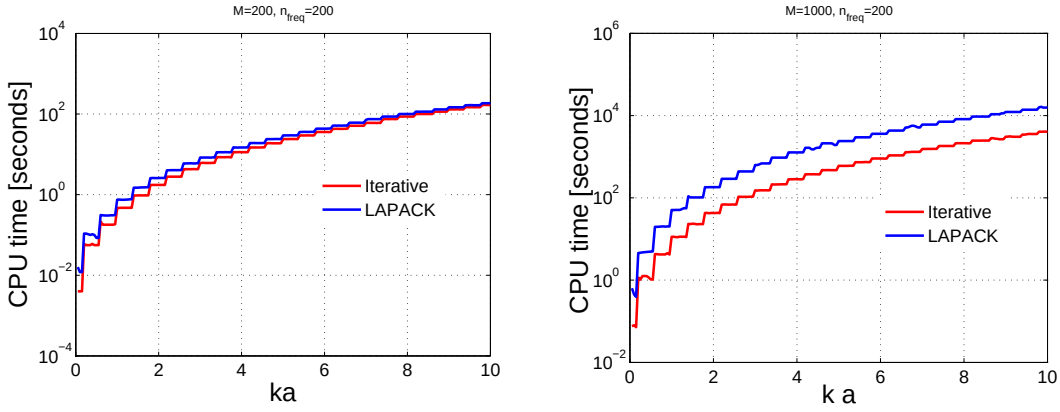

(a) CPU Time vs. ka for $M = 200$ **(b)** CPU Time vs. ka for $M = 1000$

Figure 5.8: Variation of CPU time taken to calculate the scattering coefficients $B_n^{(m)}$ with a nondimensional frequency ka for a cluster of rigid cylinders submerged in a fluid medium using two solvers: direct LAPACK and iterative TOEPLITZ solvers.

Figure 5.8 illustrates a variation of CPU time taken to calculate the $B_n^{(m)}$ coefficients with a nondimensional frequency ka. Computations are performed for $nfreq = 200$ frequency nodes at fixed values of numbers of scatterers, $M = 200 : M_x = 10, M_y = 20$ and $M = 1000 : M_x = 10, M_y = 100$. For $M = 1000$ at fixed value of $ka = 10$, it took approximately $18000/3600 = 5hours$ to evaluate the $B_n^{(m)}$ coefficients using LAPACK library and 61 minutes and 39.007 seconds using TOEPLITZ package. We can notice from graphs the advantage of iterative approach with the rise of M and ka. The iterative solver works faster and is more efficient than direct method.

To further expedite the simulation run time, the Fortran codes are parallelized using OpenMP. OpenMP is an implementation of multithreading; it runs the section of the code in parallel by dividing a task among available threads. We performed parallel computations over the frequency intervals using "OMP dynamic scheduling", "OMP static scheduling", and "OMP" without scheduling by varying the chunk size and the number of threads used. The increase of number of threads reduced a total elapsed time to solve a linear system using TOEPLITZ package. Tables 5.1 and 5.2 evaluate the efficiency of parallelization using TOEPLITZ package and OpenMP compilers, for a

configuration of $Mx = 10$ columns and $My = 20$ row of rigid cylinders at $nfreq = 200$ (frequency intervals). For a configuration of $M = 200$ cylinders the computation time reduced from 2 hours 9 minutes 11.4394 seconds using 1 thread to 14 minutes 57.2535 seconds using 16 threads with dynamic scheduling and chunck size= 2. Table 5.3 illustrates the comparison of total elapsed time to find the unknown coefficients using TOEPLITZ and LAPACK libraries on 16 threads with dynamic scheduling and chunck size= 2 varying the number of scaterers. As we can see for smaller number scatterers, $M = 200$ LAPACK library works faster but at larger value of scatterers, $M = 500$ TOEPLITZ solver is more effective and takes less run time and shows its advantage with increase of M and ka.

Number of Threads	Total Elapsed Time
1	2 hours 9 min 11.4394 sec
5	1hour 14 min 15.7641 sec
10	43 min 54.6001 sec
15	31 min 33.1283 sec
16	28 min 46.3367 sec

Table 5.1: Total elapsed time to find the unknown coefficients using TOEPLITZ library for a configuration of $M = 200$ rigid cylinders with $nfreq = 200$ (frequency intervals), and OMP without scheduling.

Chunck Size	Number of Threads	Total Elapsed Time, Dynamic Schedule	Total Elapsed Time, Static Schedule
2	5	28 min 38.3972 sec	28 min 35.7127 sec
2	10	17 min 43.8765 sec	19 min 36.9096 sec
2	15	15 min 55.0149 sec	19 min 21.3139 sec
2	16	14 min 57.2535 sec	19 min 24 sec
3	5	29 min 42.991 sec	29 min 0.9738 sec
3	10	19 min 3.5561 sec	20 min 40.601 sec
3	15	16 min 17.4695 sec	19 min 33.3069 sec
3	16	16 min 31.0644 sec	22 min 32.1263 sec
5	5	31 min 53.6569 sec	31 min 35.1488 sec
5	10	21 min 39.332 sec	21 min 38.2482 sec
5	15	18 min 45.4848 sec	18 min 45.002 sec
5	16	17 min 6.667 sec	18 min 34.0762 sec

Table 5.2: Total elapsed time to find the unknown coefficients using TOEPLITZ library using Dynamic and Static Schedules for a configuration of $M = 200$ rigid cylinders with $nfreq = 200$ (frequency intervals).

Chunck Size	Number of Threads	Number of Scatterer	Total Elapsed Time, Dynamic Schedule	Solver
2	16	$M = 200$	14 min 57.2535 sec	TOEPLITZ
2	16	$M = 500$	2 hours 28.794 min	TOEPLITZ
2	16	$M = 200$	13 min 45.08 sec	LAPACK
2	16	$M = 500$	3 hours 27.5358 min	LAPACK

Table 5.3: Total elapsed time to find the unknown coefficients using TOEPLITZ and LAPACK libraries with Dynamic Schedule for a configuration of $M = 200$ and $M = 500$ rigid cylinders with $nfreq = 200$ (frequency intervals).

Chapter 6

Acoustic active exterior cloaking

6.1 Introduction

Cloaking is intended to make an object undetectable to incident waves. The approaches proposed consist mainly of two quite distinct types of cloaking, namely passive and active. Passive cloaking requires devising a metamaterial that can steer the wave energy around the object regardless of the incident wave. Our interest here is with active cloaking, specifically in situations where the active sources lie in the exterior of the region containing the cloaked object. We call this configuration *active exterior cloaking* in keeping with prior terminology [179]. The field generated by the active sources is zero in the infinite region outside a set of circles defined by the relative positions of the sources. In this capter, we demonstrate that the integral representation of Vasquez et al. [181] for the source amplitudes can be reduced to closed-form explicit formulas. We provide analytical expressions for the source amplitude coefficients for general incidence as well as plane wave incidence. The expressions involve no more than sums of cylinder functions which can be truncated to achieve any desired accuracy. We also prove that the field generated by the active sources vanishes in the infinite region exterior to a set of circles defined by the relative positions of the sources. The active source field, by construction, cancels the incident field in the cloaked region, which is defined by the region interior to the same circular areas. The analytical results are verified by calculation of the farfield and the nearfield amplitudes, which are shown to vanish when the summation is accurately evaluated. The non-radiating nature of the active field has relevance to the inverse source problem [168]. Although for this problem, some uniqueness results are available for restricted forms of sources, e.g. "minimum energy sources" [47], in general the solution to this problem is know to be non-unique

[19]. Here we develop the solution of the active cloaking problem as a new family of non-radiating sources, with the property that they cancel a given incident field over a finite region.

We begin in 6.2 with a statement of the problem, a review of the governing equations, and a summary of the main results. The basic integral relation of Vasquez et al. [181] is derived in 6.2.2, from which the main results are shown to follow. Some example applications of the new formulas are presented in 6.5. Some implications of the general results are discussed in 6.6.

6.2 Source amplitudes for active exterior cloaking

6.2.1 Problem overview

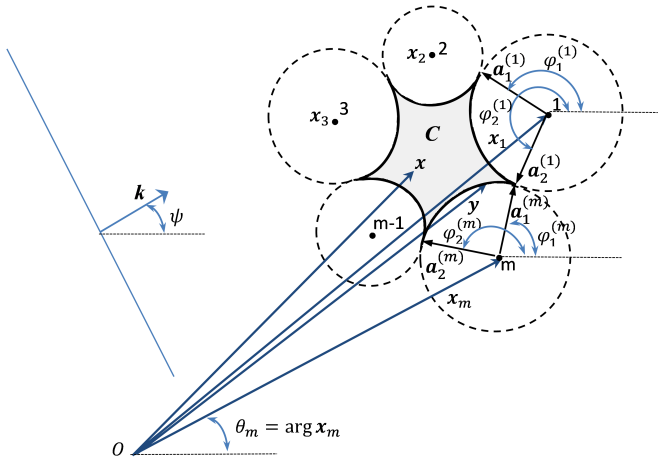

Figure 6.1: Insonification of the actively cloaked region C generated by M active point multipole sources at $\mathbf{x}_m$, $m = \overline{1, M}$. The region R is defined as the interior of the union of the dashed circular arcs, that is, the combined area comprising C and the M circular domains. The incident field in this case is a plane wave with wave vector $\mathbf{k}$ in the direction ψ.

The active cloaking devices considered here operate in two dimensions, and consist of arrays of point multipole sources located at positions $\mathbf{x}_m \in \mathbb{R}^2$, $m = \overline{1, M}$ (see Figure

6.1). The active sources lie in the exterior region with respect to the cloaked region C and this type of cloaking may therefore be called "active exterior cloaking" [179]. Objects are undetectable in the cloaked region by virtue of the destructive interference of the sources and the incident field with the result that the total wave amplitude vanishes in the cloaked region C. The advantages of this type of cloaking device are: (i) the cloaked region is not completely surrounded by a single cloaking device; (ii) only a small number of active sources are needed; (iii) the procedure works for broadband input sources; (iv) the cloaking effect is independent of the location of the scatterer in the cloaking region. A disadvantage of the active cloaking approach is that the fields near the ideal sources may become uncontrollably large. Realistically these would be replaced by regions of finite extent and thus their magnitude is reduced. A further disadvantage of the method is that the incident field must be known. However we note that with the approach proposed in this paper, the new expressions require only the expansion of the incident field into entire cylindrical waves, as compared with the line integrals derived in [182] which require knowledge of the incident field and its normal derivative.

The shaded region in Figure 6.1 denotes the cloaked zone C generated by M active point multipole sources. The boundary of C is the closed concave union of the circular arcs $m = \overline{1, M}$, $\{a_m, \phi_1^{(m)}, \phi_2^{(m)}\}$ associated with the source at $\mathbf{x}_m$. In the general case $\{a_m, \phi_1^{(m)}, \phi_2^{(m)}\}$ are distinct for different values of m. Note that the wave incidence shown in Figure 6.1 is a plane wave although the solution derived below is for arbitrary incidence. The inverse problem to be solved is to find the amplitudes of the active sources as a function of the incident wave, and to prove that the cloaked region is indeed the closed region C.

We assume time harmonic dependence $e^{-i\omega t}$, which is omitted hereafter, and consider the scalar Helmholtz equation in two dimensions. Thus the method proposed here is applicable to any physical situation described as such. For ease of discussion, however, let us consider the case of acoustics, so that the governing equation for the (time harmonic) pressure $p(\mathbf{x})$ is given by eq. (2.62). For a given incident wave, we assume there is an additional field resulting from the active sources which exactly cancels the

incident wave in some bounded region C. This additional wave field is caused by the M multipole sources located at $\mathbf{x}_m$, $m = \overline{1, M}$. The assumed form of the total field p, the incident wave p^{in}, and the active source field p^d are, respectively

$$p = p^{in} + p^d, \tag{6.1a}$$

$$p^d = \sum_{m=1}^{M} \sum_{n=-\infty}^{\infty} b_{m,n} V_n^+\big(k(\mathbf{x} - \mathbf{x}_m)\big), \tag{6.1b}$$

where p^{in} is defined in the form of eq. (2.68) with $k_\perp = k$ and $k_z = 0$: here we consider a perpendicular incidence ($\alpha = 0$), no z dependence. The wave functions $U_n^\pm(\mathbf{x})$ and $V_n^\pm(\mathbf{x})$ are defined by eqs. (2.66) and (2.70). Define the derivative functions $U_n^{\pm\prime}(\mathbf{x})$ as

$$U_n^{\pm\prime}(\mathbf{x}) = J_n'(|\mathbf{x}|) e^{\pm in \arg \mathbf{x}}. \tag{6.2}$$

In the following we write U_0 and V_0, with obvious meaning. Note that the functions $U_n^\pm(\mathbf{x})$ and $V_n^\pm(\mathbf{x})$ possess the properties given by eq. (2.71) and obey the generalized Grafs addition theorem (2.72).

The active source field p^d in (6.1b) is of the same form as considered by Vasquez et al. [180, eq. (5)]. The three dimensional analog is given in [182, eq. (40)]. The coefficients A_n, which define the incident field, include as a special case plane wave incidence in the direction ψ ($A_n = i^n e^{-in\psi}$). The active cloaking problem is now to find (i) the coefficients $b_{m,n}$ such that the total field p vanishes inside some compact region C, and (ii) to define the region C.

The principal results can be summarized in two theorems. The first provides necessary and sufficient conditions on the source amplitudes $b_{m,n}$ in order to ensure cloaking in the region C and a non-radiating source field p^d. The second provides the explicit expressions for the active source amplitudes.

Theorem 1 *Necessary and sufficient conditions on the active source coefficients $b_{m,l}$ in order to ensure zero total field ($p^{in} + p^d = 0$) inside C and no radiated field ($p^d \to 0$*

in the far field) are

$$\forall\, n \in \mathbb{Z}: \quad \sum_{m=1}^{M} \sum_{l=-\infty}^{\infty} b_{m,l} \times \begin{cases} U_{n-l}^{-}\big(k\mathbf{x}_m\big) & = 0, \\ \\ V_{n-l}^{-}\big(k\mathbf{x}_m\big) & = -A_n. \end{cases} \tag{6.3}$$

These identities provide a useful means to quantify error in active cloaking as will be seen later on. We now state the explicit form for the source amplitudes, together with the shape of the cloaked region C and the region in which the source field vanishes.

Theorem 2 *Given M active sources located at $\mathbf{x}_m$, $m = \overline{1, M}$, the required active source amplitude coefficients for the general incidence* (2.68) *are*

$$b_{m,l} = \sum_{n=-\infty}^{\infty} b_{m,ln} A_n, \quad \textit{where} \tag{6.4a}$$

$$b_{m,ln} = \frac{ka_m}{4} \sum_{p=-\infty}^{\infty} U_{n+p}^{+}\big(k\mathbf{x}_m\big) \frac{(-1)^p}{l+p} \big[J_p(ka_m) J_l'(ka_m) - J_p'(ka_m) J_l(ka_m)\big] \times \big[e^{-i(l+p)\phi_2^{(m)}} - e^{-i(l+p)\phi_1^{(m)}}\big]. \tag{6.4b}$$

This ensures cloaking (zero total field) in the region C which is the closed and bounded domain formed by taking its boundary as the closed concave union of the circular arcs defined by $\{a_m, \phi_1^{(m)}, \phi_2^{(m)}\}$ and denoted as ∂C_m, see Figure 6.1. These coefficients also ensure that the radiated field from p^d is identically zero in the region exterior to all of the circles centered at the source points:

$$p^d(\mathbf{x}) = 0 \quad \text{for } \mathbf{x} \in \mathbb{R}^2/R, \quad R \equiv C \cup \bigcup_{m=1}^{M} \{\mathbf{x} : |\mathbf{x} - \mathbf{x_m}| \le a_m\}. \tag{6.5}$$

This is the exterior to the union of the dashed circular arcs in Figure 6.1.

An alternative and more concise formulation of eq. (6.4b) is obtained using the notation of eqs. (2.66) and (2.70) with $\mathbf{a}_i^{(m)} \equiv a_m \hat{\mathbf{e}}(\phi_i^m), (i = 1, 2)$,

$$b_{m,ln} = \frac{1}{4} ka_m \sum_{p=-\infty}^{\infty} U_{n+p}^{+}(k\mathbf{x}_m) \frac{(-1)^p}{l+p} \left[U_p^{-}(k\mathbf{a}) U_l^{-\prime}(k\mathbf{a}) - U_p^{-\prime}(k\mathbf{a}) U_l^{-}(k\mathbf{a})\right]\Big|_{\mathbf{a}_1^{(m)}}^{\mathbf{a}_2^{(m)}} \tag{6.6}$$

where $\hat{\mathbf{e}}(\phi_i^m)$ is a unit vector subtended at angle ϕ_i^m, as illustrated in Figure 6.1.

An important case for which the summation in (6.4a) can be simplified is plane wave incidence. Assuming the incident field is a unit amplitude plane wave in direction ψ, $p^{in} = p_\psi$ defined by $A_n = i^n e^{-in\psi}$, results in

$$b_{m,l} = p_\psi(\mathbf{x}_m)\frac{ka_m}{4}\sum_{p=-\infty}^{\infty}\frac{i^p e^{ip\psi}}{l+p}\left[U_p^-(k\mathbf{a})U_l^{-\prime}(k\mathbf{a}) - U_p^{-\prime}(k\mathbf{a})U_l^-(k\mathbf{a})\right]\Big|_{\mathbf{a}_1^{(m)}}^{\mathbf{a}_2^{(m)}}, \quad \begin{matrix}\text{plane wave}\\ \text{incidence.}\end{matrix} \tag{6.7}$$

The form of the coefficients $b_{m,l}$ is discussed further below. Note that the term in (6.4b), (6.6) and in (6.7), corresponding to $p+l=0$ is zero, which follows from l'Hôpital's rule.

Theorems 1 and 2 are proved in the next section.

6.2.2 Proofs of Theorems 1 and 2

Theorem 1: Necessary and sufficient conditions on the source amplitudes

We first prove the constraints on the source coefficients $b_{m,l}$ given by Theorem 1, and at the same time show that they may be interpreted in terms of the near- and far-field of the active sources. To this end, we express p^d in two different forms using the generalized Graf addition theorem (2.72), Let us first consider the radiated field, assuming that p^d does not radiate energy into the far field. The first of (2.72), for $|\mathbf{x}| > |\mathbf{y}|$, allows us to rewrite p^d as a sum of multipoles at the origin:

$$p^d = \sum_{n=-\infty}^{\infty} F_n V_n^+(k\mathbf{x}) \quad \text{for} \quad |\mathbf{x}| > \max(|\mathbf{x}_m| + a_m), \tag{6.8}$$

where

$$F_n = \sum_{m=1}^{M}\sum_{l=-\infty}^{\infty} b_{m,l} U_{n-l}^-(k\mathbf{x}_m). \tag{6.9}$$

Define the farfield amplitude function $f(\theta)$, $\theta = \arg\hat{\mathbf{x}}$, such that

$$p^d(\mathbf{x}) = f(\theta)\,\frac{e^{ik|\mathbf{x}|}}{(k|\mathbf{x}|)^{1/2}} + \mathrm{O}\big((k|\mathbf{x}|)^{-3/2}\big), \quad |\mathbf{x}| \to \infty. \tag{6.10}$$

The farfield amplitude function follows from the asymptotic form of the Hankel functions as

$$f(\theta) = \sum_{n=-\infty}^{\infty} f_n e^{in\theta}, \quad f_n = \Big(\frac{2}{\pi}\Big)^{1/2} i^{-(n+\frac{1}{2})}\, F_n. \tag{6.11}$$

A measure of the nondimensional total power radiated by the sources is given by the non-negative far-field flux parameter

$$\sigma_r = \int_0^{2\pi} \mathrm{d}\,\theta |f(\theta)|^2 = 4 \sum_{n=-\infty}^{\infty} |F_n|^2. \tag{6.12}$$

Since p^d does not radiate energy into the far field, the active sources must vanish, so that $F_n = 0\,\forall n$. Imposing this in (6.9) ensures the necessity of $(6.3)_1$. The sufficiency of $(6.3)_1$ is seen immediately by substituting $(6.3)_1$ into (6.9) and (6.8) which gives $p^d = 0$ for $|\mathbf{x}| > \max(|\mathbf{x}_m| + a_m)$.

Now let us consider the near-field inside the cloaked region C where we assume that the cloaked region contains the origin and the total field is zero inside C, i.e. $p^{in}+p^d = 0$. Using the second identity in (2.72), the active source field p^d can be expressed in a form that is valid in the neighborhood of the origin (assuming $|\mathbf{x}_m| > a_m\,\forall m$),

$$p^d = \sum_{n=-\infty}^{\infty} E_n U_n^+(k\mathbf{x}) \quad \text{for} \quad |\mathbf{x}| < \min(|\mathbf{x}_m| - a_m), \tag{6.13}$$

where

$$E_n = \sum_{m=1}^{M} \sum_{l=-\infty}^{\infty} b_{m,l} V_{n-l}^-(k\mathbf{x}_m). \tag{6.14}$$

The total field vanishing in some neighbourhood of the origin thus implies that $E_n + A_n$ vanishes for every value of n. This gives rise to the necessary condition $(6.3)_2$. Sufficiency is once again immediate by assuming the form $(6.3)_2$ and back-substituting into the forms of p^d and p^{in} above.

Further implications of this result are explored after we complete the proof of Theorem 2.

Theorem 2: Explicit forms for the active source amplitudes

The Green's function $g(\mathbf{x}, \mathbf{x}')$ is defined as the solution of eq. (2.62) for source $p_s = \delta(\mathbf{x} - \mathbf{x}')$, i.e. $g(\mathbf{x}, \mathbf{x}') = -\frac{i}{4} V_0(\mathbf{x} - \mathbf{x}')$. Consider a region D such as that depicted in Figure 6.2, chosen so that it does not contain any sources. We will determine the explicit form for the active source amplitudes together with the form of D that ensures cloaking. The latter, already introduced as C, is the region depicted in Figure 6.1.

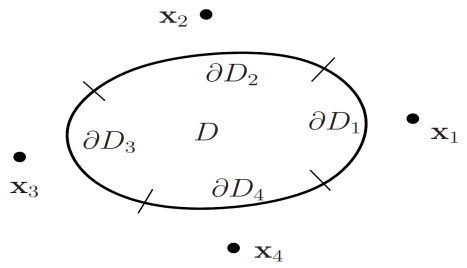

Figure 6.2: A configuration of $M = 4$ sources, and a region D in which the integral identity (6.15) holds.

By assumption, both p^{in} and p^{d} satisfy the homogeneous Helmholtz equation in D (eq. (2.62) with $P_s = 0 \; \forall \, \mathbf{x} \in D$), and therefore

$$\int_{\partial D} \mathrm{d}\, S(\mathbf{y}) \big[v(\mathbf{y}) \partial_n g(\mathbf{y}, \mathbf{x}) - g(\mathbf{y}, \mathbf{x}) \partial_n v(\mathbf{y}) \big] = v(\mathbf{x}), \quad v = \{p^{in}, p^{d}\}, \quad \mathbf{x} \in D. \tag{6.15}$$

where ∂D is the boundary of D depicted in Figure 6.2 as the union of the arcs $\partial D_m, m = \overline{1, M}$ and it is traversed counter-clockwise. We wish to determine the cloaked region $C \subset D$ which is defined by its property that the total field $p^{in} + p^{d}$ vanishes inside C, so that

$$p^{d}(\mathbf{x}) = -p^{in}(\mathbf{x}) = \frac{i}{4} \int_{\partial C} \mathrm{d}\, S(\mathbf{y}) \big[p^{in}(\mathbf{y}) \partial_n V_0\big(k(\mathbf{y}-\mathbf{x})\big) - V_0\big(k(\mathbf{y}-\mathbf{x})\big) \partial_n p^{in}(\mathbf{y}) \big], \;\; \mathbf{x} \in C. \tag{6.16}$$

Given that the boundary of C is split up, as for D into segments $\partial C_m, m = \overline{1, M}$, we can use $(2.72)_1$, in order to write, for some $\mathbf{x_0}$

$$V_0(\mathbf{y} - \mathbf{x}) = V_0(\mathbf{x} - \mathbf{x}_0 - (\mathbf{y} - \mathbf{x}_0)) = \sum_{n=-\infty}^{\infty} V_n^{+}(\mathbf{x} - \mathbf{x}_0) U_n^{-}(\mathbf{y} - \mathbf{x}_0) \tag{6.17}$$

which holds for $|\mathbf{x} - \mathbf{x}_0| > |\mathbf{y} - \mathbf{x}_0|$. Do this for each of the contours choosing $\mathbf{x}_0 = \mathbf{x}_m$ on each ∂C_m, so that

$$\begin{aligned} p^{d}(\mathbf{x}) = &- \frac{i}{4} \sum_{m=1}^{M} \sum_{n=-\infty}^{\infty} V_n^{+}\big(k(\mathbf{x} - \mathbf{x}_m)\big) \\ &\times \int_{\partial C_m} \mathrm{d}\, S_m \left(p^{in}(\mathbf{y}) \partial_n U_n^{-}\big(k(\mathbf{y} - \mathbf{x}_m)\big) - U_n^{-}\big(k(\mathbf{y} - \mathbf{x}_m) \partial_n p^{in}(\mathbf{y})\big) \right) \end{aligned} \tag{6.18}$$

where we require $|\mathbf{x} - \mathbf{x}_m| > |\mathbf{y} - \mathbf{x}_m|$ on each contour ∂C_m (recall that the integral is being considered for $\mathbf{x} \in C$). The minus sign in (6.18) arises since upon expanding

about the point $\mathbf{x}_m$, the counter-clockwise orientation with respect to the centre $\mathbf{x}_m$ is opposite to the counter-clockwise traversal of ∂C with respect to some origin inside C. Note that for this to hold simultaneously for all m the contours ∂C_m must be circular arcs as depicted in Figure 6.3. Therefore we have proved that C is the region with boundary as the closed concave union of the circular arcs defined by $\{a_m, \phi_1^{(m)}, \phi_2^{(m)}\}$ and denoted as ∂C_m (see Figure 6.1). Finally, using the form for $p^{\,d}$ given in (6.1b), we find that

$$b_{m,n} = -\frac{i}{4}\int_{\partial C_m} \mathrm{d}\, S_m \Big[p^{\,in}(\mathbf{y}) \partial_n U_n^-\big(k(\mathbf{y}-\mathbf{x}_m)\big) - U_n^-\big(k(\mathbf{y}-\mathbf{x}_m)\big) \partial_n p^{\,in}(\mathbf{y}) \Big]. \quad (6.19)$$

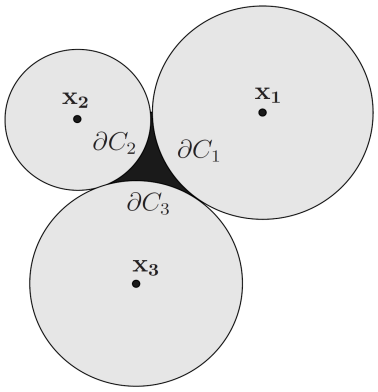

Figure 6.3: The integration curve ∂C split into $M = 3$ portions ∂C_m appropriate for the integral representation (6.18) of the active source field. The cloaked central (black) region, is bounded by ∂C_m, $m = 1, 2, 3$.

This agrees with [181, Eq. (8)] apart from a factor $i/4$ missing there. Equation (6.19) provides a direct method for calculating the multipole source amplitudes, as has been demonstrated numerically for different source configurations [181]. The result is not optimal, however, as it requires evaluation of a line integral, which can be computationally time consuming.

The explicit formula for the source amplitudes follows from eq. (6.19) by introducing the forms for the functions U_n^- as follows

$$b_{m,l} = -\frac{i}{4} k a_m \int_{\phi_1^{(m)}}^{\phi_2^{(m)}} \mathrm{d}\,\phi\, e^{-il\phi} \big[p^{\,in}(\mathbf{y}) J_l'(ka_m) - J_l(ka_m) k^{-1} \partial_n p^{\,in}(\mathbf{y}) \big]. \quad (6.20)$$

We see that the cloaked region C is indeed the subdomain of D in which Graf's theorem can be simultaneously invoked for all of the M active sources.

Consider plane wave incidence in the direction of the unit vector $\hat{\mathbf{e}}(\psi)$, $p^{in} = p_\psi(\mathbf{x})$ where

$$p_\psi(\mathbf{x}) = e^{ik\hat{\mathbf{e}}(\psi)\cdot\mathbf{x}} \quad (A_n = i^n e^{-in\psi}). \tag{6.21}$$

Then (6.20) becomes, with $\alpha_m \equiv ka_m$,

$$\begin{aligned} b_{m,l} &= \frac{\alpha_m}{4i} p_\psi(\mathbf{x}_m) \int_{\phi_1^{(m)}}^{\phi_2^{(m)}} \mathrm{d}\,\phi\, e^{-il\phi}\big[J_l'(\alpha_m) - i\mathbf{n}(\phi)\cdot\hat{\mathbf{e}}(\psi) J_l(\alpha_m)\big] p_\psi(\mathbf{y}-\mathbf{x}_m) \\ &= \frac{\alpha_m}{4i} p_\psi(\mathbf{x}_m) \int_{\phi_1^{(m)}}^{\phi_2^{(m)}} \mathrm{d}\,\phi\big[J_l'(\alpha_m) - i\cos(\phi-\psi) J_l(\alpha_m)\big] e^{i[\alpha_j\cos(\phi-\psi)-l\phi]} \\ &= \frac{\alpha_m}{4i} p_\psi(\mathbf{x}_m)\, e^{-il\psi}\big[J_l'(\alpha_m)G(\alpha_m) - J_l(\alpha_m)G'(\alpha_m)\big], \end{aligned} \tag{6.22}$$

where the function G is defined as

$$G(\alpha) = \int_{\phi_1^{(m)}-\psi}^{\phi_2^{(m)}-\psi} \mathrm{d}\,\phi\, e^{i(\alpha\cos\phi - l\phi)} = \sum_{n=-\infty}^{\infty} J_n(\alpha)\, i^n \int_{\phi_1^{(m)}-\psi}^{\phi_2^{(m)}-\psi} \mathrm{d}\,\phi\, e^{-i(n+l)\phi}. \tag{6.23}$$

The identity $e^{ix\sin\theta} = \sum_{n=-\infty}^{\infty} J_n(x) e^{in\theta}$ has been used in simplifying the form of $G(\alpha)$. Performing the integration in (6.23), we arrive at an explicit expression for the amplitude coefficients

$$b_{m,l} = u_\psi(\mathbf{x}_m)\frac{\alpha_m}{4} \sum_{p=-\infty}^{\infty} \big[J_p(\alpha_m)J_l'(\alpha_m) - J_p'(\alpha_m)J_l(\alpha_m)\big] \frac{i^p e^{ip\psi}}{p+l} \big[e^{-i(p+l)\phi_2^{(m)}} - e^{-i(p+l)\phi_1^{(m)}}\big]. \tag{6.24}$$

Now consider the incident field

$$\frac{i^{-n}}{2\pi} \int_0^{2\pi} \mathrm{d}\,\psi\, p_\psi(\mathbf{x}) e^{in\psi} = U_n^+\big(k\mathbf{x}\big) \quad (A_p = \delta_{np}). \tag{6.25}$$

It follows from integration of (6.24) that the general form of the amplitude coefficients for the general incidence (2.68) is given by (6.4b).

Finally, we turn to the question of where the active source field vanishes, noting that the integral (6.16) vanishes identically for field positions outside C [39]

$$\frac{i}{4}\int_{\partial C} \mathrm{d}\,S(\mathbf{y})\big[p^{in}(\mathbf{y})\partial_n V_0\big(k(\mathbf{y}-\mathbf{x})\big) - V_0\big(k(\mathbf{y}-\mathbf{x})\big)\partial_n p^{in}(\mathbf{y})\big] = 0, \quad \mathbf{x}\in\mathbb{R}^2/C. \tag{6.26}$$

How does this relate to the source field $p^d(\mathbf{x})$? In the course of the derivation of the coefficients $b_{m,n}$ the field $p^d(\mathbf{x})$ was expressed in the form (6.18) for $\mathbf{x}\in C$. The latter restriction on $\mathbf{x}$ can be removed since it is clear that eq. (6.18) *defines* $p^d(\mathbf{x})$ for all $\mathbf{x}$.

This is evident from the definition (6.1b) and from the identity (6.19) for $b_{m,n}$. Equation (6.26) therefore implies that $p^d(\mathbf{x})$ vanishes at all positions outside the cloaked region for which the representation (6.18) holds, i.e. $\{\mathbf{x} \notin C : \ |\mathbf{x}-\mathbf{x}_m| > |\mathbf{y}-\mathbf{x}_m|, \mathbf{y} \in \partial C_m, \ m = \overline{1,M}\}$. This is precisely the region R defined in (6.5), equal to, for instance, the exterior to the colored regions in Figure 6.3.

This completes the proof of Theorem 2.

6.3 Velocity field in an acoustic cloaked region

Let us consider a cloaked zone C generated by M active point multipole sources and calculate a total velocity field for acoustic cloaking. We assume time harmonic dependence $e^{-i\omega t}$. Let the total pressure p in an acoustic medium be defined by eq. (6.1a) as the sum of the incident wave p^{in} and the active source field p^d, where p^{in} and p^d are given respectively by eq. (2.68) and (6.1b).

We now want to find the velocity field $\mathbf{v}$ given the pressure; to do this we use the momentum balance equation (2.63) that yields

$$\mathbf{v} = -\frac{i}{\rho c k}\boldsymbol{\nabla} p, \tag{6.27}$$

where ρ is the density, c is the acoustic wave speed and $k = \omega/c$ is the wave number. Hence, the rectangular components of the velocity field are

$$\big(v_x,\, v_y\big) = -\frac{i}{\rho c k}\Big(\frac{\partial p}{\partial x},\, \frac{\partial p}{\partial y}\Big). \tag{6.28}$$

We consider a plane wave incidence in the direction of the unit vector $\hat{\mathbf{e}}(\psi)$, and the incident pressure field p^{in} in the form (6.21). Introducing eq. (6.1a) into (6.28) along with eqs. (6.1b), and (6.21) yields:

$$\begin{aligned} v_x = &-\frac{i}{\rho k c}\Big\{ik\cos\psi e^{ik\left(x\cos\psi + y\sin\psi\right)} + \sum_{m=1}^{M}\sum_{n=-\infty}^{\infty} b_{m,n} e^{in\arg(\mathbf{x}-\mathbf{x}_m)} \\ &\times\Big[\frac{k(x-x_m)}{|\mathbf{x}-\mathbf{x}_m|}H_n^{(1)'}(k|\mathbf{x}-\mathbf{x}_m|) - \frac{in(y-y_m)}{|\mathbf{x}-\mathbf{x}_m|^2}H_n^{(1)}(k|\mathbf{x}-\mathbf{x}_m|)\Big]\Big\}, \end{aligned} \tag{6.29a}$$

$$\begin{aligned} v_y = &-\frac{i}{\rho k c}\Big\{ik\sin\psi e^{ik\left(x\cos\psi + y\sin\psi\right)} + \sum_{m=1}^{M}\sum_{n=-\infty}^{\infty} b_{m,n} e^{in\arg(\mathbf{x}-\mathbf{x}_m)} \\ &\times\Big[\frac{k(y-y_m)}{|\mathbf{x}-\mathbf{x}_m|}H_n^{(1)'}(k|\mathbf{x}-\mathbf{x}_m|) + \frac{in(x-x_m)}{|\mathbf{x}-\mathbf{x}_m|^2}H_n^{(1)}(k|\mathbf{x}-\mathbf{x}_m|)\Big]\Big\}, \end{aligned} \tag{6.29b}$$

where prime in $H_n^{(1)'}(|\mathbf{z}|)$ denotes derivative with respect to argument $|\mathbf{z}|$. Using the notation $\theta_m(\mathbf{x}) = \arg(\mathbf{x} - \mathbf{x}_m)$, equation (6.29) can be simplified as:

$$v_x = \frac{1}{\rho c}\Big[\cos\psi\, p^{in} - \sum_{m=1}^{M}\sum_{n=-\infty}^{\infty} b_{m,n}\Big(i\cos\theta_m V_n^{+\prime}\big(k(\mathbf{x}-\mathbf{x}_m)\big) + n\sin\theta_m \frac{V_n^{+}\big(k(\mathbf{x}-\mathbf{x}_m)\big)}{k|\mathbf{x}-\mathbf{x}_m|}\Big)\Big], \tag{6.30a}$$

$$v_y = \frac{1}{\rho c}\Big[\sin\psi\, p^{in} - \sum_{m=1}^{M}\sum_{n=-\infty}^{\infty} b_{m,n}\Big(i\sin\theta_m V_n^{+\prime}\big(k(\mathbf{x}-\mathbf{x}_m)\big) - n\cos\theta_m \frac{V_n^{+}\big(k(\mathbf{x}-\mathbf{x}_m)\big)}{k|\mathbf{x}-\mathbf{x}_m|}\Big)\Big]. \tag{6.30b}$$

6.4 Acoustic Scattering from a Cylinder in a Cloaked Region

In this section we investigate the use of active exterior cloaking sources by considering acoustic scattering from rigid and soft cylinders of radius a immersed in water.

6.4.1 Scattering from cylinder

Let us first assume that active multiple sources are not included. Then total pressure field p is defined by (2.67) as the sum of incident p^{in} and scattered p^{sc} fields given by eqs. (2.68) and (2.69). The coefficients B_n are the desired scattering coefficients. The coefficients A_n define the incident field, as special case A_n includes a plane wave incidence in the direction ψ given by eq. (6.21). The outgoing scattered wave satisfies the corresponding boundary conditions at $r = a$, the Sommerfeld radiation condition at $r \to \infty$, and the Helmholtz equation outside the surface of a cylinder at $r > a$. For acoustically hard cylinder (rigid cylinder) the velocity of a fluid on the boundary $r = a$ is zero. This implies that the normal derivative of the total pressure field has to vanish on boundary $r = a$:

$$\frac{\partial p^{sc}(a)}{\partial r} = -\frac{\partial p^{in}(a)}{\partial r}. \tag{6.31}$$

For an acoustically soft cylinder, the total pressure field has to vanish on boundary $r = a$:

$$p = 0 \quad \texttt{or} \quad p^{sc} = -p^{in}. \tag{6.32}$$

Application of the boundary conditions (6.31) and (6.32) along with equations (6.21) and (2.69) leads to the following coefficient relations

$$B_n = T_{nn} i^n e^{in\psi}, \tag{6.33}$$

where T_{nn} is defined by eq. (3.133) for an acoustically hard cylinder (rigid cylinder) and eq. (3.134) for an acoustically soft (hollow) cylinder.

6.4.2 Cylinder in a cloaked region

Let's now assume that a cylinder is situated in some bounded cloaked region C generated by active cloaking devices. For simplicity, let us consider a cylinder surrounded by active sources having the symmetric configuration given in Figure 6.4. The center of the cylinder is at the origin that is located in the center of configuration.

The total field p is again defined as the sum of incident P^{in} and scattered P^{sc} fields:

$$p = P^{in} + P^{sc}, \tag{6.34}$$

But unlike in the previous case, now the incident field P^{in} on the cylinder consists of two parts p^{in} and p^{d}

$$P^{in} = p^{in} + p^{d} = \sum_{n=-\infty}^{\infty} (A_n + E_n) U_n^{+}\big(k\mathbf{x}\big), \tag{6.35}$$

where A_n is given by (6.21) and E_n, the near field coefficient, is defined by (6.14) .

The boundary conditions (6.31) and (6.32) yield correspondingly the following scattered field

$$P^{sc} = -\sum_{n=-\infty}^{\infty} T_{nq}(A_q + E_q)\delta_{qn} V_n^{+}\big(k\mathbf{x}\big), \tag{6.36}$$

where T_{nn} is defined by eq. (3.133) for an acoustically hard cylinder and eq. (3.134) for an acoustically soft cylinder. When the cloaking device is not active, i.e. $E_n = 0$, results coincide with ones given the in previous section, 6.4.1.

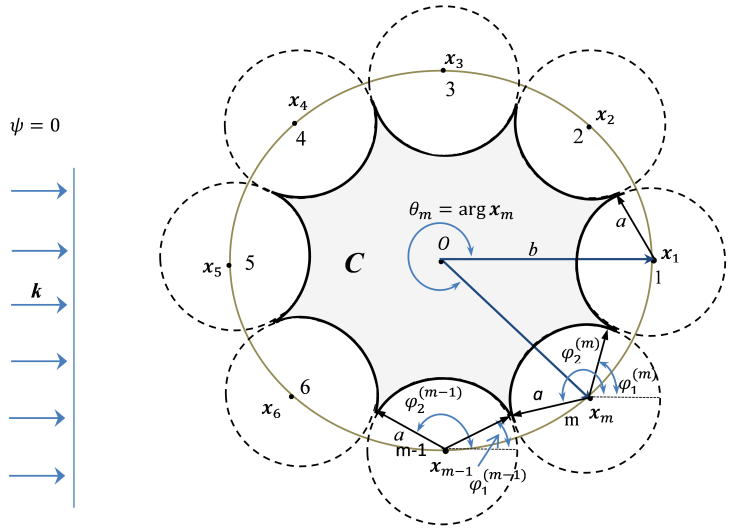

Figure 6.4: Plane wave insonification of the cloaking region C generated by $M = 8$ active sources.

6.5 Numerical examples

6.5.1 Active source configuration

We illustrate the results for plane wave incidence on configurations of the type shown in Fig. 6.4. The M sources are symmetrically located on a circle, with

$$a_m = a, \quad |\mathbf{x}_m| = b, \quad \theta_m = (m-1)\theta_0 \quad m = \overline{1, M}, \quad \text{where} \quad \theta_0 = 2\pi/M, \tag{6.37}$$

and by necessity, $a \geq b \sin \frac{\pi}{M}$. The circular arcs, which all have the same angular extent, are then defined by

$$\phi_{1,2}^{(m)} = \pi + \theta_m \mp \left| \sin^{-1}\left(\frac{b}{a}\sin\frac{\pi}{M}\right) - \frac{\pi}{M} \right|, \quad m = \overline{1, M}. \tag{6.38}$$

We take $a = b \sin \frac{\pi}{M}$ in all examples considered. Note that the cloaked region C can be formed by a minimum of 3 sources. A configuration with $M = 8$ sources is shown in Figure 6.4. All calculations were performed for plane wave incidence on configurations of the type shown in Figure 6.4 with varying numbers of sources, $M \geq 3$.

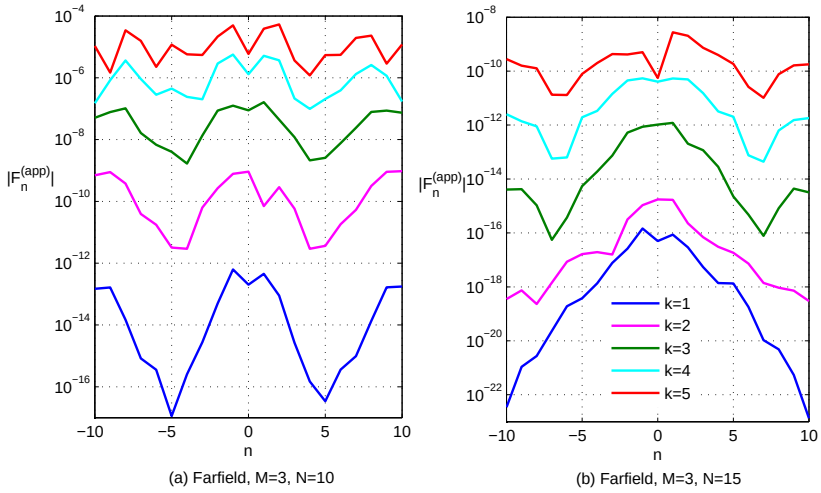

Figure 6.5: The farfield radiation amplitudes $|F_n^{(app)}|$ of eq. (6.39) for different orders of Bessel functions $n = \overline{-10, 10}$, wavenumbers $k = \overline{1, 5}$ and truncation values $N = 10$ and 15. The configuration is $M = 3$ multipole sources located at the distance $b = 1$ from the origin, with angle of incidence $\psi = 7^\circ$.

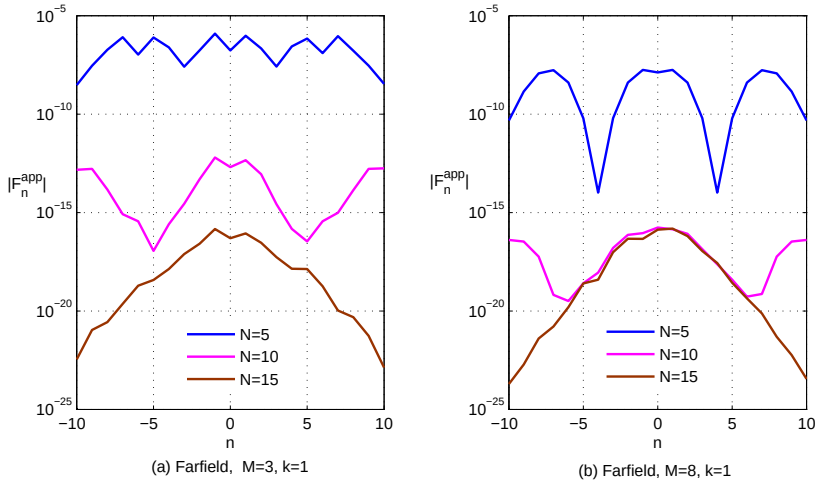

Figure 6.6: Dependence of the farfield amplitudes $|F_n^{(app)}|$ on the order n of Bessel functions for different values of N in (6.39) ($N = 5, 10, 15$) and for different numbers of active sources: (a) $M = 3$, and (b) $M = 8$. The incident wavenumber is $k = 1$.

6.5.2 Near and farfield amplitudes

The efficiency of the cloaked region is assessed by examining the farfield and nearfield as functions of various parameters. If all terms in the infinite sums in eqs. (6.9) and

(6.14) are available then the farfield is identically zero and the nearfield exactly cancels the incident wave by Theorems 1 and 2. We therefore consider truncated versions of the infinite sums so that the farfield and nearfield coefficients, F_n and E_n of eqs. (6.9) and (6.14) respectively, are approximated as

$$\left.\begin{matrix} F_n^{(app)} \\ E_n^{(app)} \end{matrix}\right\} = \sum_{m=1}^{M} \sum_{l=-N}^{N} b_{m,l} \times \begin{cases} V_{n-l}^{-}(\mathbf{x}_m), \\ U_{n-l}^{-}(\mathbf{x}_m), \end{cases} \qquad \forall\, n \in \mathbb{Z}. \tag{6.39}$$

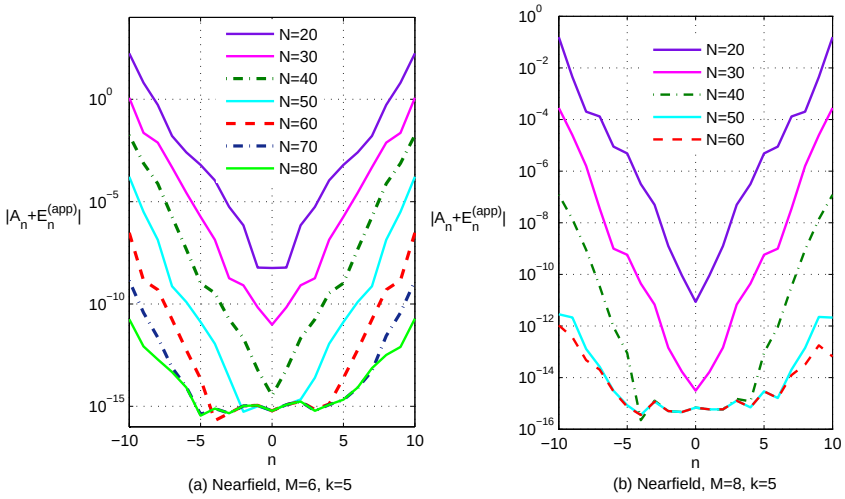

Figure 6.7: Variation of the nearfield amplitude coefficients $|A_n + E_n^{(app)}|$ for different values of the truncation size N in eq. (6.39), generated by $M = 6$ active sources in (a) and $M = 8$ sources in (b). In all cases $k = 5$.

In the limit of $N \to \infty$, exact cloaking is achieved. Restricting the summation to finite values of N is equivalent to limiting the order of the active multipole sources. The behavior of the approximate coefficients $F_n^{(app)}$ and $E_n^{(app)}$ has implications for the accuracy of the cloak, regardless of the type of object to be cloaked. Thus, the farfield coefficients determine the radiated field everywhere outside the cloak, and must necessarily be small regardless of whether or not an object is being cloaked. Similarly, the total field in the cloaked region C must be small in order to achieve cloaking. The two conditions correspond to $F_n^{(app)}$ and $E_n^{(app)} + A_n$ having small values. The examples in this subsection examine the sensitivity of these quantities. The sources are located at $b = 1$ with plane waves incident at $\psi = 17°$.

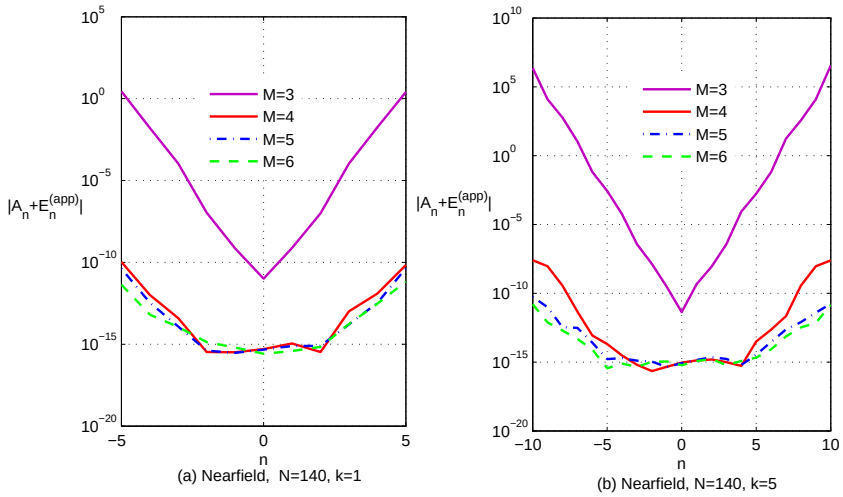

Figure 6.8: Dependence of the nearfield amplitude $|A_n + E_n^{(app)}|$ on the number of multipole sources M ($M = 3, 4, 5, 6$) at wavenumber $k = 1$ in (a) and $k = 5$ in (b).

The farfield amplitude coefficients $|F_n^{(app)}|$, $n = \overline{-10, 10}$ are depicted in Figures 6.5 and 6.6 for different values of the wavenumber k, the number of sources M, and the number of terms in summation (6.39), N. It is clear from these two figures that the error in the farfield coefficients decreases (i) as N increases, (ii) as M increases, and (iii) as k decreases. The convergence is particularly fast as a function of N. For instance, at $k = 1$ the farfield coefficients are uniformly less than 10^{-6} for all $M \geq 3$ if $N \geq 5$. Much smaller values (10^{-15} or less) for $|F_n^{(app)}|$ are easily achieved for moderate values of N, i.e. $N = 10$.

The nearfield amplitude coefficients $|A_n + E_n^{(app)}|$ are shown in Figures 6.7 to 6.9. In contrast with the farfield case, relatively large values of the truncation size N are required to obtain small nearfield coefficients. Figure 6.7 shows that N on the order of 100 or more is required to achieve accuracy comparable to the farfield coefficients. However, unlike the farfield amplitudes, it is found that the nearfield coefficients generally increase in magnitude with $|n|$, the order of the Bessel functions. The relatively large values of $|A_n + E_n^{(app)}|$ and their increase with the order $|n|$ does not necessarily mean that the total field in the nearfield is divergent. For instance, the top curve in Figure 6.7(a) indicates $|A_{10} + E_{10}^{(app)}| = \mathrm{O}(10^2)$, but this value multiplies $J_{10}(kr)$, and, for instance, $|J_{10}(kr)| < 2 \times 10^{-3}$ within C. In other words, the increasing values of

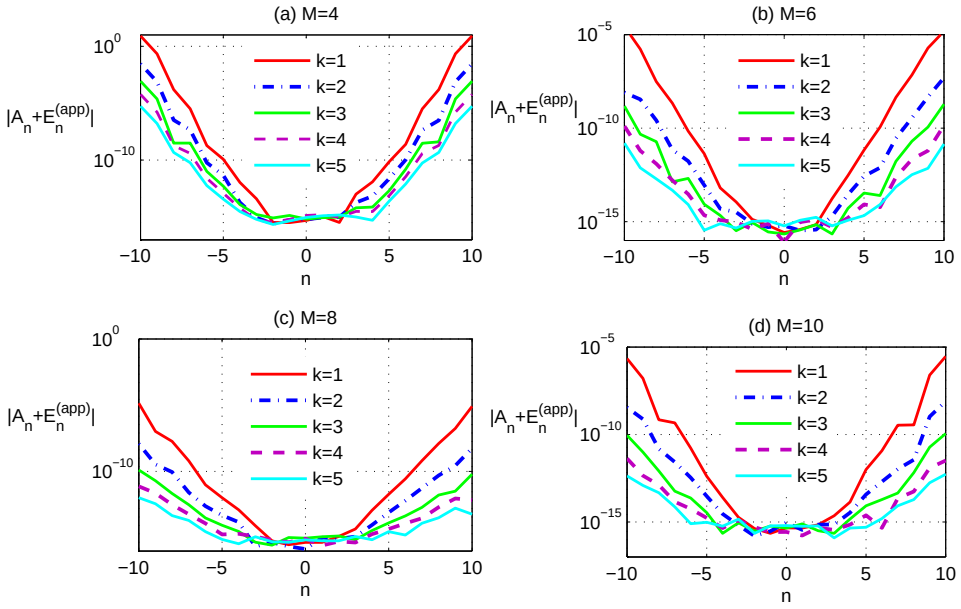

Figure 6.9: Variation of the nearfield amplitude coefficients with number of active sources ($M = 4, 6, 8, 10$) and with wavenumber ($k = \overline{1,5}$). In all cases $N = 130$.

$|A_n + E_n^{(app)}|$ with n can be balanced by the fact that $J_n(kr) = \frac{1}{n!}(\frac{kr}{2})^n + \ldots$ for small kr.

Figure 6.8 shows the dependence of the nearfield coefficients on the number of sources. The case of the minimum number of sources, $M = 3$, appears to be strikingly different from others ($M \geq 4$). As Figure 6.8 indicates, adding one more source and taking $M = 4$ reduces the error from 10^0 to 10^{-10} for $k = 1, n = \pm 5$ and from 10^{-2} to 10^{-14} for $k = 5, n = \pm 5$. Generally, as with the farfield coefficients, increasing the number of sources improves the accuracy of the nearfield amplitudes $|A_n + E_n^{(app)}|$.

Finally, Figure 6.9 shows the nearfield dependence on the wavenumber, $k = \overline{1,5}$. The accuracy actually improves with increasing k, unlike the farfield case. However, it should be borne in mind that the nearfield coefficients multiply the terms $J_n(kr)$, which increase in magnitude with k for fixed r.

The numerical results in Figures 6.5 through 6.9 show that greater accuracy is achieved using more sources, which is not unexpected. For the case of $M = 3$, the minimum number required, the nearfield coefficients could be large enough to significantly diminish the cloaking effect. This suggests taking $M = 4$ might be preferable.

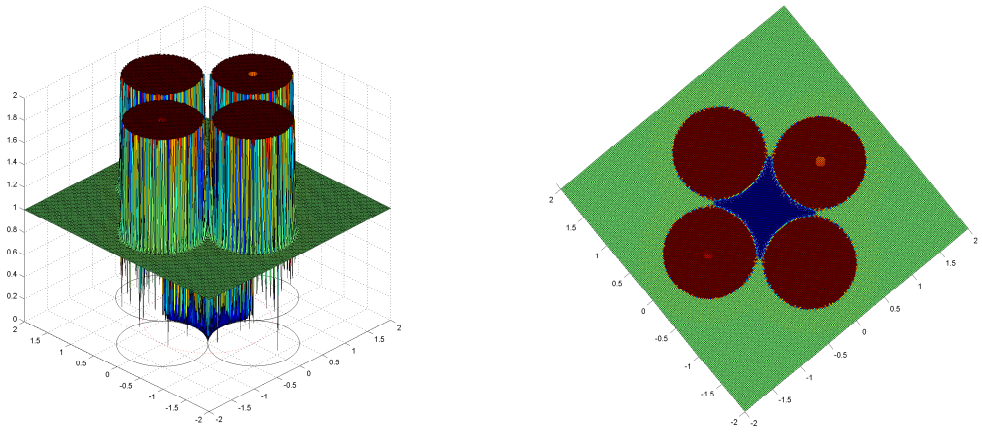

(a) 3D view **(b)** 2D view

Figure 6.10: Absolute value of total pressure field with 4 active sources, $b = 1$, angle of incidence $\psi = 17°$, wave number $k = 2$, and $N = 60$. Values above 2 in magnitude are clipped to make the plots visible

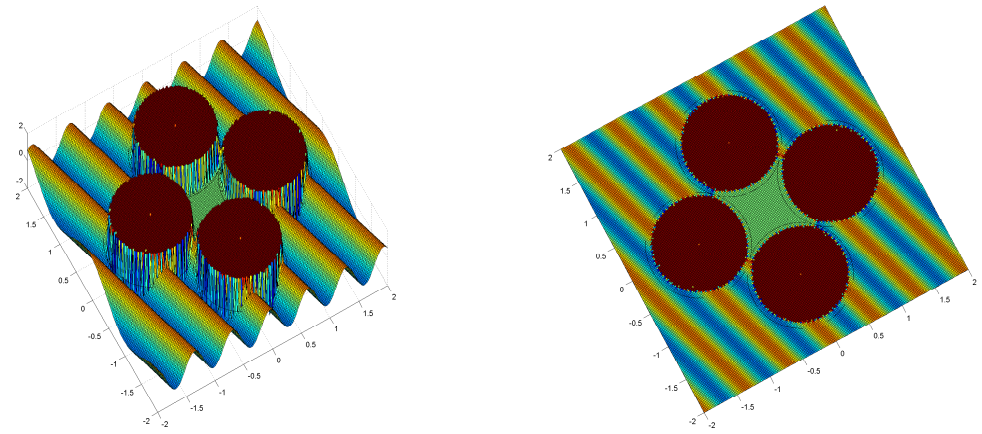

(a) 3D view **(b)** 2D view

Figure 6.11: Real part of total pressure field with 4 active sources, $b = 1$, $\psi = 17°$, wave number $k = 10$, and $N = 60$.

6.5.3 Total field

The total field for unit amplitude plane wave incidence on configurations of active sources of the type defined in Section 6.5.1 is illustrated through several examples. In all cases $b = 1$ and $\psi = 17°$. Figure 6.10 shows the absolute value of the field for four active sources: the subplots provide different perspectives, indicating that the field is indeed essentially zero in the cloaked region C, and that the radiated field u_d is zero outside the region R. The major variation in the source field is within the circular regions centered on the active sources. It is found that the field in these regions can take very large values, and therefore, for the sake of visibility we truncate the plot at an arbitrary value (here = 2). Note also that the cloaked region spills over slightly into the circular regions. This effect is perhaps easier to see in the subsequent examples.

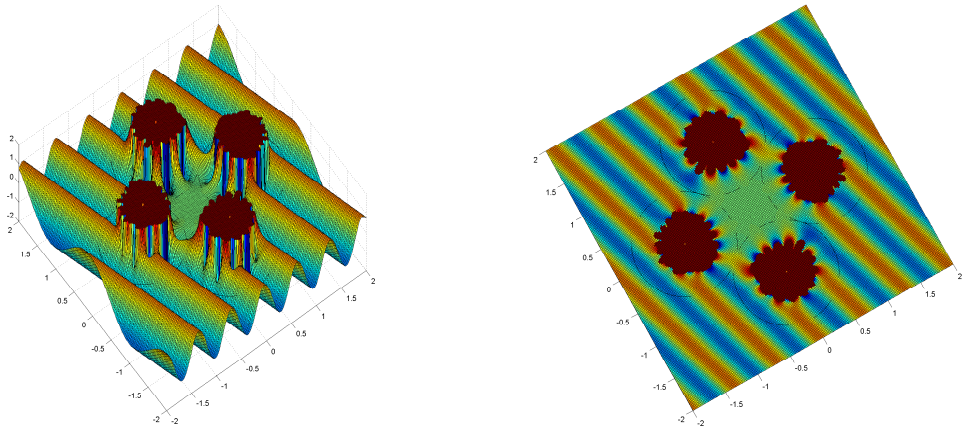

(a) 3D view **(b)** 2D view

Figure 6.12: Real part of total pressure field with 4 active sources, $\psi = 17°$, $k = 10$. The number of modes used in the truncated sum is here limited by $N = 10$.

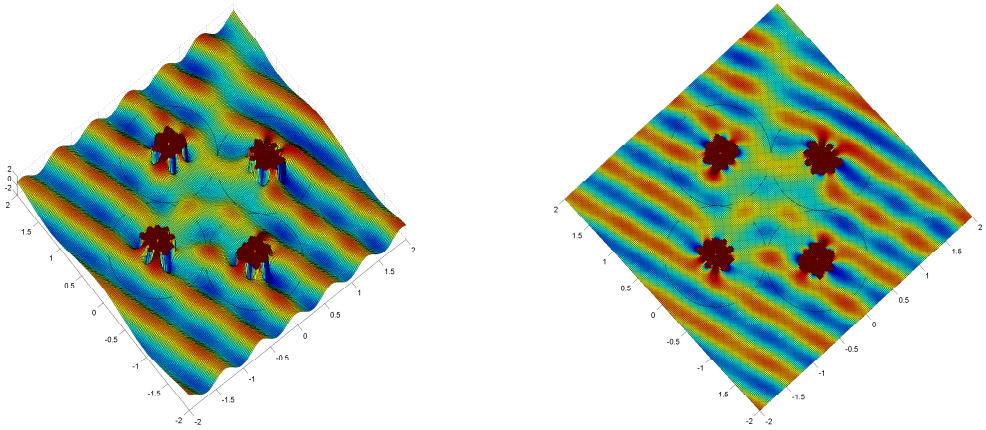

(a) 3D view **(b)** 2D view

Figure 6.13: The same as in Figure 6.12 except now $N = 5$.

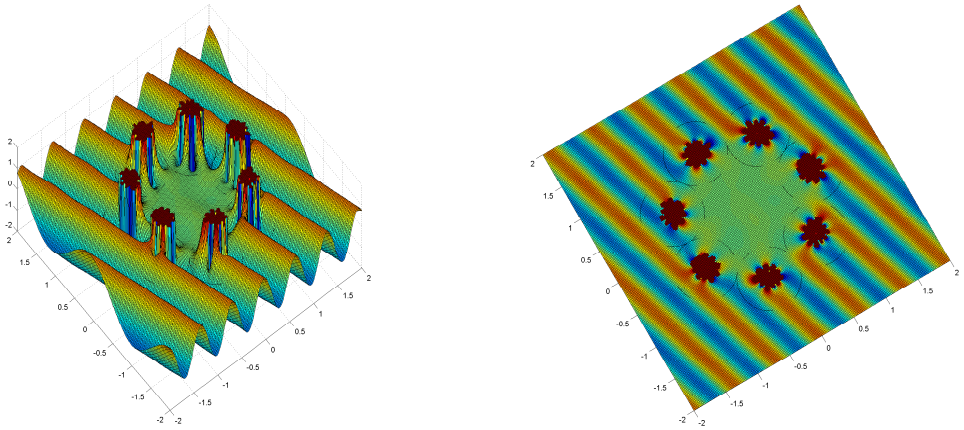

(a) 3D view **(b)** 2D view

Figure 6.14: The same as in Figure 6.13 except now $M = 7$.

Figure 6.11 considers the same $M = 4$ configuration of active sources at a higher frequency $k = 10$. The plots in this case show the real part of the total field, clearly illustrating the plane wave field in the exterior of R. The subplot on the right clearly

shows that the cloaked region is somewhat larger than C, extending partly into the circular regions. The number of modes used in Figure 6.11 ($N = 60$) is more than adequate to ensure convergence and accurate cloaking. It is more instructive to consider the effect of fewer modes, as in Figures 6.12 to 6.14. In Figure 6.12 the number of modes used is on the order of the frequency, and good accuracy is still observed. Notice the smaller footprints of the active sources, as compared with Figure 6.11, indicating that the higher modes "fill out" the regions where u_d is highly variable. Only $N = 5$ modes are used in Figure 6.13, and one can see the deterioration of the cloaking effect expected with an inadequate number of multipoles. The plane wave is clearly evident inside the cloaked region C, as are some scattering effects in the "shadow" zone. It is interesting to note that the active source footprints are reduced in size as compared with Figure 6.12. Finally, in Figure 6.14, we consider the effect of a larger number of active sources combined with a small number of modes. Comparison of Figures 6.13 and 6.14 indicates the tendency observed from the results of 6.5.2 that more active sources improves the cloaking effect. This is also to be expected from the discussion below in 6.6 which shows that for large numbers of sources only the lowest order multipoles play a significant role.

6.5.4 Scattering examples

Finally, we illustrate the effect of active exterior cloaking on plane wave scattering from rigid and soft cylinders (Neumann and Dirichlet boundary conditions, respectively). In each case, the cylinder is circular of radius $a_0 = 1$ centered at the origin, five active sources with $b = 4$ are used, the frequency is $k = 5$, and the incident wave strikes at angle $\psi = 17°$. Figures 6.15 and 6.16 compare the response from a rigid cylinder with the active cloaking turned on and turned off. The absolute value is shown in Figure 6.15 while Figure 6.16 considers only the real part of the complex field, which clearly indicates the plane wave propagating undisturbed when the cloak is active. The comparison for a soft cylinder is shown in Figures 6.17 and 6.18.

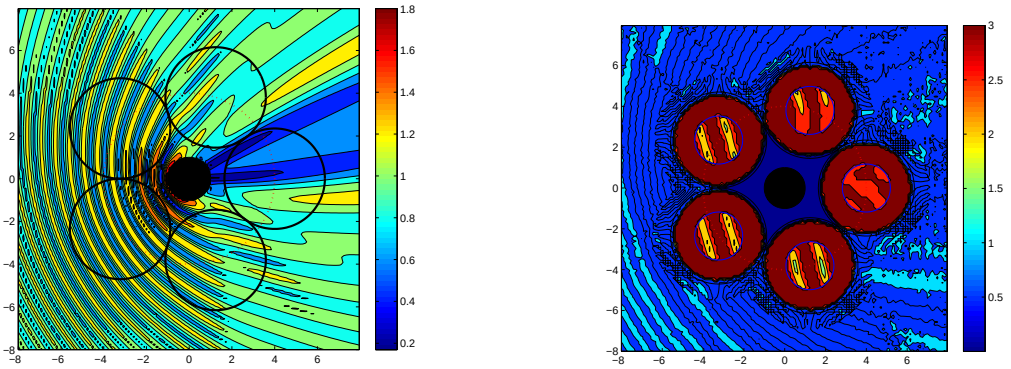

(a) Cloaking devise OFF **(b)** Cloaking devise ON

Figure 6.15: Absolute value of total pressure field when cloaking devices are inactive (left) and active (right) for scattering from the hard cylinder. Calculations are performed for a hard cylinder with $M = 5$ active sources, angle of incidence $\psi = 17°$, and wave number $ka = 5$.

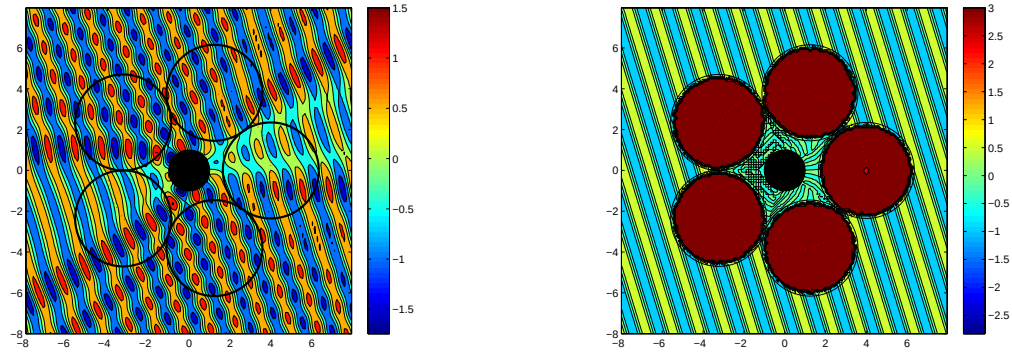

(a) Cloak inactive **(b)** Cloak active

Figure 6.16: Real value of total pressure field when cloaking devices are inactive (left) and active (right) for scattering from a hard cylinder.

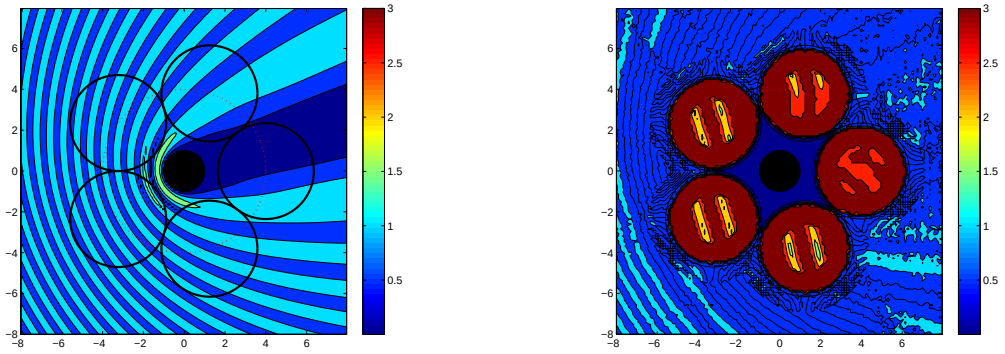

(a) Cloak inactive **(b)** Cloak active

Figure 6.17: Absolute value of total pressure field with cloaking devices are inactive (left) and active (right) for scattering from a soft cylinder: $k = 5$, $\psi = 17°$.

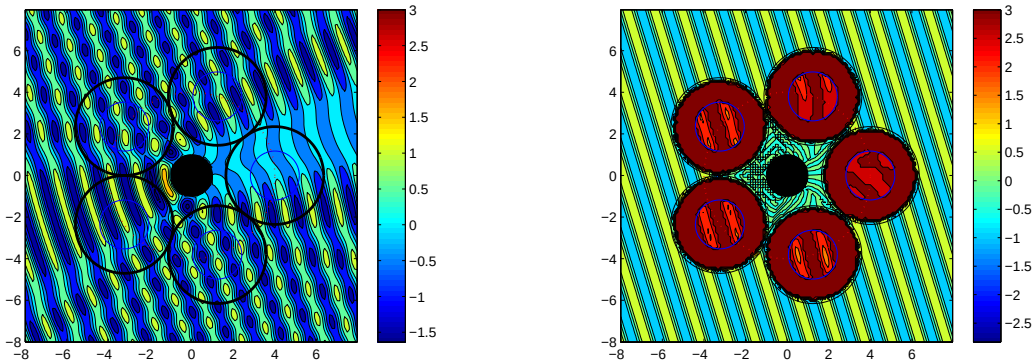

(a) Cloak inactive **(b)** Cloak active

Figure 6.18: Real part of total pressure field is displayed for a soft cyliner when cloaking devices are inactive (left) and active (right): $k = 5$, $\psi = 17°$.

6.6 Discussions and Conclusions

The numerical results of 6.5.2 indicate better convergence properties for fewer multipoles if more active sources are used. This is consistent with the finding of Du et al. [10] that the order N of the multipoles required decreases as the number of sources M

increases. It is therefore of interest to consider the limit in which many sources are available: the large M limit. Staying with the configuration of 6.5.1, the appropriate limit to consider is $(a_m =)a \approx b\pi/M$ so that $ka \ll 1$ and the small argument approximation can be used for the Bessel functions $J_n(ka_m)$ (note kb is not necessarily small). This implies that to leading order in ka the coefficients in (6.4b) reduce to

$$b_{m,ln} = \frac{i}{4}ka \times \begin{cases} (-2)\, U_n^{+\prime}(\mathbf{x}_m), & l = 0, \\ l e^{-il\theta_m}\, U_n^{+}(\mathbf{x}_m), & l = \pm 1, \\ 0, & l \neq 0, \pm 1. \end{cases} \tag{6.40}$$

The identity $J_{n-1}(x) - J_{n+1}(x) = 2J_n'(x)$ has been used to simplify the $l = 0$ term in (6.40). The source field follows from eq. (6.1b) and the identity $V_{-1}^{+}(\mathbf{x}) = -V_1^{-}(\mathbf{x}_m)$ as

$$u_d = \frac{i}{2}ka \sum_{n=-\infty}^{\infty} A_n \sum_{m=1}^{M} \times \tag{6.41}$$

$$\Big[U_n^{+}(\mathbf{x}_m) H_1^{(1)}(|\mathbf{x} - \mathbf{x}_m|) \cos\big(\arg(\mathbf{x} - \mathbf{x}_m) - \theta_m\big) - U_n^{+\prime}(\mathbf{x}_m) H_0^{(1)}(|\mathbf{x} - \mathbf{x}_m|)\Big]. \tag{6.42}$$

The field of the active sources is therefore composed of monopoles and dipoles only, with no contribution from higher multipoles. This agrees with what one might expect from the continuous limit of $M \to \infty$, i.e. a closed contour of monopoles and dipoles, but here it is obtained from the discrete solution. In fact, eq. (6.41) is

$$u_d = \frac{i}{2}a \sum_{m=1}^{M} \big[u_i(\mathbf{x}_m)\partial_n V_0(\mathbf{x} - \mathbf{x}_m) - V_0(\mathbf{x} - \mathbf{x}_m)\partial_n u_i(\mathbf{x}_m)\big], \tag{6.43}$$

which can be seen to be the discretized version of the fundamental integral identity eq. (6.16) with the correspondence $\int \mathrm{d}\, S \to 2a \sum_m$. While eq. (6.40) is thus the natural first approximation for u_d based on the integral equation (6.16), it should be realized that it was obtained here as a first order approximation of the exact expression (6.4b). The latter therefore provides the basis for a multipole expansion of the exact source field obtained by including higher powers of ka than considered in eq. (6.40). This possibility goes beyond our present interests but will be examined in a separate study dealing with approximations to the exact results of Theorem 2.

The exact source field $u_d(\mathbf{x})$ of eq. (6.1b) exhibits some interesting features. This field is, by design, equal to the negative of the incident field in the cloaking region C, and it also vanishes identically outside the concave region R defined in (6.5) The non-radiating property of u_d is as important as the fact that it exactly cancels the incident wave in C. Let us examine this more closely. Define the infinite matrix $\mathbf{S}$ with elements S_{pq} such that

$$F_p = \sum_{q=-\infty}^{\infty} S_{pq} A_q \quad \Rightarrow \quad S_{pq} = \sum_{m=1}^{M} \sum_{l=-\infty}^{\infty} b_{m,lq} U_{p-l}^{-}(\mathbf{x}_m), \tag{6.44}$$

or, using (6.6),

$$S_{pq} = \sum_{m=1}^{M} \frac{ka_m}{4} \sum_{l,n=-\infty}^{\infty} U_{p-l}^{-}(\mathbf{x}_m) U_{n+q}^{+}(\mathbf{x}_m) \frac{(-1)^n}{l+n} \left[U_n^{-}(\mathbf{a}) U_l^{-\prime}(\mathbf{a}) - U_n^{-\prime}(\mathbf{a}) U_l^{-}(\mathbf{a}) \right] \Big|_{\mathbf{a}_1^{(m)}}^{\mathbf{a}_2^{(m)}}. \tag{6.45}$$

The matrix $\mathbf{S}$ is, formally at least, like a scattering matrix. For instance, by inspection, $\mathbf{S}$ is hermitian ($S_{pq} = S_{qp}^*$). However, by design and based on Theorem 1, $\mathbf{S} \equiv 0$, and as such it could be called a zero-scattering matrix. Alternatively, it can be viewed as a formula for generating non-radiating fields. This has relevance to the *inverse source problem* [168]. It is known that solutions to the inverse source problem are non-unique [19], although some uniqueness results are available for restricted forms of sources, e.g. "minimum energy sources" [47]. The solution of the active cloaking problem as developed here has generated a new family of non-radiating sources, with the property that they cancel a given incident field over a finite region.

By definition, an active source cloaking strategy requires solution of an inverse problem: find the active source amplitudes associated with a given incident field in order to exactly cancel the latter in some finite region. The results given in Theorem 2 provide closed-form solutions for the inverse problem for an arbitrary time harmonic incident wave field. These new expressions require only the expansion of the incident field into entire cylindrical waves and can be evaluated to any degree of accuracy by increasing the truncation parameter N associated with the number of modes of the active source. Simultaneously the fact that the active source field has been shown to vanish identically outside the region R defined in (6.5) means that the active field is

non-radiating. This latter property is just as important as its ability to nullify the incident wave in the region C.

The necessary and sufficient conditions on the active source coefficients, given in Theorem 1 provide a means to quantify the error in active cloaking when the number of modes is finite. These errors have been analyzed here in some specific scenarios. It has been shown that the error in the far-field amplitude decreases as N increases, M increases and k decreases. In particular, there is a great sensitivity to the increase in N; relatively small errors can be attained in the far-field amplitudes for moderate N, say $N \sim 10$. On the other hand for small errors in the *near-field* amplitudes, relatively large values of N are required. Furthermore, there is a striking reduction in error when moving from the case of $M = 3$ to $M = 4$, motivating the latter as a preference. In contrast to the far-field case, errors decrease for *increasing* k.

Numerical results were given which illustrate the cloaking effect in various instances, including the presence of a sound-soft and sound-hard circular cylinder. In the appropriate limits, perfect theoretical active cloaking is achieved. The availability of closed-form active source amplitudes opens the door for possible studies on practical realization of active cloaking devices.

The case of many sources, where the active field degenerates to one involving a sum of monopole and dipole sources, is worthy of further, separate study relating to the multipole expansion associated with the active field. Finally, the non-radiating nature of the active source field is especially noteworthy. The associated scattering matrix, defined in (6.45) (which is zero by design), is therefore associated with a new family of non-radiating source solutions which would appear to be useful in the so-called *inverse source problem*.

Chapter 7

Elastic active exterior cloaking

The main function of a cloaking device is to render an object invisible to some incident wave as seen by some external observer. The aim of active exterior cloaking is to render the total field zero inside some prescribed domain (the *cloak* or *zone of silence*), whilst ensuring that the active field itself is non-radiating. The technique introduced in the early active exterior cloaking work [112] and described in Chapter 6 enables a cloaked region to be identified clearly by the use of Graf's addition theorem. This approach allows precise determination of the necessary source amplitudes. In this Chapter, we will generalize the idea of active acoustic exterior cloaking [112] to include the elastodynamic properties of medium. An active elastodynamic cloak destructively interferes with an incident time harmonic in-plane (coupled compressional/shear) elastic wave to produce zero total elastic field over a finite spatial region. A cloaking of a finite region in two dimensions from time harmonic elastic waves is achieved using a discrete set of point multipole forces. The amplitudes of the sources are uniquely determined by the incident wave through a set of explicit expressions.

As yet, it does not appear that active exterior cloaking has been applied to the elastodynamic context. This Chapter will focus on the relevant two-dimensional active elastodynamic cloaking problem. In general, elastodynamic cloaking problems are more difficult to study than their acoustic or electromagnetic counterparts. Indeed, in the case of passive elastodynamic cloaking, this is due to the lack of invariance of Navier's equations under coordinate transformations [102] unless we relax the minor symmetry property of the required elastic modulus tensor. The latter can be achieved by using Cosserat materials [25, 117] or by employing nonlinear pre-stress of hyperelastic materials [119, 120, 115]. Here we show how the active approach to cloaking can be

employed in the elastodynamic case for the fully coupled two-dimensional (in-plane) compressional/shear wave problem. As in the approach of [112], we write down the relevant integral equation by employing the isotropic Green's tensor in this case. The required source amplitudes for arbitrary wave incidence can be determined explicitly by using Graf's addition theorem.

Results presented in this Chapter were published in [108]. We shall begin in Section 7.1 with a statement of the problem, a review of the governing equations, and a summary of the main results. The relevant integral relation is derived in Section 7.2, from which the main results regarding the explicit form of the source amplitudes are shown to follow. We consider both compressional and transverse (shear) wave incidence. We also describe the form of the active source field and the issues associated with divergence described above. Numerical results follow in Section 7.3.

7.1 Problem formulation and main results

7.1.1 Problem overview

Let us consider the two-dimensional configuration where the active cloaking devices consist of arrays of point multipole sources located at positions $\mathbf{x}_m \in \mathbb{R}^2$, $m = \overline{1, M}$ as depicted in Figure 7.1. These sources can give rise to both shear and compressional elastic waves. The active sources lie in the exterior region with respect to the cloaked region C and for this reason, this type of cloaking is called *active exterior cloaking* [179]. Objects are undetectable in the cloaked region by virtue of the destructive interference of the sources and the incident field with the result that the total wave amplitude vanishes in the cloaked region C. As described in [112], this gives rise to three significant advantages over passive cloaking: (i) the cloaked region is not completely surrounded by a single cloaking device; (ii) only a small number of active sources are needed; (iii) the procedure works for broadband input sources. The principal disadvantage of the method is, of course, that the incident field must be known.

The M active sources give rise to a cloaked zone C is indicated in Figure 7.1 by the shaded region whose boundary C is the closed concave union of the circular arcs

∂C_m $m = \overline{1, M}$, $\{a_m, \theta_1^{(m)}, \theta_2^{(m)}\}$ associated with the source at $\mathbf{x}_m$. In the general case $\{a_m, \theta_1^{(m)}, \theta_2^{(m)}\}$ are distinct for different values of m. Note that the wave incidence shown in Figure 7.1 is a plane wave although the solution derived below is for arbitrary incidence. We therefore have to determine the amplitudes of the active sources as a function of the incident wave, and then prove that the cloaked region is indeed the closed region C as indicated in Figure 7.1. Let us also define the notation $\mathcal{A}_m$ as the circular domain of radius a_m that contains the mth active source at its centre. We also define the union of these domains $\mathcal{A} = \cup_{m=1}^{M} \mathcal{A}_m$.

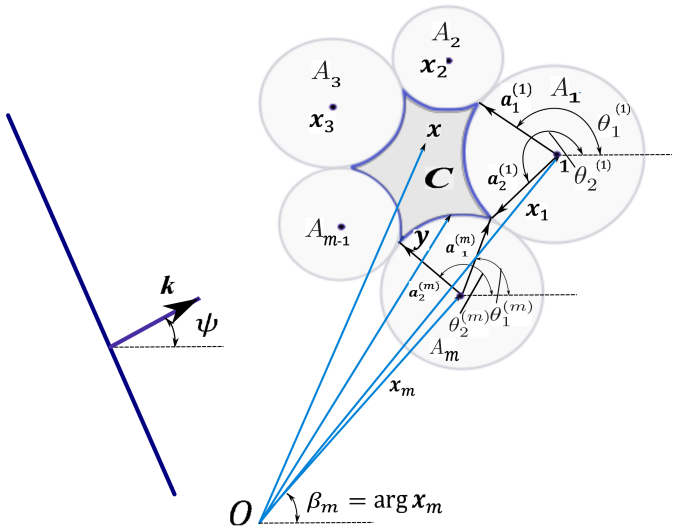

Figure 7.1: Insonification of the actively cloaked region C generated by M active point multipole sources at $\mathbf{x}_m$, and active source regions $\mathcal{A}_m$, $m = \overline{1, M}$. The incident field in this case is a plane wave with wave vector $\mathbf{k}$ in the direction ψ.

The governing equations for P/SV in-plane wave propagation are given in Section 2.3.2. Navier's equations in two dimensions for the displacement $\mathbf{u} = (u_1, u_2)$, $u_j = u_j(x_1, x_2)$, are given by eq. (2.78). Substitution of Helmholtz decomposition (2.56) for the displacement into Navier's equations leads to separate Helmholtz equations (2.80) for the scalar potentials Φ and Ψ.

We seek the total wave field in the form of an incident wave, $\mathbf{u}_i$, plus the active

source field, $\mathbf{u}_d$, such that

$$\mathbf{u}(\mathbf{x}) = \mathbf{u}_i + \mathbf{u}_d \quad \Rightarrow \quad \Phi(\mathbf{x}) = \Phi_i + \Phi_d, \qquad \Psi(\mathbf{x}) = \Psi_i + \Psi_d. \tag{7.1}$$

We assume the general form of an incident field in the regular basis, and hence

$$\begin{pmatrix} \Phi_i \\ \Psi_i \end{pmatrix} = \sum_{n=-\infty}^{\infty} \begin{pmatrix} A_n^{(p)} U_n^+(k\mathbf{x}) \\ A_n^{(s)} U_n^+(K\mathbf{x}) \end{pmatrix}, \tag{7.2a}$$

$$\begin{pmatrix} \Phi_d \\ \Psi_d \end{pmatrix} = \sum_{m=1}^{M} \sum_{n=-\infty}^{\infty} \begin{pmatrix} B_{m,n}^{(p)} V_n^+(k(\mathbf{x}-\mathbf{x}_m)) \\ B_{m,n}^{(s)} V_n^+(K(\mathbf{x}-\mathbf{x}_m)) \end{pmatrix}, \tag{7.2b}$$

where the functions $U_n^{\pm}(\boldsymbol{z})$ and $V_n^{\pm}(\boldsymbol{z})$ are defined by equations (2.66) and (2.70). In the following we write U_0 and V_0, with obvious meaning.

7.1.2 Summary of the main results

Here we shall state the main results and the required source amplitudes to enable perfect active cloaking together with necessary and sufficient conditions on these amplitudes. The latter ensures we can compare accuracy of the cloaking technique. We shall prove these results in Section 7.2. Let $\{a_m, \theta_1^{(m)}, \theta_2^{(m)}\}$ define the circular arc ∂C_m of the closed boundary of the cloaked region associated with the source at $\mathbf{x}_m$. The active

source amplitude coefficients for the general form of an incident field (7.2a) are

$$\begin{pmatrix} B_{m,\,l}^{(p)} \\ \\ B_{m,\,l}^{(s)} \end{pmatrix} = \sum_{n=-\infty}^{\infty} \begin{pmatrix} B_{m,\,ln}^{(p)}\, A_n^{(p)} \\ \\ B_{m,\,ln}^{(s)}\, A_n^{(s)} \end{pmatrix}, \quad \text{where} \tag{7.3a}$$

$$\begin{aligned} \begin{pmatrix} B_{m,\,ln}^{(p)} \\ \\ B_{m,\,ln}^{(s)} \end{pmatrix} =& \frac{1}{4(ka_m)^2} \sum_{q=-\infty}^{\infty} (-1)^q \big[e^{-i(q+l)\theta_2^{(m)}} - e^{-i(q+l)\theta_1^{(m)}} \big] \\ & \cdot \left\{ U_{n+q}^{+}(k\mathbf{x}_m) \begin{pmatrix} v_1(ka_m,\, Ka_m) \\ v_2(ka_m,\, Ka_m) \end{pmatrix} + U_{n+q}^{+}(k\mathbf{x}_m) \begin{pmatrix} -v_2(Ka_m,\, ka_m) \\ v_1(Ka_m,\, ka_m) \end{pmatrix} \right\}, \end{aligned} \tag{7.3b}$$

$$\mathbf{v}(\alpha, \beta) = \begin{pmatrix} v_1 \\ v_2 \end{pmatrix} = \begin{pmatrix} \big[\frac{\alpha_s^{(m)^2}}{q+l} - 2q \big] \alpha J_l'(\alpha) & i \big[\frac{\alpha_s^{(m)^2}}{q+l} - 2l \big] \alpha J_l(\alpha) \\ \\ -i \big[\alpha_s^{(m)^2} - 2lq \big] J_l(\beta) & -2\alpha_p^{(m)} \alpha_s^{(m)} J_l'(\beta) \end{pmatrix} \begin{pmatrix} J_q(\alpha) \\ \\ iJ_q'(\alpha) \end{pmatrix}. \tag{7.3c}$$

The derivation of eq. (7.3) is given in Section 7.2.5. Alternatively defining a vector $\mathbf{a}_i^{(m)} \equiv a_m \hat{\mathbf{e}}(\theta_i^{(m)})(i = 1,\, 2)$, and incorporating eqs. (2.66) and (6.2), eq. (7.3b) reduces to the form

$$\begin{aligned} \begin{pmatrix} B_{m,\,ln}^{(p)} \\ \\ B_{m,\,ln}^{(s)} \end{pmatrix} =& \frac{1}{4\alpha_s^{(m)^2}} \sum_{q=-\infty}^{\infty} (-1)^q \Big\{ U_{n+q}^{+}(k\mathbf{x}_m) \begin{pmatrix} V_1(k\mathbf{a},\, K\mathbf{a}) \\ V_2(k\mathbf{a},\, K\mathbf{a}) \end{pmatrix} \\ & + U_{n+q}^{+}(K\mathbf{x}_m) \begin{pmatrix} -V_2(K\mathbf{a},\, k\mathbf{a}) \\ V_1(K\mathbf{a},\, k\mathbf{a}) \end{pmatrix} \Big\} \Big|_{\mathbf{a}_1^{(m)}}^{\mathbf{a}_2^{(m)}}, \quad \text{where} \end{aligned} \tag{7.4a}$$

$$\mathbf{V}(\boldsymbol{\alpha}, \boldsymbol{\beta}) = \begin{pmatrix} V_1 \\ V_2 \end{pmatrix} = \begin{pmatrix} \big[\frac{\alpha_s^{(m)^2}}{q+l} - 2q \big] \alpha U_l^{-\prime}(\boldsymbol{\alpha}) & i \big[\frac{\alpha_s^{(m)^2}}{q+l} - 2l \big] \alpha U_l^{-}(\boldsymbol{\alpha}) \\ \\ -i \big[\alpha_s^{(m)^2} - 2lq \big] U_l^{-}(\boldsymbol{\beta}) & -2\alpha_p^{(m)} \alpha_s^{(m)} U_l^{-\prime}(\boldsymbol{\beta}) \end{pmatrix} \begin{pmatrix} U_q^{-}(\boldsymbol{\alpha}) \\ \\ iU_q^{-\prime}(\boldsymbol{\alpha}) \end{pmatrix}. \tag{7.4b}$$

The active source coefficients $B^{(p)}_{m,l}$ and $B^{(s)}_{m,l}$ must satisfy the necessary conditions:

$$\forall\, n \in \mathbb{Z}: \qquad \sum_{m=1}^{M}\sum_{l=-\infty}^{\infty} \times \begin{cases} B^{(p)}_{m,l} U^{-}_{n-l}(k\mathbf{x}_m) & = 0, \\ B^{(s)}_{m,l} U^{-}_{n-l}(K\mathbf{x}_m) & = 0, \\ B^{(p)}_{m,l} V^{-}_{n-l}(k\mathbf{x}_m) & = -A^{(p)}_{n}, \\ B^{(s)}_{m,l} V^{-}_{n-l}(K\mathbf{x}_m) & = -A^{(s)}_{n}. \end{cases} \tag{7.5}$$

Note that in eq. (7.5), for an incident longitudinal wave, $A^{(s)}_n = 0$ and so the term on the right hand side of the fourth identity vanishes, whereas for a transverse incident wave, $A^{(p)}_n = 0$, and as a result the right hand side of the third equation reduces to zero. The constraints on $B^{(p)}_{m,l}$ and $B^{(s)}_{m,l}$ will be used to estimate an error in the active cloaking region in the following sections by truncating an infinite sum in (7.5).

7.2 Solution for the source amplitudes

We begin the derivation by formulating the problem as an integral equation.

7.2.1 Integral equation

With knowledge of the Green's tensor $\mathbf{G} = [G_{ik}]$ defined by (2.94) we can now develop an integral equation for the displacement. Indeed, if $\mathbf{u}$ is a solution of the homogeneous equations in an infinite domain containing a finite region D and $\boldsymbol{\sigma}$ is the associated stress, then by definition of the Green's tensor,

$$\int_{\partial D} \mathrm{d}\, S n_i \big[u_j(\mathbf{y})\Sigma_{ijk}(\mathbf{y}-\mathbf{x}) - \sigma_{ij}(\mathbf{y})G_{jk}(\mathbf{y}-\mathbf{x})\big] = \begin{cases} u_k(\mathbf{x}), & \mathbf{x} \in D, \\ 0, & \mathbf{x} \notin D. \end{cases} \tag{7.6}$$

Equation (7.6) holds for both $\mathbf{u}_i$ and $\mathbf{u}_d$ separately inside the cloaked region, since both are assumed to be regular there (this is a definition of exterior cloaking). Also, by

its definition the total field is zero inside the cloaked region with boundary ∂C, and therefore

$$\mathbf{u}_d(\mathbf{x}) = -\int_{\partial C} \mathrm{d}\, S\mathbf{n}\cdot\big[\mathbf{u}_i(\mathbf{y})\cdot\boldsymbol{\Sigma}(\mathbf{y}-\mathbf{x}) - \boldsymbol{\sigma}_i(\mathbf{y})\cdot\mathbf{G}(\mathbf{y}-\mathbf{x})\big], \quad \mathbf{x}\in C. \tag{7.7}$$

This is the fundamental relation used to find the source amplitudes.

7.2.2 General expressions for the source amplitudes

Following the procedure for the acoustic problem we first substitute the assumed form of $\mathbf{u}_d$ into the left member of (7.7). Then we partition the integral in the right member into M segments over $\{\partial C_m, m=\overline{1,M}\}$ and identify each line integral with the m^{th} component of $\mathbf{u}_d$, i.e. the part of the source field from the multipoles at $\mathbf{x}_m$. Thus,

$$\begin{aligned} 0 = \sum_{m=1}^{M}\Bigg\{ &\int_{\partial C_m} \mathrm{d}\, S\mathbf{n}\cdot\big[\mathbf{u}_i(\mathbf{y})\cdot\boldsymbol{\Sigma}(\mathbf{y}-\mathbf{x}) - \boldsymbol{\sigma}_i(\mathbf{y})\cdot\mathbf{G}(\mathbf{y}-\mathbf{x})\big] \\ &+ \sum_{n=-\infty}^{\infty}\Big(B^{(p)}_{m,n}\nabla V_n^{+}(k(\mathbf{x}-\mathbf{x}_m)) + B^{(s)}_{m,n}\nabla\times\mathbf{k}V_n^{+}(K(\mathbf{x}-\mathbf{x}_m))\Big)\Bigg\}, \quad \mathbf{x}\in C. \end{aligned} \tag{7.8}$$

We now use the generalized Graf addition theorem (2.72). The idea is to write $\boldsymbol{\Sigma}(\mathbf{y}-\mathbf{x})$ and $\mathbf{G}(\mathbf{y}-\mathbf{x})$ in (7.8) in terms of sources at $\mathbf{x}_m$. This suggests using (2.72) for $\mathbf{y}-\mathbf{x}\to(\mathbf{y}-\mathbf{x}_m)-(\mathbf{x}-\mathbf{x}_m)$ subject to $|\mathbf{y}-\mathbf{x}_m|<|\mathbf{x}-\mathbf{x}_m|$. Hence, using (2.95),

$$\begin{aligned} \mathbf{G}(\mathbf{y}-\mathbf{x}) = \frac{i}{4\rho\omega^2}\sum_{n=-\infty}^{\infty}\Big\{ &\nabla\nabla U_n^{-}\big(k(\mathbf{y}-\mathbf{x}_m)\big)V_n^{+}\big(k(\mathbf{x}-\mathbf{x}_m)\big) \\ &+ (\nabla\times\mathbf{k})(\nabla\times\mathbf{k})U_n^{-}\big(K(\mathbf{y}-\mathbf{x}_m)\big)V_n^{+}\big(K(\mathbf{x}-\mathbf{x}_m)\big)\Big\}. \end{aligned} \tag{7.9}$$

By virtue of the dependence of the Green's function on $\mathbf{y}-\mathbf{x}$, the derivatives $\nabla\nabla$ can be understood as $\nabla_y\nabla_y$ or $\nabla_x\nabla_x$ or $-\nabla_y\nabla_x$, with the same equivalence for $(\nabla\times\mathbf{k})(\nabla\times\mathbf{k})$. Inspection of (7.8) suggests that the forms $-\nabla_y\nabla_x$ and $-(\nabla_y\times\mathbf{k})(\nabla_x\times\mathbf{k})$ are appropriate. Taking into account the negative sign in $\nabla\nabla\to-\nabla_y\nabla_x$, the Green's function can be written in the form

$$\begin{aligned} \mathbf{G}(\mathbf{y}-\mathbf{x}) = \frac{-i}{4\rho\omega^2}\sum_{n=-\infty}^{\infty}\Big\{ &\nabla_y U_n^{-}\big(k(\mathbf{y}-\mathbf{x}_m)\big)\nabla_x V_n^{+}\big(k(\mathbf{x}-\mathbf{x}_m)\big) \\ &+ (\nabla_y\times\mathbf{k})U_n^{-}\big(K(\mathbf{y}-\mathbf{x}_m)\big)(\nabla_x\times\mathbf{k})V_n^{+}\big(K(\mathbf{x}-\mathbf{x}_m)\big)\Big\}. \end{aligned} \tag{7.10}$$

Substituting from (7.10) into (7.8), and identifying the coefficients of $\nabla V_n^+(k(\mathbf{x}-\mathbf{x}_m))$ and $\nabla\times\mathbf{k}V_n^+(K(\mathbf{x}-\mathbf{x}_m))$, yields

$$B_{m,n}^{(p)} = \frac{-i}{4\rho\omega^2}\int_{\partial C_m} \mathrm{d}\,S\mathbf{n}\cdot\big[\boldsymbol{\sigma}_i(\mathbf{y})\cdot\nabla U_n^-\big(k(\mathbf{y}-\mathbf{x}_m)\big) - \mathbf{u}_i(\mathbf{y})\cdot\boldsymbol{\sigma}^{(p)}\big(k(\mathbf{y}-\mathbf{x}_m)\big)\big], \tag{7.11a}$$

$$B_{m,n}^{(s)} = \frac{-i}{4\rho\omega^2}\int_{\partial C_m} \mathrm{d}\,S\mathbf{n}\cdot\big[\boldsymbol{\sigma}_i(\mathbf{y})\cdot(\nabla\times\mathbf{k})U_n^-\big(K(\mathbf{y}-\mathbf{x}_m)\big) - \mathbf{u}_i(\mathbf{y})\cdot\boldsymbol{\sigma}^{(s)}\big(K(\mathbf{y}-\mathbf{x}_m)\big)\big], \tag{7.11b}$$

where

$$\sigma_{ij}^{(p)}\big(k(\mathbf{y}-\mathbf{x}_m)\big) = C_{ijpq}U_{n,pq}^-\big(k(\boldsymbol{y}-\mathbf{x}_m)\big), \tag{7.11c}$$

$$\sigma_{ij}^{(s)}\big(K(\mathbf{y}-\mathbf{x}_m)\big) = C_{ijpq}e_{pr3}U_{n,rq}^-\big(K(\mathbf{y}-\mathbf{x}_m)\big). \tag{7.11d}$$

7.2.3 Integral expressions for arbitrary incidence

The integrals in (7.11) can be reduced by using the fact that ∂C_m is the arc of the circle of radius a_m centered at $\mathbf{x}_m$, which is the origin of the shifted coordinates $\mathbf{y}-\mathbf{x}_m$. The integration is therefore simplified using polar coordinates centered at $\mathbf{x}_m$, combined with the expressions for the displacements and traction components in polar coordinates given in terms of the potentials,

$$u_r = \Phi_{,r} + \frac{1}{r}\Psi_{,\theta}, \quad u_\theta = \frac{1}{r}\Phi_{,\theta} - \Psi_{,r}, \tag{7.12a}$$

$$\sigma_{rr} = -\lambda k^2\Phi + 2\mu\big(\Phi_{,rr} + \frac{1}{r}\Psi_{,r\theta} - \frac{1}{r^2}\Psi_{,\theta}\big), \tag{7.12b}$$

$$\sigma_{r\theta} = 2\mu\big(\frac{1}{r}\Phi_{,r\theta} - \frac{1}{r^2}\Phi_{,\theta}\big) + \mu\big(\frac{1}{r^2}\Psi_{,\theta\theta} - \Psi_{,rr} + \frac{1}{r}\Psi_{,r}\big). \tag{7.12c}$$

The four distinct terms in the integrals of (7.11), such as $\mathrm{d}\,S\mathbf{n}\cdot\boldsymbol{\sigma}_i(\mathbf{y})\cdot\nabla U_n^-\big(k(\mathbf{y}-\mathbf{x}_m)\big)$, then follow by identifying $\Phi\to U_n^-\big(k\mathbf{a}\big)$, $\Psi\to U_n^-\big(K\mathbf{a}\big)$, where $\mathbf{a}(\theta)\equiv\mathbf{y}-\mathbf{x}_m$ is the radial vector of constant magnitude a_m. Thus,

$$\begin{aligned}\mathrm{d}\,S\mathbf{n}\cdot\boldsymbol{\sigma}_i\cdot\nabla U_n^- &= \mathrm{d}\,S\Big[\sigma_{irr}\frac{\partial}{\partial r}U_n^-\big(k\mathbf{a}\big) + \sigma_{ir\theta}\frac{1}{r}\frac{\partial}{\partial\theta}U_n^-\big(k\mathbf{a}\big)\Big]\\ &= \mathrm{d}\,\theta\,\Big(\sigma_{irr}ka_mU_n^{-\prime}(k\mathbf{a}) - in\sigma_{ir\theta}U_n^-(k\mathbf{a})\Big),\end{aligned} \tag{7.13a}$$

$$\begin{aligned}
\mathrm{d}\,S\mathbf{n}\cdot\boldsymbol{\sigma}^{(p)}\cdot\mathbf{u}_i &= \mathrm{d}\,S\big[u_{ir}\sigma_{rr}^{(p)}+u_{i\theta}\sigma_{r\theta}^{(p)}\big]\\
&= \mathrm{d}\,\theta\frac{\mu}{a_m}\Big(u_{ir}\Big[\big(2n^2-K^2a_m^2\big)U_n^-(k\mathbf{a})-2ka_m{U_n^-}'(k\mathbf{a})\Big]\\
&\qquad + u_{i\theta}\,2in\big[U_n^-(k\mathbf{a})-ka_m{U_n^-}'(k\mathbf{a})\big]\Big), \qquad (7.13b)\\
\mathrm{d}\,S\mathbf{n}\cdot\boldsymbol{\sigma}_i\cdot(\nabla\times\mathbf{k})U_n^- &= \mathrm{d}\,S\Big[\sigma_{irr}\frac{1}{r}\frac{\partial}{\partial\theta}U_n^-\big(K\mathbf{a}\big)-\sigma_{ir\theta}\frac{\partial}{\partial r}U_n^-\big(K\mathbf{a}\big)\Big]\\
&= -\,\mathrm{d}\,\theta\Big(in\sigma_{irr}U_n^-(K\mathbf{a})+Ka_m\sigma_{ir\theta}{U_n^-}'(K\mathbf{a})\Big), \qquad (7.13c)\\
\mathrm{d}\,S\mathbf{n}\cdot\boldsymbol{\sigma}^{(s)}\cdot\mathbf{u}_i &= \mathrm{d}\,S\big[u_{ir}\sigma_{rr}^{(s)}+u_{i\theta}\sigma_{r\theta}^{(s)}\big]\\
&= \mathrm{d}\,\theta\frac{\mu}{a_m}\Big(u_{ir}\,2in\big[U_n^-(K\mathbf{a})-Ka_m{U_n^-}'(K\mathbf{a})\big]\\
&\qquad + u_{i\theta}\big[\big((Ka_m)^2-2n^2\big)U_n^-(K\mathbf{a})+2Ka_m{U_n^-}'(K\mathbf{a})\big)\Big). \qquad (7.13d)
\end{aligned}$$

Noting the reversal of the sense of the integral in equation (7.11) and incorporating equation (7.13a) leads to

$$\begin{aligned}
B_{m,l}^{(p)} =& \frac{1}{4K^2}\int_{\theta_1^{(m)}}^{\theta_2^{(m)}}\mathrm{d}\,\theta\,e^{-i\,l\,\theta}\Big\{i\alpha_p^{(m)}J_l{}'(\alpha_p^{(m)})\frac{\sigma_{irr}}{\mu}+\,l\,J_l(\alpha_p^{(m)})\frac{\sigma_{ir\theta}}{\mu}\\
&+i\Big[\big({\alpha_s^{(m)}}^2-2\,l^2\big)J_l(\alpha_p^{(m)})+2\alpha_p^{(m)}J_l{}'(\alpha_p^{(m)})\Big]\frac{u_{ir}}{a_m}+2\,l\Big[J_l(\alpha_p^{(m)})-\alpha_p^{(m)}J_l{}'(\alpha_p^{(m)})\Big]\frac{u_{i\theta}}{a_m}\Big\}, \qquad (7.14a)\\
B_{m,l}^{(s)} =& \frac{1}{4K^2}\int_{\theta_1^{(m)}}^{\theta_2^{(m)}}\mathrm{d}\,\theta\,e^{-i\,l\,\theta}\Big\{-i\alpha_s^{(m)}J_l{}'(\alpha_s^{(m)})\frac{\sigma_{ir\theta}}{\mu}+lJ_l(\alpha_s^{(m)})\frac{\sigma_{irr}}{\mu}\\
&-i\Big[\big({\alpha_s^{(m)}}^2-2\,l^2\big)J_l(\alpha_s^{(m)})+2\,\alpha_s^{(m)}J_l{}'(\alpha_s^{(m)})\Big]\frac{u_{i\theta}}{a_m}+2\,l\,\Big[J_l(\alpha_s^{(m)})-\alpha_s^{(m)}J_l{}'(\alpha_s^{(m)})\Big]\frac{u_{ir}}{a_m}\Big\}, \qquad (7.14b)
\end{aligned}$$

where $\alpha_p^{(m)}=k\,a_m$, $\alpha_s^{(m)}=K\,a_m$, $\theta_1^{(m)}$ and $\theta_2^{(m)}$ are the angular positions of the vectors $\mathbf{a}_i^{(m)}\equiv a_m\hat{\mathbf{e}}(\theta_i^{(m)})$, $i=1,2$, which describe the initial and final positions of segment ∂C_m (see Figure 7.1). Equations (7.14) provide expressions for the source amplitudes for any time harmonic incident field.

Let us now specialize the result to the specific case of plane wave incidence. This is important in its own right but also allows us to derive the general incident wave case by integration as we shall show.

7.2.4 Plane wave incidence

Let us define

$$u_{\psi_p}(\mathbf{x}) = e^{ik\hat{\mathbf{e}}(\psi_p)\cdot\mathbf{x}}, \quad u_{\psi_s}(\mathbf{x}) = e^{ik_s\hat{\mathbf{e}}(\psi_s)\cdot\mathbf{x}}, \tag{7.15}$$

where $\hat{\mathbf{e}}(\psi_\alpha) = (\cos\psi_\alpha, \sin\psi_\alpha)$ such that u_{ψ_α} correspond to compressional ($\alpha = p$) and shear ($\alpha = s$) plane waves of unit amplitude.

Longitudinal incident plane wave

Consider now longitudinal plane wave incidence

$$\Phi_i(\mathbf{x}) = A_p u_{\psi_p}(\mathbf{x}) \tag{7.16}$$

where $A_p \equiv const$ is a known wave amplitude. Then using the relation $\Phi_i(\mathbf{y}) = \Phi_i(\mathbf{x}_m)u_{\psi_p}(\mathbf{a})$ with $\mathbf{a} = a_m\hat{\mathbf{e}}(\theta)$, and eq. (7.12) with $\Phi = \Phi_i$, $\Psi = 0$, reduces equation (7.14) to the form:

$$\begin{aligned} B_{m,l}^{(p)} = \frac{\Phi_i(\mathbf{x}_m)}{4\kappa\alpha_s^{(m)}} \int_{\theta_1^{(m)}}^{\theta_2^{(m)}} \mathrm{d}\,\theta\, e^{-i\,l\,\theta} u_{\psi_p}(\mathbf{a}) \Big\{ & i\alpha_p^{(m)2} J_l{}'(\alpha_p^{(m)}) \big[2\sin^2(\theta-\psi_p) - \kappa^2\big] \\ & + l\alpha_p^{(m)} J_l(\alpha_p^{(m)}) \sin 2(\theta-\psi_p) - i2l\sin(\theta-\psi_p)\Big[J_l(\alpha_p^{(m)}) - \alpha_p^{(m)} J_l{}'(\alpha_p^{(m)})\Big] \\ & - \cos(\theta-\psi_p)\Big[\big(\alpha_s^{(m)2} - 2\,l^2\big) J_l(\alpha_p^{(m)}) + 2\alpha_p^{(m)} J_l{}'(\alpha_p^{(m)})\Big]\Big\}, \end{aligned} \tag{7.17a}$$

$$\begin{aligned} B_{m,l}^{(s)} = \frac{\Phi_i(\mathbf{x}_m)}{4\kappa\alpha_s^{(m)}} \int_{\theta_1^{(m)}}^{\theta_2^{(m)}} \mathrm{d}\,\theta\, e^{-i\,l\,\theta} u_{\psi_p}(\mathbf{a}) \cdot \Big\{ & \big[2\sin^2(\theta-\psi_p) - \kappa^2\big]\, l\, \alpha_p^{(m)} J_l(\alpha_s^{(m)}) \\ & - i\sin 2(\theta-\psi_p)\alpha_p^{(m)}\alpha_s^{(m)} J_l{}'(\alpha_s^{(m)}) + i2\,l\,\cos(\theta-\psi_p)\Big[J_l(\alpha_s^{(m)}) - \alpha_s^{(m)} J_l{}'(\alpha_s^{(m)})\Big] \\ & - \sin(\theta-\psi_p)\Big[\big(\alpha_s^{(m)2} - 2\,l^2\big) J_l(\alpha_s^{(m)}) + 2\alpha_s^{(m)} J_l{}'(\alpha_s^{(m)})\Big]\Big\}, \end{aligned} \tag{7.17b}$$

where $\kappa = K/k$. Then noting that $u_{\psi_p}(\mathbf{a}) = e^{ika_m\cos(\theta-\psi_p)} = e^{i\alpha_p^{(m)}\cos(\theta-\psi_p)}$, equation (7.17) can be written

$$B_{m,l}^{(p)} = \frac{i\Phi_i(\mathbf{x}_m)}{4\kappa\alpha_s^{(m)}} e^{-i\,l\,\psi_p} \cdot \Big\{ {\alpha_p^{(m)}}^2 J_l'(\alpha_p^{(m)}) \Big[2L_0''(\alpha_p^{(m)}) - \big(\kappa^2 - 2\big) L_0(\alpha_p^{(m)}) \Big] - 2\,l\alpha_p^{(m)} J_l(\alpha_p^{(m)}) L_1'(\alpha_p^{(m)}) - 2lL_1(\alpha_p^{(m)}) \Big[J_l(\alpha_p^{(m)}) - \alpha_p^{(m)} J_l'(\alpha_p^{(m)}) \Big] + L_0'(\alpha_p^{(m)}) \Big[\big({\alpha_s^{(m)}}^2 - 2\,l^2\big) J_l(\alpha_p^{(m)}) + 2\alpha_p^{(m)} J_l'(\alpha_p^{(m)}) \Big] \Big\}, \tag{7.18a}$$

$$B_{m,l}^{(s)} = \frac{\Phi_i(\mathbf{x}_m)}{4\kappa\alpha_s^{(m)}} e^{-i\,l\,\psi_p} \cdot \Big\{ l\alpha_p^{(m)} J_l(\alpha_s^{(m)}) \Big[2{L_0}''(\alpha_p^{(m)}) - \big(\kappa^2 - 2\big) L_0(\alpha_p^{(m)}) \Big] - 2\,\alpha_p^{(m)}\alpha_s^{(m)} J_l'(\alpha_s^{(m)}) L_1'(\alpha_p^{(m)}) + 2\,l\,L_0'(\alpha_p^{(m)}) \Big[J_l(\alpha_s^{(m)}) - \alpha_s^{(m)} J_l'(\alpha_s^{(m)}) \Big] - L_1(\alpha_p^{(m)}) \Big[\big({\alpha_s^{(m)}}^2 - 2\,l^2\big) J_l(\alpha_s^{(m)}) + 2\alpha_s^{(m)} J_l'(\alpha_s^{(m)}) \Big] \Big\}, \tag{7.18b}$$

where the functions $L_0(\alpha)$ and $L_1(\alpha)$ are defined by

$$L_j(\alpha) = \int_{\theta_1^{(m)} - \psi_p}^{\theta_2^{(m)} - \psi_p} \mathrm{d}\,\theta\,(\sin\theta)^j\, e^{i(\alpha\cos\theta - l\theta)}, \quad j = 0, 1. \tag{7.19}$$

$L_0(\alpha)$ can be evaluated by using the Jacobi-Anger identity $e^{ix\sin\theta} = \sum_{n=-\infty}^{\infty} J_n(x) e^{in\theta}$,

$$\begin{aligned} L_0(\alpha) &= \sum_{n=-\infty}^{\infty} J_n(\alpha)\, i^n \int_{\theta_1^{(m)} - \psi_p}^{\theta_2^{(m)} - \psi_p} \mathrm{d}\,\theta\, e^{-i(n+l)\theta} \\ &= \sum_{n=-\infty}^{\infty} J_n(\alpha)\, i^{n+1}\, \frac{e^{i(n+l)\psi_p}}{n+l} \big[e^{-i(n+l)\theta_2^{(m)}} - e^{-i(n+l)\theta_1^{(m)}} \big]. \end{aligned} \tag{7.20}$$

Integration by parts yields $L_1(\alpha)$ in the form

$$L_1(\alpha) = -\frac{l}{\alpha} L_0(\alpha) - \frac{1}{i\alpha}\, e^{i(\alpha\cos\theta - l\theta)} \Big|_{\theta_1^{(m)} - \psi_p}^{\theta_2^{(m)} - \psi_p}. \tag{7.21}$$

Taking into account the Jacobi-Anger identity and equation (7.20), the function $L_1(\alpha)$ and its derivative $L_1'(\alpha)$ can be expressed

$$L_1(\alpha) = \frac{1}{\alpha} \sum_{n=-\infty}^{\infty} J_n(\alpha)\, n\, i^{n+1}\, \frac{e^{i(n+l)\psi_p}}{n+l} \cdot \big[e^{-i(n+l)\theta_2^{(m)}} - e^{-i(n+l)\theta_1^{(m)}} \big], \tag{7.22a}$$

$$L_1'(\alpha) = \frac{1}{\alpha^2} \sum_{n=-\infty}^{\infty} n\, i^{n+1} \big[\alpha {J_n}'(\alpha) - J_n(\alpha) \big]\, \frac{e^{i(n+l)\psi_p}}{n+l} \cdot \big[e^{-i(n+l)\theta_2^{(m)}} - e^{-i(n+l)\theta_1^{(m)}} \big]. \tag{7.22b}$$

Introducing the explicit results for the functions $L_0(\alpha)$ and $L_1(\alpha)$ into (7.18) yields expressions for the amplitude coefficients in the form:

$$B_{m,l}^{(p)} = \frac{\Phi_i(\mathbf{x}_m)}{4\kappa^2} \sum_{q=-\infty}^{\infty} \frac{i^{q+2} e^{iq\psi_p}}{q+l} \cdot \Bigg\{ \alpha_p^{(m)} J_l{}'(\alpha_p^{(m)}) \Big[2J_q{}''(\alpha_p^{(m)}) - \big(\kappa^2 - 2\big) J_q(\alpha_p^{(m)}) \Big] - \frac{2\,l\,q}{\alpha_p^{(m)}} J_l(\alpha_p^{(m)}) \Big[J_q{}'(\alpha_p^{(m)}) - \frac{1}{\alpha_p^{(m)}} J_q(\alpha_p^{(m)}) \Big] + J_q'(\alpha_p^{(m)}) \Big[2J_l{}'(\alpha_p^{(m)}) + \frac{{\alpha_s^{(m)}}^2 - 2l^2}{\alpha_p^{(m)}} J_l(\alpha_p^{(m)}) \Big] - \frac{2l\,q}{\alpha_p^{(m)}} J_q(\alpha_p^{(m)}) \Big[\frac{1}{\alpha_p^{(m)}} J_l(\alpha_p^{(m)}) - J_l{}'(\alpha_p^{(m)}) \Big] \Bigg\} \cdot \Big[e^{-i(q+l)\theta_2^{(m)}} - e^{-i(q+l)\theta_1^{(m)}} \Big], \tag{7.23a}$$

$$B_{m,l}^{(s)} = \frac{\Phi_i(\mathbf{x}_m)}{4\kappa} \sum_{q=-\infty}^{\infty} \frac{i^{q+1} e^{iq\psi_p}}{q+l} \cdot \Bigg\{ \frac{l}{\kappa} J_l(\alpha_s^{(m)}) \Big[2J_q{}''(\alpha_p^{(m)}) - \big(\kappa^2 - 2\big) J_q(\alpha_p^{(m)}) \Big] - 2\,q\,J_l{}'(\alpha_s^{(m)}) \Big[J_q{}'(\alpha_p^{(m)}) - \frac{1}{\alpha_p^{(m)}} J_q(\alpha_p^{(m)}) \Big] + 2l J_q{}'(\alpha_p^{(m)}) \Big[\frac{1}{\alpha_s^{(m)}} J_l(\alpha_s^{(m)}) - J_l{}'(\alpha_s^{(m)}) \Big] - \frac{q}{\alpha_p^{(m)}} J_q(\alpha_p^{(m)}) \Big[\frac{{\alpha_s^{(m)}}^2 - 2\,l^2}{\alpha_s^{(m)}} J_l(\alpha_s^{(m)}) + 2J_l{}'(\alpha_s^{(m)}) \Big] \Bigg\} \cdot \Big[e^{-i(q+l)\theta_2^{(m)}} - e^{-i(q+l)\theta_1^{(m)}} \Big]. \tag{7.23b}$$

After some simplification eq. (7.23) can be written as

$$\begin{pmatrix} B_{m,l}^{(p)} \\ \\ B_{m,l}^{(s)} \end{pmatrix} = \frac{\Phi_i(\mathbf{x}_m)}{4{\alpha_s^{(m)}}^2} \sum_{q=-\infty}^{\infty} i^q e^{iq\psi_p} \cdot \Big[e^{-i(q+l)\theta_2^{(m)}} - e^{-i(q+l)\theta_1^{(m)}} \Big] \cdot \begin{pmatrix} \Big[\frac{{\alpha_s^{(m)}}^2}{q+l} - 2q \Big] \alpha_p^{(m)} J_l{}'(\alpha_p^{(m)}) & i \Big[\frac{{\alpha_s^{(m)}}^2}{q+l} - 2l \Big] \alpha_p^{(m)} J_l(\alpha_p^{(m)}) \\ \\ -i \big[{\alpha_s^{(m)}}^2 - 2lq \big] J_l(\alpha_s^{(m)}) & -2\alpha_p^{(m)} \alpha_s^{(m)} J_l{}'(\alpha_s^{(m)}) \end{pmatrix} \begin{pmatrix} J_q(\alpha_p^{(m)}) \\ \\ i J_q'(\alpha_p^{(m)}) \end{pmatrix}. \tag{7.24}$$

Transverse plane wave incidence

Consider now an incident transverse plane wave

$$\Psi_i = A_s e^{iK\hat{\mathbf{e}}(\psi_s)\cdot\mathbf{x}}, \tag{7.25}$$

where $A_s \equiv const$ is a known transverse wave amplitude. Then equation (7.14) will have the form:

$$B_{m,l}^{(p)} = \frac{\Psi_i(\mathbf{x}_m)}{4\alpha_s^{(m)}} \int_{\theta_1^{(m)}}^{\theta_2^{(m)}} \mathrm{d}\,\theta\, e^{-i\,l\,\theta} \Psi_i(\mathbf{a}) \Big\{ i\alpha_p^{(m)} \alpha_s^{(m)} J_l{}'(\alpha_p^{(m)}) \sin 2(\theta-\psi)$$
$$+ l\,\alpha_s^{(m)} J_l(\alpha_p^{(m)}) \cos 2(\theta-\psi) + \sin(\theta-\psi)\Big[\big({\alpha_s^{(m)}}^2 - 2l^2\big) J_l(\alpha_p^{(m)}) + 2\alpha_p^{(m)} J_l{}'(\alpha_p^{(m)})\Big]$$
$$- 2il\cos(\theta-\psi)\Big[J_l(\alpha_p^{(m)}) - \alpha_p^{(m)} J_l{}'(\alpha_p^{(m)})\Big]\Big\}, \tag{7.26a}$$

$$B_{m,l}^{(s)} = \frac{\Psi_i(\mathbf{x}_m)}{4\alpha_s^{(m)}} \int_{\theta_1^{(m)}}^{\theta_2^{(m)}} \mathrm{d}\,\theta\, e^{-i\,l\,\theta} \Psi_i(\mathbf{a}) \cdot \Big\{ l\alpha_s^{(m)} J_l(\alpha_s^{(m)}) \sin 2(\theta-\psi)$$
$$- i\cos 2(\theta-\psi) {\alpha_s^{(m)}}^2 J_l{}'(\alpha_s^{(m)}) - i2\,l\sin(\theta-\psi)\Big[J_l(\alpha_s^{(m)}) - \alpha_s^{(m)} J_l{}'(\alpha_s^{(m)})\Big]$$
$$- \cos(\theta-\psi)\Big[\big({\alpha_s^{(m)}}^2 - 2l^2\big) J_l(\alpha_s^{(m)}) + 2\alpha_s^{(m)} J_l{}'(\alpha_s^{(m)})\Big]\Big\}. \tag{7.26b}$$

As before, note that $\Psi_i(\mathbf{a}) = e^{i\alpha_s^{(m)}\cos(\theta-\psi_s)}$. Introducing the functions $L_0(\alpha)$ and $L_1(\alpha)$ given by (7.19), reduces equation (7.26) to

$$B_{m,l}^{(p)} = \frac{1}{4\kappa} \Psi_i(\mathbf{x}_m) e^{-i\,l\,\psi_s} \Big\{ 2\alpha_s^{(m)} J_l{}'(\alpha_p^{(m)}) L_1{}'(\alpha_s^{(m)}) - l\,\kappa J_l(\alpha_p^{(m)}) \big[2L_0{}''(\alpha_s^{(m)})$$
$$+ L_0(\alpha_s^{(m)})\big] - 2l\Big[\frac{1}{\alpha_p^{(m)}} J_l(\alpha_p^{(m)}) - J_l{}'(\alpha_p^{(m)})\Big] L_0{}'(\alpha_s^{(m)}) + L_1(\alpha_s^{(m)})$$
$$\cdot \Big[\frac{{\alpha_s^{(m)}}^2 - 2l^2}{\alpha_p^{(m)}} J_l(\alpha_p^{(m)}) + 2J_l{}'(\alpha_p^{(m)})\Big]\Big\}, \tag{7.27a}$$

$$B_{m,l}^{(s)} = \frac{i}{4} \Psi_i(\mathbf{x}_m) e^{-i\,l\,\psi_s} \cdot \Big\{ -2\,l J_l(\alpha_s^{(m)}) L_1{}'(\alpha_s^{(m)}) + \alpha_s^{(m)} J_l{}'(\alpha_s^{(m)}) \big[2L_0{}''(\alpha_s^{(m)}) + L_0(\alpha_s^{(m)})\big]$$
$$- 2\,l\Big[\frac{1}{\alpha_s^{(m)}} J_l(\alpha_s^{(m)}) - J_l{}'(\alpha_s^{(m)})\Big] L_1(\alpha_s^{(m)}) + L_0{}'(\alpha_s^{(m)})$$
$$\cdot \Big[\frac{{\alpha_s^{(m)}}^2 - 2l^2}{\alpha_s^{(m)}} J_l(\alpha_s^{(m)}) + 2J_l{}'(\alpha_s^{(m)})\Big]\Big\}. \tag{7.27b}$$

Incorporating equations (7.20) and (7.22), the amplitudes will have the form

$$B_{m,l}^{(p)} = \frac{\Psi_i(\mathbf{x}_m)}{4{\alpha_s^{(m)}}^2} \sum_{q=-\infty}^{\infty} i^{q+1} e^{iq\psi_s} \cdot \big[e^{-i(q+l)\theta_2^{(m)}} - e^{-i(q+l)\theta_1^{(m)}}\big]$$
$$\cdot \Big\{ 2\alpha_p^{(m)} \alpha_s^{(m)} J_l{}'(\alpha_p^{(m)}) J_q{}'(\alpha_s^{(m)}) + \big[{\alpha_s^{(m)}}^2 - 2lq\big] J_l(\alpha_p^{(m)})\, J_q(\alpha_s^{(m)})\Big\}, \tag{7.28a}$$

$$B_{m,l}^{(s)} = \frac{\Psi_i(\mathbf{x}_m)}{4\alpha_s^{(m)}} \sum_{q=-\infty}^{\infty} \frac{i^q e^{iq\psi_s}}{q+l} \cdot \big[e^{-i(q+l)\theta_2^{(m)}} - e^{-i(q+l)\theta_1^{(m)}}\big]$$
$$\cdot \Big\{ -\Big[{\alpha_s^{(m)}}^2 - 2l(q+l)\Big] J_l(\alpha_s^{(m)}) J_q{}'(\alpha_s^{(m)}) + \Big[{\alpha_s^{(m)}}^2 - 2q(q+l)\Big] J_l{}'(\alpha_s^{(m)}) J_q(\alpha_s^{(m)})\Big\}. \tag{7.28b}$$

Alternatively, the source amplitudes can be written as

$$\begin{pmatrix} B_{m,l}^{(s)} \\ \\ -B_{m,l}^{(p)} \end{pmatrix} = \frac{\Psi_i(\mathbf{x}_m)}{4{\alpha_s^{(m)}}^2} \sum_{q=-\infty}^{\infty} i^q e^{iq\psi_s} \left[e^{-i(q+l)\theta_2^{(m)}} - e^{-i(q+l)\theta_1^{(m)}} \right] \cdot \begin{pmatrix} \left[\frac{{\alpha_s^{(m)}}^2}{q+l} - 2q \right] \alpha_s^{(m)} J_l'(\alpha_s^{(m)}) & i \left[\frac{{\alpha_s^{(m)}}^2}{q+l} - 2l \right] \alpha_s^{(m)} J_l(\alpha_s^{(m)}) \\ \\ -i \left[{\alpha_s^{(m)}}^2 - 2lq \right] J_l(\alpha_p^{(m)}) & -2\alpha_p^{(m)} \alpha_s^{(m)} J_l'(\alpha_p^{(m)}) \end{pmatrix} \begin{pmatrix} J_q(\alpha_s^{(m)}) \\ \\ iJ_q'(\alpha_s^{(m)}) \end{pmatrix}. \tag{7.29}$$

Plane wave incidence summarized

Adding the separate results of eqs. (7.24) and (7.29) gives for combined incidence

$$\Phi_i = A_p e^{ik\hat{\mathbf{e}}(\psi_p)\cdot\mathbf{x}}, \quad \Psi_i = A_s e^{ik_s\hat{\mathbf{e}}(\psi_s)\cdot\mathbf{x}}, \tag{7.30}$$

the source amplitudes

$$\begin{pmatrix} B_{m,l}^{(p)} \\ \\ B_{m,l}^{(s)} \end{pmatrix} = \frac{1}{4{\alpha_s^{(m)}}^2} \sum_{q=-\infty}^{\infty} i^q \left[e^{-i(q+l)\theta_2^{(m)}} - e^{-i(q+l)\theta_1^{(m)}} \right] \cdot \left\{ \Phi_i(\mathbf{x}_m) e^{iq\psi_p} \begin{pmatrix} v_1(\alpha_p^{(m)}, \alpha_s^{(m)}) \\ v_2(\alpha_p^{(m)}, \alpha_s^{(m)}) \end{pmatrix} + \Psi_i(\mathbf{x}_m) e^{iq\psi_s} \begin{pmatrix} -v_2(\alpha_s^{(m)}, \alpha_p^{(m)}) \\ v_1(\alpha_s^{(m)}, \alpha_p^{(m)}) \end{pmatrix} \right\} \tag{7.31}$$

where the vector $\mathbf{v}(\alpha, \beta) = (v_1,\, v_2)^T$ is defined in (7.3c).

7.2.5 Arbitrary incident field as superposition of plane incident waves

The general form of the incident field given by equation (7.2a) can be constructed as a superposition of plane incident waves of the form (7.30). This will enable us to find the general form of the amplitude coefficients for incident waves of general form as a superposition of solutions for plane waves given by (7.31). Recall the incident field for a combined incident plane wave having the form:

$$\begin{pmatrix} \Phi_i(\mathbf{x}) \\ \Psi_i(\mathbf{x}) \end{pmatrix} = \begin{pmatrix} A_p e^{ik\hat{\mathbf{e}}(\psi_p)\cdot\mathbf{x}} \\ A_s e^{iK\hat{\mathbf{e}}(\psi_s)\cdot\mathbf{x}} \end{pmatrix} = \sum_{q=-\infty}^{\infty} \begin{pmatrix} i^q e^{-iq\psi_p} U_q^+(k\mathbf{x}) \\ i^q e^{-iq\psi_s} U_q^+(K\mathbf{x}) \end{pmatrix}. \tag{7.32}$$

Multiplying the first row of equation (7.32) by $(i^{-(n+q)}/2\pi)e^{i(n+q)\psi_p}$ and the second row by $(i^{-(n+q)}/2\pi)e^{i(n+q)\psi_s}$, integrating with respect to ψ_p and ψ_s respectively between 0 and 2π and then evaluating at $\mathbf{x} = \mathbf{x}_m$ we find

$$\frac{i^{-(n+q)}}{2\pi}\int_0^{2\pi} \mathrm{d}\,\psi_p\,\Phi_i(\mathbf{x}_m)e^{i(n+q)\psi_p} = U^+_{n+q}(k\mathbf{x}_m), \tag{7.33a}$$

$$\frac{i^{-(n+q)}}{2\pi}\int_0^{2\pi} \mathrm{d}\,\psi_s\,\Psi_i(\mathbf{x}_m)e^{i(n+q)\psi_s} = U^+_{n+q}(K\mathbf{x}_m). \tag{7.33b}$$

To obtain the form of the amplitude coefficients given by eq. (7.3) for the general incidence (7.2a), we multiply the first and second of equations of (7.31) by $A_n^{(p)}\gamma_n(\psi_p,\psi_s)$ and $A_n^{(s)}\gamma_n(\psi_p,\psi_s)$ respectively, where $\gamma_n(\psi_p,\psi_s) = i^{-2n}/(2\pi)^2 e^{in\psi_p}e^{in\psi_s}$, carry out the double integration with respect to ψ_p and ψ_s between 0 and 2π, incorporate (7.33) and sum over all $n \in \mathbb{Z}$.

7.2.6 Necessary and sufficient conditions on the source amplitudes

In this section, we will define the constraints on the active source coefficients $B^{(p)}_{m,n}$ and $B^{(s)}_{m,n}$ by expressing the active source field $\mathbf{u}_d$ in terms of near-field and far-field source amplitudes and using Graf's theorem (2.72). When $|\mathbf{x}| > |\mathbf{y}|$, the components of $\mathbf{u}_d$ can be defined as a sum of multipoles at the origin using the first identity in (2.72)

$$\left.\begin{aligned} \Phi_d &= \sum_{n=-\infty}^{\infty} F_n^{(p)} V_n^+(k\mathbf{x}), \\ \Psi_d &= \sum_{n=-\infty}^{\infty} F_n^{(s)} V_n^+(K\mathbf{x}), \end{aligned}\right\} \quad \text{for} \quad |\mathbf{x}| > \max(|\mathbf{x}_m| + a_m), \tag{7.34}$$

where

$$F_n^{(p)} = \sum_{m=1}^{M}\sum_{l=-\infty}^{\infty} B^{(p)}_{m,l} U^-_{n-l}(k\mathbf{x}_m), \quad F_n^{(s)} = \sum_{m=1}^{M}\sum_{l=-\infty}^{\infty} B^{(s)}_{m,l} U^-_{n-l}(K\mathbf{x}_m). \tag{7.35}$$

If the active field Φ_d and Ψ_d does not radiate into the far-field, then we must have $F_n^{(p)} = 0,\ F_n^{(s)} = 0,\ \forall\, n$ ensuring the necessity of $(7.5)_{1,2}$. Sufficiency is guaranteed by substituting the expressions $(7.5)_{1,2}$ into an assumed far-field of the form (7.34).

Next we consider the near-field. Assuming $|\mathbf{x}_m| > a_m\ \forall m$ and using the general form

of an incident field given by (7.2a), the near-field source amplitudes can be obtained as

$$\left.\begin{aligned}\Phi_d &= \sum_{n=-\infty}^{\infty} E_n^{(p)} U_n^+(k\mathbf{x}),\\ \Psi_d &= \sum_{n=-\infty}^{\infty} E_n^{(s)} U_n^+(K\mathbf{x}),\end{aligned}\right\} \quad \text{for} \quad |\mathbf{x}| > \max(|\mathbf{x}_m| - a_m), \tag{7.36}$$

where

$$E_n^{(p)} = \sum_{m=1}^{M}\sum_{l=-\infty}^{\infty} B_{m,l}^{(p)} V_{n-l}^-(k\mathbf{x}_m), \quad E_n^{(s)} = \sum_{m=1}^{M}\sum_{l=-\infty}^{\infty} B_{m,l}^{(s)} V_{n-l}^-(K\mathbf{x}_m). \tag{7.37}$$

If the total field is zero in the near-field, then we must have $E_n^{(p)} + A_n^{(p)}$ and $E_n^{(s)} + A_n^{(s)}$ ensuring the necessity of $(7.5)_{3,4}$. Sufficiency is guaranteed by substituting the expressions $(7.5)_{3,4}$ into an assumed near-field of the form (7.36).

7.2.7 Divergence of the active field summation

The infinite sum expression for the active source fields defined by (7.2b) with source amplitudes (7.3a)-(7.3c) is formally valid only in $|\mathbf{x}-\mathbf{x}_m| > a_m$. That is, the expression is not itself valid in the domain $\mathcal{A}$ in which the sources reside! A valid form could be obtained by using the alternative version of Graf's addition theorem in the domain $\mathcal{A}_m$ associated with the arc ∂C_m, but the usual form of Graf's in the domain $\mathcal{A}_m$ associated with all other $\partial C_n, n \neq m$. We would then be assured that the active field is zero everywhere outside C. However if we were to do this, the mth source would not be present in the domain $\mathcal{A}_m$ since the active field would be bounded by construction.

Active cloaking therefore requires that we use the expression (7.2b) with source amplitudes (7.3a)-(7.3c) for the active field everywhere, but we must take a finite number of terms in the multipole expansion. That is, we use the source amplitudes that appear in the infinite sum as motivation for the choice of source amplitudes that should be chosen in an active field that contains only a finite number of multipoles. This ensures a finite (but large) field inside $\mathcal{A}$. We should note that this type of difficulty and the fact that it may be used to our advantage in the anti-sound context was noted by Kempton [84].

With a finite sum for the active field therefore, the integral equation (7.6) is not perfectly satisfied but instead

$$\mathbf{u}(\mathbf{x}) \approx \begin{cases} 0, & \mathbf{x} \in C, \\ \mathbf{u}_i(\mathbf{x}), & \mathbf{x} \notin C \cup \mathcal{A}, \end{cases} \tag{7.38}$$

and the field is large (but finite) inside $\mathcal{A}$. Finally we note that a straightforward truncation of the active field may not be optimal in terms of cloaking and ensuring a non-radiating field. This issue will be considered elsewhere.

7.3 Numerical examples

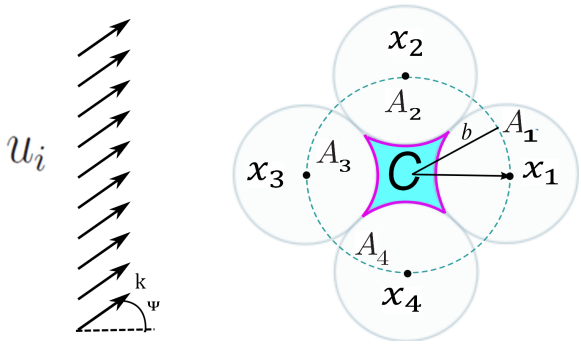

Figure 7.2: Plane wave insonification of the cloaking region C generated by four ($M = 4$) active sources placed at the corners of a square.

The numerical calculations for active source configurations of the type shown in Fig. 7.2 are performed for plane longitudinal and transverse incident waves of a unit amplitude, ($A_p = 1,\ A_s = 0$) and ($A_p = 0,\ A_s = 1$), for angles of incidence $\psi_p = \psi_s = 7^o$. Variable values are taken for the wavenumbers k_p and k_s, the number of sources M, and the number of terms N in summations (7.35) and (7.37) (the truncation size). The M active sources are symmetrically located on a circle of radius b, with

$$a_m = a, \quad |\mathbf{x}_m| = b, \quad \beta_m = (m-1)\beta_0, \quad \beta_0 = 2\pi\Big(\frac{m-1}{M}\Big), \quad m = \overline{1, M}, \tag{7.39}$$

where β_m is the argument of vector $\mathbf{x}_m$, and $a \geq b \sin\frac{\pi}{M}$. The circular arcs are defined by

$$\theta_{1,2}^{(m)} = \pi + \beta_m \mp \left| \sin^{-1}\left(\frac{b}{a}\sin\frac{\pi}{M}\right) - \frac{\pi}{M} \right|, \quad m = \overline{1, M}. \tag{7.40}$$

In all examples, we take $a = b \sin \frac{\pi}{M}$ and consider an elastic medium having a property of aluminum with $c_p = 6427\, m/s$, $c_s = 3112\, m/s$, $\rho = 2694\, kg/m^3$ [79].

7.3.1 The scattering amplitudes

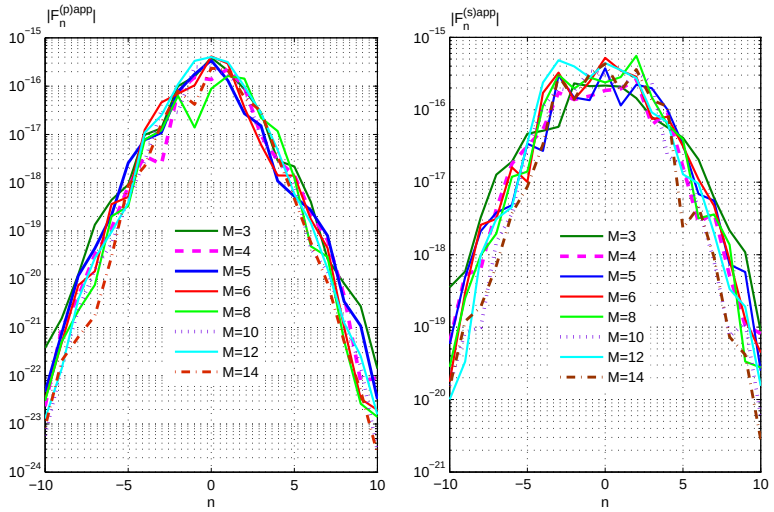

Figure 7.3: Variation of the far-field amplitude coefficients with number of active sources ($M = \overline{3, 14}$) for transverse incident waves. In all cases $N = 100$, $\psi_s = 7^o$.

Consider the truncated versions of the infinite sums in eq. (7.37) for the farfield amplitudes $F_n^{(p)}$ and $F_n^{(s)}$, and eq. (7.35) for the nearfield amplitudes $E_n^{(p)}$ and $E_n^{(s)}$:

$$\left.\begin{matrix} F_n^{(p)app} \\ E_n^{(p)app} \end{matrix}\right\} = \sum_{m=1}^{M} \sum_{l=-N}^{N} B_{m,l}^{(p)} \times \left\{\begin{matrix} U_{n-l}^{-}(\mathbf{x}_m), \\ V_{n-l}^{-}(\mathbf{x}_m), \end{matrix}\right. \qquad \forall\, n \in \mathbb{Z}, \tag{7.41a}$$

$$\left.\begin{matrix} F_n^{(s)app} \\ E_n^{(s)app} \end{matrix}\right\} = \sum_{m=1}^{M} \sum_{l=-N}^{N} B_{m,l}^{(s)} \times \left\{\begin{matrix} U_{n-l}^{-}(\mathbf{x}_m), \\ V_{n-l}^{-}(\mathbf{x}_m), \end{matrix}\right. \qquad \forall\, n \in \mathbb{Z}. \tag{7.41b}$$

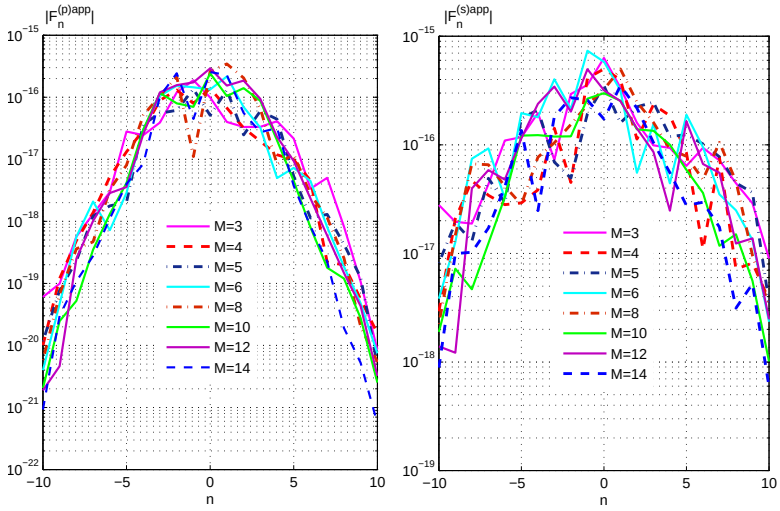

Figure 7.4: Variation of the far-field amplitude coefficients with number of active sources ($M = \overline{3, 14}$) for longitudinal incident waves. In all cases $N = 100$, $\psi_s = 7^o$.

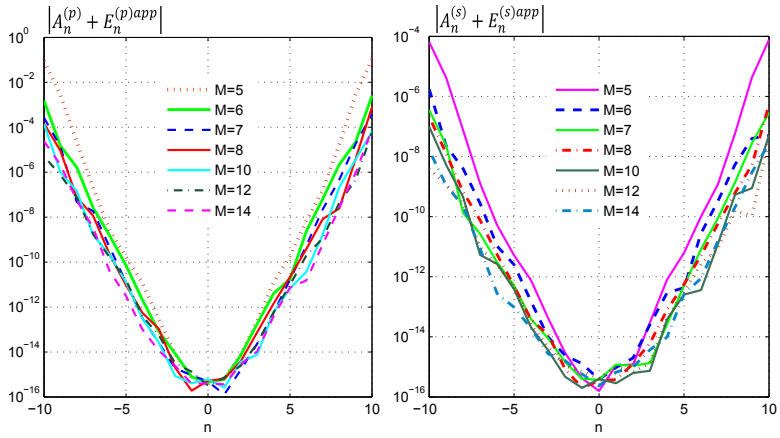

Figure 7.5: Dependence of the near-field amplitude coefficients on n, the order of Bessel function, varying the number of active sources ($M = \overline{5, 14}$) for transverse wave incidence. In all cases $N = 100$, $\psi_s = 7^o$.

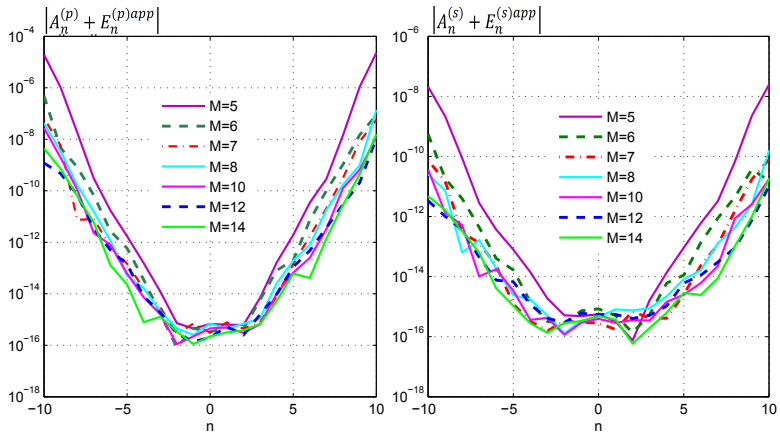

Figure 7.6: Variation of the near-field amplitude coefficients with number of active sources ($M = \overline{5, 14}$) for longitudinal incident waves. In all cases $N = 100$, $\psi_s = 7^o$.

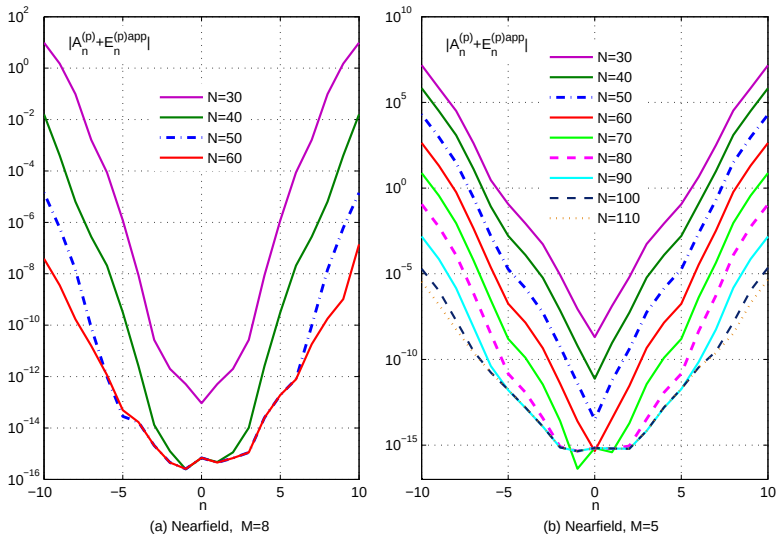

Figure 7.7: The near-field amplitude coefficients as a function of n, the order of Bessel function for different values of the truncation size N in (7.41) generated by different numbers of active sources: (a) $M = 5$ and (b) $M = 8$, for longitudinal incident waves.

The approximate near-field $E_n^{(p)app}$, $E_n^{(s)app}$ and far-field $F_n^{(p)app}$, $F_n^{(s)app}$ amplitudes are calculated at the incident shear wavenumber $K = 5$ by varying the number of active sources M and the truncation size N. The dependence of the far-field coefficients $|F_n^{(p)app}|$, $|F_n^{(s)app}|$ is illustrated in Fig. 7.3 for transverse and in Fig. 7.4 for longitudinal wave incidences. As M increases, the far-field coefficients fluctuate at small $|n|$, and

decrease at larger values of $|n|$ for both compressional and shear incident waves.

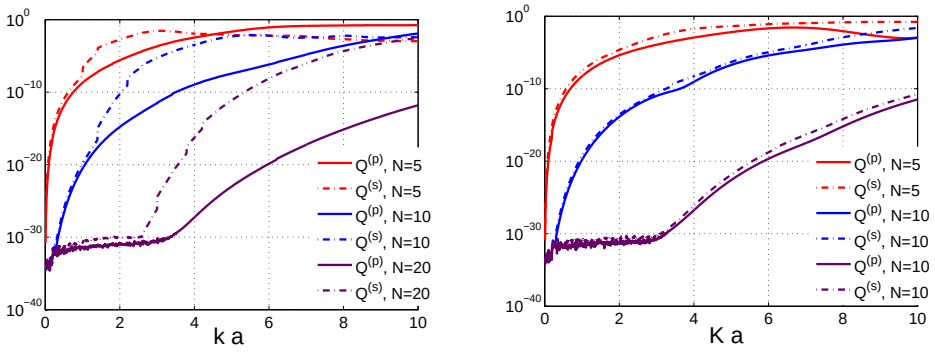

(a) $Q^{(p)}$ and $Q^{(s)}$ vs. ka **(b)** $Q^{(p)}$ and $Q^{(s)}$ vs. Ka

Figure 7.8: The total scattering cross sections $Q^{(p)}$ and $Q^{(s)}$ versus (a) the normalized wave number ka for a longitudinal wave incidence with $M = 3$, and (b) Ka for a transverse wave incidence with $M = 3$.

The variation of the near-field coefficients $|A_n^{(p)} + E_n^{(p)app}|$, $|A_n^{(s)} + E_n^{(s)app}|$ with the number of sources M is depicted in Fig. 7.5 for transverse and in Fig. 7.6 for longitudinal incident waves. For longitudinal wave incidence, the near-field $|A_n^{(p)} + E_n^{(p)app}|$ is less than 10^{-4} and $|A_n^{(s)} + E_n^{(s)app}|$ is less than 10^{-7}. On the contrary, the results are less accurate for transverse waves, as the near-field $|A_n^{(p)} + E_n^{(p)app}|$ approaches the order of 10^{-1} and $|A_n^{(s)} + E_n^{(s)app}|$ reaches a value 10^{-4}.

Figure 7.7 displays the near-field amplitude coefficients $|A_n^{(p)} + E_n^{(p)app}|$ and $|A_n^{(s)} + E_n^{(s)app}|$ as functions of n, the order of the Bessel function, for different values of N and M. The accuracy of the near-field coefficients improves as N and M increase. Increasing the number of sources M allows a decrease in the truncation size N and the order of error.

7.3.2 Farfield response

The radiated farfield when $\mathbf{x} \to \infty$ is given by eq. (7.34). Using the asymptotic expansion of the Hankel function for large argument yields the farfield behavior of $\mathbf{u}_d$

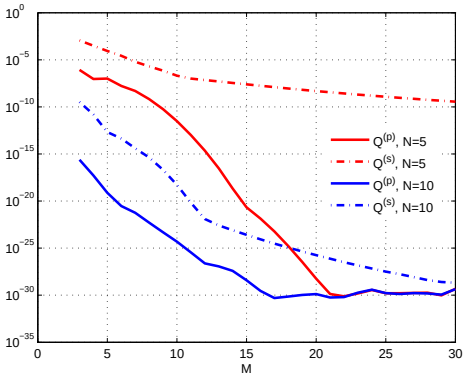

(a) Longitudinal incidence, $k = 2$, $\psi_p = 7^o$

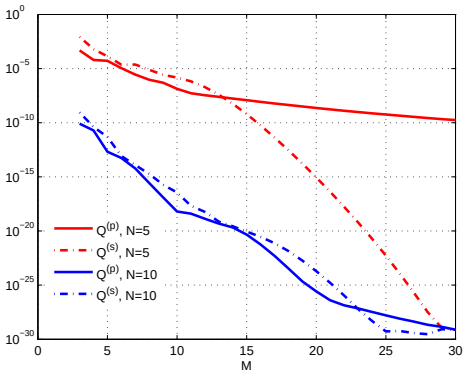

(b) Transverse incidence, $K = 2$, $\psi_s = 7^o$

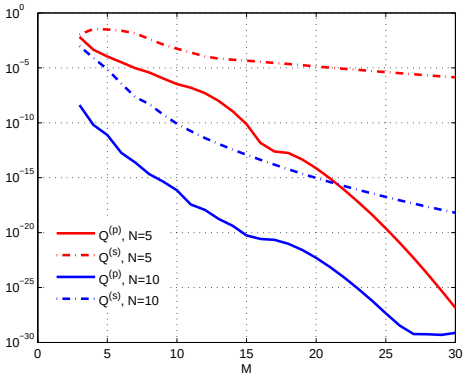

(c) Longitudinal incidence, $k = 5$, $\psi_p = 7^o$

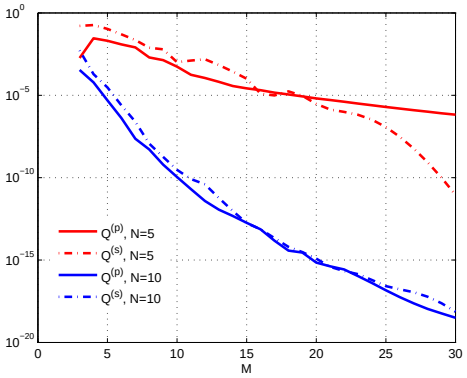

(d) Transverse incidence, $K = 5$, $\psi_s = 7^o$

Figure 7.9: The total scattering cross sections $Q^{(p)}$ and $Q^{(s)}$ versus number of active sources for longitudinal ((a) and (c))and transverse ((b) and (d)) wave incidence for $k = 2$ and $k = 5$ with $K = \kappa\, k$ and $\kappa = c_p/c_s$ when cloaking devices are ON.

$$\Phi_d = f^{(p)}(\theta)\frac{e^{ik|\mathbf{x}|}}{\sqrt{k|\mathbf{x}|}}\Big[1 + O\Big(\frac{1}{k|\mathbf{x}|}\Big)\Big], \quad \Psi_d \quad = f^{(s)}(\theta)\frac{e^{iK|\mathbf{x}|}}{\sqrt{K|\mathbf{x}|}}\Big[1 + O\Big(\frac{1}{K|\mathbf{x}|}\Big)\Big], \quad (7.42)$$

where $f^{(p)}$ and $f^{(s)}$ are the farfield amplitude functions defined such that

$$f^{(\alpha)}(\theta) = \sum_{n=-\infty}^{\infty} f_n^{(\alpha)} e^{in\theta}, \quad f_n^{(\alpha)} = \sqrt{\frac{2}{\pi}} e^{-i(n\frac{\pi}{2}+\frac{\pi}{4})} F_n^{(\alpha)}, \quad \alpha = p,\, s. \qquad (7.43)$$

The total power radiated by the sources is $\Sigma(\theta) = \Sigma^{(p)}(\theta) + \Sigma^{(s)}(\theta)$ where the non-negative compressional and shear far-field averaged flux vector components are:

$$\Sigma^{(\alpha)}(\theta) = \int_0^{2\pi} d\theta |f_n^{(\alpha)}|^2 = 4 \sum_{n=-\infty}^{\infty} |F_n^{(\alpha)}|^2, \quad \alpha = p,\, s. \tag{7.44}$$

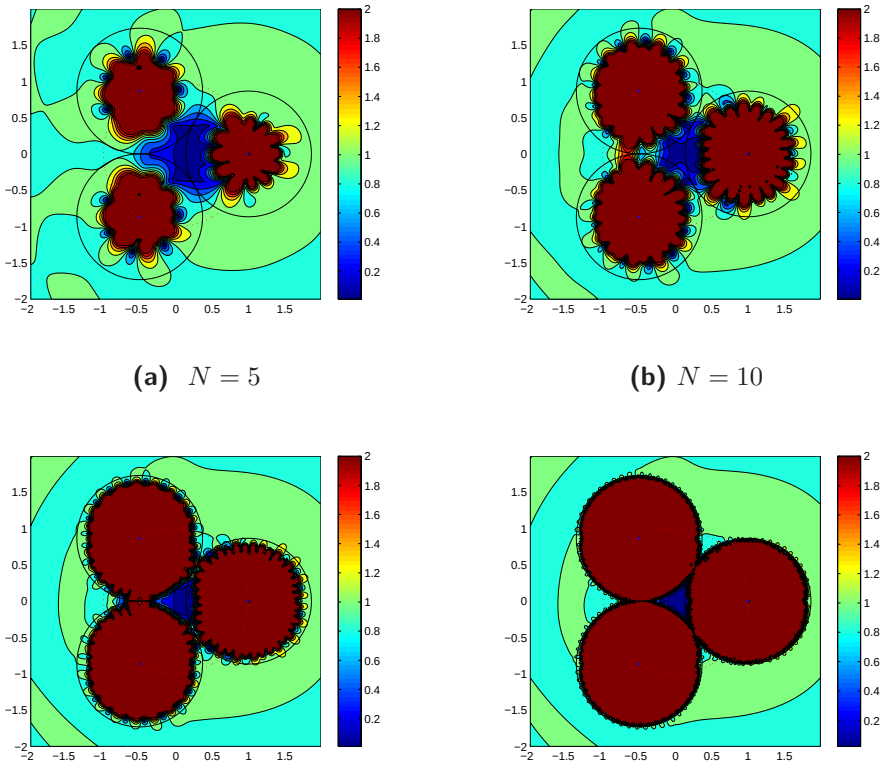

(a) $N = 5$ **(b)** $N = 10$

(c) $N = 20$ **(d)** $N = 50$

Figure 7.10: Absolute value of displacement vector component $|u_x|/k$ for $N = 5$ (a), $N = 10$ (b), $N = 20$ (c) and $N = 50$ (d) when cloaking devices are active with $M = 3, k = 2$ for longitudinal wave incidence.

The non-dimensional total scattering cross sections are then

$$Q = Q^{(p)} + Q^{(p)}, \quad \text{where} \quad Q^{(\alpha)} = \frac{4}{\widetilde{k}a} \sum_{n=-\infty}^{\infty} |F_n^{(\alpha)}|^2, \quad \alpha = p,\, s \tag{7.45}$$

where $\widetilde{k} = k$ for compressional incident waves and $\widetilde{k} = K$ for shear incident waves. The $Q^{(p)}$ and $Q^{(s)}$ are normalized by $a = a_1$, the radius of multipole source A_1, see Figure 7.1.

Results for the total scattering cross sections $Q^{(p)}$ and $Q^{(s)}$ for longitudinal and transversal wave incidence are depicted in Figure 7.8 versus the normalized wave number $\widetilde{k}a$, and in Figure 7.9 against the number of active sources M, where $\widetilde{k} = k$ for P wave incidence and $\widetilde{k} = K$ for SV wave incidence. These show that the error increases with the rise of wave number $\widetilde{k}$, but can be reduced by increasing M and N. Increase of N reduces the error sharply in all cases.

7.3.3 Total displacement field

Longitudinal plane wave incidence

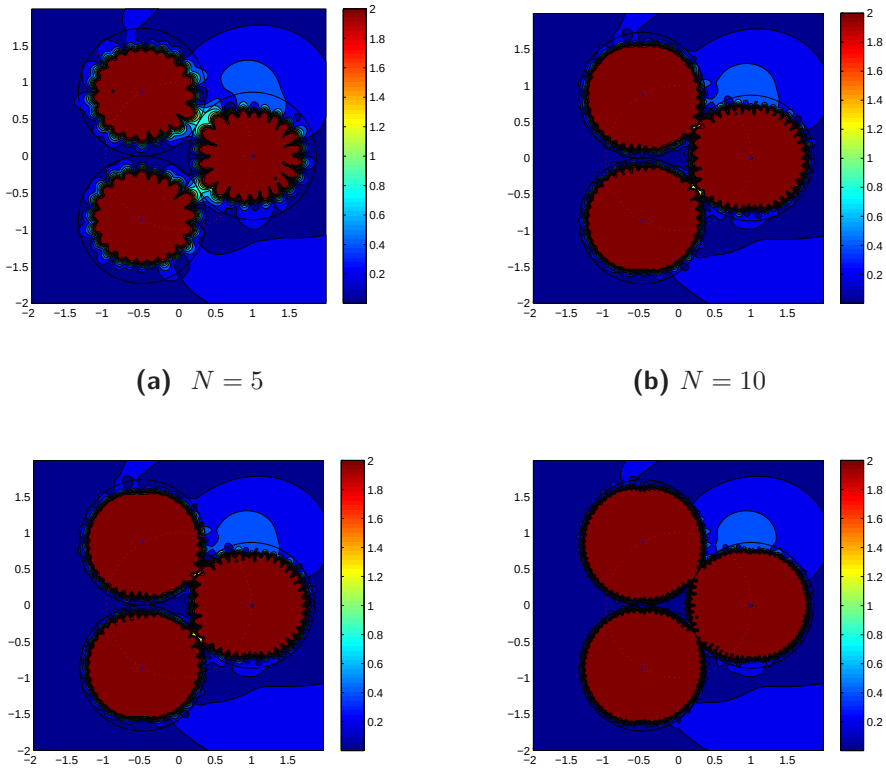

(a) $N = 5$ **(b)** $N = 10$

(c) $N = 20$ **(d)** $N = 30$

Figure 7.11: Absolute value of displacement vector component $|u_y|/k$ for $N = 5$ (a), $N = 10$ (b), $N = 20$ (c) and $N = 30$ (d) when cloaking devices are active with $M = 3, k = 2$ for longitudinal wave incidence.

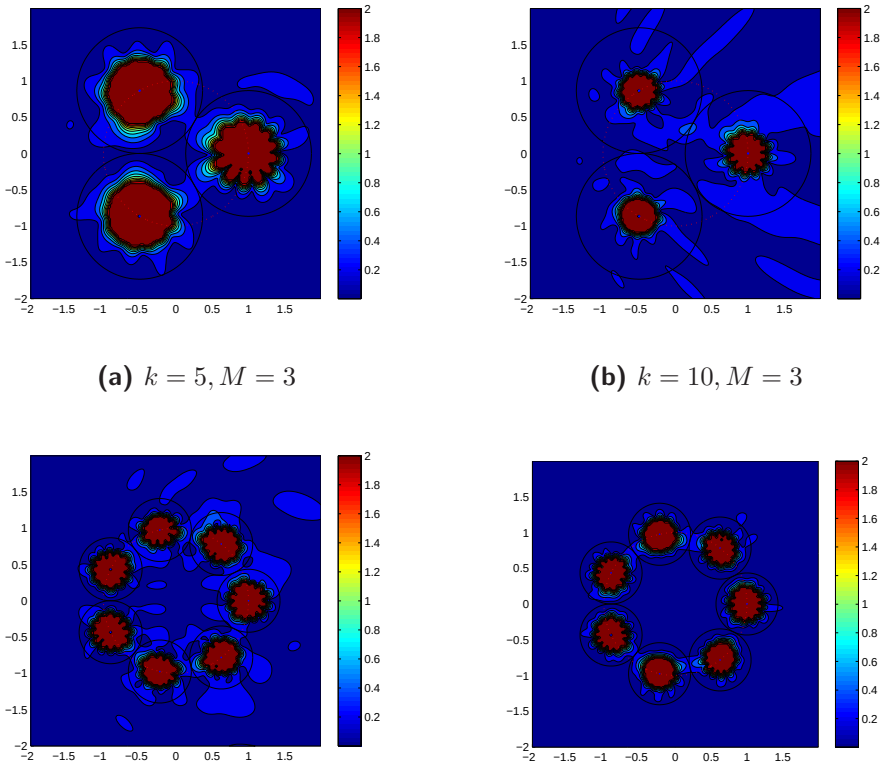

(a) $k = 5, M = 3$ **(b)** $k = 10, M = 3$

(c) $k = 5, M = 7$ **(d)** $k = 10, M = 7$

Figure 7.12: Absolute value of displacement vector component $|u_y|/k$ for $k = 10, M = 3$ (a), $k = 10, M = 3$ (b), $k = 5, M = 7$ (c) and $k = 10, M = 7$ (d). Cloaking devices are active, $N = 5$, for longitudinal wave incidence.

First, consider longitudinal plane wave incidence of the form (7.16). The total displacement vector components in Cartesian coordinates are

$$\big(u_x,\, u_y\big) = \Big(\frac{\partial \Phi_i}{\partial x} + \frac{\partial \Phi_d}{\partial x} + \frac{\partial \Psi_d}{\partial y},\, \frac{\partial \Phi_i}{\partial y} + \frac{\partial \Phi_d}{\partial y} - \frac{\partial \Psi_d}{\partial x}\Big). \tag{7.46}$$

Introducing eq. (7.16) and (7.2b) into (7.46) yields

$$\begin{aligned}\frac{u_x}{k} = \sum_{m=1}^{M}\sum_{n=-\infty}^{\infty}\Bigg[B_{m,n}^{(p)}\Bigg(\cos\theta_m V_n^{+\prime}\big(k(\mathbf{x}-\mathbf{x}_m)\big) - in\sin\theta_m\frac{V_n^{+}\big(k(\mathbf{x}-\mathbf{x}_m)\big)}{k|\mathbf{x}-\mathbf{x}_m|}\Bigg)\\ + B_{m,n}^{(s)}\Bigg(\kappa\sin\theta_m V_n^{+\prime}\big(K(\mathbf{x}-\mathbf{x}_m)\big) + in\cos\theta_m\frac{V_n^{+}\big(K(\mathbf{x}-\mathbf{x}_m)\big)}{k|\mathbf{x}-\mathbf{x}_m|}\Bigg)\Bigg] + i\cos\psi_p\Phi_i,\end{aligned} \tag{7.47}$$

$$\frac{u_y}{k} = \sum_{m=1}^{M} \sum_{n=-\infty}^{\infty} \Bigg[B_{m,n}^{(p)} \Bigg(\sin\theta_m V_n^{+\prime}\big(k(\mathbf{x}-\mathbf{x}_m)\big) + in\cos\theta_m \frac{V_n^{+}\big(k(\mathbf{x}-\mathbf{x}_m)\big)}{k|\mathbf{x}-\mathbf{x}_m|} \Bigg) + B_{m,n}^{(s)} \Bigg(-\kappa\cos\theta_m V_n^{+\prime}\big(K(\mathbf{x}-\mathbf{x}_m)\big) + in\sin\theta_m \frac{V_n^{+}\big(K(\mathbf{x}-\mathbf{x}_m)\big)}{k|\mathbf{x}-\mathbf{x}_m|} \Bigg) \Bigg] + i\sin\psi_p\,\Phi_i, \tag{7.48}$$

where

$$\theta_m(\mathbf{x}) = \arg(\mathbf{x}-\mathbf{x}_m). \tag{7.49}$$

Transverse plane wave incidence

Transverse incident plane waves are of the form (7.25). The total displacement vector components in Cartesian coordinates are

$$(u_x,\, u_y) = \Big(\frac{\partial\Phi_d}{\partial x} + \frac{\partial\Psi_i}{\partial y} + \frac{\partial\Psi_d}{\partial y},\, \frac{\partial\Phi_d}{\partial y} - \frac{\partial\Psi_i}{\partial x} - \frac{\partial\Psi_d}{\partial x}\Big). \tag{7.50}$$

Introducing eq. (7.25) and (7.2b) into (7.50) yields

$$\frac{u_x}{K} = \sum_{m=1}^{M} \sum_{n=-\infty}^{\infty} \Bigg[B_{m,n}^{(p)} \Bigg(\kappa^{-1}\cos\theta_m V_n^{+\prime}\big(k(\mathbf{x}-\mathbf{x}_m)\big) - in\sin\theta_m \frac{V_n^{+}\big(k(\mathbf{x}-\mathbf{x}_m)\big)}{K|\mathbf{x}-\mathbf{x}_m|} \Bigg) + B_{m,n}^{(s)} \Bigg(\sin\theta_m V_n^{+\prime}\big(K(\mathbf{x}-\mathbf{x}_m)\big) + in\cos\theta_m \frac{V_n^{+}\big(K(\mathbf{x}-\mathbf{x}_m)\big)}{K|\mathbf{x}-\mathbf{x}_m|} \Bigg) \Bigg] + i\sin\psi_s\Psi_i, \tag{7.51}$$

$$\frac{u_y}{K} = \sum_{m=1}^{M} \sum_{n=-\infty}^{\infty} \Bigg[B_{m,n}^{(p)} \Bigg(\kappa^{-1}\sin\theta_m V_n^{+\prime}\big(k(\mathbf{x}-\mathbf{x}_m)\big) + in\cos\theta_m \frac{V_n^{+}\big(k(\mathbf{x}-\mathbf{x}_m)\big)}{K|\mathbf{x}-\mathbf{x}_m|} \Bigg) + B_{m,n}^{(s)} \Bigg(-\cos\theta_m V_n^{+\prime}\big(K(\mathbf{x}-\mathbf{x}_m)\big) + in\sin\theta_m \frac{V_n^{+}\big(K(\mathbf{x}-\mathbf{x}_m)\big)}{K|\mathbf{x}-\mathbf{x}_m|} \Bigg) \Bigg] - i\cos\psi_s\,\Psi_i, \tag{7.52}$$

where θ_m is defined by (7.49).

Results

The magnitude of the displacement vector components u_x and u_y are evaluated for $\psi_p = 7^\circ$ for various values of the truncation size N, the number of sources M, and the compressional wavenumber k. Greater accuracy is observed, as expected, with

increased N and M. However, large N and M require longer computation time, and some numerical experimentation is necessary to find the smallest values for which the displacement field vanishes to the desired degree in the cloaked region.

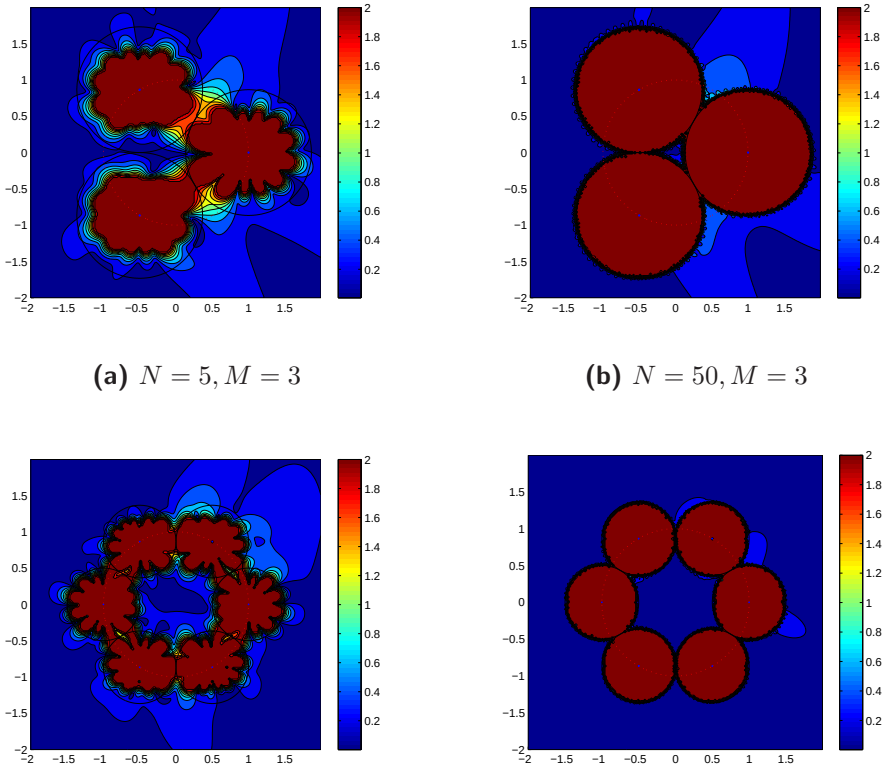

(a) $N = 5, M = 3$ **(b)** $N = 50, M = 3$

(c) $N = 5, M = 6$ **(d)** $N = 50, M = 6$

Figure 7.13: Absolute value of displacement vector component $|u_x|/K$ for $N = 5, M = 3$ (a), $N = 50, M = 3$ (b), $N = 5, M = 6$ (c) and $N = 50, M = 6$ (d) when cloaking devices are active with $k = 2, K = 4.1305$ for transverse wave incidence.

The magnitudes of $|u_x|/k$ and $|u_y|/k$ are depicted in Fig. 7.10 and Fig. 7.11 for longitudinal incidence at different values of N when cloaking devices are active with $M = 3, k = 2$. As expected, the increase of N is accompanied by the reduction of magnitudes $|u_x|/k$ and $|u_y|/k$ in the cloaked region.

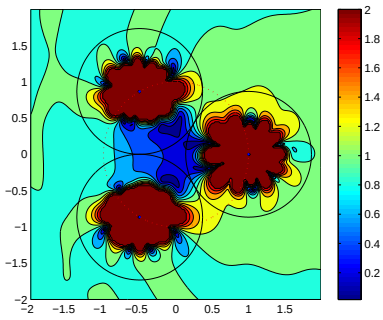

(a) $N = 5, k = 2$

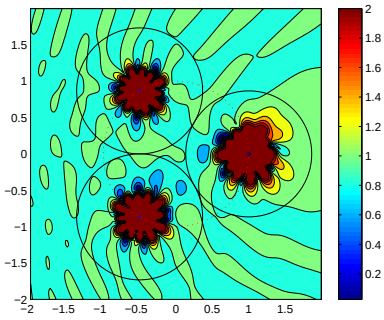

(b) $N = 5, k = 5$

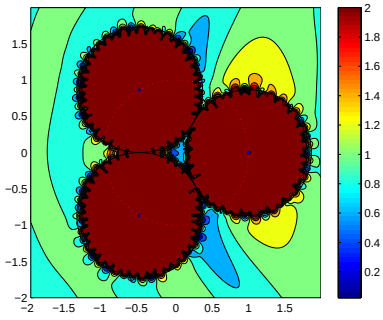

(c) $N = 20, k = 2$

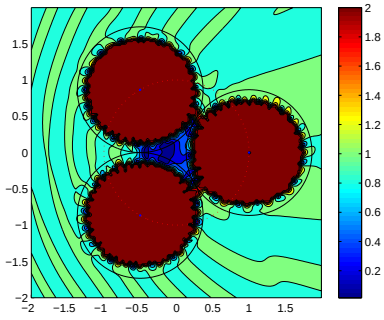

(d) $N = 20, k = 5$

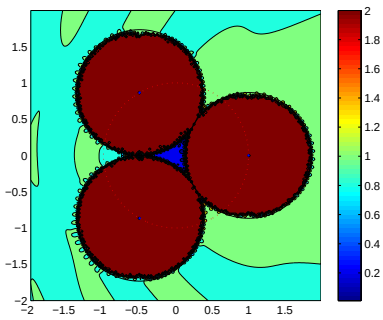

(e) $N = 50, k = 2$

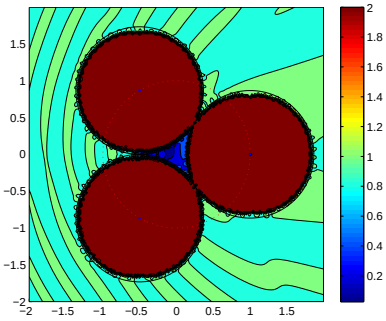

(f) $N = 50, k = 5$

Figure 7.14: Absolute value of displacement vector components $|u_y|/K$ for $N = 5, k = 2$ (a), $N = 5, k = 5$ (b), $N = 20, k = 2$ (c), $N = 20, k = 5$ (d), $N = 50, k = 2$ (e), and $N = 50, k = 5$ (f) with $M = 3$ active sources for transverse wave incidence when cloaking devices are active.

Figure 7.12 illustrates $|u_y|/k$ for longitudinal incidence with $N = 5$ changing the

values of k and M whilst Fig. 7.13 and Fig. 7.14 show corresponding values of $|u_x|/K$ and $|u_y|/K$ for shear incidence, varying N and M with $k = 2$ for the former, and altering the values of N and k with $M = 3$ for the latter. Comparison of these results shows that at higher frequencies, e.g., larger values of k, greater accuracy is achieved by increasing the number of sources M, whereas at lower frequencies the smallest number of sources required, $M = 3$, produces reasonable cloaking, although enhanced with increased values of N.

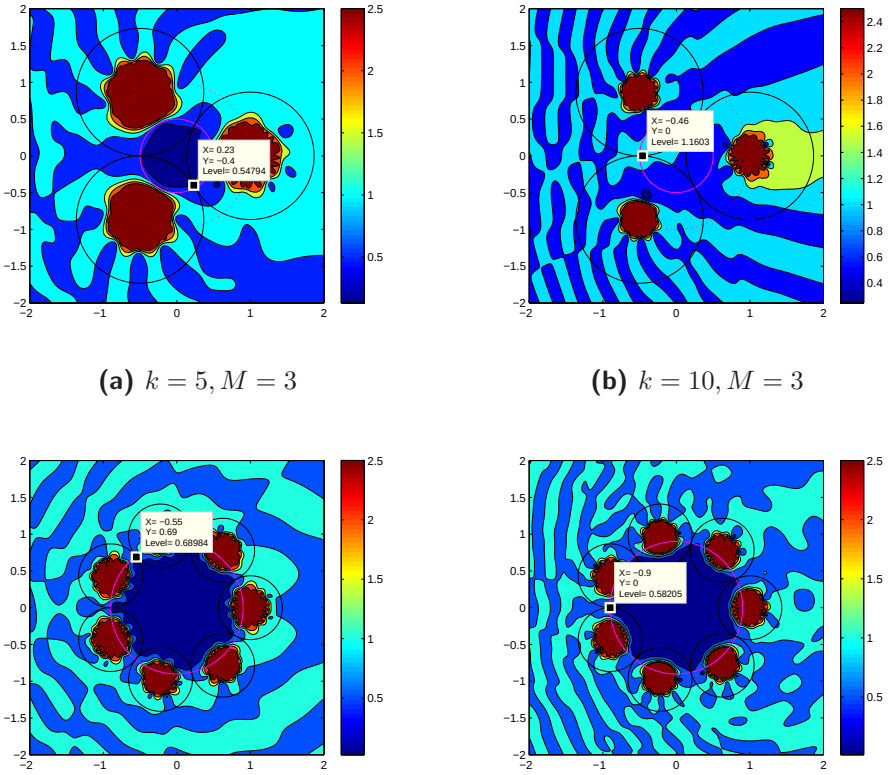

(a) $k = 5, M = 3$ **(b)** $k = 10, M = 3$

(c) $k = 5, M = 7$ **(d)** $k = 10, M = 7$

Figure 7.15: The magnitude of the total displacement field with its maximum absolute amplitude in a cloaked region generated by $M = 3$ active sources with $k = 5$ (a) and $k = 10$ (b), and by $M = 7$ active sources with $k = 5$ (c) and $k = 10$ (d) for a longitudinal wave incidence with $\psi_p = 7°$, $N = 5$ while cloaking devices are active.

The magnitude of the total displacement field and its absolute maximum amplitude

inside the cloaked region is depicted in Fig. 7.15 with parameters used in Fig. 7.12. Comparison of these results shows that at higher frequencies, i.e., larger values of k_p, greater accuracy is achieved by increasing the number of sources M, whereas at lower frequencies the smallest number of sources required, i.e. $M = 3$, produces reasonable cloaking, although this is enhanced with increased values of N.

Chapter 8

Concluding remarks and future work

In this chapter, we summarize the main ideas and important results of this dissertation and point out the future work that must be considered.

8.1 Conclusions

Theoretical predictions and numerical results associated with the propagation, and multiple scattering of acoustic and elastic waves in layered cylindrical structures and heterogeneous anisotropic solids are presented in this dissertation. The main importance and novelty of this work is in the development of a series of fast, robust, rapidly convergent iterative techniques that we provided to expedite the solution of MS problems. The iterative methods are developed using Neumann series expansion and taking advantage of the Block Toeplitz structure of the linear system. The techniques are very general, and suitable for parallel computations and for a large number of MS problems in complex media, i.e. acoustic, elastic, electromagnetic, etc.

An acoustic and elastic single scattering by elastic isotropic multilaminate cylinders is studied using the Global matrix method. The oblique single scattering of incident waves inclined at an arbitrary angle to a transverse-isotropic solid is considered. The recursive impedance matrix is developed for radially heterogeneous anisotropic solids, and specifically, cylindrically and spherically anisotropic solids are examined. An explicit method is introduced for finding the impedance in piecewise uniform, transverse-isotropic material. Numerical results, performed in Matlab and COMSOL, represent total and scattered fields around the scatterer and a far-radiated field for a time harmonic incident plane wave and point source.

Active exterior cloaking devices are designed for acoustic and elastic media using

multipole sources. The approach is based on representing the incident field in terms of Bessel functions at each source position, which leads to a linear system of equations for the source amplitudes that can be solved in closed form. The numerical simulations presented here indicate that a small number of multipoles provide adequate cancellation at low frequencies. This suggests a natural way to extend ideas based on monopoles to more elaborate source distributions composed of finite numbers of multipoles of low order. The present results provide a means to establish realistic strategies for practical application.

8.2 Future work

The concept employed in this work to develop rapidly convergent iterative techniques can be extended to model three-dimensional scattering problems. The proposed techniques can be applied to model 3D MS problems in complex media such as acoustic, elastodynamic, electromagnetic, and porous and viscoelastic heterogeneous media. Specifically, these techniques can be applied to the trabecular bone, acoustic metamaterial absorbers, gradient index devices, dynamically tunable structures, cloaking, remote fish classification, and effective parameters of heterogeneous media. Preliminary work along these lines has been provided in [12] for electromagnetic scattering by 3D spheres.

The results presented here for active cloaking models provide a first step in the direction of realistic active control of acoustic and elastic waves. Applications to structure borne waves, surface waves, and even geophysical waves, are possible. However, as a *control* problem, many issues remain to be addressed. One of the issues is how to achieve at the time the silencing one region of space and reducing the unavoidable source noise that must be generated in another, larger, region. In practice, it is not possible to achieve an exact field cancellation. It requires the truncation of the series and balance the decrease in cloaking accuracy with whatever amplitude level is deemed acceptable in the source region. This is obviously a crucial aspect and one that remains to be studied in detail. We have pointed out some similarities with parallel issues in active noise control. Future studies will examine analogies in these topics, and will consider the low frequency end of the spectrum.

References

[1] M. Abramowitz and I. Stegun. *Handbook of Mathematical Functions with Formulas, Graphs, and Mathematical Tables*. Dover, New York, 1974.

[2] J. D. Achenbach. *Wave Propagation in Elastic Solids*. North Holland, 1987.

[3] R. Adams. *A Class of Robust and Efficient Iterative Methods for Wave Scattering Problems*. PhD thesis, Virginia Polytechnic Institute and State University, 1998.

[4] F. Ahmad. Guided waves in a transversely isotropic cylinder immersed in a fluid. *J. Acoust. Soc. Am.*, 109(3):886–890, 2001.

[5] F. Ahmad and A. Rahman. Acoustic scattering by transversely isotropic cylinders. *Int. J. Engng. Sc.*, 38:325–335, February 2000.

[6] B. Anderson and J. Moore. *Optimal filtering*. Prentice-Hall, 1979.

[7] X. Antoine, C. Chniti, and K. Ramdani. On the numerical approximation of high-frequency acoustic multiple scattering problems by circular cylinders. *J. Comp. Phys.*, 227:1754–1771, 2008.

[8] X. Antoine, K. Ramdani, and T. Bertrand. Étude numérique de la résolution par équations intégrales de la diffraction multiple par des disques. In *10éme Congrés Français d'Acoustique. 12-16 Avril 2010. Lyon*, 2010.

[9] O. Arushanian, M. Samarin, V. Voevodin, , E. Tyrtyshnikov, B. Garbow, J. Boyle, W. Cowell, and K. Dritz. The Toeplitz package user guide. Technical report, Science Research Computing Center, Moscow State University and Mathematics and Computer Science Devison, Argonne National Laboratory, 1983.

[10] S. Banach. *Theory of Linear Operations*. Dover Books on Mathematics, Translated by F. Jellett, 1932.

[11] B. Barrowes, F. Teixeira, and J. Kong. Fast algorithm for matrix-vector multiply of asymmetric multilevel block-toeplitz matrices. In *Antennas and Propagation Society International Symposium, IEEE, Volume: 4*, 2001.

[12] B. E. Barrowes, F. L. Teixeira, and J. A. Kong. Fast algorithm for matrix vector multiply of asymmetric multilevel block-toeplitz matrices in 3-d scattering. *Microwave & Opt.Tech. Let.*, 31(1):26–32, 2001.

[13] P. Y. L. Bas, F. Luppé, J. M. Conoir, and H. Franklin. N-shell cluster in water: Multiple scatteing and splitting of resonances. *J. Acoust. Soc. Am.*, 115(3):1460–1467, 2004.

[14] G. Baxter. Polynomials defined by a difference system. *Bull. Amer. Math. Soc.*, 66:187–190, 1960.

[15] G. Baxter. Polynomials defined by a difference system. *J. Math. Anal. Appl.*, 2:223–263, 1961.

[16] G. Baxter and I. J. Hirschman. An explicit inversion formula for finite section Wiener- Hopf operators. *Bull. Amer. Math. Soc.*, 70:820–823, 1964.

[17] P. Beattie, R. Chivers, and L. Anson. Utrasonic backscattering from solid cylindrical inclusions in solid elastic matrices: A comparison of theory and experiment. *J. Acoust. Soc. Am.*, 94:3421–3427, 1993.

[18] S. Biwa, S. Yamamoto, F. Kobayashi, and N. Ohno. Computational multiple scattering analysis for shear wave propagation in unidirectional composites. *Int. J. Solids Struct.*, 41:435457, 2004.

[19] N. Bleistein and J. K. Cohen. Nonuniqueness in the inverse source problem in acoustics and electromagnetics. *J. Math. Phys.*, 18(2):194–201, 1977.

[20] Y. Bobrovnitskii. Impedance acoustic cloaking. *New J. Phys.*, 12:043049, 2010.

[21] Boström. Multiple scattering of elastic waves by bounded obstacles. *J. Acoust. Soc. Am.*, 67(2):399–413, 1980.

[22] G. Box, G.E. amnd Junkins. *Time series analysis; Forecasting and control.* Holden-Day, San Francisco, 1970.

[23] L. M. Brekhovskikh. *Waves in Layered Media.* Academic, New York, 1960.

[24] C. Brezinski. *Bi-orthogonality and its application to numerical analysis.* Marcel Dekker, Inc., 1992.

[25] M. Brun, S. Guenneau, and A. B. Movchan. Achieving control of in-plane elastic waves. *Appl. Phys. Lett.*, 94:061903, 2009.

[26] V. Buchwald. Rayleigh waves in transversely isotropic media. *Q. J. Mech. Appl. Math.*, 14:293–317, 1961.

[27] L. Cai. Multiple scattering in single scatterers. *J. Acoust. Soc. Am.*, 115:986–995, 2004.

[28] L. Cai and J. H. J. Williams. Large-scale multiple scattering problems. *Ultrasonics*, 37:453462, 1999.

[29] L.-W. Cai. *Multiple Scattering of Elastic Waves in Fiber Reinforced Composites, Sc.D. Thesis,.* PhD thesis, Massachusetts Institute of Technology, Cambridge, MA,, 1998.

[30] L.-W. Cai. Scattering of antiplane shear waves by layered circular elastic cylinder. *J. Acoust. Soc. Am.*, 115:515–522, 2004.

[31] L.-W. Cai. Acoustical scattering by arrays of cylinders in waveguides. *J. Acoust. Soc. Am.*, 122(3):1340–1351, 2007.

[32] P. Chadwick. Wave propagation in transversely isotropic heat conducting elastic materials. *Mathematika*, 17:255–274, 1970.

[33] H. Chen and C. T. Chan. Acoustic cloaking in three dimensions using acoustic metamaterials. *Appl. Phys. Lett.*, 91(18):183518+, 2007.

[34] H. Chen and C. T. Chan. Acoustic cloaking and transformation acoustics. *J. Phys. D*, 43(11):113001+, 2010.

[35] H.-Y. Chen, T. Yang, X.-D. Luo, and H.-R. Ma. The impedance-matched reduced acoustic cloaking with realizable mass and its layered design. *Chin. Phys. Lett.*, 25(10):3696–3697, May 2008.

[36] K. Chen. *Matrix Preconditioning Techniques and Applications.Cambridge monographs on Applied and Computational Mathematics.* Cambridge University Press, New York, 2005. Editors: Ablowitz, M. J. and Davis, S. H. and Hinch, and E. J. Iserles, A. and Ockendon, J. and Olver, P. J.

[37] S. Cheng. Multiple scattering of elastic waves by parallel cylinders. *J. Appl. Mech.*, 36:523527, 1969.

[38] L. Collatz. *The numerical treatment of differential equations.* Springer, Berlin, 3rd edition edition, 1960.

[39] D. L. Colton and R. Kress. *Integral Equation Methods in Scattering Theory.* Krieger, Melbourne, FL, 1991.

[40] J. M. Conoir and A. N. Norris. Effective wave numbers and reflection coefficients for an elastic medium containing random configurations of cylindrical scatterer. *Wave Motion*, 47:183–197, 2010.

[41] S. A. Cummer and D. Schurig. One path to acoustic cloaking. *New J. Phys.*, 9(3):45+, 2007.

[42] D. K. Dacol and G. J. Orris. Wave number of the coherent acoustic field in a medium with randomly distributed spheres. *Journal of Physics A: Mathematical and Theoretical*, 42(20):205001+, 2009.

[43] Y. Decanini, A. Folacci, P. Cabrielli, and J.-L. Rossi. Algebraic aspects of multiple scattering by two parallel cylinders: Classification and physical interpretation of scattering resonances. *J. Sound & Vibr.*, 221(5):785–804, 1999.

[44] Y. Decanini, A. Folacci, E. Fourniery, and P. Gabrielli. Exact S-matrix for N-disc systems and various boundary conditions:. *J. Phys. A: Math. Gen.*, 31:7865–7889, 1998.

[45] Y. Decanini, A. Folacci, E. Fourniery, and P. Gabrielliz. Exact S-matrix for N-disc systems and various boundary conditions: II. determination and partial classification of resonances. *J. Phys. A: Math. Gen.*, 31:78917900, 1998.

[46] C. Delorme and J. Rinkel. Random walks on the nonnegative integers with a left-bounded generator. *Probability & mathematical statistics*, 31(1):119139, 2011.

[47] A. J. Devaney and R. P. Porter. Holography and the inverse source problem. Part II: Inhomogeneous media. *J. Opt. Soc. Am. A*, 2(11):2006–2011, 1985.

[48] J. W. Dunkin. Computations of modal solutions in layered elastic media at high frequencie. *Bull. Seism. Soc. Amer.*, 55:335–358, 1965.

[49] N. G. Einspruch and R. Truell. Scattering of a plane longitudinal wave by a spherical fluid obstacle in an elastic medium. *J. Acoust. Soc. Am.*, 32(2):214–220, 1960.

[50] N. G. Einspruch, E. J. Witterholt, and R. Truell. Scattering of a plane transverse wave by a spherical obstacle in an elastic medium. *J. Appl. Phys.*, 31:806–818, 1960.

[51] P. S. Epstein and R. R. Carhart. The absorption of sound in suspensions and emulsions. I. Water fog in air. *J. Acoust. Soc. Am.*, 25:553–565, 1953.

[52] D. Evans and R. Porter. Near-trapping of waves by circular arrays of vertical cylinders. *Appl. Ocean Research*, 19:83–99, 1997.

[53] Y. Fan, F. Honarvar, A. N. Sinclair, and M. R. Jafari. Circumferential resonance modes of solid elastic cylinders excited by obliquely incident acoustic waves. *J. Acoust. Soc. Am.*, 113(1):102–113, 2003.

[54] Y. Fan, A. N. Sinclair, and F. Honarvar. Scattering of a plane acoustic wave from a transversely isotropic cylinder encased in a solid elastic medium. *J. Acoust. Soc. Am.*, 106(3):1229–1236, 1999.

[55] J. J. Faran. Sound scattering by solid cylinders and spheres. *J. Acoust. Soc. Am.*, 23(4):405–418, 1951.

[56] L. Flax and H. aÜberall. Resonant scattering of elastic waves from spherical solid inclusions. *J. Acoust. Soc. Am.*, 67(5):1432–1842, 1980.

[57] L. Flax, V. Varadan, and V. Varadan. Scattering of an obliquely incident acoustic wave by an infinite cylinder. *J. Acoust. Soc. Am.*, 68:1832–1835, 1980.

[58] L. Foldy. The multiple scattering of waves. i. general theory of isotropic scattering by randomly distributed scatterers. *Phys. Rev.*, 67:107119, 1945.

[59] G. Freud. *Orthogonal Polynomials*. Pergamon Press, 1971.

[60] R. Freund and H. Zha. Formally biorthogonal polynomials and a look-ahead levinson algorithm for general toeplitz systems. *Lin.Alg & its appl.*, 188,189:255–303, 1993.

[61] C. R. Fuller, S. J. Elliott, and P. A. Nelson. *Active control of vibration*. Academic Press, London, 1996.

[62] P. Gaspard and S. Rice. Exact quantization of the scattering from a classically chaotic repellor. *J. Chem. Phys.*, 90:2255–2262, 1989.

[63] G. C. Gaunaurd. Elastic and acoustic resonance wave scattering. *Appl. Mech. Rev.*, 42:143–192, 1989.

[64] L. Y. Geronimus. *Orthogonal Polynomials*. Consultant's Bureau, New York, (translation from Russian), 1961.

[65] I. C. Gohberg and A. A. Semencul. On the inversion of finite Toeplitz matrices and their continuous analogs. *Mat. Issled.*, 7(2):201–223, 1972.

[66] U. Grenander and G. Szegö. *Toeplitz Forms and Their Applications*. University of California Press, 1958. Editors: Evans, G. C. and Neyman, J. and Loéve, M. and Szeg´o.

[67] M. Grote and K. C. Dirichlet-to-Neumann boundary conditions for multiple scatteing problems. *J. Comp. Phys.*, 201:630–650, 2004.

[68] D. Guicking. On the invention of active noise control by Paul Lueg. *J. Acoust. Soc. America*, 87:2251–2254, 1990.

[69] H. Gustafson and P. Stepanishen. Effects of multiple scattering and acoustic interactions among two parallel hydrophones and a planar baffle. *J. Acoust. Soc. Am.*, 69(2):380–389, 1981.

[70] S. Hasheminejad and M. A. Alibakhshi. Dynamic viscoelastic and multiple scattering effects in fiber suspensions. *J. Dispersion Sc. & Tech.*, 27:219234, 2006.

[71] S. Hasheminejad and R. Avazmohammadi. Acoustic diffraction by a pair of poroelastic cylinders. *Z. Angew. Math. Mech.*, 86(8):589 605, 2006.

[72] S. Hasheminejad and M. Rajabi. Acoustic scattering characteristics of a thick-walled orthotropic cylindrical shell at oblique incidence. *Ultrasonics*, 47(1-4):32–48, December 2007.

[73] S. Hasheminejad and M. Rajabi. Scattering and active acoustic control from a submerged piezoelectric-coupled orthotropic hollow cylinder. *J. Sound. Vib.*, 318(1-2):50–73, November 2008.

[74] G. Heinig and K. Rost. *Algebraic Methods for Toeplitz-like Matrices and Operators*. Birkhäuser Verlag, Basel-Boston-Stuttgart, 1984. Gohberg, I.Editor.

[75] K. F. Herzfeld. The scattering of sound-waves by small elastic spheres. *Phil. Mag. Series 7*, 9(59):741 751, 1930.

[76] R. Hickling. Analysis of echoes from a solid elastic sphere in water. *J. Acoust. Soc. Am.*, 34:1582–1592, 1962.

[77] F. Honarvar, Y. Fan, and A. N. Sinclair. Scattering of acoustic waves from immersed transversely isotropic cylinders (l). *J. Acoust. Soc. Am.*, 114(1):45–47, 2003.

[78] F. Honarvar and A. N. Sinclair. Acoustic wave scattering from transversely isotropic cylinders. *J. Acoust. Soc. Am.*, 100:57–63, 1996.

[79] F. Honarvar and A. N. Sinclair. Scattering of an obliquely incident plane wave from a circular clad rod. *J. Acoust. Soc. Am.*, 102:41–48, 1997.

[80] F. Honarvar and A. N. Sinclair. Response to representation of the displacement in terms of scalar functions for use in transversely isotropic materials [j. acoust. soc. am. 104, 3675 (1998)]. *J. Acoust. Soc. Am.*, 104:3677, 1998.

[81] W. Huang, S. Brisuda, and I. Rokhlin. Ultrasonic wave scattering from fiber-matrix interphases. *J. Acoust. Soc. Am.*, 97:807–817, 1995.

[82] J. Jamali, M. Naei, F. Honarvar, and M. Rajabi. Acoustic scattering and radiation force function experienced by functionally graded cylindrical shells. *J. Mech.*, 27 (2):227–243, 2011.

[83] T. Kailath, A. Vieira, and M. Morf. Inverses of toeplitz operators, innovations, and orthogonal polynomials. *SIAM Review*, 20(1):106–119, 1978.

[84] A. J. Kempton. The ambiguity of acoustic sources - a possibility for active control. *J. Sound Vibration*, 48:475–483, 1976.

[85] I. Klyukin and V. Chabanov. Sound diffraction by a plane grating of cylinders. *Sov. Phys. Acoust.*, 20(6), 1975.

[86] L. Knopoff. Scattering of shear waves by spherical obstacles. *Geophysics*, 24(2):209–219, 1959.

[87] M. G. Krein. The continuous analogs of theorems on polynomials orthogonal on the unit circle. *Dokl. Akad. Nauk SSSR*, 104:637–640, 1955.

[88] V. Kubenko. Diffraction of acoustic waves by two nonparallel circular cylinders. *Sov. Appl. Mech.*, 25 (1):34–41, 1989.

[89] F. Leon, F. Lecroq, D. Decultot, and G. Maze. Scattering of an obliquely incident acoustic wave by an infinite hollow cylindrical shell. *J. Acoust. Soc. Am.*, 91:1388–1397, 1992.

[90] U. Leonhardt. Optical conformal mapping. *Science*, 312(5781):1777–1780, June 2006.

[91] S. Lethuillier, J. Conoir, P. Pareige, and J. Izbicki. Resonant acoustic scattering by a finite linear grating of elastic shells. *Ultrasonics*, 41:655662, 2003.

[92] T. Li and M. Ueda. Sound scattering of a plane wave obliquely incident on a cylinder. *J. Acoust. Soc. Am.*, 86:2363–2368, 1989.

[93] W. Lin and A. Raptis. Sound scattering by a group of oscillatory cylinders. *J. Acoust. Soc. Am.*, 77(1):15 – 28, 1985.

[94] Z. Liu and L. Cai. Three-dimensional multiple scattering of elastic waves by spherical inclusions. *J. Vib. Acoust.*, 131:1–11, 2009.

[95] S. Lonné. *Modélisation de la propagation ultrasonore dans les matériaux composites obtenus par le procédé de fabrication RTM (Resin Transfer Molding).* PhD thesis, L'Université Bordeaux 1, 2003.

[96] F. Luppé, J.-M. Conoir, and S. Robert. Coherent waves in a multiply scattering poro-elastic medium obeying Biot's theory. *Waves in Random and Complex Media*, 18(2):241–254, 2008.

[97] P. A. Martin. Acoustic scattering by inhomogeneous spheres. *J. Acoust. Soc. Am.*, 111(5):2013–2018, 2002.

[98] P. A. Martin. *Multiple Scattering: Interaction of Time-harmonic Waves with N Obstacles*. Cambridge University Press, New York, 2006.

[99] G. Maze, J. Izbicki, and J. Ripoche. Resonances of plates and cylinders: Guided waves. *J. Acoust. Soc. Am.*, 77:1352–1357, 1985.

[100] R. J. McKinnell. Active vibration isolation by cancelling bending waves. *Proc. Roy. Soc. A*, 421:357–393, 1989.

[101] D. A. Miller. On perfect cloaking. *Opt. Express*, 14(25):12457–12466, December 2006.

[102] G. W. Milton, M. Briane, and J. R. Willis. On cloaking for elasticity and physical equations with a transformation invariant form. *New J. Phys.*, 8:248–267, 2006.

[103] P. J. Morris. The scattering of sound from a spatially distributed axisymmetric cylindrical source by a circular cylinder. *J. Acoust. Soc. Am.*, 97(5):2651–2656, 1995.

[104] P. M. Morse and H. Feshbach. *Methods of Theoretical Physics, Vol. I.* McGraw-Hill, New York, 1953.

[105] P. M. Morse and H. Feshbach. *Methods of Theoretical Physics, Vol. II.* McGraw-Hill, New York, 1953.

[106] P. A. Nelson and S. J. Elliott. *Active control of sound*. Academic Press, London, 1992.

[107] A. Niklasson and S. K. Datta. Scattering by an infinite transversely isotropic cylinder in a transversely isotropic medium. *Wave Motion*, 27(2):169–185, February 1998.

[108] A. Norris, F. Amirkulova, and W. Parnell. Active elastodynamic cloaking. *Math. Mech. Solids*, 19(6):603–625, 2014.

[109] A. Norris and N. Vasudevan. Acoustic wave scattering from thin shell structures. *J. Acoust. Soc. Am.*, 92:3320–3336, 1992.

[110] A. N. Norris. Scattering of elastic waves by spherical inclusions with applications to low frequency wave propagation in composites. *Int. J. Engng. Sc.*, 24(8):1271–1282, 1986.

[111] A. N. Norris. Acoustic cloaking theory. *Proc. R. Soc. A*, 464:2411–2434, 2008.

[112] A. N. Norris, F. A. Amirkulova, and W. J. Parnell. Source amplitudes for active exterior cloaking. *Inverse Problems*, 28 (10) 105002, 2012.

[113] A. N. Norris and A. J. Nagy. Acoustic metafluids made from three acoustic fluids. *J. Acoust. Soc. Am.*, 128(4):1606–1616, 2010.

[114] A. N. Norris, A. J. Nagy, and F. A. Amirkulova. Stable methods to solve the impedance matrix for radially inhomogeneous cylindrically anisotropic structures. *J. Sound. Vib.*, 332:25202531, 2013.

[115] A. N. Norris and W. J. Parnell. Hyperelastic cloaking theory: Transformation elasticity with prestressed solids. *Proc. Roy. Soc. A*, in press, 2012.

[116] A. N. Norris and A. L. Shuvalov. Wave impedance matrices for cylindrically anisotropic radially inhomogeneous elastic materials. *Q. J. Mech. Appl. Math.*, 63:1–35, 2010.

[117] A. N. Norris and A. L. Shuvalov. Elastic cloaking theory. *Wave Motion*, 49:525–538, 2011.

[118] A. N. Norris and A. L. Shuvalov. Elastodynamics of radially inhomogeneous spherically anisotropic elastic materials in the stroh formalism. *Proc. R. Soc. A*, page 112, 2011.

[119] W. J. Parnell. Nonlinear pre-stress for cloaking from antiplane elastic waves. *Proc. R. Soc. A*, 468:563–580, 2012.

[120] W. J. Parnell, A. N. Norris, and T. Shearer. Employing pre-stress to generate finite cloaks for antiplane elastic waves. *Appl. Phys. Lett.*, 100:171907, 2012.

[121] M. C. Pease. *Methods of Matrix Algebra*. Academic Press, New York, 1965.

[122] J. B. Pendry, D. Schurig, and D. R. Smith. Controlling electromagnetic fields. *Science*, 312(5781):1780–1782, 2006.

[123] B. Peterson and S. Ström. Matrix formulation of acoustic scattering from an arbitrary number of scatterers. *J. Acoust. Soc. Am.*, 56(3):771–780, 1974.

[124] B. Peterson and S. Ström. Matrix formulation of acoustic scattering from multilayered scatterers. *J. Acoust. Soc. Am.*, 57(1):2–13, 1975.

[125] B. Peterson, V. K. Varadan, and V. V. Varadan. Scattering of elastic waves by a fluid inclusion. *J. Acoust. Soc. Am.*, 73 (5):1487–1493, 1983.

[126] B. Peterson, V. V. Varadan, and V. K. Varadan. On the multiple scattering of waves from obstacles with solid-fluid interfaces. In *Acoustic, Electromagnetic and Elastic Wave Scattering - Focus on the T - matrix Approarch*, 1980.

[127] M. D. Pocock and S. P. Walker. The complex bi-conjugate gradient solver applied to large electromagnetic scattering problems, computational costs and cost scalings. *IEEE Transactions on Antennas and Propagation, AP*, 45(1):140146, 1997.

[128] G. Polya, G. Szegö. *Aufgaben und Lehrsätze aus der Analysis. I - II. (Problems and Theorems in Analysis)*. Springer,Verlag- Berlin- Heidelberg. Originally published as Vol. 216 of the Grundlehren der mathematischen Wissenschaften, 1971.

[129] L. Pustilnil'kov. Toeplitz and Hankel matrices and their applications. *Progresses of Math. Sciences*, 39(4(238)):53–84, 1984.

[130] Z. Qia, F. Jin, K. Kishimoto, and T. Lu. Scattering of elastic P-waves by a transversely isotropic piezoelectric cylinder embedded in a polymer matrix. *Smart Mat. Struct.*, 17(4):045019+, 2008.

[131] R. P. Radlinski and T. J. Meyers. Radiation patterns and radiation impedances of a pulsating cylinder surrounded by a circular cage of parallel cylindrical rods. *J. Acoust. Soc. Am.*, 56(3):842–848, 1974.

[132] A. Rahman and F. Ahmad. Representation of the displacement in terms of scalar functions for use in transversely isotropic materials. *J. Acoust. Soc. Am.*, 104(6):3675–3676, 1998.

[133] M. Rajabi and S. Hasheminejad. Acoustic resonance scattering from a multilayered cylindrical shell with imperfect bonding. *Ultrasonics*, 49(1-4):682–695, December 2009.

[134] L. Rall. *Computational Solution of Nonlinear Operator equations*. John Wiley & Sons, Inc. New York, 1969.

[135] L. Rayleigh. *Theory of sound, Vol.2*. MacMillan and Company, Ltd, 1878.

[136] S. I. Rokhlin and W. Huang. Ultrasonic wave interaction with a thin anisotropic layer between two anisotropic solids: Exact and asymptotic-boundary-condition methods. *J. Acoust. Soc. Am.*, 92:1729–1742, 1992.

[137] S. I. Rokhlin and L. Wang. Stable recursive algorithm for elastic wave propagation in layered anisotropic media: Stiffness matrix method. *J. Acoust. Soc. Am.*, 112(3):822–834, 2002.

[138] S. I. Rokhlin and L. Wang. A compliance/stiffness matrix formulation of general Greens function and effective permittivity for piezoelectric multilayers. *IEEE Trans. Ultrason., Ferroel., and Freq. Contr.*, 51(4):453–463, 2004.

[139] Y. Saad. *Iterative Methods for Sparse Linear Systems*. PWS Pub. Co., Boston, 1996.

[140] Y. Saad. *Iterative Methods for Sparse Linear Systems*. SIAM, 2003.

[141] S. Sancar and Y. H. Pao. Spectral analysis of elastic pulses backscattered from two cylindrical cavities in a solid. part i. *J. Acoust. Soc. Am.*, 69(6):1591–1596, 1981.

[142] H. Sato and Y. Shindo. Multiple scattering of plane elastic waves in a fiber-reinforced composite medium with graded interfacial layers. *J. Solids & Struc.*, 38:2549–2571, 2001.

[143] C. L. Scandrett, J. E. Boisvert, and T. R. Howarth. Acoustic cloaking using layered pentamode materials. *J. Acoust. Soc. Am.*, 127(5):2856–2864, 2010.

[144] R. Scharstein. Acoustic scattering from two parralel soft cylinders. In *In Rroceedings: Southestcon. Apr. 12-15*, 1992.

[145] H. Schmidt and F. Jensen. A full wave solution for propagation in multilayered viscoelastic media with application to gaussian beam reflection at fluid–solid interfaces. *J. Acoust. Soc. Am.*, 77:813–825, 1985.

[146] L. M. Schwartz and D. L. Johnson. Long-wavelength acoustic propagation in ordered and disordered suspensions. *Physical Review B*, 30 (8):4302–4313, 1984.

[147] J. Sessarego, J. Sageloli, R. Guillermin, and H. Überall. Scattering by an elastic sphere embedded in an elastic isotropic medium. *J. Acoust. Soc. Am.*, 104:2836–2844, 1998.

[148] R. Sheikhhassani and M. Dravinski. Scattering of a plane harmonic sh wave by multiple layered inclusions. *Wave Motion*, 51:517–532, 2014.

[149] S. E. Sherer. Scattering of sound from axisymetric sources by multiple circular cylinders. *J. Acoust. Soc. Am.*, 115 (2):488–496, 2004.

[150] A. L. Shuvalov. A sextic formalism for three-dimensional elastodynamics of cylindrically anisotropic radially inhomogeneous materials. *Proc. R. Soc. A*, 459(2035):1611–1639, 2003.

[151] B. Simon. *Orthogonal Polynomials on the Unit Circle. Part I - II.* AMS Colloquium Publications, Volume 54, 2005. Friedlander, S.J.:EDitor.

[152] A. Sinclair and R. Addison. Acoustic diffraction spectrum of a SiC fiber in a solid elastic medium. *J. Acoust. Soc. Am.*, 94:1126–1135, 1993.

[153] S. Sodagar, F. Honarvar, and A. N. Sinclair. Multiple scattering of an obliquely incident plane acoustic wave from a grating of immersed cylindrical shells. *Applied Acoustics*, 72:1–10, 2011.

[154] F. L. Spitzer and C. J. Stone. A class of toeplitz forms and their applications to probability theory. *J. Math.*, 4:253277., 1960. Illinois J. Math.

[155] T. Sumiya, S. Biwa, and G. Haïat. Computational multiple scattering analysis of elastic waves in unidirectional composites. *Wave Motion*, 51:253–270, 2014.

[156] G. Szegö. Beiträge zur Theorie der Toeplitzschen Formen. *Math.Z.*, 6:167–202, 1920.

[157] G. Szegö. *Orthogonal Polynomials.* American Mathematical Society Colloquium Publications, Vol. XXIII. American Mathematical Society. Providence, Rhode Island, 1959.

[158] P. Tchebichef. Sur les fractions continues. *J. de Math. Pures et Appliquées*, 3(2):289–323, 1858.

[159] E. N. Thrower. The computation of the dispersion of elastic waves in layered media. *J. Sound. Vib.*, 2:210–226, 1965.

[160] T. C. T. Ting. *Anisotropic Elasticity: Theory and Applications.* Oxford University Press, 1996.

[161] T. C. T. Ting. Pressuring, shearing, torsion and extension of a circular tube or bar of cylindrically anisotropic material. *Proc. R. Soc. A*, 452(1954):2397–2421, November 1996.

[162] A. Titovich and F. Amirkulova. Tuned elastic shells with matched acoustic impedance and sound speed in water. *J. Acoust. Soc. Am.*, 134(5):4067, 2013.

[163] A. Titovich and A. Norris. Acoustic scattering from an infinitely long cylindrical shell with an internal mass attached by multiple axisymmetrically distributed stiffeners. *submitted to J. Acoust. Soc. Am.*, 2014.

[164] O. Toeplitz. Zur theorie der quadratishen und bilinearen unendlichvielen veräderlichen, i Teil: Theories des l-formen. *Matt. Ann.*, 70:351–376, 1911.

[165] D. Torrent, A. Hákansson, F. Cervera, and J. Sánchez-Dehesa. Homogenization of two-dimensional clusters of rigid rods in air. *Phys. Rev. Lett.*, 96:204302, 2006.

[166] D. Torrent and J. Sánchez-Dehesa. Broadband acoustic cloaking based on the homogenization of layered materials. *Wave Motion*, 48:497504, 2011.

[167] W. Trench. An algorithm for the inversion of finite Toeplitz matrices. *SIAM J. Appl. Math,*, 12(3):515–522, 1964.

[168] N. L. Tsitsas and P. A. Martin. Finding a source inside a sphere. *Inverse Problems*, 28(1):015003+, Jan. 2012.

[169] V. Twersky. Multiple scattering of radiation by an arbitrary configuration of parallel cylinder. *J. Acoust. Soc. Am.*, 24(1):42–46, 1952.

[170] E. E. Tyrtyshnikov. *Toeplitz Matrices, Some Analogs and Applications (in Russian)*. OVM RAN,, 1989.

[171] H. Überall. Acoustics of shells. *Acoustical Physics*, 47:115–139, 2001.

[172] Y. Urzhumov, F. Ghezzo, J. Hunt, and D. R. Smith. Acoustic cloaking transformations from attainable properties. *New J. Phys.*, 12:073014, 2010.

[173] V. Varadan and V. K. Varadan. Configurations with finite numbers of scatterers—a self-consistent T-matrix approach. *J. Acoust. Soc. Am.*, 70(1):213–217, 1981.

[174] V. Varadan and V. K. Varadan. Comments on recent criticism of the T-matrix method. *J. Acoust. Soc. Am.*, 84(6):2280–2284, 1988.

[175] V. Varadan, V. K. Varadan, and Y.-H. Pao. Multiple scattering of elastic waves by cylinders of arbitrary cross section. i. sh waves. *J. Acoust. Soc. Am.*, 63(5):1310–1319, 1978.

[176] V. K. Varadan, Y. Ma, and V. V. Varadan. Multiple scattering of compressional and shear waves by fiber-reinforced composite materials. *J. Acoust. Soc. Am.*, 80(1):333–339, 1986.

[177] V. K. Varadan and V. V. Varadan, editors. *Acoustic, Electromagnetic and Elastic Wave Scattering - Focus on the T - matrix Approarch*. Pergamon Press Inc, 1980.

[178] V. Varatharajulu. Reciprocity relations and forward amplitude theorems for elastic waves. *J. Math. Phys.*, 18(4):537–543, 1977.

[179] F. G. Vasquez, G. W. Milton, and D. Onofrei. Active exterior cloaking for the 2D Laplace and Helmholtz equations. *Phys. Rev. Lett.*, 103:073901, 2009.

[180] F. G. Vasquez, G. W. Milton, and D. Onofrei. Broadband exterior cloaking. *Opt. Express*, 17:14800–14805, 2009.

[181] F. G. Vasquez, G. W. Milton, and D. Onofrei. Exterior cloaking with active sources in two dimensional acoustics. *Wave Motion*, 49:515–524, 2011.

[182] F. G. Vasquez, G. W. Milton, D. Onofrei, and P. Seppecher. Transformation elastodynamics and active exterior acoustic cloaking. In S. Guenneau and R. Craster, editors, *Acoustic Metamaterials: Negative Refraction, Imaging, Lensing and Cloaking*, pages 1–1. Canopus Academic Publishing and Springer SBM, 2012.

[183] N. D. Veksler, J. L. Izbicki, and J. M. Conoir. Elastic wave scattering by a cylindrical shell. *Wave Motion*, 1999.

[184] V. Voevodin. *Foundations of Numerical Linear Algebra*. Nauka-Press, 1977.

[185] V. V. Voevodin and E. E. Tyrtyshnikov. *Numerical Processes with Toeplitz Matrices*. Nauka, Moscow (in Russian), 1987.

[186] P. C. Waterman and R. Truell. Multiple scattering of waves. *Journal of Mathematical Physics*, 2(4):512–537, 1961.

[187] A. Werby. The acoustical background for a submerged elastic shell. *J. Acoust. Soc. Am.*, 90:3279–3287, 1991.

[188] A. Wirzba. Quantum mechanics and semiclassics of hyperbolic n-disk scattering systems. *Physics Reports*, 309:1 – 116, 1999.

[189] R. Yang and A. K. Mal. Multiple scattering of elastic waves in a fiber-reinforced composite. *J. Mech. Phys. Solids*, 42:1945–1968, 1994.

[190] C. F. Ying and R. Truell. Scattering of a plane longitudinal wave by a spherical obstacle in an isotropically elastic solid. *J. Appl. Phys.*, 27:1086–1097, 1956.

[191] F. Záviška. Über die beugung elektromagnetischer wellen an parallelen, unendlich langen kreiszylindern. *Annalen der Physik, 4 Folge*, 40:10231056, 1913.